




ADVERTIMENT. L'accés als continguts d'aquesta tesi queda condicionat a l'acceptació de les condicions d'ús establertes per la següent llicència Creative Commons:  <https://creativecommons.org/licenses/?lang=ca>

ADVERTENCIA. El acceso a los contenidos de esta tesis queda condicionado a la aceptación de las condiciones de uso establecidas por la siguiente licencia Creative Commons:  <https://creativecommons.org/licenses/?lang=es>

WARNING. The access to the contents of this doctoral thesis it is limited to the acceptance of the use conditions set by the following Creative Commons license:  <https://creativecommons.org/licenses/?lang=en>

PhD Thesis



Universitat Autònoma
de Barcelona

Departament
d' Enginyeria
Electrònica

[Novel high-resolution BAW ultrasonic sensors based on CMOS-compatible AlN transducers operated in a pulse-echo scheme]

Jesús Yáñez Sotelo

2023

Director: Nuria Barniol, PhD.

Preface

This effort consists of a compilation of my research work performed from October 2018 to September 2021 in the Departament d' Enginyeria Electrònica, at Bellaterra, Spain, and it has been submitted to Universitat Autònoma de Barcelona in partial fulfillment of the requirements for the degree of DOCTOR OF PHILOSOPHY. This PhD thesis has been supervised by Professor Nuria Barniol, Full Professor at the University and Leader of the Electronics Circuits and Systems Research Group (ECAS).

Jesús Yáñez Sotelo
2023

Acoustic wave technologies and devices have been in commercial use for telecommunications, pressure sensing for automotive, non-destructive testing and healthcare for more than 60 years; their application also extends to industry and academia, where dozens of physical, chemical, and biological sensors can be found. Most acoustic wave devices can be used as sensors because they are sensitive to mechanical, chemical, or electrical perturbations on their surfaces, being able to monitor not only mass/density changes, but also changes in elastic modulus, viscosity, dielectric and conductivity properties. Examples of sensors based on acoustic waves include: temperature sensors, moisture, strain, pressure, shock, acceleration, flow, viscosity, ionic contaminants, pH levels, electric, magnetic and radiation fields, gas and explosives.

The Quartz Crystal Microbalance (QCM), a resonator made of a piezoelectric material sandwiched between two metallic electrodes, embodies the typical operating mechanism of most acoustic wave devices: By applying an alternate voltage to its electrodes, the structure experiences deformations at a determined resonant frequency, which may change depending on disturbances on its surface such as addition or removal of mass or changes on their environment such as temperature drift. Despite the extensive use of QCM in various disciplines of science and technology in past decades, current thin film acoustic wave devices fabricated with MEMS technology are smaller, thinner, can reach higher frequencies for improved resolution and can be monolithically integrated with CMOS circuitry, thus offering low-cost and mass production of acoustic wave microsensors ready to be integrated in Lab-on-a-Chip systems. The Thin Film Bulk Acoustic Resonators (FBAR) are the latest development thin film acoustic wave devices; they have a structure similar to QCM devices but with the advantage of being several orders of magnitude smaller and capable of work in the GHz range, which provides them with superior sensitivity. Unfortunately, membrane-type FBARs have low yield at fabrication due to residual stress and when operating as sensors they tend to be brittle when submerged in liquid environments, whereas FBARs using Bragg acoustic mirrors require multiple precisely controlled deposition steps for the acoustic mirrors, raising complexity of the device and causing its performance to be dependent on manufacturing defects. The output signal of most acoustic wave sensors is frequency shift of their resonance modes, which are correlated with quantitative measurement of physical changes on the detection surface or chemical or biological molecules bound to the chemically modified surface in the case of biosensors.

The latter represents one of the main drawbacks of current acoustic wave devices; most of them require elaborate mechanisms for signal control and relatively complex read-out circuitry capable of detecting frequency shift in the impedance curve caused by changes of the acoustic load coupled to the resonator. To overcome that problem, this work describes the design, simulation, characterization and tests of a BAW sensor operating in longitudinal mode capable of studying the compressional properties of fluids by interrogating the liquid samples with short pulses of ultrasound. This would allow applications such as identification and classification different liquids at microscale or studying concentration changes of mixtures simply by measuring difference in output voltage level.

This contribution overcomes current restrictions of film acoustic resonators such as fragility of operation in liquid environments, high manufacturing cost or limitations regarding narrow microchannels; offering an alternative to applications that demand ultra-low consumption, miniaturization, versatility and ease of readout.

Acknowledgements

Initially, I would like to thank Dr. Nuria Barniol for directing this work during my stay in her research group. Her advice and proposals was the key to participation in international conferences and to maintaining optimism throughout three years of design, manufacturing and many hours in the laboratory. It has been an honor to know her and gain some of her knowledge and values.

Thanks to Dr. Arantxa Uranga for her advice in laboratory seminars and for her support with doctoral administrative stuff. I am grateful to my lab partners Ivan and Vassil for their technical support and tips for Finite Element Analysis simulations. Special thanks to Eyglis for her lessons regarding the use of lab instrumentation and for hers CAD designs of PMUTs, which I have included in this thesis as “alternative solid resonators”. I must thank Dr. Anibal Pacheco for his help on radio frequency issues and tips for de-embedding of scattering parameters. Special thanks to Javier Hellín for his enormous support in the creation of test devices, test boards and other laboratory gadgets, without forgetting the photography lessons he gave me when we had free time. Thanks to my "family" in Barcelona, Antonio and Yanet, who welcomed me into their place and made me feel at home. Finally, I thank the city of Barcelona for the pleasant stay, for the friendships I have made on the bicycle, and for the unforgettable walks across its streets that helped distract me when things went difficult.

I am especially grateful to my wife, who motivated me to pursue my doctorate and for her strength when the pandemic put "an ocean of distance" between us for more than a year. I thank my parents and siblings, for their unconditional support in all my projects. Thanks to my little nephews; who unknowingly have motivated me to finish this document.

Thank God for all of the above.

Contents

Preface	ii
Summary	iii
Acknowledgements	v
Chapter 1: Introduction	
1.1 Introduction	1
1.2 Acoustic wave technology overview	2
1.2.1 Propagation modes of acoustic waves	4
1.2.2 The Quartz Crystal Microbalance (QCM)	5
1.3 MEMS based acoustic wave devices (thin film piezoelectric MEMS)	6
1.3.1 Surface Acoustic Wave devices (SAW)	7
1.3.2 Thin Film Bulk Acoustic Resonators (FBARs)	8
1.4 High-overtone Bulk Acoustic Resonator (HBAR)	12
1.5 Motivation and contributions of this thesis	13
1.5.1 Motivation of the thesis	13
1.5.2 Contributions to the art	14
1.5.3 Academic contributions	14
1.6 Thesis outline	15
References	16
Chapter 2: Theory	
2.1 System description	26
2.1.1 HBAR sensor working as a Pulse-Echo Transducer	27
2.1.2 HBAR sensor working as an Acoustic Resonator	28
2.2 Studying fluid compressional properties at microscale using longitudinal bulk acoustic waves	29
2.3 Piezoelectric transduction in longitudinal BAW devices and their input impedance	30
2.4 Input impedance of HBARs with electrodes of non-negligible thickness	35
2.5 Distribution of acoustic pulses at the detection surface	39
References	43
Chapter 3: Design, Simulation, and Fabrication	
3.1 Selection of the piezoelectric material and the manufacturing process	45
3.1.1 Piezoelectric materials	45
3.1.2 Manufacturing process	46
3.2 Operating frequency	49
3.2.1 Acoustic resonators based on the PiezoMUMPs process	49
3.2.2 Pulse-echo transducer based on the PiezoMUMPs process	53
3.3 Microtransducer Design	54

3.3.1 Effective area (lateral dimensions) and expected Time-of-Flight for the Pulse-echo devices	55
3.3.2 Effective area (lateral dimensions) of the Resonating devices	57
3.4 Finite Element Simulations	59
3.4.1 FEM for Acoustic Resonators (input impedance and measuring principle)	60
3.4.2 FEM for Pulse-echo Transducers (input impedance and measuring principle)	64
3.5 Fabrication	
3.5.1 Process overview	73
3.5.2 Process flow for Acoustic Resonators	74
3.5.3 Process flow for the Pulse-Echo Transducers	80
References	84
Chapter 4: Characterization & Experimental Setup	
4.1 Electrical Characterization for Acoustic Resonators	87
4.1.1 Measurement of scattering parameters	88
4.1.2 Measurement of electromechanical coupling k_{eff}^2	90
4.2 Carrier waveguide, S_{11} measurement calibration (de-embedding), and S_{11} to Z conversion	91
4.2.1 Design of the carrier PCB (Grounded Coplanar Waveguide)	91
4.2.2 S_{11} measurement calibration (de-embedding)	93
4.2.3 Conversion from S_{11} to Z_{in}	96
4.3 Electrical Characterization for the Pulse-Echo Transducers	98
4.4 Test Setup for pulse-echo transducers, Frequency & Time response, and Digital Filtering (post-processing)	100
4.4.1 Test setup for pulse-echo transducers	100
4.4.2 Frequency and Time responses for the pulse-echo system	103
4.4.3 Digital filtering & post-processing for received echoes	104
References	107
Chapter 5: Results and Conclusions	
5.1 HBAR device operating under a pulse-echo regime	109
5.2 Applications of pulse-echo transducers	110
5.2.1 Identification and classification of liquids by their specific acoustic impedance	111
5.2.2 Detection of concentration changes in solutions	113
5.2.3 Sensing of compressional properties of liquids (Acoustic impedance and Bulk Modulus)	116
5.3 Application of the alternative readout method (resonator)	117
5.4 Conclusion and Outlook	120
5.4.1 Other feasible applications: Multiphase flow sensor for real-time detection of slug velocity in microchannels and impedance imaging (fingerprint sensor)	121
References	124
Appendix A: Code: MCU configuration, tools created for post-processing of measurement files and implementation of analytic models used for device design (MATLAB).	126

CHAPTER 1

Introduction

1.1 Introduction

Portability, faster reaction time and minimal reagent consumption are some of the future landscapes expected by the bio and chemical analysis at the microscale [1]. The term “Lab-on-a-chip” (LOC) refers to a developing technology entangled in scaling analytical laboratory processes down to a chip-format; it involves the manipulation and study of minute amounts of liquid samples flowing along channels with narrow dimensions ranging from tens to hundreds of micrometers. Nowadays, miniaturization techniques allow fabrication of structures, sensors and actuators with sub-micrometer precision (Figure 1.1), which has paved the way for emergent microfluidic applications such as point-of-care diagnostics, genomic and proteomic research, analytical chemistry, environmental monitoring, and the detection of biohazards [2].

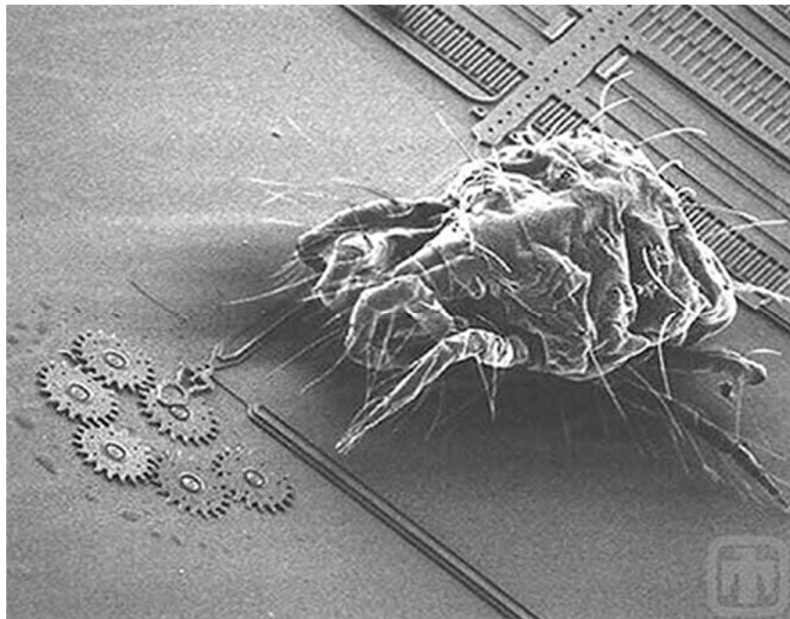


Figure 1.1: SEM image of a mite approaching to microscale gears
(Image: Sandia National Laboratories, www.mems.sandia.gov).

The term "sensor" refers to devices that detect and monitor a physical or chemical parameter (i.e. vibration, pressure, and flow), and provide an output signal that is a function of changes in the measured physical phenomenon [3], whereas “actuator” refers to a devices driven by an input signal

in order to produce stress/strain, force/torque or mechanical motion. Both sensors and actuators are collectively categorized as "transducers", which refers to devices that convert energy from one domain to another [4]. Currently, transducers can be fabricated at micro/nanoscale using microelectromechanical systems technology (MEMS), which takes advantage of the well-established semiconductor fabrication processes to create microactuators, microsensors, electric and electronic components and diverse other mechanical devices at a chip-level [5]. MEMS transducers comprise a multi-billion industry ranging from tire pressure automotive sensors to the accelerometers and gyroscopes included in almost every consumer electronic device [6].

One of the world's largest and fastest-growing industries for MEMS research is the healthcare industry, where multiple medical applications such as microneedles [7, 8], cardiac devices [9, 10], *in-vivo* drug delivery systems [11–14], and lab-on-a-chip systems [15–17] for fast chemical/biological analysis have been demonstrated. The key technology behind a “lab-on-chip” is microfluidics, a class of MEMS devices meant to handle tiny volumes of liquids (typically from a few picolitres to a few of microliters), enabling point-of-care diagnosis and providing a portable solution to analyze body fluids in a very cost-effective way [18].

Microfluidic technology is more than microchannels, such systems typically involve: Methods for introducing reagents and samples (micro-valves and/or micropumps [19]), methods for moving these fluids around the different stages of the chip and for combining and mixing liquids (micro-mixers, micro-filters [20]), and various other components for detection and analysis (micro-sensors, and micro-reservoirs [21, 22]). However, one of the major challenges is that sensing and actuating functions are done through different mechanisms which are often fabricated using different processes and materials [23]. In this regard, acoustic wave devices offer the possibility of being used for both sensing and actuation; therefore, most of the preparation and sensing tasks can be implemented solely using acoustic devices, reducing costs and complexity of the whole system.

1.2 Acoustic wave technology overview

Acoustic wave technologies and devices have been in commercial use for telecommunications [24, 25], pressure sensing for automotive [26–28], environmental sensing [29–33] and healthcare [34–38] for more than 60 years [39]; their application also extends to industry and academia, where dozens of physical sensors for humidity, temperature, mass, etc. can be found [40–45]. In the case of biosensors, acoustic sensors stand out from other label-free approaches such as the Surface Plasmon Resonance spectroscopy (SPR) [46], sensors based in nanowires [47] or nanotubes [48], microcantilevers [49], and photonic techniques such as sensors based in photonic crystals [50], optical microcavity resonators [51], reflective interferometry [52], and imaging ellipsometry [53]; as they can be used for both bio-sensing and microfluidics applications (actuation), which are the major components in lab-on-a-chip systems, thus offering simple operation (electrical signal), high sensitivity, small size, low cost, and no need for bulky optical detection systems [54]. Modern sensor research is largely focused on label-free detection protocols [55] since the labeling process (typically performed using fluorescent markers, enzymes, radioactive species, or quantum dots) impede real-time binding kinetics, as well as they require additional time and imply increased costs [56].

Acoustic wave transducers are so named because their detection mechanism is a mechanical or acoustic wave generated by a piezoelectric element included in the device. Piezoelectricity refers to the production of electrical charges in a material when it is subjected to mechanical stress (direct piezoelectric effect) and vice versa; when an electrical field is applied the material undergoes mechanical deformation (inverse piezoelectric effect) [57]. This occurs in anisotropic materials whose internal structures lack a center of symmetry. Some piezoelectric materials include: quartz (SiO_2), lithium tantalite (LiTaO_3), lithium niobate (LiNbO_3), sapphire (Al_2O_3), lead zirconate titanate ($\text{Pb}(\text{Zr},\text{Ti})\text{O}_3$, PZT), barium strontium titanate ($\text{Ba}_x\text{Sr}_{1-x}\text{TiO}_3$, BST), AlN, ZnO, GaN, SiC and InN [58]. Figure 1.2 offers an example of a MEMS device based on the direct piezoelectric effect.

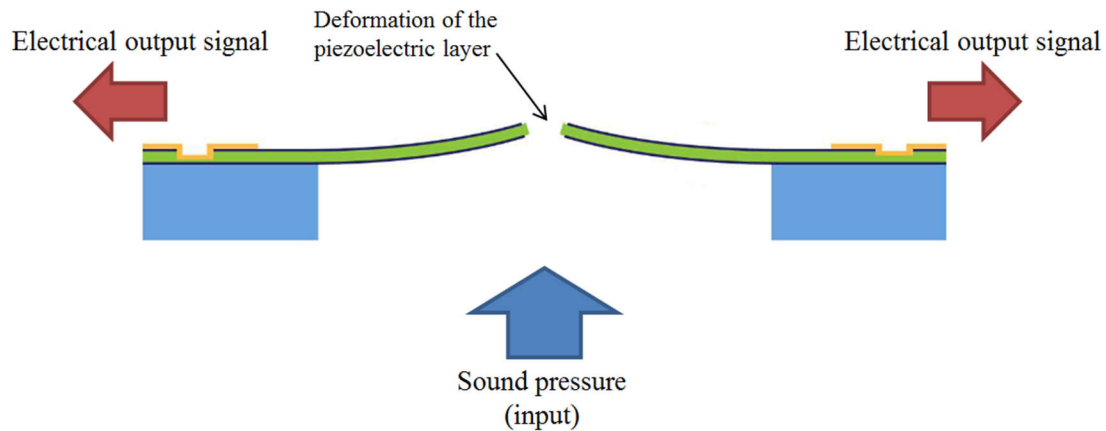


Figure 1.2: Piezoelectric Microphone. This type of microphone exploits the direct piezoelectric effect, in which incoming pressure sound waves deflect the material generating electrical charges on the plates. That is converted to a voltage output signal (Vesper Technologies Inc.).

As generated acoustic waves propagate through or on the surface of the material, changes to the characteristics of the propagation path affect the velocity or amplitude of the wave. Changes in velocity can be monitored by measuring the frequency or phase characteristics of the sensor and can then be correlated to the corresponding physical quantity being measured. Wave variations can be attributed to: a) Intrinsic factors such as material properties: density, elasticity, phase transformation, viscosity, conductivity, permittivity, changes in carrier concentration and mobility. b) Extrinsic factors such as mass loading, temperature, deformation, pressure, strain, stress, humidity, pH values, ultraviolet (UV) and infrared (IR) sources, externally applied electric/magnetic fields and charge injection [23].

Most acoustic wave devices can be used as sensors because they are sensitive to mechanical, chemical, or electrical perturbations on their surfaces, being able to monitor not only mass/density changes, but also changes in elastic modulus, viscosity, dielectric and conductivity properties [39]. Examples of sensors based on acoustic waves include: temperature sensors, moisture, strain, pressure, shock, acceleration, flow, viscosity, ionic contaminants, pH levels, electric, magnetic and radiation fields, gas and explosives [59].

1.2.1 Propagation modes of acoustic waves

Acoustic waves are elastic waves propagating through gases, liquids and solids; its propagation in bulk solids is divided in two main categories: Longitudinal (compressional) waves, and transverse (shear) waves [60]. In longitudinal waves, also known as compressional or pressure waves, the particle displacement is parallel to the direction of wave propagation i.e. particles oscillate back and forth relative to their individual equilibrium positions and in the same direction of wave propagation as depicted in Figure 1.3a, that is, energy propagates through rarefaction and compression of an elastic medium. On the other hand, particle displacement in transverse waves occurs perpendicular to the direction of wave propagation, that is, particles do not move along with the direction of wave propagation as represented in Figure 1.3b. Other elliptical or complex vibrations of particles are possible in solids, such as the surface (Rayleigh) waves and the Lamb (plate) waves. Rayleigh waves are perturbations traveling along the surface of solid materials; in this case particle motion is described as a combination of both longitudinal and transverse components [61], moving in an elliptical path as shown in Figure 1.3c.

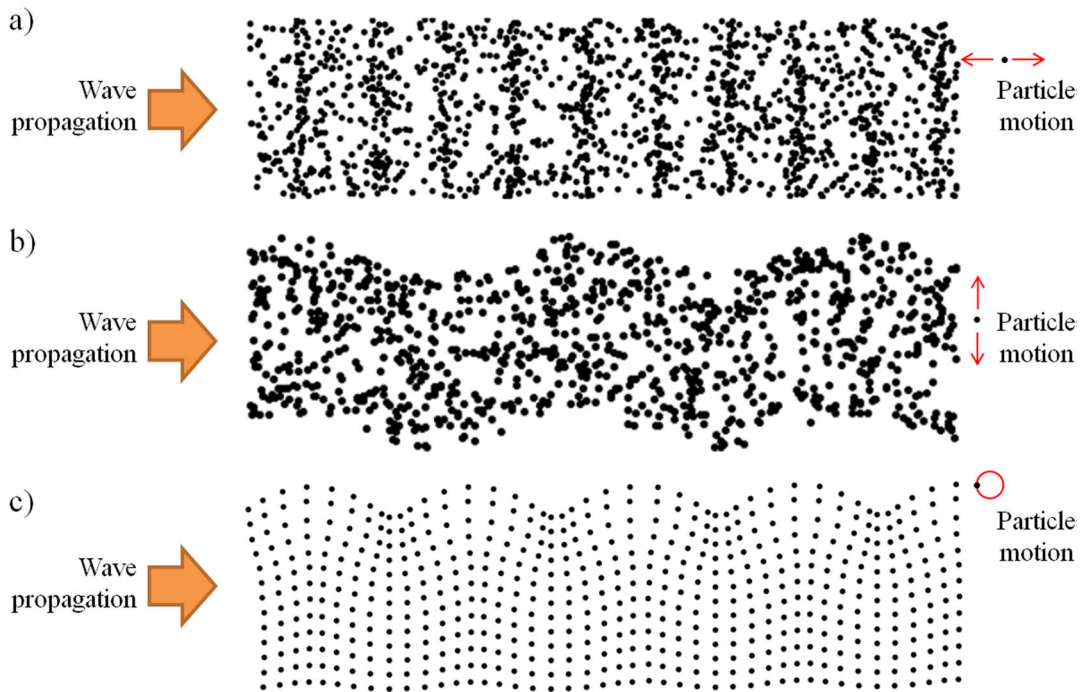


Figure 1.3: Propagation modes of acoustic waves in bulk solids. a) In longitudinal waves the particle displacement is parallel to the direction of wave propagation; particles oscillate back and forth relative to their individual equilibrium positions and in the same direction of wave propagation. b) In shear waves the particle displacement is perpendicular to the direction of wave propagation; particles oscillate up and down whereas the wave propagation is left to right. c) In surface waves (Rayleigh) particle motion describes elliptical paths; it is a combination of both longitudinal and transverse waves.

It is important to emphasize that compression waves (longitudinal) are the only mode of propagation in liquids and gasses [60], so transducers operating in shear mode are considered to be better for operation in liquids than those operating in longitudinal mode since a shear acoustic transducers does not displace molecules perpendicular to the resonator surface, and there is considerably less energy radiated into the liquid than the case of longitudinal devices [56].

Acoustic wave transducers are mainly categorized in two classes: a) Bulk Acoustic Wave devices (BAW), where the generated acoustic waves propagate through the material, and b) Surface Acoustic Wave devices (SAW), where acoustic waves propagate on the surface of the material. Figure 1.4 shows the different modes of BAW and SAW devices [23].

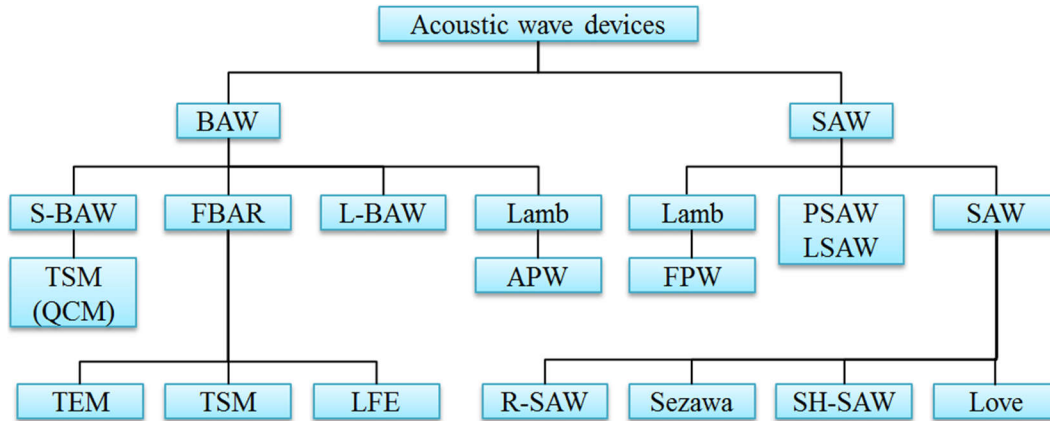


Figure 1.4: Classification of acoustic wave devices. On the one hand, the main types of BAWs are Longitudinal BAW (L-BAW), shear BAW (S-BAW), acoustic plate Love wave (APW) and the Thin-Film Bulk Acoustic Resonator (FBAR) working on thickness extension mode (TEM), thickness shear mode (TSM) or lateral field excitation (LFE). On the other hand, the main types of SAWs are the pseudo-surface acoustic waves (PSAW) or Leaky SAWs (LSAW), the flexural plate Love wave (FPW), and different modes of SAW such as the Rayleigh SAW (R-SAW), Sezawa mode waves, shear-horizontal SAWs (SH-SAWs) and SAW producing Love waves.

1.2.2 The Quartz Crystal Microbalance (QCM)

The most commonly reported BAW device is the quartz crystal microbalance (QCM) [62]. It is a thickness shear mode (TSM) resonator made of a piezoelectric material (typically quartz) sandwiched between two metallic electrodes. On applying an alternate voltage signal to its electrodes, the structure experiences shear deformations at a determined resonant frequency. That frequency is modified depending on disturbances on its surface such as addition or removal of mass or depending on their environment (exposure to air or liquid, temperature, etc.) [63]. QCM is suitable for both gas and liquid operation because it works on thickness shear mode, which minimizes radiation of energy in liquid media. Figure 1.5a offers a 3D representation of this device.

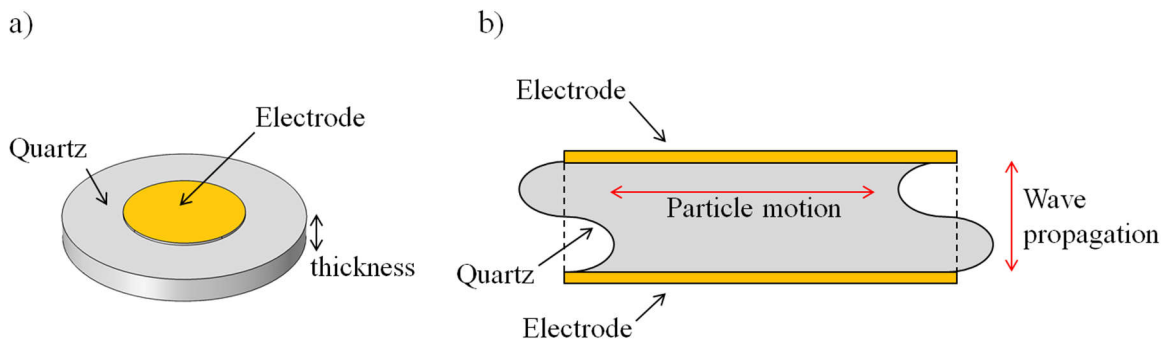


Figure 1.5: A schematic view of quartz crystal microbalance (QCM). a) 3D representation showing the quartz piezoelectric material and its top electrode. b) 2D representation of the QCM working in thickness shear mode, where individual particle movement is perpendicular to wave propagation.

The typical application of QCM is as a thickness monitor for deposited solid thin films [64], but it have been used in diverse applications in various disciplines of science and technology: Detection of metals in vacuum, vapors, chemical analytes, environmental pollutants, biomolecules [66, 67], disease biomarkers, cells, and pathogens, corrosion studies, detection in gas chromatography, and in industry for controlling thickness and composition of sputtered materials [63]. The frequency shift Δf due to mass deposition Δm of elastic subjects, which do not dissipate any energy during oscillation, is explained by the Sauerbrey equation as [65]:

$$\Delta f = \frac{2f_0^2}{S_A\sqrt{\rho_q\mu_q}}\Delta m$$

Where: f_0 is the resonant frequency of the fundamental mode in Hz (typically 10 MHz [55]), S_A is the electrode area in cm^2 , and ρ_q and μ_q are density and shear module of quartz respectively. This equation shows a linear relationship between the resonant frequency shift and mass loaded onto any resonator as long as the deposited mass is rigid, distributed evenly in the surface, and the frequency change is less than 2%. Sauerbrey's equation dictates that mass sensitivity is subjected to the fundamental resonance frequency of the device. The fundamental mode f_0 of a cavity of thickness t is $t = \lambda/2$, and in turn the frequency is related to the velocity of sound waves in the material as $v = f/\lambda$, therefore the resonance frequency depends on the thickness of the quartz wafer:

$$f_0 = \frac{v}{2t}$$

Unfortunately, resonance frequencies for QCM are limited to tens of MHz because the thickness of practical devices typically ranges 0.5 – 1 mm; reducing thickness beyond this point would make them mechanically unstable and fragile, limiting the achievable mass sensitivity [68]. Moreover, their large surface area ($\sim 1 \text{ cm}^2$) and their bulk structure nature are not ideal for integration with CMOS circuitry, limiting their applications as biosensors in terms of cost, operation, scalability and miniaturization [62]. Recently there has been an accelerated development of MEMS fabrication and piezoelectric thin film deposition technologies mainly driven by the mobile communications industry. As the thickness of the piezoelectric determines the frequency of resonance in thickness-mode resonators, current thin film devices with sub-micrometer thickness are able to reach resonant frequencies of tens of GHz [69].

1.3 MEMS based acoustic wave devices (thin film piezoelectric MEMS)

The study of acoustic resonators based on piezoelectric thin films began in the 1980s, with suspended piezoelectric membranes creating bulk longitudinal acoustic waves, achieving resonance frequencies of hundreds of MHz [70]. However, enthusiasm waned in the early 1990s due to the fragility of the membranes and low reproducibility of the device [68]. Years later, with the development of MEMS micromachining techniques and the improvement in piezoelectric material deposition techniques, the strength issues vanished allowing the arrival of novel applications such as micrometric accelerometers, ultrasonic and force microsensors, microactuators, MEMS microphones, and energy harvesting transducers [71]. Currently, lithography techniques inherited from the semiconductor industry allow accurate thickness control and selective deposition of piezoelectric material [72]. In this way, other components, such as microchannels, can be directly

fabricated on the same substrate without presence of the piezoelectric material. Furthermore, thin film acoustic wave devices can be monolithically integrated with standard CMOS technologies in the same wafer, improving the system performance whereas cost and footprint is reduced.

Thin film acoustic wave devices fabricated with MEMS technology are smaller, thinner, can reach higher frequencies and can be monolithically integrated with CMOS circuitry, allowing low-cost mass production of acoustic wave microsensors. The Surface Acoustic Wave devices (SAW) and the Thin Film Bulk Acoustic Resonators (FBARs) are the most used acoustic wave devices based on MEMS.

1.3.1 Surface Acoustic Wave devices (SAW)

A typical Surface Acoustic Wave device based on MEMS technology consists of metallic interdigitated transducers (IDTs) lithographically patterned over a piezoelectric substrate. They could be used as resonators or as delay lines depending of the design of the IDTs; SAW resonators IDTs are fabricated in a central position with acoustic reflectors on both sides to trap the acoustic energy within a cavity, whereas SAW delay lines consist of a transmitter IDT to generate surface acoustic waves and a receiving IDT to detect those waves [73]. Figure 1.6a presents a 3D schematic of a Rayleigh mode SAW (R-SAW) sensor in the delay line configuration.

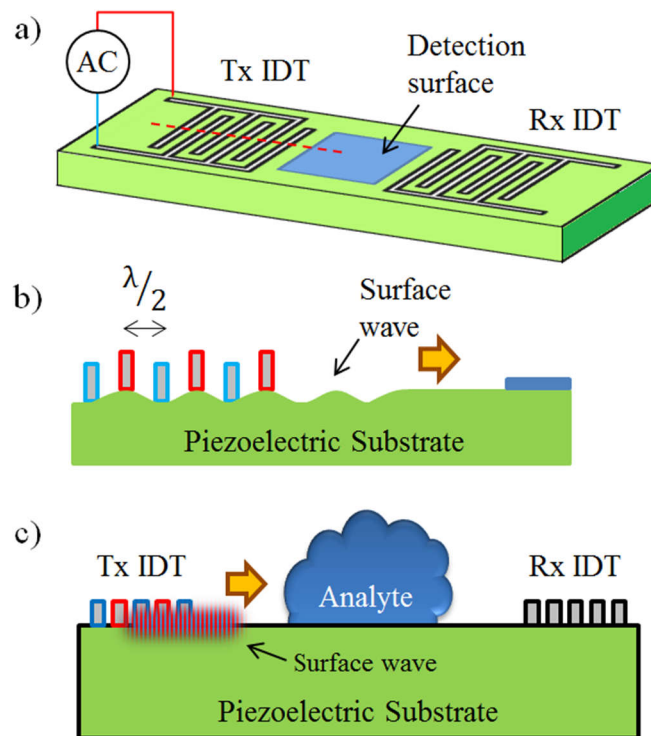


Figure 1.6: Schematic of a SAW sensor in the delay line configuration. a) 3D representation of the device consisting of metallic IDTs lithographically patterned over a piezoelectric substrate. b) 2D cross-sectional schematic showing the operation mechanism; when an alternating electric signal is applied to the Tx IDT, a Rayleigh wave is generated in the piezoelectric substrate. c) The analyte is located in the path of the wave; changes in the output signal are correlated to physical or chemical changes in the detection surface.

In the delay line configuration, each IDT is an array of comb-shaped electrodes connected to an alternating voltage source to create alternating positive and negative electric fields between its metallic fingers. Due to the inverse piezoelectric effect, these alternating regions induce mechanical strains between the fingers of the electrodes producing Rayleigh waves on the surface of the substrate [74]. The 2D cross-sectional representation of the transmitter transducer (Tx IDT) in Figure 1.6b shows a simplified schematic of the operation mechanism; when the alternating electric signal is applied to the Tx IDT, the alternate polarity of the half-wavelength-separated electrodes causes compression and rarefaction of the piezoelectric material and thereby an acoustic wave that travels along the substrate surface is generated [75].

As shown in Figure 1.6c, the produced Rayleigh wave propagates along the surface until it reaches the receiving transducer (Rx IDT), which is another set of interdigitated electrodes that uses the direct piezoelectric effect to produce an output electrical signal in response to the received mechanical perturbation. Since the surface wave has to cross the detection surface on its way from the Tx IDT to the Rx IDT, the recorded changes in the output signal such as a time delay in the acoustic wave propagation, frequency shift or amplitude attenuation are correlated to physical or chemical changes in the detection surface.

R-SAW devices could offer frequencies in the GHz range, and thus enhanced sensitivity compared to QCM [55]. They have found a large number of applications as sensors, including viscosity and density sensors [76, 77], temperature sensors [78, 79], gas sensors [80–82], and also for microfluidics (actuators) [83–86], however, they are unsuitable for liquid phase sensing or humid conditions due to dissipation of the acoustic wave energy into the liquid. This problem is addressed by the shear SAW devices (SH-SAW) and the Love mode devices; in SH-SAWs the cutting angle of the piezoelectric is adjusted in such way that the particle displacement is changed to the shear mode, which does not significantly couple acoustic energy into the liquid, whereas the Love mode devices use the same SH-SAW structure adding a thin wave-guide layer over its surface causing acoustic energy to remain trapped within this thin layer. Both approaches allow real-time sensing in liquid media [87, 88], but are inefficient actuators for microfluidic applications [23].

Since diffraction is related to the length of the fingers in IDTs [75] and due to the requirement of both an input IDT and an output IDT, the footprint of these devices is large compared to other MEMS acoustic devices such as the Thin Film Bulk Acoustic Resonator (FBAR), limiting its use in miniaturized systems

1.3.2 Thin Film Bulk Acoustic Resonators (FBARs)

Similarly to the Quartz Cristal Microbalance, Thin Film Acoustic Resonators (FBARs) are Bulk Acoustic Wave devices with similar structure and operation principle, however, the thickness of the piezoelectric layer in FBARs is several orders of magnitude thinner due to current advances in microfabrication and deposition techniques; allowing the creation of sub-micron thick piezoelectric layers [62]. Since the fundamental mode f_0 of a BAW resonator in longitudinal mode depends on both the thickness t and the sound velocity v in the material ($f_0 = v/2t$), resonance of FBARs ranges from sub-GHz to tens of GHz, enabling higher sensitivity as sensor than QCM and SAW according to the Sauerbrey equation [68].

The basic configuration of FBAR consists of a thin piezoelectric film membrane sandwiched between two metallic electrodes of negligible thickness as depicted in Figure 1.7a. The active layer is acoustically isolated from the supporting substrate in such way that when applying an alternating electric voltage across the electrodes a standing wave is generated within the piezoelectric as shown in Figure 1.7b. The acoustic energy remains confined in the piezoelectric material due to the large acoustic impedance mismatch between the solid materials of the resonator and the air [89]. There are two basic resonating modes in FBARs devices; the thickness longitudinal mode (TLM), which confines a longitudinal wave between the electrodes and the thickness shear mode (TSM), which confines a shear wave [55]. The key difference is the 34.5° orientation of the piezoelectric crystal in thickness shear mode FBARs [90].

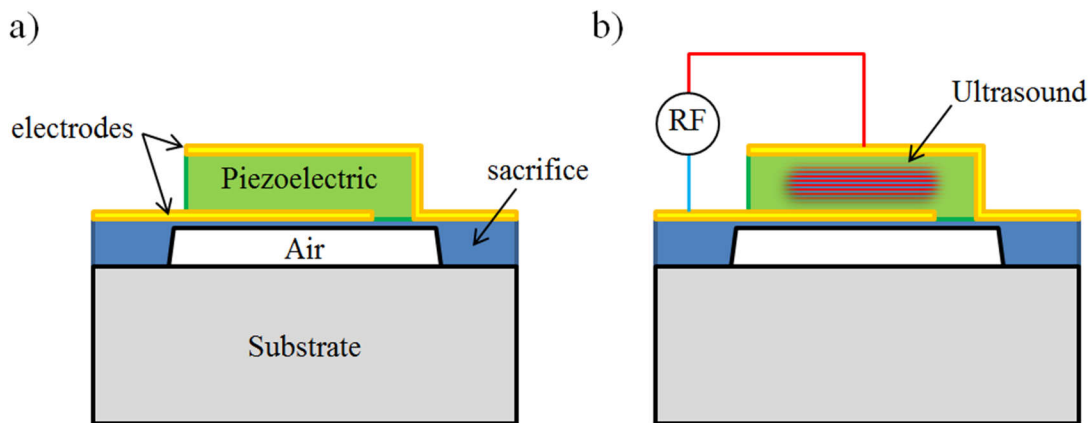


Figure 1.7: 2D cross-section schematic of an FBAR operating in longitudinal mode (thickness extension).
a) Basic configuration of a FBAR device; it consist of a thin piezoelectric layer sandwiched between two metallic electrodes of negligible thickness, acoustically isolated from the supporting substrate. b) By applying a voltage signal to its electrodes, a standing mechanical wave is generated within the active layer and it remains trapped due to acoustic impedance mismatch between solids and air.

The most important application of FBARs is as filters and duplexers in smartphones and telecommunications equipment; however, they have been extensively studied for sensing applications recently [73]. The detection principle as a sensor is similar to QCM and it follows the Sauerbrey equation; the resonance frequency f_0 decreases when additional mass is loaded to the sensing surface, which is typically located on the upper electrode. The output signal of FBAR sensors is usually frequency, therefore resonant frequency shift can be correlated with quantitative measurement of physical changes on the detection surface or chemical or biological molecules bound to the chemically modified surface in the case of biosensors. Due to the reduced base-mass and higher operation frequency respect to QCM and SAW, small changes on the detection surface cause large frequency shifts (typically in the MHz range), making the signal easily detected with electronic circuitry [62].

Typical applications of FBARs as sensors are detection of mass changes to calculate concentration of an analyte (gravimetric measurements) [91, 92], however, multiple applications have recently emerged such as: pressure and temperature sensors [93–95], viscosity sensors [96, 97], humidity [98, 99], electromagnetic waves [100, 101], etc., being the TLM FBARs mainly used in gaseous phase sensing, while the TSM devices are able to work in both dry and liquid environments due to their lower dissipation of acoustic energy in the liquid media [102].

FBARs are typically manufactured either by using bulk micromachining (trench-type FBAR), or by etching a sacrificial layer (air-cavity FBAR). In the former, a suspended piezoelectric membrane and its excitation electrodes are left after etching away the bulk substrate underneath as depicted in the cross section representation of Figure 1.8a. Contrarily, the air-cavity FBARs require etching of a sacrificial layer previously buried below the piezoelectric material, as shown in Figure 1.8b. Both structures allow confinement of acoustic energy within the piezoelectric because it is effectively isolated from the substrate.

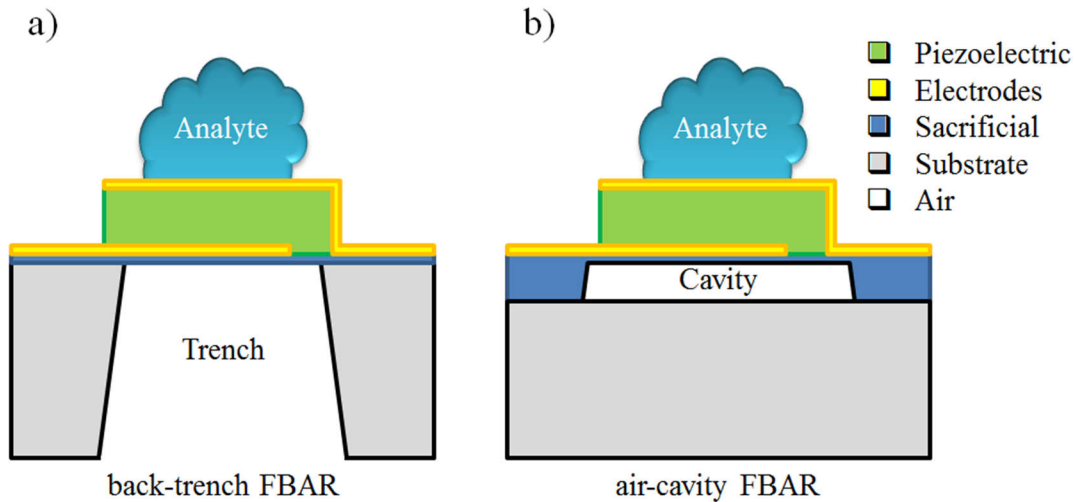


Figure 1.8: Schematics of membrane type FBARs with air boundaries to confine acoustic energy. a) Trench-type FBAR created from etching away the underlying substrate. b) Cavity-type FBAR created after selective etching of the sacrificial material previously deposited on the substrate

FBARs present various advantages over QCM or SAW, such as smaller footprint, reduced power consumption, increased sensitivity due to its operating frequency in the GHz range, and they can be fabricated monolithically together with RF circuitry [103]. However, membrane-type FBARs have low yield at fabrication due to residual stress and when operating as sensors they tend to be brittle when submerged in liquid environments [23]. A third type of FBARs known as Solidly Mounted Resonators (SMR) address these issues related to fragility of suspended membranes; in this case the resonator is acoustically isolated from the substrate by adding a Bragg Reflector to its structure, resulting in a completely solid structure of improved mechanical robustness as depicted in the scheme of Figure 1.9. The Bragg acoustic mirror in SMRs is composed of multiple pairs of quarter-wavelength layers with high acoustic impedance (Z_{ac}) contrast that effectively confines the acoustic energy within the transducer layer [104]. Since there are no air gaps in this structure, SMRs are useful when improved mechanical robustness and better heat dissipation capabilities are required. The Bragg mirror acts as an effective acoustic reflector so that standing waves can be similarly formed between the two metallic electrodes. In terms of sensitivity, the performance of an SMR is slightly lower compared to an identically designed FBAR resonating at the same frequency [105].

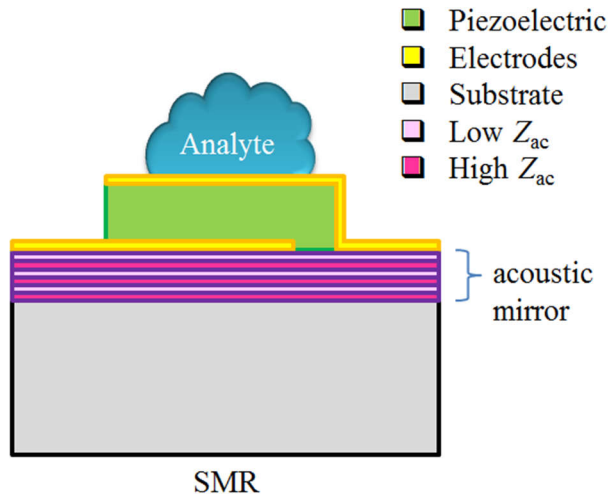


Figure 1.9: Schematic of a Bragg reflector type FBAR (SMR). The resonator is acoustically isolated from the substrate by adding a Bragg Reflector to its structure, resulting in a completely solid structure of improved mechanical robustness.

Unfortunately, SMRs require multiple precisely controlled deposition steps for the acoustic mirrors, raising complexity of the device and causing its performance to be dependent on manufacturing defects.

Table 1.1 offers a comparative of the key parameters of QCM, SAW, and FBAR.

	QCM	SAW	FBAR
Typical constitutive materials	Quartz Au electrodes	Piezoelectric: ZnO, AlN, PZT Substrate: Quartz, LiNbO3	Piezoelectric: ZnO, AlN, PZT Substrate: Si, Si3N4, SiO2
Wave mode	Shear	Rayleigh, Sezawa, Shear, Love, Lamb	Longitudinal, Shear
Operating frequency	kHz to a few MHz	Hundreds of MHz to tens of GHz	Hundreds of MHz to tens of GHz
Relative sensitivity	Low	Medium	High
Typical size	millimeters	Hundreds of micrometers	Tens of micrometers
Monolithic CMOS integration	No	Yes	Yes
Readout method	Frequency shift	Frequency shift, Time delay	Frequency shift
Advantages	<ul style="list-style-type: none"> • Detection in dry and wet environment • Highly available • Low cost • Mature technology 	<ul style="list-style-type: none"> • Low power consumption • Wireless capabilities • Multiple propagation modes • Operation in wet and dry environments • Higher sensitivity than QCM 	<ul style="list-style-type: none"> • Higher sensitivity than QCM and SAW • Low power consumption • Wireless capabilities • Size is much smaller than QCM and SAW • Small base mass

Table 1.1: Comparison of the key parameters of QCM, SAW, and FBAR, related to sensing applications.

	QCM	SAW	FBAR
Problems	<ul style="list-style-type: none"> Limited detection resolution due to its lower operating frequency Difficult integration with miniaturized systems due to its larger dimensions 	<ul style="list-style-type: none"> Higher cost compared to QCM Affected by temperature drift Not a pure shear mode, causing attenuation in liquid operation 	<ul style="list-style-type: none"> Fragile membrane (Air-gap FBARs) Performance is dependent of accuracy of fabrication (SMR) Higher cost Lower availability Difficult signal control and measurement

Table 1.1: (Continued)

1.4 High-overtone Bulk Acoustic Resonator (HBAR)

Table 1.1 has presented the advantages of FBARs compared to QCM and SAW technologies, such as their lower footprint in the wafer and their higher frequency of operation/sensitivity, however, the fragility of their thin membrane limits their application as a sensor in harsh environments and their yield at fabrication. These drawbacks of FBARs could be solved by another type of bulk acoustic wave device called High-overtone Bulk Acoustic Resonator (HBAR), which is also simpler to manufacture than FBARs or SMRs.

The HBARs or OMR (overmoded resonators) are acoustic wave devices composed of a piezoelectric film, equipped with top and bottom electrodes, deposited on a thicker substrate of low acoustic losses (Figure 1.10a). Unlike the case of FBARs, the piezoelectric is not acoustically isolated from the substrate that supports it, but rather the acoustic energy is allowed to leak into the substrate generating standing waves through the whole thickness of the device, i.e. the substrate is used as a cavity resonator for the acoustic wave (Figure 1.10b) [106].

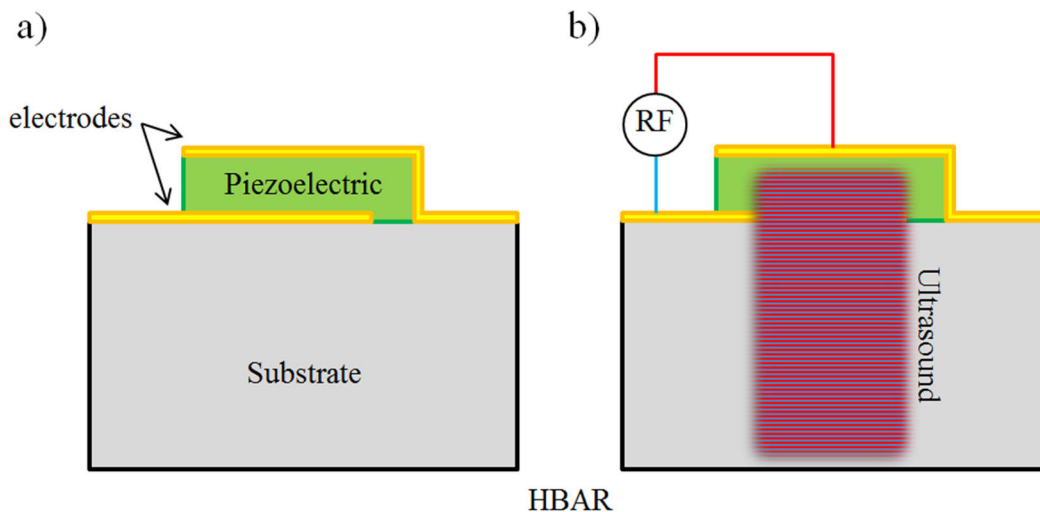


Figure 1.10: 2D representation of an HBAR operating in longitudinal mode (thickness extension). a) Materials and layers involved. b) Standing wave of ultrasound trapped in the thickness of the device whenever the piezoelectric is driven by an RF source.

The origin of these structures is found in the first bulk wave delay lines; the piezoelectric layer emits an acoustic bulk wave package that propagates in the substrate, reflects on its back, and returns to the transducer that reconverts it into an electric signal [107]. The study of HBAR devices was mainly related to the replacement of SAW devices in passive RF applications, such as filters and oscillators, due to their smaller size and higher frequency of operation [108], but several sensor applications have been achieved recently: environmental [109, 110], temperature [111, 112], gravimetric [113, 114], pressure [115], viscosity [116], and also applications for quantum mechanics research [117–119] and consumer electronics, such as impedance imagers for fingerprint sensing and computing applications using HBAR devices under a pulse-echo regime [120–122]. The latter is of remarkable interest since pulse-echo mode of operation could provide potential physical sensors with ease of reading, since they will only require measurement of output peak voltage instead of the frequency shift detection necessary for the case of sensors operating as resonators.

1.5 Motivation and contributions of this thesis

1.5.1 Motivation of the thesis

The previous sections have offered an overview to the main acoustic wave technologies and devices used for the construction of sensors and actuators in telecommunications, automotive, environmental sensing, and healthcare. Devices such as the Quartz Crystal Microbalance (QCM), the Surface Acoustic Wave technologies (SAW) and the Thin-Film Bulk Acoustic Resonators (FBAR) stand out due to their possibility of label-free detection, tiny size, high sensitivity and wide availability, however, they remain some areas of opportunity to be solved as Table 1.1 has shown. From the reviewed art some remarks can be made:

- QCM: It is a mature and widely adopted technology whose detection resolution is limited due to the operating frequency that finely thinned substrates can reach before becoming mechanically unstable. Its relatively large dimensions make its integration with modern miniaturized systems difficult.
- SAW: A micromachined technology offering higher sensitivity than QCM (higher operating frequency), low power consumption and wireless capabilities. It requires patterning of several metallic interdigitated transducers (IDTs) on the wafer surface, using a relatively large area of the chip for its implementation. It is not possible to excite a pure shear mode, causing severe attenuation during liquid operation.
- FBAR: It offers higher sensitivity than both QCM and SAW due to its operating frequency in the GHz range. It is also a micromachined technology of low power consumption and wireless capabilities, unfortunately, devices based on thin membranes (air-gap FBARs) are fragile when operating as sensors in liquid media, whereas performance of Solidly Mounted Resonators (SMRs) is dependent of their manufacture since it is required a precisely controlled deposition of the layers constituting their acoustic reflector.

The readout method of these devices consists of detecting changes in their resonance frequency in response to chemical or physical stimuli of the study analyte, therefore it is required mechanisms for signal control and relatively complex read-out circuitry capable of detecting frequency shift in the impedance curve caused by changes of the acoustic load coupled to the resonator [23]. Taking

the previous remarks into account, the motivation of this work is the development of miniaturized acoustic sensors that offer:

- **Simpler readout method:** The system output is voltage level.
- **Mechanical robustness:** The sensor must be completely solid, i.e., avoid thin membranes that break during operation.
- **Easy manufacture and high yield:** The sensor must not require release of moving elements that may affect the yield during its manufacture nor require controlled deposition of multiple layers as in the case of mirrors in SMRs.
- **Reduced footprint:** At GHz it is possible to build transducers with lateral dimensions smaller than 100 μm that avoid diffraction of ultrasound pulses.
- **Low power consumption:** Low operating voltage improves its ability to be included in portable systems. An operating voltage of less than 1 Volt is intended.
- **Compatibility with CMOS:** Piezoelectric materials deposited at low temperature (such as Aluminum Nitride) have demonstrated the capacity for monolithic integration of piezoelectric transducers and their CMOS circuitry for excitation and reading.
- **Low input impedance:** The input impedance should be close to 50 ohms to facilitate its integration with commercial radio frequency equipment.

1.5.2 Contributions to the art

In regard to the foregoing, the contribution of this work to the state of the art consists of provide an alternative for the noninvasive study of liquid samples at microscales; envisioned for real-time applications where low-power consumption, easy readout method and size matters. The latter will be accomplished using an HBAR microstructure working under a pulse-echo regime to study compressional properties of liquids by interrogating those samples with short pulses of ultrasound. This would allow applications such as identification and classification different liquids at microscale or studying concentration changes of mixtures simply by measuring difference in output voltage level.

1.5.3 Academic contributions

The project has been presented at four International Conferences, whose conference proceedings papers are available as:

- J. Yanez, E. Ledesma, A. Uranga and N. Barniol, AlN-based HBAR ultrasonic resonator for fluid detection in microchannels with multi-frequency operation capability over the GHz range, IEEE International Ultrasonics Symposium (IUS), China 2021, pp. 1–4, <https://doi.org/10.1109/IUS52206.2021.9593369>
- J. Yanez, A. Uranga and N. Barniol, Multi-frequency thin film HBAR microtransducer for acoustic impedance sensing over the GHz range, 21st International Conference on Solid-state sensors, Actuators and Microsystems (Transducers), EEUU 2021, pp. 1347–1350, <https://doi.org/10.1109/Transducers50396.2021.9495750>
- J. Yanez, E. Ledesma, A. Uranga and N. Barniol, Improved Electromechanical Transduction for PiezoMUMPS HBAR Impedance Sensors, 2020 Joint Conference of the IEEE International Frequency Control Symposium and International Symposium on

Applications of Ferroelectrics (IFCS-ISAF), EEUU 2020, pp. 1–5, <https://doi.org/10.1109/IFCS-ISAF41089.2020.9234913>

- J. Yanez, F. Torres, A. Uranga and N. Barniol, A feasibility study of AlN ultrasonic transducers fabrication using the multi-user PiezoMUMPs process for fingerprint scanning at GHz range, 15th Conference on Ph.D Research in Microelectronics and Electronics (PRIME), Switzerland 2019, pp. 293–296, <https://doi.org/10.1109/PRIME.2019.8787767>

This work also resulted in the following Journal Paper:

- Jesus Yanez, Arantxa Uranga, Nuria Barniol, Fluid compressional properties sensing at microscale using a longitudinal bulk acoustic wave transducer operated in a pulse-echo scheme, Sensors and Actuators A: Physical, vol. 334 (2022), <https://doi.org/10.1016/j.sna.2021.113334>

1.6 Thesis outline

Chapter 2: Theory. This chapter describes the proposed system based on a 'High-overtone Acoustic Resonator' (HBAR). Later is described the operating mechanism (pulse-echo) and also an alternative detection mechanism (the HBAR sensor used as an acoustic resonator). Finally, it is presented an analytical review of the operating principle and the interaction between longitudinal acoustic waves and liquids; presenting analytical models that will be used for the sensor design and also analytical models that predict operation.

Chapter 3: Design, Simulation, and Fabrication. This chapter offers justification of the selected piezoelectric material by discussing advantages and disadvantages of several piezoelectric materials used in manufacture of MEMS microtransducers. Next, the acoustic characteristics of the materials used in the manufacturing process are presented and analytical predictions of the impedance curve of the device are made. Later, the analytical models reviewed in the previous chapter are used to establish the lateral dimensions of the transducer and to predict the path of the ultrasound pulse from emission to reception. In this chapter are presented the Finite Element models that were constructed to perform Frequency Domain & Time Domain multiphysics simulations to support analytical predictions. The complementary part of the chapter presents the selected manufacturing process and describes the main manufacturing rules that have been used to guarantee the correct manufacture and operation of the sensors. The “step-by-step” description of the flow used to fabricate the devices is presented, as well as the design for lithography masks.

Chapter 4: Characterization & Experimental Setup. The first part of this chapter details the procedures followed to validate that the manufactured resonators work according to design. Next is described the process to isolate mathematically the electrical response of the resonator from parasitic contributions of cables and connectors. The complementary part of the chapter details the procedure to validate the pulse-echo devices and describes in detail the experimental setup to drive and read the pulse-echo transducers. The digital post-processing tools are also presented.

Chapter 5: Results & Conclusions. The first part of this chapter compares the performance of the fabricated pulse-echo device to the analytical predictions and Finite Element Analysis simulations. It continues with demonstration of applications such as: Detection of presence of liquids in

microchannels, impedance imaging (fingerprint sensor), identification and classification of liquids by their specific acoustic impedance, detection of concentration change in solutions, and sensing of compressional properties of liquids (Acoustic impedance and Bulk Modulus). Later, an application for the alternative readout method (as resonator) is presented. This chapter ends with Conclusions.

References

- [1] Lauren McNeill, et al., Lab-on-a-Chip approaches for the detection of controlled drugs, including new psychoactive substances: A systematic review, *Forensic Chemistry*, vol. 26, 2021, <https://doi.org/10.1016/j.forc.2021.100370>
- [2] Yuksel Temiz, et al., Lab-on-a-chip devices: How to close and plug the lab?, *Microelectronic Engineering*, vol. 132, 2015, pp. 156–175, <https://doi.org/10.1016/j.mee.2014.10.013>
- [3] Dobrivojic Popovich, *Mechatronics in Engineering Design and Product Development*, CRC Press, 2019.
- [4] Ian Sinclair, *Sensors and Transducers*, Newnes, 2001.
- [5] Abdullah Saleh Algamili, et al., A Review of Actuation and Sensing Mechanisms in MEMS-Based Sensor Devices, *Nanoscale Research Letters*, vol. 16, 2021, <https://doi.org/10.1186/s11671-021-03481-7>
- [6] Yole, Status of the MEMS Industry 2022, (<https://www.yolegroup.com/product/report/status-of-the-mems-industry-2022-mis/>), 2022, (accessed 12 December 2022)
- [7] Gust H. Bardy, et al., Amiodarone or an implantable cardioverter–defibrillator for congestive heart failure, *New England Journal of Medicine*, vol. 352 (3), pp. 225–237, 2005, <https://doi.org/10.1056/NEJMoa043399>
- [8] Valentina Kutiyfa, et al., Multicenter Automatic Defibrillator Implantation Trial–Subcutaneous Implantable Cardioverter Defibrillator (MADIT S-ICD): Design and clinical protocol, *American Heart Journal*, vol. 189, pp. 158–166, 2017, <https://doi.org/10.1016/j.ahj.2017.04.014>
- [9] Andreas Haerberlin, et al., The first batteryless, solar-powered cardiac pacemaker, *Heart Rhythm*, vol. 12 (6), pp. 1317–1323, 2015, <https://doi.org/10.1016/j.hrthm.2015.02.032>
- [10] E. Y. Chow, et al., Wireless MEMS-based implantable medical device for cardiology, *Wireless MEMS Networks and Applications: Elsevier*, pp. 77–100, 2017, <https://doi.org/10.1016/B978-0-08-100449-4.00004-X>
- [11] Ankur Gupta and Pramod Pal, Micro-electro-mechanical system–based drug delivery devices, *Bioelectronics and Medical Devices*, pp. 183–210, 2019, <https://doi.org/10.1016/B978-0-08-102420-1.00010-8>
- [12] Hyunjoo Lee, et al., MEMS devices for drug delivery, *Advanced drug delivery reviews*, vol. 128, pp. 132–147, 2018, <https://doi.org/10.1016/j.addr.2017.11.003>

- [13] Hirokazu Kaji, et al., Drug delivery devices for retinal diseases, *Advanced drug delivery reviews*, vol. 128, pp. 148–157, 2018, <https://doi.org/10.1016/j.addr.2017.07.002>
- [14] Khushwant S Yadav, et al., E-drug delivery: a futuristic approach, *Drug discovery today*, vol. 24 (4), pp. 1023–1030, 2019, <https://doi.org/10.1016/j.drudis.2019.02.005>
- [15] Daniel Figeys and Devanand Pinto, Lab-on-a-chip: a revolution in biological and medical sciences, *Analytical chemistry*, vol. 72 (9), pp 330–335, 2000, <https://doi.org/10.1021/ac002800y>
- [16] Vasudha Shukla, et al., Lab-on-a-Chip platforms for biophysical studies of cancer with single-cell resolution, *Trends in biotechnology*, vol. 36 (5), pp. 549–561, 2018, <https://doi.org/10.1016/j.tibtech.2018.02.007>
- [17] Dimitrios P. Nikolelis and Georgia-Paraskevi Nikoleli, *Nanotechnology and Biosensors*, Elsevier, 2018, <https://doi.org/10.1016/C2017-0-00358-0>
- [18] Aviru Kumar Basu, Adreeja Basu, Sagnik Ghosh and Shantanu Bhattacharya, *MEMS Applications in Biology and Healthcare*, AIP Publishing Books, 2021, <https://doi.org/10.1063/9780735423954>
- [19] Rishi Kant, et al., Digitally controlled portable micropump for transport of live micro-organisms, *Sensors Actuators A: Physical*, vol. 265 (1), pp. 138–151, 2017, <https://doi.org/10.1016/j.sna.2017.05.016>
- [20] P. F. Caton, and R. M. White, MEMS microfilter with acoustic cleaning, 14th IEEE International Conference on Micro Electro Mechanical Systems, pp. 479–482, 2001, <https://doi.org/10.1109/MEMSYS.2001.906583>
- [21] Rishi Kant, et al., Optimization of design and characterization of a novel micro-pumping system with peristaltic motion, *Microsystem Technologies*, vol. 19, pp. 563–575, 2013, <https://doi.org/10.1007/s00542-012-1658-y>
- [22] George Whitesides, The origins and the future of microfluidics, *Nature*, vol. 442, pp. 368–373, 2006, <https://doi.org/10.1038/nature05058>
- [23] Y. Q. Fu, et al., Advances in piezoelectric thin films for acoustic biosensors, acoustofluidics and lab-on-chip applications, *Progress in Materials Science*, vol. 89, pp. 31–91, 2017, <https://doi.org/10.1016/j.pmatsci.2017.04.006>
- [24] Ken-ya Hashimoto, *Surface Acoustic Wave Devices in Telecommunications*, Springer, 2000, <https://doi.org/10.1007/978-3-662-04223-6>
- [25] G. Macchiarella and G. B. Stracca, SAW Devices for Telecommunications: Examples and Applications, 1982 Ultrasonics Symposium, pp. 247–251, 1982, <https://doi.org/10.1109/ULTSYM.1982.197823>

- [26] D. E. Cullen and G. K. Montress, Progress in the Development of SAW Resonator Pressure Transducers, 1980 Ultrasonics Symposium, pp. 696–701, 1980, <https://doi.org/10.1109/ULTSYM.1980.197489>
- [27] T. M. Reeder, D. E. Cullen and M. Gilden, SAW Oscillator Pressure Sensors, 1975 Ultrasonics Symposium, pp. 264–268, 1975, <https://doi.org/10.1109/ULTSYM.1975.196515>
- [28] A. Pohl, et al., Monitoring the tire pressure at cars using passive SAW sensors, 1997 IEEE Ultrasonics Symposium Proceedings, pp. 471–474, vol. 1, 1997, <https://doi.org/10.1109/ULTSYM.1997.663065>
- [29] Natalia Levit, et al., High surface area polymer coatings for SAW-based chemical sensor applications, Sensors and Actuators B: Chemical, vol. 82 (2–3), pp. 241–249, 2002, [https://doi.org/10.1016/S0925-4005\(01\)01018-8](https://doi.org/10.1016/S0925-4005(01)01018-8)
- [30] T. Nakamoto, K. Nakamura and T. Moriizumi, Study of oscillator-circuit behavior for QCM gas sensor, 1996 IEEE Ultrasonics Symposium, pp. 351–354, vol. 1, 1996, <https://doi.org/10.1109/ULTSYM.1996.583990>
- [31] E. J. Staples, Electronic nose simulation of olfactory response containing 500 orthogonal sensors in 10 seconds, 1999 IEEE Ultrasonics Symposium, pp. 417–423, vol. 1, 1999, <https://doi.org/10.1109/ULTSYM.1999.849432>
- [32] Henry Wohltjen and Raymond Dessy, Surface acoustic wave probe for chemical analysis. I. Introduction and instrument description, Analytical Chemistry, vol. 51 (9), pp. 1458–1475, 1979, <https://doi.org/10.1021/ac50045a024>
- [33] J. J. Caron, J. C. Andle and J. F. Vetelino, Surface acoustic wave substrates for gas sensing applications, 1995 IEEE Ultrasonics Symposium, pp. 461–466, vol. 1, <https://doi.org/10.1109/ULTSYM.1995.495620>
- [34] J. C. Andle, et al., An acoustic plate mode immunosensor, 1989 IEEE Ultrasonics Symposium, pp. 579–584, vol. 1, <https://doi.org/10.1109/ULTSYM.1989.67050>
- [35] J. C. Andle, et al., Detection of nucleic acid hybridization with an acoustic plate mode microsensor, 1990 IEEE Symposium on Ultrasonics, pp. 291–294, vol. 1, <https://doi.org/10.1109/ULTSYM.1990.171370>
- [36] D.S. Ballantine, Jr., et al., Acoustic Wave Sensors: Theory, Design, and Physico-Chemical Applications, Academic Press, 1996, <https://doi.org/10.1016/B978-0-12-077460-9.X5000-X>
- [37] B. A. Cavić, et al., Acoustic waves and the study of biochemical macromolecules and cells at the sensor-liquid interface, The Analyst, vol. 124 (10), pp. 1405–1420, 1999, <https://doi.org/10.1039/a903236c>
- [38] A. Janshoff, H. J. Galla, and C. Steinem, Piezoelectric Mass-Sensing Devices as Biosensors—An Alternative to Optical Biosensors?, Angewandte Chemie, vol. 39 (22), pp. 4004–4032, 2000, [https://doi.org/10.1002/1521-3773\(20001117\)39:22<4004::aid-anie4004>3.0.co;2-2](https://doi.org/10.1002/1521-3773(20001117)39:22<4004::aid-anie4004>3.0.co;2-2)

- [39] Y. Q. Fu, et al., Recent developments on ZnO films for acoustic wave based bio-sensing and microfluidic applications: a review, *Sensors and Actuators B: Chemical*, vol. 143 (2), pp. 606–619, 2010, <https://doi.org/10.1016/j.snb.2009.10.010>
- [40] W. D. Bowers, R. L. Chuan, and T. M. Duong, A 200 MHz surface acoustic wave resonator mass microbalance, *Review of Scientific Instruments*, vol. 62, pp. 1624–1629, 1991 <https://doi.org/10.1063/1.1142442>
- [41] J. D. N. Cheeke, N. Tashtoush and N. Eddy, Surface acoustic wave humidity sensor based on the changes in the viscoelastic properties of a polymer film, 1996 IEEE Ultrasonics Symposium, vol. 1, pp. 449 – 452, <https://doi.org/10.1109/ULTSYM.1996.584009>
- [42] A. L. Smith, H. M. Shirazi, Quartz Microbalance Microcalorimetry: A new method for studying polymer-solvent thermodynamics, *Journal of Thermal Analysis and Calorimetry*, vol. 59, pp. 171–186, 2000, <https://doi.org/10.1023/A:1010192113958>
- [43] A. L. Smith, et al., A mass/heat flow sensor combining shear mode resonators with thermoelectrics: principles and applications, 2003 IEEE International Frequency Control Symposium and 17th European Frequency and Time Forum, pp. 1062–1065, 2003, <https://doi.org/10.1109/FREQ.2003.1275237>
- [44] J. Bastermeijer, et al., A novel readout system for microacoustic viscosity sensors, 2002 IEEE Ultrasonics Symposium, vol. 1, pp. 489–492, 2002, <https://doi.org/10.1109/ULTSYM.2002.1193448>
- [45] C. E. Weld, et al., Temperature measurement using surface skimming bulk waves, 1999 IEEE Ultrasonics Symposium. Proceedings, vol. 1, pp. 441–444, 1999, <https://doi.org/10.1109/ULTSYM.1999.849436>
- [46] J. Homola, S. Yee, and G. Gauglitz, Surface plasmon resonance sensors: review, *Sensors and Actuators B: Chemical*, vol. 54 (1–2), pp. 3–15, 1999, [https://doi.org/10.1016/S0925-4005\(98\)00321-9](https://doi.org/10.1016/S0925-4005(98)00321-9)
- [47] Y. Cui, et al., Nanowire Nanosensors for Highly Sensitive and Selective Detection of Biological and Chemical Species, *Science*, vol. 293 (5533), pp. 1289–1292, <https://doi.org/10.1126/science.1062711>
- [48] B. L. Allen, P. D. Kichambare and A. Star, Carbon nanotube field-effect-transistor-based biosensors, *Advanced Materials*, vol. 19, pp. 1439–1451, 2007, <https://doi.org/10.1002/adma.200602043>
- [49] Aviru K. Basu, Adreeja Basu, Shantanu Bhattacharya, Micro/Nano fabricated cantilever based biosensor platform: A review and recent progress, *Enzyme and Microbial Technology*, vol. 139, pp. 141–229, 2020, <https://doi.org/10.1016/j.enzmictec.2020.109558>
- [50] B. Cunningham, et al., Colorimetric resonant reflection as a direct biochemical assay technique, *Sensors and Actuators B: Chemical*, vol. 81 (2–3), pp. 316–328, 2002, [https://doi.org/10.1016/S0925-4005\(01\)00976-5](https://doi.org/10.1016/S0925-4005(01)00976-5)

- [51] F. Vollmer and S. Arnold, Whispering-gallery-mode biosensing: label-free detection down to single molecules, *Nature Methods*, vol. 5, pp. 591–596, 2008, <https://doi.org/10.1038/nmeth.1221>
- [52] Oguzhan Avci, et al., Interferometric Reflectance Imaging Sensor (IRIS)—A Platform Technology for Multiplexed Diagnostics and Digital Detection, *Sensors*, vol. 15 (7), pp. 17649–17665, 2015, <https://doi.org/10.3390/s150717649>
- [53] Haoyu Liu, et al., Imaging ellipsometry biosensor: Basic theory, principles of operation, and applications, *Journal of Vacuum Science & Technology B*, vol. 38 (2), 2020, <https://doi.org/10.1116/1.5129596>
- [54] K. Lange, B. Rapp, M. Rapp, Surface acoustic wave biosensors: a review, *Analytical and Bioanalytical Chemistry*, vol. 391 (5), pp. 1509–1519, 2008 <https://doi.org/10.1007/s00216-008-1911-5>
- [55] Adnan Mujahid, et al., An Overview of High Frequency Acoustic Sensors—QCMs, SAWs and FBARs—Chemical and Biochemical Applications, *Sensors*, vol. 19 (20), 2019, <https://doi.org/10.3390/s19204395>
- [56] Wei Pang, et al., Piezoelectric microelectromechanical resonant sensors for chemical and biological detection, *Lab on a Chip*, vol. 12 (1), pp. 29–44, 2012, <https://doi.org/10.1039/C1LC20492K>
- [57] Nilanjan Dey, et al., *Acoustic Sensors for Biomedical Applications*, Springer, 2018, <https://doi.org/10.1007/978-3-319-92225-6>
- [58] R. Weigel et al., Microwave acoustic materials, devices, and applications, *IEEE Transactions on Microwave Theory and Techniques*, vol. 50 (3), pp. 738–749, 2002, doi: <https://doi.org/10.1109/22.989958>
- [59] Adeel Afzal, et al., Advanced vapor recognition materials for selective and fast responsive surface acoustic wave sensors: A review, *Analytica Chimica Acta*, vol. 787, pp. 36–49, 2013, <https://doi.org/10.1016/j.aca.2013.05.005>
- [60] R.M. Belchamber, PROCESS ANALYSIS | Acoustic Emission, *Encyclopedia of Analytical Science (Second Edition)* Elsevier, pp. 324–331, 2005, <https://doi.org/10.1016/B0-12-369397-7/00706-8>
- [61] Lord Rayleigh, On Waves Propagated along the Plane Surface of an Elastic Solid. *Proceedings of the London Mathematical Society*, vol. s1-17 (1), pp. 4–11, 1885, <https://doi.org/10.1112/plms/s1-17.1.4>
- [62] Yi Zhang, et al., Film bulk acoustic resonators (FBARs) as biosensors: A review, *Biosensors and Bioelectronics*, vol. 116, pp. 1–15, 2018, <https://doi.org/10.1016/j.bios.2018.05.028>
- [63] Sandeep Kumar Vashist and Priya Vashist, Recent Advances in Quartz Crystal Microbalance-Based Sensors, *Journal of Sensors*, vol. 2011, <https://doi.org/10.1155/2011/571405>

- [64] C. Lu and A. W. Czanderna, *Methods and Phenomena vol 7: Applications of Piezoelectric Quartz Crystal Microbalances*, Elsevier, 1984.
- [65] Abdulrahman Alassi, et al., Quartz Crystal Microbalance Electronic Interfacing Systems: A Review, *Sensors*, vol. 17 (12), 2017, <https://doi.org/10.3390/s17122799>
- [66] Frank Caruso, et al., Quartz crystal microbalance study of DNA immobilization and hybridization for nucleic Acid sensor development, *Analytical Chemistry*, vol. 69 (11), pp. 2043–2049, 1997, <https://doi.org/10.1021/ac961220r>
- [67] Jacob L. Jordan and Erik J. Fernandez, QCM-D sensitivity to protein adsorption reversibility, *Biotechnology and Bioengineering*, vol. 101 (4), pp. 837–842, 2008, <https://doi.org/10.1002/bit.21977>
- [68] Junning Gao, et al., Recent developments of film bulk acoustic resonators, *Functional Materials Letters*, vol. 09 (3), 2016, <https://doi.org/10.1142/S1793604716300024>
- [69] Clemens C. W. Ruppel, Acoustic Wave Filter Technology—A Review, *IEEE Transactions on Ultrasonics, Ferroelectrics, and Frequency Control*, vol. 64 (9), pp. 1390–1400, 2017, <https://doi.org/10.1109/TUFFC.2017.2690905>
- [70] K. M. Lakin and J. S. Wang, UHF Composite Bulk Wave Resonators, 1980 *Ultrasonics Symposium*, pp. 834–837, 1980, <https://doi.org/10.1109/ULTSYM.1980.197515>
- [71] Asif Khan, et al., Piezoelectric thin films: An integrated review of transducers and energy harvesting. *Smart Materials and Structures*, vol. 25 (5), 2016, <https://doi.org/10.1088/0964-1726/25/5/053002>
- [72] Chang Eom and Susan Trolier-McKinstry, Thin-film piezoelectric MEMS, *MRS Bulletin*, vol. 37 (11), pp. 1007–1017, 2012, <https://doi.org/10.1557/mrs.2012.273>
- [73] Ioana Voiculescu and Anis Nurashikin Nordin, Acoustic wave based MEMS devices for biosensing applications, *Biosensors and Bioelectronics*, vol. 33 (1), pp. 1–9, 2012, <https://doi.org/10.1016/j.bios.2011.12.041>
- [74] Debdyuti Mandal and Sourav Banerjee, Surface Acoustic Wave (SAW) Sensors: Physics, Materials, and Applications, *Sensors*, vol. 22 (3), pp. 820, 2022, <https://doi.org/10.3390/s22030820>
- [75] Jagannath Devkota, et al., SAW Sensors for Chemical Vapors and Gases, *Sensors*, vol. 17 (4), pp. 801, 2017, <https://doi.org/10.3390/s17040801>
- [76] B. Yildirim, et al., Surface Acoustic Wave Viscosity Sensor with Integrated Microfluidics on a PCB Platform, *IEEE Sensors Journal*, vol. 18 (6), pp. 2305–2312, 2018, <https://doi.org/10.1109/JSEN.2018.2797546>
- [77] C. J. Cheng, et al., Guided SH-SAW Sensing System for Liquid Viscosity Sensing Applications, *Sensor Letters*, vol. 9 (2), pp. 605–608, 2011, <https://doi.org/10.1166/sl.2011.1572>

- [78] Xuhang Zhou, et al., Novel Multilayer SAW Temperature Sensor for Ultra-High Temperature Environments, *Micromachines*, vol. 12 (6), pp. 643, <https://doi.org/10.3390/mi12060643>
- [79] Xu Gao, et al., Development of Wireless and Passive SAW Temperature Sensor with Very High Accuracy, *Applied Sciences*, vol. 11 (16), pp. 7422, 2021, <https://doi.org/10.3390/app11167422>
- [80] A. Bryant, et al., Gas detection using surface acoustic wave delay lines, *Sensors and Actuators*, vol. 4, pp. 105–111, 1983, [https://doi.org/10.1016/0250-6874\(83\)85014-8](https://doi.org/10.1016/0250-6874(83)85014-8)
- [81] Christine G. Fox and John F. Alder, Surface acoustic wave sensors for atmospheric gas monitoring. A review, *Analyst* vol. 114 (9), pp. 997–1004, 1989, <https://doi.org/10.1039/AN9891400997>
- [82] Xiudong Wang, et al., Development of a SnO₂/CuO-coated surface acoustic wave-based H₂S sensor with switch-like response and recovery, *Sensors and Actuators B: Chemical*, vol. 169, pp. 10–16, 2012, <https://doi.org/10.1016/j.snb.2012.01.002>
- [83] Jin-Chen Hsu, et al., Acoustophoretic Control of Microparticle Transport Using Dual-Wavelength Surface Acoustic Wave Devices, *Micromachines*, vol. 10 (1), 2019, <https://doi.org/10.3390/mi10010052>
- [84] Myeong Chan Jo, Rasim Guldiken, Dual surface acoustic wave-based active mixing in a microfluidic channel, *Sensors and Actuators A: Physical*, vol. 196, pp. 1–7, 2013, <https://doi.org/10.1016/j.sna.2013.03.028>
- [85] Jr-Hung Tsai and Liwei Lin, Active microfluidic mixer and gas bubble filter driven by thermal bubble micropump, *Sensors and Actuators A: Physical*, vol. 97, pp. 665–671, 2002, [https://doi.org/10.1016/S0924-4247\(02\)00031-6](https://doi.org/10.1016/S0924-4247(02)00031-6)
- [86] Richie J. Shilton, et al., Nanoliter-droplet acoustic streaming via ultra-high frequency surface acoustic waves, *Advanced Materials*, vol. 26, pp. 4941–4946, 2014, <https://doi.org/10.1002/adma.201400091>
- [87] Adnan Mujahid, et al., Imprinted sol–gel materials for monitoring degradation products in automotive oils by shear transverse wave, *Analytica Chimica Acta*, vol. 675 (1), pp. 53–57, 2010, <https://doi.org/10.1016/j.aca.2010.07.005>
- [88] Nicole Barié, et al., Vacuum-deposited wave-guiding layers on STW resonators based on LiTaO₃ substrate as love wave sensors for chemical and biochemical sensing in liquids, *Ultrasonics*, vol. 50 (6), pp. 606–612, 2010, <https://doi.org/10.1016/j.ultras.2009.12.006>
- [89] Ken-Ya Hashimoto, *RF Bulk Acoustic Wave Filters for Communications*, Artech House Publishers, 2009.
- [90] Lifeng Qin, et al., Analytical study of dual-mode thin film bulk acoustic resonators (FBARs) based on ZnO and AlN films with tilted c-axis orientation. *IEEE Transactions on Ultrasonics*

Ferroelectrics, and Frequency Control, vol. 57 (8), pp. 1840–1853, <https://doi.org/10.1109/TUFFC.2010.1623>

[91] R. Gabl, et al., Novel integrated FBAR sensors: a universal technology platform for bio- and gas-detection, SENSORS, vol. 2, pp. 1184–1188, 2003, <https://doi.org/10.1109/ICSENS.2003.1279132>

[92] R. Gabl, et al., First results on label-free detection of DNA and protein molecules using a novel integrated sensor technology based on gravimetric detection principles, Biosensors and Bioelectronics, vol. 19 (6), pp. 615–620, 2004, [https://doi.org/10.1016/S0956-5663\(03\)00259-8](https://doi.org/10.1016/S0956-5663(03)00259-8)

[93] Kuan-Hsun Chiu, et al., High-Performance Film Bulk Acoustic Wave Pressure and Temperature Sensors, Japanese Journal of Applied Physics, vol. 46, 2007, <https://doi.org/10.1143/JJAP.46.1392>

[94] X. L. He, et al., Film bulk acoustic resonator pressure sensor with self-temperature reference, Journal of Micromechanics and Microengineering, vol. 22 (12), 2012, <https://doi.org/10.1088/0960-1317/22/12/125005>

[95] X. L. He, et al., A Single FBAR-Based Temperature and Pressure Sensors, Key Eng. Materials, vol. 562–565, pp. 188–191, 2013, <https://doi.org/10.4028/www.scientific.net/KEM.562-565.188>

[96] J. Weber, et al., High Frequency Viscosity Sensing with FBARs, 2006 IEEE International Frequency Control Symposium and Exposition, pp. 117–122, 2006, <https://doi.org/10.1109/FREQ.2006.275362>

[97] G. Wingqvist, et al., Shear mode AlN thin film electro-acoustic resonant sensor operation in viscous media, Sensors and Actuators B: Chemical, vol. 123 (1), pp. 466–473, 2007 <https://doi.org/10.1016/j.snb.2006.09.028>

[98] Xiaotun Qiu, et al., Film Bulk Acoustic-wave Resonator (FBAR) based humidity sensor, IEEE 5th International Conference on Nano/Micro Engineered and Molecular Systems, pp. 445–449, 2010, <https://doi.org/10.1109/NEMS.2010.5592429>

[99] Xiaotun Qiu, and H. Yu, Monitoring relative humidity using ZNO based film bulk acoustic-wave resonator, In Humidity Sensors: Types, Nanomaterials and Environmental Monitoring, pp. 161–176, Nova Science Publishers, Inc., 2011.

[100] Xiaotun Qiu, et al., Film bulk acoustic-wave resonator based ultraviolet sensor, Applied Physics Letters, vol. 94 (15), 2009, <https://doi.org/10.1063/1.3122342>

[101] Ziyu Wang, et al., ZnO based film bulk acoustic resonator as infrared sensor, Thin Solid Films, vol. 519 (18), pp. 6144–6147, 2011, <https://doi.org/10.1016/j.tsf.2011.03.134>

[102] M. DeMiguel-Ramos, B. Díaz-Durán, J.M. Escolano, M. Barba, T. Mireia, J. Olivares, M. Clement, E. Iborra, Gravimetric biosensor based on a 1.3GHz AlN shear-mode solidly mounted resonator, Sensors and Actuators B: Chemical, vol. 239, pp. 1282–1288, 2017, <https://doi.org/10.1016/j.snb.2016.09.079>

- [103] T. Mirea, J. Olivares, M. Clement, E. Iborra, Impact of FBAR design on its sensitivity as in-liquid gravimetric sensor, *Sensors and Actuators A: Physical*, vol. 289, pp. 87–93, 2019, <https://doi.org/10.1016/j.sna.2019.02.012>
- [104] Si-Hyung Lee, et al., Influence of electrode configurations on the quality factor and piezoelectric coupling constant of solidly mounted bulk acoustic wave resonators, *Journal of Applied Physics*, vol. 92, pp. 4062–4069, 2002, <https://doi.org/10.1063/1.1505977>
- [105] L. García-Gancedo et al., Experimental comparison of FBARs and SMRs responsivities to mass loadings, 2012 IEEE International Ultrasonics Symposium, pp. 1545–1548, 2012, <https://doi.org/10.1109/ULTSYM.2012.0386>
- [106] Emmanuel Defaÿ, *Integration of Ferroelectric and Piezoelectric Thin Films: Concepts and Applications for Microsystems*, Wiley, 2013.
- [107] K. M. Lakin, G. R. Kline and K. T. McCarron, High-Q microwave acoustic resonators and filters, *IEEE Transactions on Microwave Theory and Techniques*, vol. 41 (12), pp. 2139–2146, 1993, <https://doi.org/10.1109/22.260698>
- [108] S. Ballandras, T. Baron, E. Lebrasseur, G. Martin, D. Gachon, A. Reinhardt, P.P. Lassagne, J.M. Friedt, L. Chommeloux and D. Rabus, High overtone Bulk Acoustic Resonators: application to resonators, filters and sensors, *Acoustics 2012*, 2012, <https://hal.archives-ouvertes.fr/hal-00811239>
- [109] G. D. Mansfeld, Theory of high overtone bulk acoustic wave resonator as a gas sensor, 13th International Conference on Microwaves, Radar and Wireless Communications (MIKON), pp. 469–472, vol. 2, 2000, <https://doi.org/10.1109/MIKON.2000.913971>
- [110] G. D. Mansfeld and I. M. Kotelyansky, The development of a new class of BAW microwave acoustic devices for ecological monitoring, 2002 IEEE Ultrasonics Symposium, vol. 1, pp. 909–912, 2002, <https://doi.org/10.1109/ULTSYM.2002.1193544>
- [111] G. D. Mansfeld, S. G. Alekseev, I. M. Kotelyansky, A. G. Kirillov and V. S. Veretin, BAW microwave temperature sensor, 2004 IEEE SENSORS, vol. 2, pp. 876–878, 2004, <https://doi.org/10.1109/ICSENS.2004.1426310>
- [112] E. Courjon, B. François, G. Martin, W. Daniau, T. Baron, M. Loschonsky, J.M. Friedt, B. Belgacem, L. Reindl, and S. Ballandras, High overtone bulk acoustic resonators for high temperature sensing applications, 2013 Joint European Frequency and Time Forum & International Frequency Control Symposium (EFTF/IFC), pp. 992–995, 2013, <https://doi.org/10.1109/EFTF-IFC.2013.6702287>
- [113] Hao Zhang, Wei Pang and Eun Sok Kim, High-frequency bulk acoustic resonant microbalances in liquid, 2005 IEEE International Frequency Control Symposium and Exposition, pp. 5, 2005, <https://doi.org/10.1109/FREQ.2005.1573905>
- [114] H. Zhang, W. Pang and E. S. Kim, Miniature high-frequency longitudinal wave mass sensors in liquid, *IEEE Transactions on Ultrasonics, Ferroelectrics, and Frequency Control*, vol. 58 (1), pp. 255–258, 2011, <https://doi.org/10.1109/TUFFC.2011.1794>

- [115] T. Baron, D. Gachon, J.P. Romand, S. Alzuaga, S. Ballandras, J. Masson, L. Catherinot, and M. Chatras, A pressure sensor based on a HBAR micromachined structure, 2010 IEEE International Frequency Control Symposium, pp. 361–364, 2010, <https://doi.org/10.1109/FREQ.2010.5556312>
- [116] Y. Yamakawa, K.h. Sano, R. Karasawa and T. Yanagitani, A new type wide-frequency-range shear viscosity sensor using c-axis tilted ScAlN thin film on temperature stable AT-cut quartz thick plate, 2017 IEEE International Ultrasonics Symposium (IUS), pp. 1–4, 2017, <https://doi.org/10.1109/ULTSYM.2017.8092486>
- [117] V. Gokhale, B. Downey, D. Katzer, N. Nepal, R. Stroud, D. Meyer, and, A. Lang, Epitaxial bulk acoustic wave resonators as highly coherent multi-phonon sources for quantum acoustodynamics, Nature Communications, vol. 11, 2020, <https://doi.org/10.1038/s41467-020-15472-w>
- [118] T. A. Gosavi, E. R. MacQuarrie, G. D. Fuchs and S. A. Bhave, HBAR as a high frequency high stress generator, 2015 IEEE International Ultrasonics Symposium (IUS), pp. 1–4, 2015, <https://doi.org/10.1109/ULTSYM.2015.0361>
- [119] M. Bild, U. von Luepke, Y. Yang, M. Drimmer, H. Doeleman, and Y. Chu, Circuit quantum acousto-dynamics with bulk acoustic wave resonators, APS March Meeting Abstracts, 2021, <https://ui.adsabs.harvard.edu/abs/2021APS..MARF31002B>
- [120] M. Abdelmejeed, J. Kuo, A. Ravi and A. Lal, Cmos Controlled Ghz Ultrasonic Impedance Imager, 20th International Conference on Solid-State Sensors, Actuators and Microsystems & Eurosensors XXXIII (TRANSDUCERS & EUROSENSORS XXXIII), pp. 57–60, 2019, <https://doi.org/10.1109/TRANSDUCERS.2019.8808493>
- [121] J. Hoople, J. Kuo, S. Ardanuç and A. Lal, Chip-scale reconfigurable phased-array sonic communication, 2014 IEEE International Ultrasonics Symposium, pp. 479–482, 2014, <https://doi.org/10.1109/ULTSYM.2014.0119>
- [122] A. Lal, GHz ultrasonics for on chip delay lines, communications, timing, memory, and sensing, 2017 Joint Conference of the European Frequency and Time Forum and IEEE International Frequency Control Symposium (EFTF/IFCS), pp. 138–138, 2017, <https://doi.org/10.1109/FCS.2017.8088826>

2.1 System description

Figure 2.1 shows the concept of the measurement system; this representation shows a typical micro analysis system using MEMS technologies for its implementation over one side of a silicon wafer, carrying liquid samples of interest. While traditional approaches for liquid detection, such as SAW, require large areas of the system's layout to be implemented, the HBAR approach studied in this work requires no area of the microfluidic system since its piezoelectric transducer is patterned at the opposite face of the wafer, generating bulk acoustic waves that travel across the thickness of the silicon substrate to interact with liquid samples.

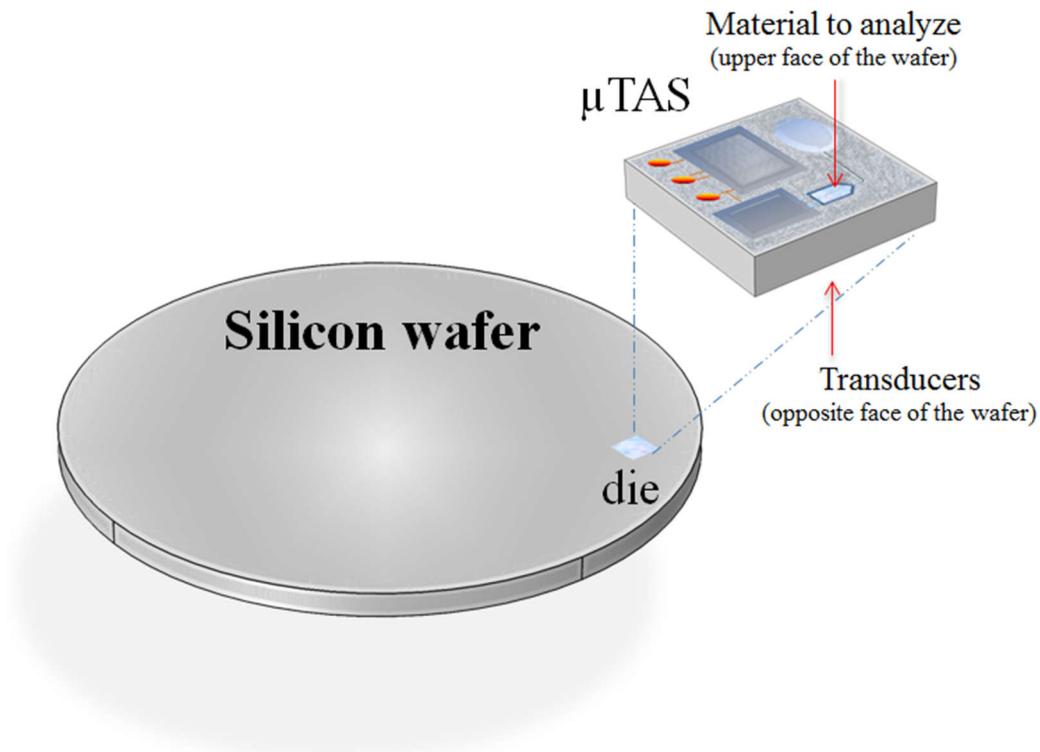


Figure 2.1: 3D representation of the measurement system. The upper face of the chip contains a liquid sample to analyze, while the acoustic sensors are located on the opposite (lower) face of the die, generating bulk waves through the silicon substrate to interact with the sample.

The operating mechanism is based on interaction of longitudinal bulk acoustic waves traveling across the thickness of the silicon substrate and liquid samples placed at the upper face of the chip. This Chapter describes the main operation mode, the sensor working under a pulse-echo regime, and also is presented an alternative approach using a similar structure as resonator. Later, theoretical models to predict the operation of both approaches are presented, as well as useful equations for their design.

2.1.1 HBAR sensor working as a Pulse-Echo Transducer

Chapter 1 presented the simplest HBAR; a bulk acoustic device consisting of a thin piezoelectric layer coupled to an acoustic substrate. Unlike FBARs or SMRs, this device allows leakage of acoustic energy into the substrate, enabling the thickness of the substrate to be used as a transport medium for ultrasound packets emitted by the transducer to interact with materials placed on the opposite side of the chip [1]. The zoomed section in Figure 2.2 shows a 3D representation of such system: the lower face of the chip carries the piezoelectric transducer that emits and receives the ultrasound packets that travel across the silicon thickness to interact with the sample placed at the opposite face of the chip.

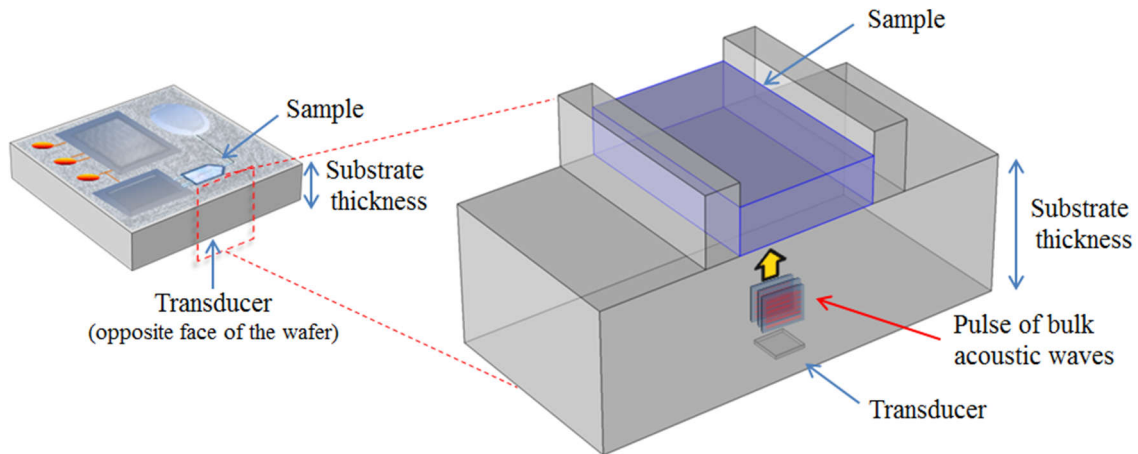


Figure 2.2: A 3D transparent slice representing the concept of the sensor: The lower face of the wafer carries the transducer that emits and receives pulses of bulk waves through the thickness of the wafer while the upper face remains free of electronics and cables and is used as a detection surface carrying liquid samples.

The detection mechanism consists of measuring the degree of acoustic impedance mismatch between the silicon body and the liquid samples. Depending on the physical properties of each sample, a different amount of acoustic energy will be reflected back towards the transducer, according with equation 1 [2].

$$|\Gamma| = \frac{|Z_{material} - Z_{substrate}|}{Z_{material} + Z_{substrate}} \quad (1)$$

With $Z_{substrate}$ as the acoustic impedance of the substrate, and $Z_{material}$ as the acoustic impedance of material to be evaluated. Figure 2.3 describes the operation at different slices of time: a) The pulse of ultrasound has been recently emitted and travels (with direction indicated by the blue arrow) across the thickness of the substrate to reach the liquid sample at the opposite face of the

wafer. b) Once the acoustic packet has reached the sample, the acoustic impedance discontinuity at the solid-liquid interface causes a part of the pulse to be reflected back towards its emitting piezoelectric element. The latter provides information about the analyte, since the amount of energy reflected corresponds with the acoustic impedance mismatch between the silicon substrate and the material to study, and therefore, depends on the physical properties of each sample.

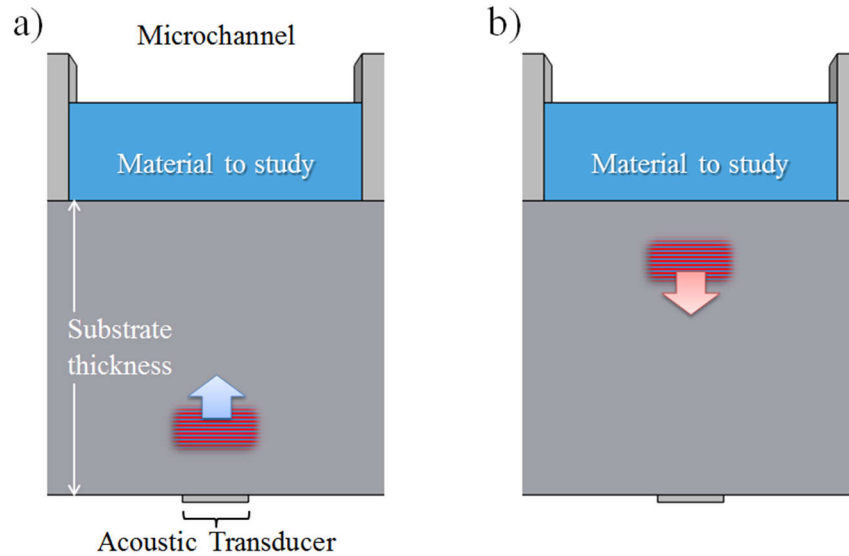


Figure 2.3: 2D representation of the device's operation at two different moments in time: a) The pulse of ultrasound has been recently emitted and travels (with direction indicated by the blue arrow) across the thickness of the substrate to reach the liquid sample at the opposite face of the wafer. b) Once it has interacted with the sample, the acoustic pulse begins its journey back towards its source to be recorded.

Assuming that such sensor is able to classify reflected acoustic pulses according to their amplitude (differences caused by physical or biochemical changes in the liquid sample), the readout mechanism would simply consist of measurement of the voltage level produced by the transducer every time it is hit by an acoustic echo in a determined time-of-flight (ToF).

2.1.2 HBAR sensor working as an Acoustic Resonator

Figure 2.4a shows the representation of the alternative sensor; a structure similar to that shown in Figure 2.2, but working as an acoustic resonator. When a continuous low-power RF signal is applied to this HBAR it produces standing pressure waves in the thickness of its silicon substrate (assuming constituting materials with acoustic impedances in the same order of magnitude). If the microchannel is empty, i.e. filled only with the air that surrounds the sensor, equation 1 predicts 99.996 % of reflection at the solid/air interfaces, considering $Z_{subs} = 19.7E + 6$ Rayl and $Z_{mat} = 400$ Rayl as the acoustic impedances of the silicon substrate and the gas (air), respectively. The latter indicates that the acoustic energy generated by the transducer will remain trapped within the thickness of the substrate because of the acoustic impedance mismatch between the solid materials constituting the sensor and the air present at both the upper and the lower faces of the chip. This ideal condition of *lossless reflection* causes the appearance of a well-defined resonance peak as represented by Figure 2.4b.

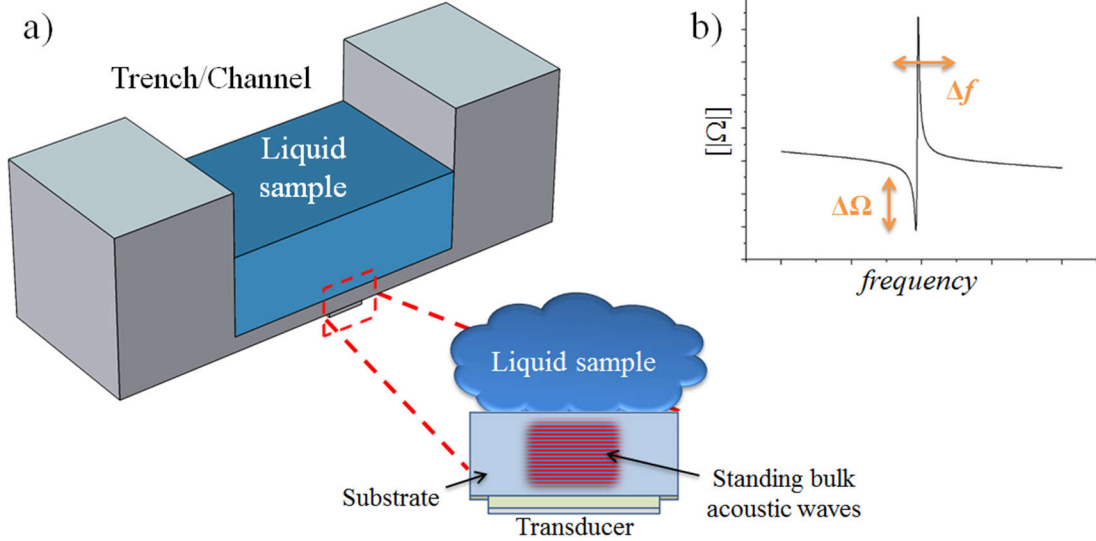


Figure 2.4: a) 3D representation of the sensor, the lower face of the wafer carries the transducer while the opposite side can be used as a totally electronics-free detecting surface. The zoomed section is a 2D representation of the device; the transducer is coupled to an acoustic substrate generating stationary bulk waves in the whole stack of materials. b) The acoustic energy remains trapped within the solid structure causing the appearance of well-defined resonances, both changes in the amplitude of the resonance and detectable frequency shifts are expected accordingly to specific physical properties of each liquid sample.

On the other hand, when the trench is filled with the analytical sample the acoustic impedance mismatch decreases, allowing leakage of energy within the liquid domain, causing both a decrease in amplitude of the resonance peaks and a detectable change of resonant frequency [3].

2.2 Studying fluid compressional properties at microscale using longitudinal bulk acoustic waves

The sensing mechanism described in the previous section is based on the interaction between longitudinal acoustic waves within the solid sensor and the opposition exerted by fluids to acoustic flow (its acoustic impedance). The complex acoustic impedance of materials Z^* is related to density ρ and the dynamic complex modulus $M^*(\omega)$ as [4]:

$$Z^* = \sqrt{\rho M^*(\omega)} \quad (2)$$

With $\omega = 2\pi f$ as the angular frequency. In the case of longitudinal waves, M^* is a function of the complex compressibility modulus (Bulk modulus) K^* and the shear modulus G^* [4]:

$$M^*(\omega) = K^*(\omega) + \frac{4}{3}G^*(\omega)$$

The complex modulus K^* is stated as $K^* = K' + iK''$ [5], where K' is the storage modulus representing the elastic part and K'' is the loss modulus, representing the viscous part. Similarly for

the shear modulus we have $G^* = G' + iG''$, with G' as the shear storage modulus and G'' as the shear loss modulus. For Newtonian media the shear modulus G^* can be reduced to its imaginary part $G^* \approx iG''$ [6], so that the dynamic modulus of the liquid for longitudinal waves is:

$$M^*(\omega) = K' + iK'' + i\frac{4}{3}G''$$

The loss moduli K'' and G'' are respectively related to compressional and shear viscosities as: $\mu_B = K''/\omega$ and $\mu = G''/\omega$ [6, 7], where μ_B is the real part of the bulk viscosity and μ is the real part of the shear viscosity. Thus, the dynamic modulus of a liquid subjected to a longitudinal compressive force:

$$M^*(\omega) = K' + i\omega\left(\mu_B + \frac{4}{3}\mu\right) \quad (3)$$

In the case of liquids, the real part of the bulk modulus K' is related to the speed of sound c as $K' = \rho c^2$. Therefore, substituting equation 3 in equation 2, the complex acoustic impedance of a liquid subjected to a pressure wave is [3, 8]:

$$Z_{liquid} = Z_{real} \sqrt{\left[1 + i\frac{\omega}{\rho c^2}\left(\mu_B + \frac{4}{3}\mu\right)\right]} \quad (4)$$

$$Z_{real} = \rho c \quad (5)$$

The latter indicates that compressional information such as the Bulk Modulus and the specific Acoustic Impedance can be obtained by interrogating a liquid sample with pulses of longitudinal waves produced by a transducer. Although the approximation $Z_{liquid} = \rho_{liquid}c_{liquid}$ could offer accurate results in most applications, it is important consider the complex term in equation 4 for high-frequency transducers and liquid samples which viscosity exceeds 10 cP [9].

2.3 Piezoelectric transduction in longitudinal BAW devices and their input impedance

The most straight forward method of generating internal pressure waves in a solid bulk is by using a piezoelectric transducer. Piezoelectricity is the physical property that causes polarization and charge accumulation in certain crystals, ceramics and other solids when external mechanical stress is applied, being the dipole created proportional to the amplitude of the force exerted. This phenomenon called “direct piezoelectric effect” is linear, so that changing the direction of the strain leads to an inverse sign of the dipole created [10]. This physical property also works in reverse; electrical fields applied to these materials leads to mechanical deformation of its structure.

Assuming constant temperature (isothermal), the equations governing such energy transformations are given by [11]:

$$\begin{aligned} S &= s^E T + d_t E \\ D &= dT + \varepsilon^T E \end{aligned} \quad (6)$$

With S as the mechanical strain, D as the charge density, T represents the mechanical stress, E is the electric field, d_t indicates transposition of the d -matrix (which is a piezoelectric constant), and the superscripts T and E indicate that permittivity ε and compliance s are measured under constant stress and electric field conditions respectively. These coupled piezoelectric equations can also be expressed choosing T and D as the independent variables, or S and E , or S and D , using appropriate conversion of piezoelectric constants [11].

$$\begin{aligned} S &= s^D T + g_t D \\ E &= -gT + \beta^T D \end{aligned}$$

$$\begin{aligned} T &= c^E S - e_t E \\ D &= eS + \varepsilon^S E \end{aligned}$$

$$\begin{aligned} T &= c^D S - h_t D \\ E &= -hS + \beta^S D \end{aligned}$$

Where d , g , e , and h are the piezoelectric constants. A necessary condition for the piezoelectricity phenomenon is absence of a center of symmetry; therefore these materials are intrinsically anisotropic. The piezoelectric constants relate second-order tensors (Stress or Strain) to vectors (charge density or electric field), so that they are represented as third-order tensors. For the case of equation 6:

$$\begin{aligned} \begin{bmatrix} S_1 \\ S_2 \\ S_3 \\ S_4 \\ S_5 \\ S_6 \end{bmatrix} &= \begin{bmatrix} s_{11} & s_{12} & s_{13} & s_{14} & s_{15} & s_{16} \\ s_{21} & s_{22} & s_{23} & s_{24} & s_{25} & s_{26} \\ s_{31} & s_{32} & s_{33} & s_{34} & s_{35} & s_{36} \\ s_{41} & s_{42} & s_{43} & s_{44} & s_{45} & s_{46} \\ s_{51} & s_{52} & s_{53} & s_{54} & s_{55} & s_{56} \\ s_{61} & s_{62} & s_{63} & s_{64} & s_{65} & s_{66} \end{bmatrix} \begin{bmatrix} T_1 \\ T_2 \\ T_3 \\ T_4 \\ T_5 \\ T_6 \end{bmatrix} + \begin{bmatrix} d_{11} & d_{12} & d_{13} \\ d_{21} & d_{22} & d_{23} \\ d_{31} & d_{32} & d_{33} \\ d_{41} & d_{42} & d_{43} \\ d_{51} & d_{52} & d_{53} \\ d_{61} & d_{62} & d_{63} \end{bmatrix} \begin{bmatrix} E_1 \\ E_2 \\ E_3 \end{bmatrix} \\ \\ \begin{bmatrix} D_1 \\ D_2 \\ D_3 \end{bmatrix} &= \begin{bmatrix} d_{11} & d_{12} & d_{13} & d_{14} & d_{15} & d_{16} \\ d_{21} & d_{22} & d_{23} & d_{24} & d_{25} & d_{26} \\ d_{31} & d_{32} & d_{33} & d_{34} & d_{35} & d_{36} \end{bmatrix} \begin{bmatrix} T_1 \\ T_2 \\ T_3 \\ T_4 \\ T_5 \\ T_6 \end{bmatrix} + \begin{bmatrix} \varepsilon_{11} & \varepsilon_{12} & \varepsilon_{13} \\ \varepsilon_{21} & \varepsilon_{22} & \varepsilon_{23} \\ \varepsilon_{31} & \varepsilon_{32} & \varepsilon_{33} \end{bmatrix} \begin{bmatrix} E_1 \\ E_2 \\ E_3 \end{bmatrix} \end{aligned}$$

However, for the case of the systems described in Figure 2.2 and Figure 2.4, it is not necessary deformation of the piezoelectric material in all directions to create bulk waves inside the silicon substrate, but rather expansion and contraction of its thickness. Figure 2.5a is a 3-D representation of the piezoelectric element isolated from the substrate, the active material (green) is sandwiched between two thin metal electrodes that when connected to a voltage source will cause expansion of the structure in the direction indicated by the red arrows.

Since lateral dimensions w and l are much larger than the thickness t , the plate can be considered to be laterally clamped (lateral displacement $S = 0$). Other pertinent assumption is negligible electric flux leakage of the insulating medium (lossless piezoelectric), this suggest that D and S could be chosen as independent variables:

$$\begin{aligned} T &= c^D S - h_t D \\ E &= -h S + \beta^S D \end{aligned} \quad (7)$$

Where h is a piezoelectric constant, c is the stiffness and β is the inverse permittivity.

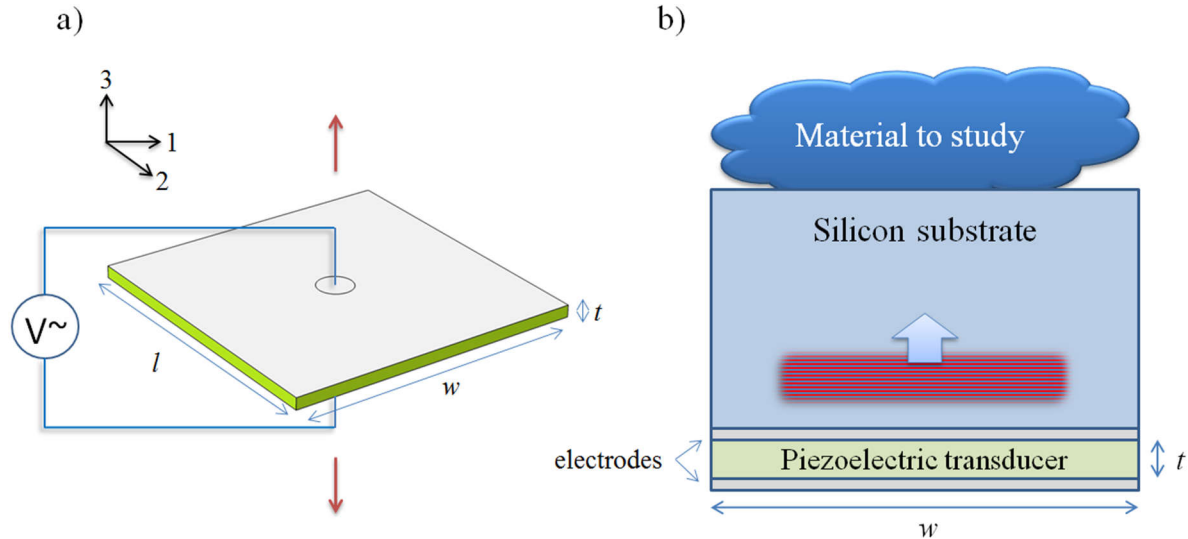


Figure 2.5: a) 3-D representation of the piezoelectric layer, isolated from the substrate; it is sandwiched between electrodes of negligible thickness to drive the material on its thickness extensional mode, causing mechanical displacement of the structure in the x_3 (3) direction. b) 2-D representation of the measurement system; periodic displacement of the piezoelectric in the x_3 direction cause bulk acoustic waves when coupled to an acoustic substrate, which travel across the thickness of the wafer (with direction indicated by the blue arrow) to interact with the sample.

If lateral dimensions are considered as “clamped” and considering homogenous displacement of the plates in the z -direction (3-direction, thickness expansion), equation 7 reduces to:

$$T_3 = c_{33}^D S_3 - h_{33} D_3 \quad (8a)$$

$$E_3 = -h_{33} S_3 + \beta_{33}^S D_3 \quad (8b)$$

This is related to the wave equation since strain is defined as $S_3 = \partial u_3 / \partial x_3$. The wave equation for this case is [12]:

$$\frac{\partial^2 u_3}{\partial t^2} = \frac{c_{33}^D}{\rho} \frac{\partial^2 u}{\partial x_3^2}$$

Where u_3 is the particle displacement in the 3-direction x_3 and ρ is density. The general solution has the form:

$$u_3 = \left[A \sin \frac{\omega x_3}{v_D} + B \cos \frac{\omega x_3}{v_D} \right] e^{-i\omega t}$$

Where v_D is the longitudinal wave velocity of the plate:

$$v_D = \sqrt{\frac{c_{33}^D}{\rho}}$$

Taking the derivative $S_3 = \partial u_3 / \partial x_3$, and substituting in equation 8a using the boundary condition $T_3 = 0$ at $x_3 = 0$ (zero stress at the free bottom boundary):

$$0 = \left\{ c_{33}^D \left[\frac{\omega}{v_D} (A \cos(0) - B \sin(0)) \right] - h_{33} D_3 \right\} e^{-i\omega t}$$

$$A = \frac{h_{33} D_3 v_D}{c_{33}^D \omega}$$

Applying the condition $T_3 = 0$ at $x_3 = t_{piezo}$ (zero stress at the free upper boundary) to equation 8a and solving for B :

$$B = \frac{h_{33} D_3 v_D}{c_{33}^D \omega} \frac{\cos\left(\frac{\omega t_{piezo}}{v_D}\right) - 1}{\sin\left(\frac{\omega t_{piezo}}{v_D}\right)}$$

Where t_{piezo} is the thickness of the transducer. The latter gives an analytical value for S_3 :

$$S_3 = \left\{ \frac{h_{33} D_3}{c_{33}^D} \left[\cos\left(\frac{\omega x_3}{v_D}\right) - \frac{\cos\left(\frac{\omega t_{piezo}}{v_D}\right) - 1}{\sin\left(\frac{\omega t_{piezo}}{v_D}\right)} \sin\left(\frac{\omega x_3}{v_D}\right) \right] \right\} e^{-i\omega t} \quad (9)$$

Since a constant electric field is assumed (parallel plates), the voltage is found with the relationship $E = dV / t_{piezo}$ that is, taking the integral of the electric field (equation 8b) over the thickness of the body [10]:

$$\int_{V_a}^{V_b} dV = \int_0^{t_{piezo}} E dx_3$$

$$V = \int_0^{t_{piezo}} -h_{33}S_3 + \beta_{33}^S D_3$$

Substituting S_3 from equation 9 and solving:

$$V = -\beta_{33}^S D_3 t_{piezo} + \frac{h_{33}^2 D_3 v_D}{c_{33}^D \omega} \left(2 \tan \left(\frac{\omega t_{piezo}}{2v_D} \right) \right)$$

The electric displacement field D_3 (electric induction) is related to current I as [12]:

$$\begin{aligned} I &= A \frac{dD_3}{dt} \\ &= -j\omega A D_3 \end{aligned}$$

Where A is the electrode area formed by w and l (Figure 2.5a). The input electrical impedance of the resonator is $Z_{in} = V/I$.

$$Z_{in} = \frac{\beta_{33}^S D_3 t_{piezo} + \frac{h_{33}^2 D_3 v_D}{c_{33}^D \omega} \left(2 \tan \left(\frac{\omega t_{piezo}}{2v_D} \right) \right)}{j\omega A D_3}$$

$$= \frac{t_{piezo} + \frac{h_{33}^2 v_D}{\beta_{33}^S c_{33}^D \omega} \left(2 \tan \left(\frac{\omega t_{piezo}}{2v_D} \right) \right)}{j\omega A \epsilon_{33}^S}$$

Where $\epsilon_{33}^S = 1/\beta_{33}^S$ is the permittivity [F/m]. This equation also includes an important concept formed by the term: $h_{33}^2/\beta_{33}^S c_{33}^D$, called the electromechanical coupling coefficient (k_t^2). Neglecting losses, it is a measure of the conversion efficiency between mechanical and electric energy (and vice versa) [13]. Rearranging terms this leads to the equation for a piezoelectric layer operating in the thickness expansion mode [11]:

$$Z_{in} = \frac{1}{j\omega C_0} \left[1 - k_t^2 \frac{\tan \left(\frac{\omega t_{piezo}}{2v^D} \right)}{\frac{\omega t_{piezo}}{2v^D}} \right] \quad (10)$$

$$k_t^2 = \frac{h_{33}^2}{\beta_{33}^S c_{33}^D}$$

$$C_0 = \frac{e_{33}^S A}{t_{piezo}}$$

Where C_0 is the clamped (static) capacitance. Figure 2.6 exemplifies the electrical response of a hypothetical piezoelectric layer of AlN, with side $w = 80 \mu\text{m}$ and thickness $t_{\text{piezo}} = 3 \mu\text{m}$, operating on its thickness extensional mode. Material properties correspond to values found in the COMSOL Multiphysics Library [14]. Since constitutive equations in COMSOL, and material properties, appear on Stress-Charge form, the following conversions between piezoelectric coefficients [11] were applied:

$$h_{33} = e_{33}^S / \epsilon_{33}^S \quad (11)$$

$$c_{33}^D = c_{33}^E + (e_{33}^S h_{33}) \quad (12)$$

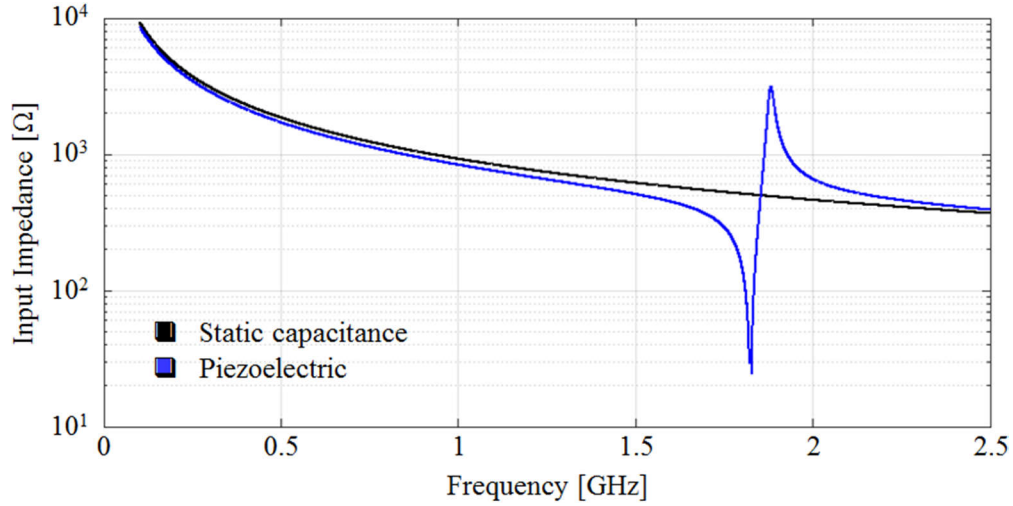


Figure 2.6: Analytical input impedance plot. The black trace is the static capacitance for a thin piezoelectric resonator with side $w = 80 \mu\text{m}$ and thickness $t_{\text{piezo}} = 3 \mu\text{m}$. The blue trace corresponds with its piezoelectric behavior (equation 10), where resonance and anti-resonance peaks appear in the 1.5 – 2 GHz range.

The black trace in Figure 2.6 corresponds with the static capacitance $\epsilon_{33}^S A / t_{\text{piezo}}$, while the blue trace corresponds with equation 10. Note that both traces accompany each other except for the interval between 1.5 – 2 GHz, where resonance and anti-resonance peaks appear indicating piezoelectric activity. The latter corresponds with the expected mechanical resonance f_N of such structure [15]:

$$f_N = N \frac{v_{\text{piezo}}}{2t_{\text{piezo}}} \quad (13)$$

Where v_{piezo} is the acoustic velocity of the longitudinal wave appearing in the thickness of the piezoelectric layer, and N is an integer multiplier.

2.4 Input impedance of HBARs with electrodes of non-negligible thickness

The previous section presented a piezoelectric layer with lateral dimensions much larger than its thickness, surrounded by negligible electrodes, bringing into being the simplest bulk acoustic wave resonator, operating in its thickness extensional mode. Here, such transducer is considered as

coupled to a much thicker acoustic substrate. The zoomed section in Figure 2.7 shows a 2-D representation of a simple HBAR, which is formed by a thin piezoelectric transducer (operating in thickness extensional mode) coupled to a largely thicker substrate.

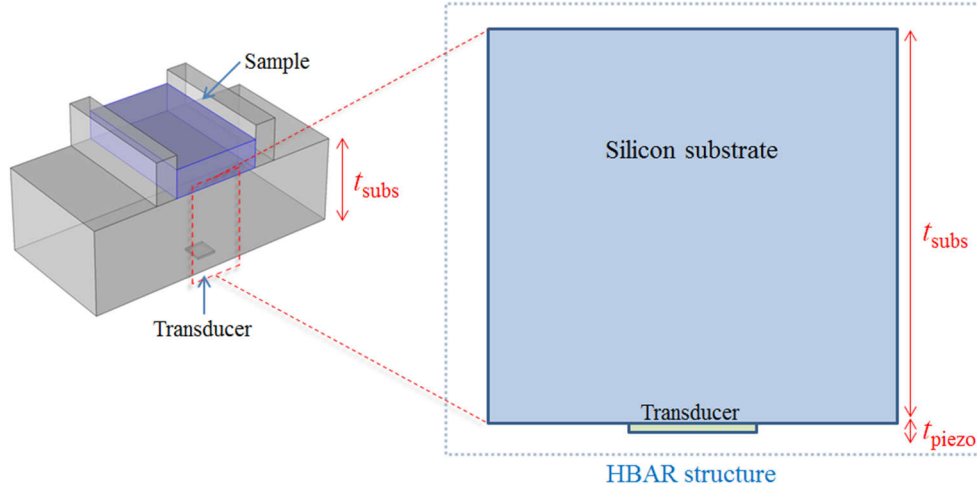


Figure 2.7: 2-D representation of the HBAR structure formed by the thin piezoelectric layer coupled to a largely thicker substrate.

When a continuous low-power RF signal is applied to the electrodes, the thickness extensional mode of the piezoelectric film is activated producing longitudinal pressure waves that leaks into the silicon substrate (Figure 2.8a), whenever both materials have acoustic impedance within the same order of magnitude (equation 1). If air is present in both the upper and in the lower side of the stack of solid materials, the acoustic energy remains trapped in the thickness of the whole structure because of the high degree of acoustic impedance mismatch between solid materials and gas (Figure 2.8b). As an example, at the silicon/air interface in the upper part of the structure, it is expected 99.996 % reflection of acoustic energy towards the interior of the structure according to equation 1 (using $Z_{air} = 398 \text{ Rayl}$ and $Z_{silicon} = 19.7E + 6 \text{ Rayl}$, as the acoustic impedance values of ‘air’ and ‘silicon’ respectively [9]).

The fundamental mode Δf_0 of this composite structure is found by relating the acoustic velocity of longitudinal waves across the whole HBAR v_{hbar} and its total thickness t_{hbar} [16]. Since the thickness $t_{subs} \gg t_{piezo}$, the fundamental mode is commonly approximated by using solely the acoustic velocity of longitudinal waves across the substrate v_{subs} and its thickness t_{subs} :

$$\Delta f_0 = \frac{v_{hbar}}{2t_{hbar}} \approx \frac{v_{subs}}{2t_{subs}} \quad (14)$$

For this composite resonator consisting of a thin piezoelectric layer coupled to a thicker substrate, the analytical expression of the input electrical impedance is [17]:

$$Z_{in} = \frac{1}{j\omega C_0} \left[1 - \frac{k_t^2}{\gamma} \frac{2 \tan \frac{\gamma}{2} + z_b \tan \gamma_s}{1 + z_b \frac{\tan \gamma_s}{\tan \gamma}} \right] \quad (15)$$

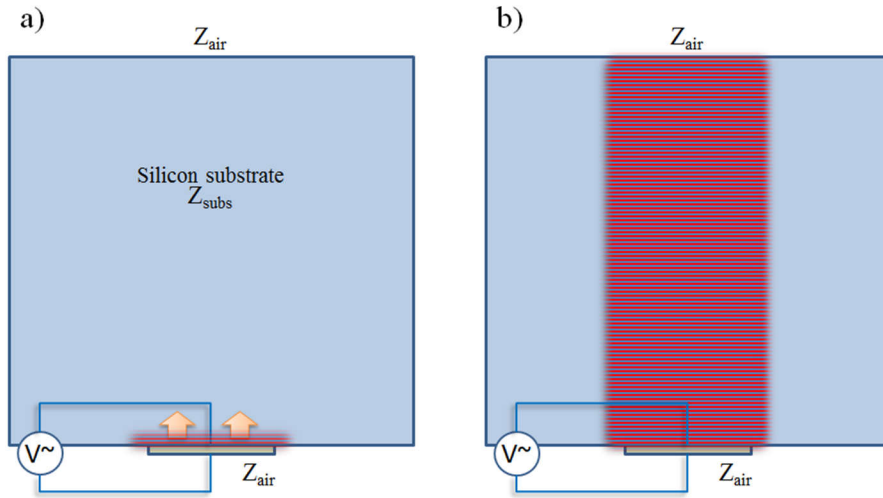


Figure 2.8: a) Acoustic energy produced by the transducer leaks into the substrate if the acoustic impedances of both materials are similar. b) Acoustic energy remains trapped in the thickness of the structure because of the low acoustic impedance of the air that surrounds it.

Being $\gamma = 2\pi f(t_{\text{piezo}}/v_{\text{piezo}})$, $\gamma_s = 2\pi f(t_{\text{subs}}/v_{\text{subs}})$, $z_b = Z_s/Z_0$, with Z_s and Z_0 as the acoustic impedance of the substrate and the piezo film, respectively. Since stationary bulk waves are established between top and bottom free surfaces, all the possible harmonics of the fundamental mode of the structure can exist, therefore, the electrical response obtained by equation 15 leads to a frequency comb formed by the fundamental mode of the structure Δf_0 and its multiple harmonics, modulated by the resonance of the piezoelectric [18].

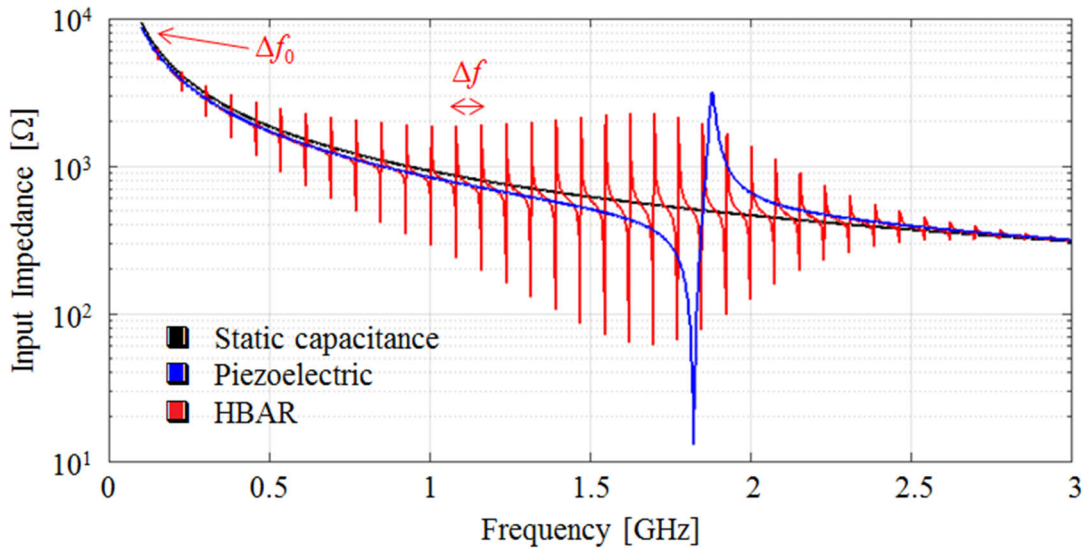


Figure 2.9: Analytical impedance plot obtained from equation 15 (red trace), using a hypothetical piezoelectric resonator (side $w = 80 \mu\text{m}$ and thickness $t_{\text{piezo}} = 3 \mu\text{m}$), coupled to a $60 \mu\text{m}$ silicon substrate. The piezoelectric resonance (blue trace) was included as reference.

This analytical plot (Figure 2.9) was calculated with equation 15 assuming an AlN transducer such as the one used for the example of Figure 2.6, but this time coupled to a silicon substrate of

thickness $t_{subs} = 60 \mu m$. The fundamental mode of the structure agrees with equation 14 ($\Delta f_0 \sim 80 MHz$), followed by its multiple harmonics separated by Δf . An important aspect of this device is the fact that modes are much favorably excited near the resonance of the piezoelectric than anywhere else in the spectrum [19]. In practice, the more the thickness of the piezo is reduced (higher frequencies), the more difficult it is to manufacture electrodes of negligible thickness, and therefore the effect of electrodes becomes relevant since specific acoustic impedance of the metallic electrodes and its thickness respect to the wavelength adds modifications to the input impedance curve of the HBAR [20]. Figure 2.10 show all the layers involved in the actual device.

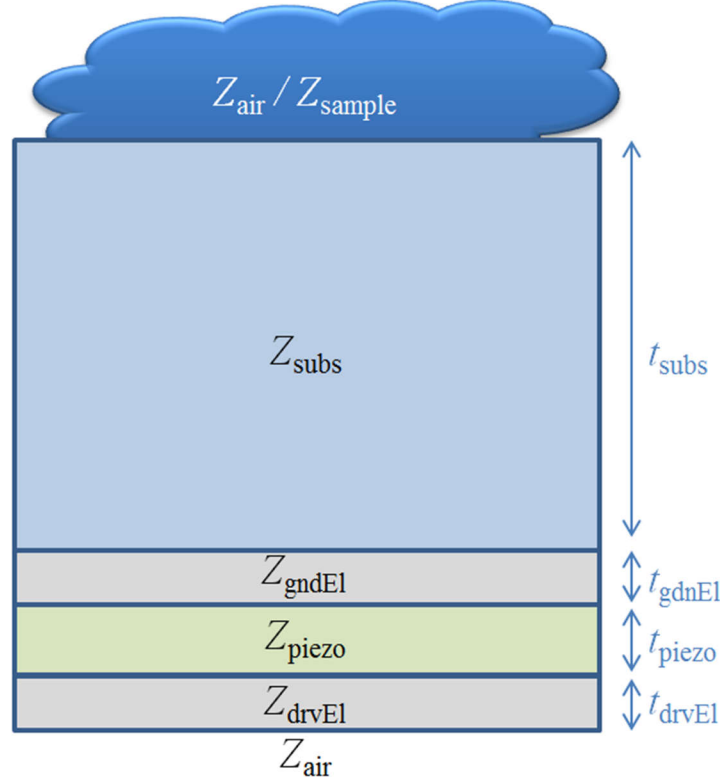


Figure 2.10: Layers constituting the actual device.

In this case, the analytical expression for the input impedance, taking in account the effect of electrodes, is [21]:

$$Z_{in} = \frac{1}{j\omega C_0} \left[1 - \frac{k_t^2}{\gamma} \frac{(z_b + z_2) \sin \gamma + j2(1 - \cos \gamma)}{(z_b + z_2) \cos \gamma + j(1 + z_b z_2) \sin \gamma} \right] \quad (16)$$

Where ω is the angular frequency, C_0 is the clamped capacitance of the resonator, k_t^2 is the electromechanical coupling factor of the piezoelectric material, $\gamma = 2\pi f(t_{piezo}/v_{piezo})$, $z_b = Z_b/Z_{piezo}$ where Z_{piezo} is the acoustic impedance of the piezoelectric material and $Z_b = jZ_{drvEl} \tan \gamma_{drvEl}$ with Z_{drvEl} as the acoustic impedance of the drive electrode and $\gamma_{drvEl} = 2\pi f(t_{drvEl}/v_{drvEl})$, where t_{drvEl} is the thickness of the drive electrode and v_{drvEl} its sound velocity, $z_2 = Z_{Low}/Z_{piezo}$, and:

$$Z_{Low} = j \frac{Z_{subs} \cos \gamma_{gndEl} \sin \gamma_{subs} + Z_{gndEl} \sin \gamma_{gndEl} \cos \gamma_{subs}}{\cos \gamma_{gndEl} \cos \gamma_{subs} - \left(\frac{Z_{subs}}{Z_{gndEl}} \right) \sin \gamma_{gndEl} \sin \gamma_{subs}}$$

Being Z_{gndEl} and Z_{subs} the acoustic impedances of the reference (ground) electrode and that of the substrate, $\gamma_{gndEl} = 2\pi f(t_{gndEl}/v_{gndEl})$ where t_{gndEl} is the thickness of the reference electrode and v_{gndEl} its sound velocity, and $\gamma_{subs} = 2\pi f(t_{subs}/v_{subs})$. Figure 2.11 show the effect of non-negligible electrodes in the electrical response.

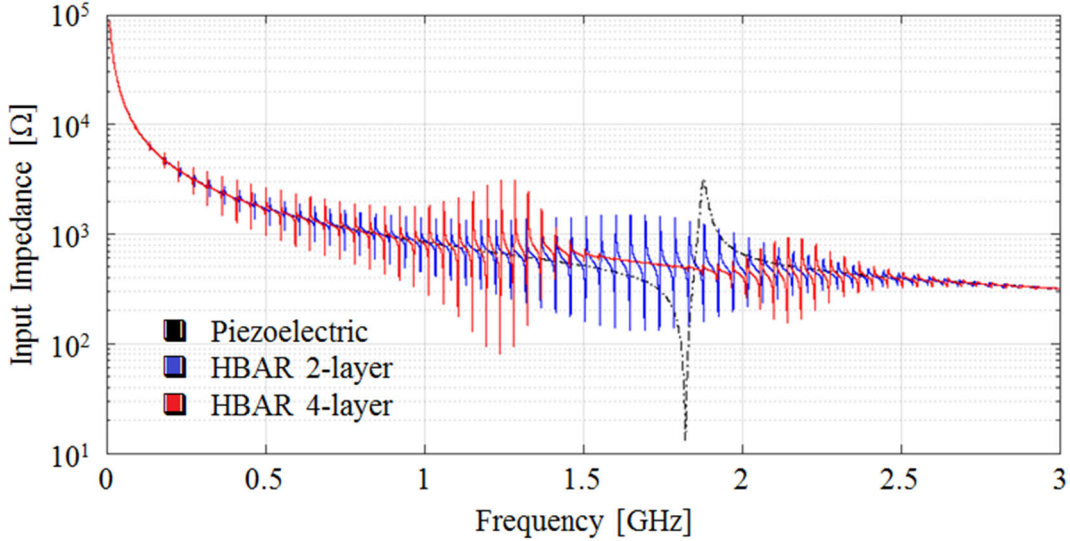


Figure 2.11: Analytical impedance plot showing the effect of non-negligible electrodes. The blue trace corresponds to a simple HBAR consisting of a $3 \mu\text{m}$ piezoelectric layer coupled to a $100 \mu\text{m}$ silicon substrate (equation 15). The red trace corresponds to calculation including non-negligible $1 \mu\text{m}$ electrodes (equation 16), modes with improved amplitude at lower frequencies were obtained.

The blue trace in Figure 2.11 is the input impedance of a simple HBAR formed by the previously mentioned piezoelectric layer of thickness $t_{piezo} = 3 \mu\text{m}$, coupled to a silicon substrate of thickness $t_{subs} = 100 \mu\text{m}$. In this case, the amplitude of lower order modes is very small compared to the amplitude of modes at frequencies close to the resonance of the piezoelectric [22]. On the other hand, the red trace uses equation 16 to plot the electrical response of a similar HBAR, including electrodes of thickness $t = 1 \mu\text{m}$, obtaining modes with improved amplitude at lower frequencies.

2.5 Distribution of acoustic pulses at the detection surface

The previous section showed HBAR devices operating as resonators, i.e. driven by continuous voltage sources causing generation of stationary bulk waves in the substrate (Figure 2.8b), exposing the electrical response of this kind of composite resonators, and operative frequencies. Here is described and HBAR structure used in a pulse-echo scenario (as in Figure 2.2).

The first condition is to avoid creation of stationary waves in the silicon bulk, for this, electrodes should be driven for a shorter time than the required for longitudinal waves to travel from the transducer to the detection surface (on the opposite side of the wafer), that is:

$$\tau_{op} < ToF$$

$$ToF = \frac{t_{subs}}{v_{subs}} \quad (17)$$

Where ToF (Time-of-Flight) is the time it takes for the bulk acoustic waves to complete their travel from the piezoelectric transducer to the detection surface, and it depends on the thickness of the substrate t_{subs} and its longitudinal sound velocity v_{subs} . A complementary condition is to guarantee the emission and reception of acoustic energy in the form of "packets", that is, reducing diffraction of the bulk waves on their round trip through the thickness of the wafer. From physics is known that emitters with dimensions comparable or smaller than the wavelength will produce waves that fade out in the propagation medium due to diffraction (Figure 2.12b), and the narrower the transducer the greater the vanishing is into the propagating medium [23].

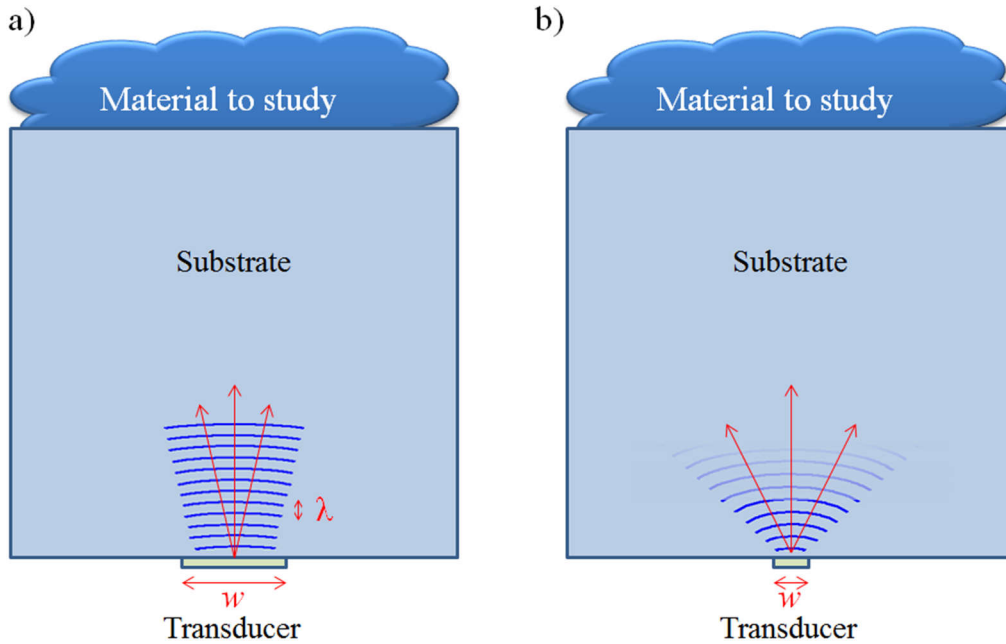


Figure 2.12: Diffraction represented schematically; for determined wavelength diffraction is more pronounced the smaller the transducer width w . a) Transducer width w is several times larger than λ , thus bulk waves are propagated with low loss towards the liquid sample. b) Transducer width w is comparable to λ , causing vanishing of acoustic waves into the medium.

Diffraction can be understood using Huygens' principle, which states that each point on a wavefront may be considered as a source of spherical secondary waves interfering each other [24]. In Figure 2.13 the transducer is represented as an array of individual point sources emitting plane waves (with same characteristics) meeting at the same point (the detection surface). The resulting distribution of energy in that surface is the vector sum of the amplitudes of individual waves, and is represented by the interference pattern in yellow. The maximum intensity in the central zone can be justified by noting that the Huygens wavelets from all the punctual sources travel about the same distance (red arrows) to reach the center of the pattern and thus they arrive with the same phase, gathering their individual amplitude (constructive interference). Contrarily, waves traveling different distances

(green arrows) arrive “out of phase” respect to each other causing destructive interference. Those zones with zero amplitude correspond to angles for which the distance traveled differs by an odd number of half wavelengths. For this one-dimensional example (where $t_{subs} \gg w$) the condition for destructive interference can be estimated by [2]:

$$\sin \theta \approx \frac{\lambda}{w} \quad (18)$$

Where w is the lateral dimension of the transducer (its width), θ the angle formed between the central axis of Figure 2.13 and the point in the detection interface where the minima of the main lobe will appear, and λ is the wavelength of the longitudinal acoustic wave traveling in the substrate, which is related to the operating frequency f_{op} as:

$$\lambda = \frac{v_{subs}}{f_{op}} \quad (19)$$

With v_{subs} as the longitudinal sound velocity for solids, defined by:

$$v_{subs} = \sqrt{\frac{K + \frac{4}{3}G}{\rho}} = \sqrt{\frac{E(1 - \nu)}{\rho(1 + \nu)(1 - 2\nu)}} \quad (20)$$

Where K is the bulk modulus of the solid medium, G the shear modulus, ρ density, E the Young modulus, and ν the Poisson’s ratio. As an example, let us suppose a squared transducer of width $w = 60 \mu m$, operating at 1 GHz, coupled to a silicon substrate of thickness $t_{subs} = 600 \mu m$, Young Modulus $E_{Si} = 170 GPa$, Poisson ratio $\nu_{Si} = 0.28$ and density $\rho_{Si} = 2329 kg/m^3$ (Figure 2.14). Using equation 19 and 18 it is found that the angle θ formed with the central axis of Figure 2.14a (blue dashed line) and the point in the detection interface where the minima of the main lobe will appear is $\theta \approx 9.26^\circ$, i.e., if the detection surface is $600 \mu m$ far from the transducer, the diffraction minima at the detection surface will appear $\sim 98 \mu m$ far from the central axis. Figure 2.14b show the normalized pressure distribution of this hypothetical acoustic wave at the detection surface; this pressure distribution in far field conditions was analytically obtained from equation 21 [25], plotting only distribution along θ .

$$p(r, \theta, \varphi, t) = j \frac{kv_{subs}u_a\rho w^2}{2r\pi} \frac{\sin \alpha \sin \beta}{\alpha \beta} e^{[j(\omega t - kr)]} \quad (21)$$

$$\alpha = (kw \sin \theta \sin \varphi)/2$$

$$\beta = (kw \sin \theta \cos \varphi)/2$$

Where k is the wavenumber, v_{subs} is the sound velocity in silicon, u_a is the transducer vibration velocity, ρ is the medium density, w is the width of the squared transducer, ω is the angular

frequency and r is the distance from the transducer to the point to evaluate $P(\theta)$. As seen in Figure 2.14b, the main lobe of the acoustic pulse should interact with $200\ \mu\text{m}$ of the detection surface, delimited by nodes of destructive interference (diffraction minima) $\sim 100\ \mu\text{m}$ far from the central axis, which agrees well with the approximation of equation 18.

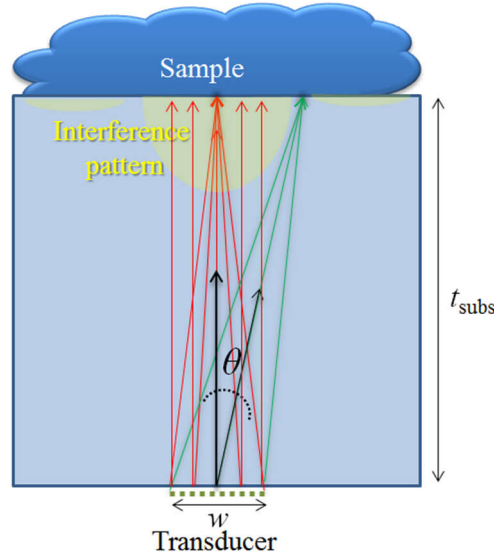


Figure 2.13: Representation of the expected distribution of acoustic energy (in yellow) interacting with the sample at the detection surface. Supposing a transducer formed by an array of individual punctual sources (radiating isotropically), the maximum intensity of energy at the center of the detection surface can be justified by noting that wavelets from all the punctual sources travel about the same distance (red arrows), arriving with the same phase (constructive interference). Contrarily, waves traveling different distances (green arrows) arrive out of phase respect to each other producing destructive interference.

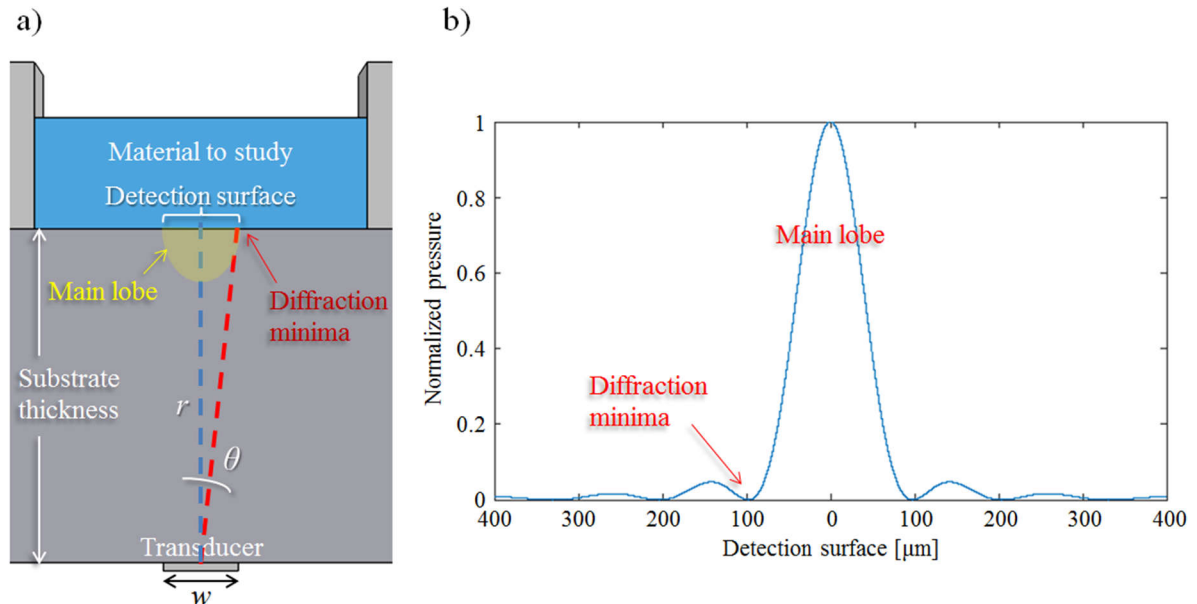


Figure 2.14: Acoustic pressure distribution at the detection surface, using a transducer of width $w = 60\ \mu\text{m}$, operating at 1 GHz, $600\ \mu\text{m}$ apart from the sample. a) Cross-section schematic of the sensor. b) Normalized pressure showing the size of pressure lobe at the detection surface.

References

- [1] M. Abdelmejeed, J. Kuo, A. Ravi and A. Lal, Cmos Controlled Ghz Ultrasonic Impedance Imager, 20th International Conference on Solid-State Sensors, Actuators and Microsystems & Eurosensors XXXIII (TRANSDUCERS & EUROSENSORS XXXIII), pp. 57 – 60, 2019, <https://doi.org/10.1109/TRANSDUCERS.2019.8808493>
- [2] Lawrence E. Kinsler, Austin R. Frey, Alan B. Coppens, James V. Sanders, Fundamentals of Acoustics, 4th edition, John Wiley & Sons Inc, 2000.
- [3] Yao Lu, Menglun Zhang, Hongxiang Zhang, Yuan Jiang, Hao Zhang, Wei Pang, Microfluidic bulk modulus measurement by a nanowavelength longitudinalacoustic-wave microsensor in the nonreflective regime, Physical Review Applied, vol. 11, 2019, <https://doi.org/10.1103/PhysRevApplied.11.044091>
- [4] C. Verdier, P.Y. Longin, M. Piau, Dynamic shear and compressional behavior of polydimethylsiloxanes: Ultrasonic and low frequency characterization, Rheologica Acta, vol. 37, pp. 234–244, 1998, <https://doi.org/10.1007/s003970050111>
- [5] Marc Meyers and Krishan Chawla. Mechanical Behavior of Materials, 2nd Edition, Cambridge University Press, 2009.
- [6] C. Verdier, M. Piau, Acoustic wave propagation in two-phase viscoelastic fluids: the case of polymer emulsions, J. Acoustical Society of America, vol. 101 (4), pp. 1868 – 1876, 1997, <https://doi.org/10.1121/1.418238>
- [7] D.J. Dos Santos, D.J. Carastan, L.B. Tavares, G.F. Batalha, Polymeric Materials Characterization and Modeling, Comprehensive Materials Processing, vol. 2, pp. 37 – 63, 2014, <https://doi.org/10.1016/B978-0-08-096532-1.00205-3>
- [8] Y. Lu, H. Zhang, Y. Jiang, H. Zhang, W. Pang and M. Zhang, Bulk modulus measurement of microfluidics by longitudinal bulk acoustic wave sensors, 2018 IEEE Micro Electro Mechanical Systems (MEMS), pp. 854 – 857, 2018, <https://doi.org/10.1109/MEMSYS.2018.8346690>
- [9] Jesus Yanez, Arantxa Uranga, Nuria Barniol. Fluid compressional properties sensing at microscale using a longitudinal bulk acoustic wave transducer operated in a pulse-echo scheme. Sensors and Actuators A: Physical, vol. 334, 2022, <https://doi.org/10.1016/j.sna.2021.113334>
- [10] Ken-Ya Hashimoto, RF Bulk Acoustic Wave Filters for Communications, Artech House Publishers, 2009.
- [11] IEEE Standard on Piezoelectricity, ANSI/IEEE Std 176-1987, 1988, <https://doi.org/10.1109/IEEESTD.1988.79638>
- [12] Warren P. Mason, Physical acoustics: Principles and methods, Academic Press, 1964.
- [13] Emmanuel Defaÿ, Integration of Ferroelectric and Piezoelectric Thin Films: Concepts and Applications for Microsystems, John Wiley & Sons, 2013.

- [14] COMSOL Multiphysics (version 5.3a; COMSOL Inc: 2017).
- [15] Harmeet Bhugra and Gianluca Piazza, Piezoelectric MEMS Resonators, Springer, 2017.
- [16] Joel Rosenbaum, Bulk Acoustic Wave Theory and Devices, Artech House, 1988
- [17] Warren P. Mason and R. N. Thurston, Physical acoustics: Principles and methods, Academic Press, 1972.
- [18] Marco G. Beghi, Modeling and Measurement Methods for Acoustic Waves and for Acoustic Microdevices, IntechOpen, 2013.
- [19] S. Ballandras, T. Baron, E. Lebrasseur, G. Martin, D. Gachon, A. Reinhardt, P.-P. Lassagne, J.-M. Friedt, L. Chommeloux and D. Rabus, High overtone Bulk Acoustic Resonators: application to resonators, filters and sensors, Acoustics, 2012, <https://hal.archives-ouvertes.fr/hal-00811239>
- [20] J. Yanez, E. Ledesma, A. Uranga and N. Barniol, Improved Electromechanical Transduction for PiezoMUMPS HBAR Impedance Sensors, 2020 Joint Conference of the IEEE International Frequency Control Symposium and International Symposium on Applications of Ferroelectrics (IFCS-ISAF), pp. 1 – 5, 2020, <https://doi.org/10.1109/IFCS-ISAF41089.2020.9234913>
- [21] Y. Zhang, Z. Wang and J.D.N. Cheeke, Simulation of electromechanical coupling coefficient by modified modal frequency spectrum method including the electrode effect, Ultrasonics, vol. 28, pp. 114 – 117, 2000, [https://doi.org/10.1016/S0041-624X\(99\)00172-9](https://doi.org/10.1016/S0041-624X(99)00172-9)
- [22] S. Pao, M. Chao, Z. Wang, C. Chiu, K. Lan, Z. Huang, L. Shih, and C. Wang, Analysis and experiment of HBAR frequency spectra and applications to characterize the piezoelectric thin film and to HBAR design, 2002 IEEE International Frequency Control Symposium and PDA Exhibition, pp. 27 – 35, 2002, <https://doi.org/10.1109/FREQ.2002.1075851>
- [23] David Halliday, Robert Resnick and Jearl Walker, Fundamentals of Physics, Wiley, 2018.
- [24] John C. Morrison, Modern Physics for Scientist and Engineers, Academic Press, 2009.
- [25] G. Fan, J. Li and C. Wang, Design and analysis of MEMS linear phased array, Micromachines, vol. 7, 2016, <https://doi.org/10.3390/mi7010008>

Design, Simulation, and Fabrication

3.1 Selection of the piezoelectric material and the manufacturing process

3.1.1 Piezoelectric materials

Quartz is the most widely used piezoelectric material for the creation of sensors and actuators due to its almost linear response even under extreme stress or extreme electric field conditions and its stability against temperature shifts [1]; an example of this is the wide adoption of the QCM for gravimetric measurements in academia and industry. However, smaller sensors with improved sensitivity would require thinning the quartz layer to such an extent that it would be mechanically unstable and brittle [2]. In this regard, the development of the MEMS industry and the improvement of the piezoelectric film deposition technologies have supported adoption of a great variety of piezoelectric materials such as zinc oxide (ZnO), aluminum nitride (AlN), lead zirconium titanate (PZT), and lithium niobate (LiNbO₃) for the creation of sensors due to their capability of deposition as thin films and possible integration with integrated circuits for creation of low-cost mass-production miniature sensors [3, 4].

Among those piezoelectric materials compatible with thin film deposition technologies, the lead zirconium titanate (PZT) and the lithium niobate hold a significantly higher piezoelectric coupling coefficient ($k_t^2 > 20\%$) which is attractive for transducers and actuators requiring large displacements. Unfortunately, due to its high acoustic loss at high frequencies and low sound wave velocities, PZT is mostly used for low frequency devices that not require high Q [5]. Compared with PZT, the zinc oxide (ZnO) offer larger longitudinal acoustic velocity (although significantly lower coupling, $k_t^2 \sim 9\%$). This semiconductor material is, alongside the AlN, one of the most popular thin film materials in SAW-based microfluidics and FBAR devices due to the ease of implementation in manufacture processes. Its controlled texture and film stoichiometry during fabrication allow films of tens of microns thick to be deposited, being a good choice for thick film SAWs or ultrasonic devices operating in the lower frequency range [1]. Unfortunately, acoustic losses, temperature coefficient and dielectric losses are higher than the case of AlN, limiting the operation to lower frequencies. A major drawback towards monolithic integration with electronics is that this material is considered as incompatible and contaminant in CMOS processes [2].

Although deposition and texture control of AlN are more difficult than that of ZnO, this material offer advantages for high frequency devices, such as the largest longitudinal velocity for acoustic waves, and lower dielectric losses. While electromechanical coupling is comparable to that of the ZnO ($k_t^2 \sim 7\%$, for AlN), this material is fully compatible with CMOS and MEMS processes, and therefore, it is the material selected for this work with a view to a future monolithic integration with CMOS processes. Table 3.1 show a comparison of these piezoelectric materials compatible with thin film deposition technologies.

	PZT	ZnO	AlN
ρ [kg/m ³]	7570	5610 - 5720	3250 - 3300
v_{mat} [m/s]	4500	6336	11000
k_t^2 [%]	~ 20	~ 9	~ 7
Intrinsic loss	High	Low	Very Low
CMOS compatible	No	No	Yes

Table 3.1: Comparison of main piezoelectric materials compatible with thin film deposition technologies. On the one side is the PZT with higher electromechanical coupling and lower longitudinal velocity. In the opposite side is AlN, with lower coupling but higher longitudinal velocity and lower dielectric losses. AlN is fully compatible with the CMOS process for monolithic integration.

3.1.2 Manufacturing process

PiezoMUMPs is a commercial multi-user process designed for general purpose micromachining of piezoelectric MEMS. This process provides a 0.5 μm AlN layer over a thicker Silicon-On-Insulator (SOI) wafer for creation of devices such as energy harvesters, sensors, ultrasonic transducers, microphones, and actuators. Figure 3.1 presents a cross sectional representation of layers and materials in this process, while Table 3.2 lists material properties, thicknesses (t_{mat}) and acoustic impedances of these materials. Quantities correspond to default values from COMSOL library [6].

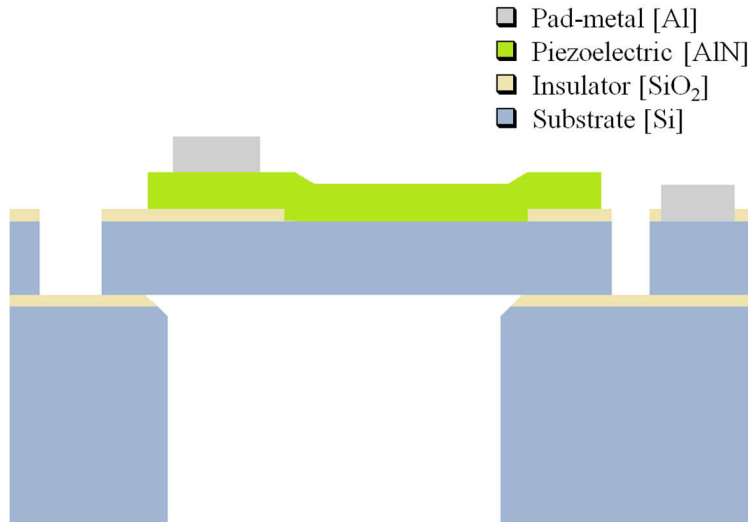


Figure 3.1: Cross sectional representation showing the available materials in the PiezoMUMPs process (not to scale). It is a commercial multi-user process, designed for general purpose micromachining of piezoelectric MEMS in a Silicon-on-Insulator framework (SOI). This is a simple 5-mask level which provides a 0.5 μm layer of AlN for the creation of piezoelectric devices such as energy harvesters, sensors, ultrasonic transducers, microphones, and actuators.

Material	t_{mat} [μm]	ρ [kg/m^3]	v_{mat} [m/s]	$Z \approx \rho v_{\text{mat}}$ [Rayl]
Air		1.14	350	398
Al	1	2700	6450	17.41E+6
AlN	0.5	3300	10954	36.15E+6
Doped Si	10 ± 1	2329	8457	19.69E+6
SiO ₂	1	2200	5848	12.87E+6
Si <100>	400 ± 5	2329	8457	19.69E+6

Table 3.2: Properties of materials constituting the stack available in PiezoMUMPs process. Quantities correspond to default values from COMSOL library and their respective acoustic impedance is obtained by the approximation $Z \approx \rho v_{\text{mat}}$, with v_{mat} as the longitudinal sound velocity of each material.

This process could be used for both the creation of the resonant devices described in the previous chapter, and for the pulse-echo transducers.

In the case of resonators, the AlN layer can be sandwiched between the metallic Al electrode and the superficially doped silicon substrate (electrically conductive), allowing excitation of the thickness extensional mode of the piezoelectric. For this device, both the buried oxide and the 400 μm of silicon substrate are removed to create a trench/microchannel to transport liquid samples. Figure 3.2 show the implementation of the resonant devices using this manufacturing technology:

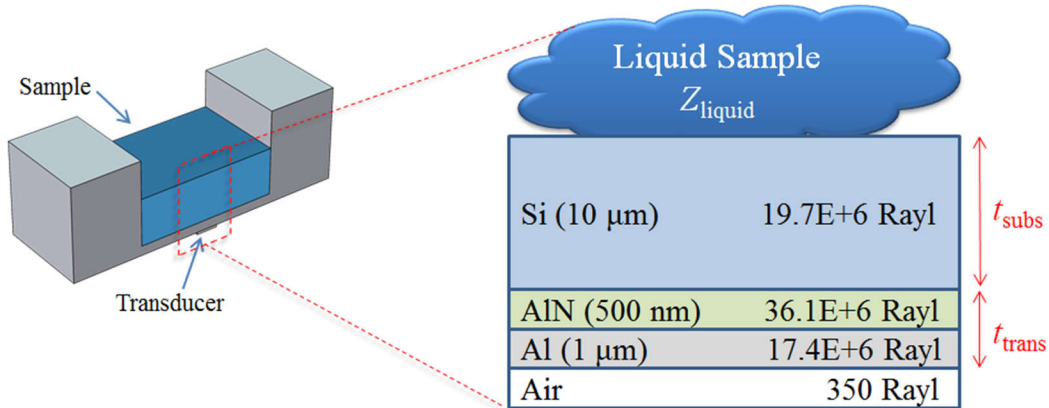


Figure 3.2: 3D representation of the resonant sensor, the lower face of the wafer carries the resonator while the opposite side can be used as a totally electronics-free detecting surface. The zoomed section is a 2D representation of the stack of materials that make up the resonator; the piezoelectric layer is AlN, sandwiched between conductive materials for excitation of thickness extensional modes generating stationary bulk waves in the substrate. The 2D representation is not to scale and is flipped upside down respect to Figure 3.1.

Based on specifications in Table 3.2 and according to equation 1 of Chapter 2, more than 99.9 % of the acoustic energy will remain trapped within the thickness of this 3-layer solid structure as long as the piezoelectric layer is driven by a continuous RF source. The electrical response of such device will present sharp resonance peaks (as in Figure 2.11 of Chapter 2) as long as there is ‘air’ on the sensing surface. According with equation 16 of Chapter 2, amplitude and frequency of these resonant peaks will change in presence of liquid samples, allowing identification and classification of different liquids according with their specific acoustic impedance.

Contrarily, to create a pulse-echo device both the buried oxide and the thicker 400 μm substrate should be preserved:

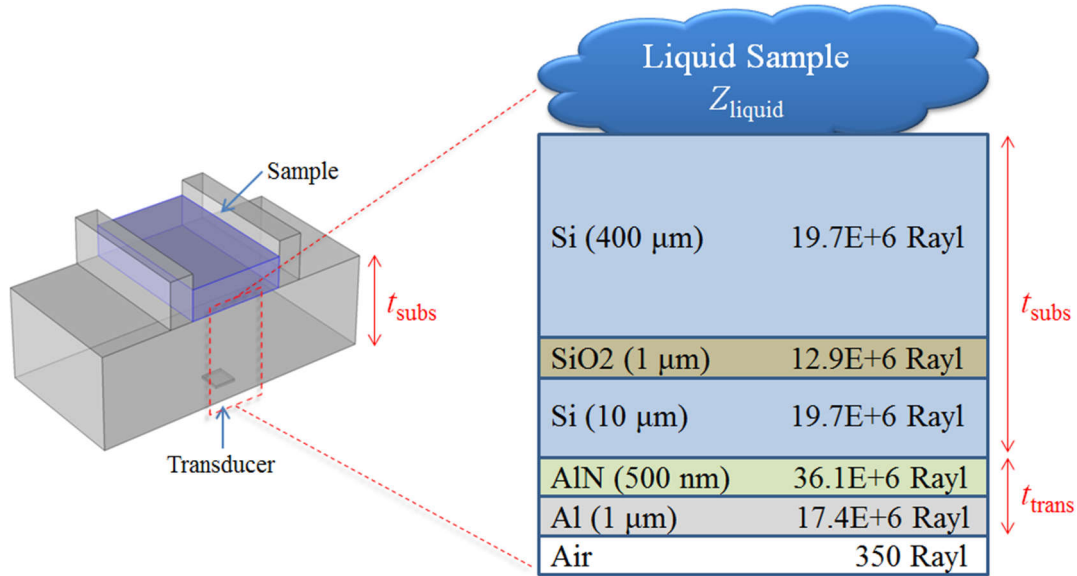


Figure 3.3: A 3D transparent slice representing the concept of the pulse-echo sensor: The lower face of the wafer carries the transducer that emits and receives pulses of bulk waves through the thickness of the wafer while the upper face remains free of electronics and cables and is used as a detection surface carrying liquid samples. The zoomed section is a 2D representation of the stack of materials that make up the transducer; the piezoelectric material is AlN, sandwiched between conductive materials for excitation of thickness extensional modes.

Here, the crystalline silicon substrate could be used as propagating medium, transporting pulses of bulk waves generated by the transducer. According with equation 1 of Chapter 2 and assuming negligible losses due to diffraction and attenuation, more than 99.9 % of the energy traveling across the substrate should be reflected if ‘air’ is present in the detection surface and, as an example, around to 86 % of reflection is expected in the case of ‘water’ in the detection surface (using 995.6 kg/m³ as water density and 1511 m/s as its sound velocity). Since the amount of energy transferred to the liquid sample depends on the specific acoustic impedance of each sample, echoes reflected back towards the transducer will produce different voltage levels depending on the acoustic properties of each liquid sample. Table 3.3 shows expected reflection coefficients for other liquid samples.

Material	Density ρ [kg/m ³]	Acoustic velocity v [m/s]	Viscosity μ [cP]	Bulk modulus $K' = \rho v^2$ [GPa]	Acoustic impedance $Z \approx \rho v$ [Rayl]	Γ (Eq. 1)
Air	1.14 ⁽⁷⁾	349.1 ⁽⁸⁾	0.018 ⁽⁷⁾	1.3893E-04	398	1
Ethanol	780.1 ⁽⁹⁾	1105.7 ⁽¹⁰⁾	1.06 ⁽¹¹⁾	0.9537	0.8625E+06	0.9161
FC-70	1924 ⁽¹²⁾	680 ⁽¹³⁾	3.36 ⁽¹²⁾	0.8896	1.3083E+06	0.8754
DI Water	995.6 ⁽¹⁴⁾	1511.4 ⁽¹⁵⁾	0.79 ⁽¹⁶⁾	2.2743	1.5047E+06	0.8580
Glycerol	1254 ⁽¹⁷⁾	1902 ⁽¹⁸⁾	552.1 ⁽¹⁷⁾	4.5364	2.3851E+06	0.7839

Table 3.3: Expected reflection coefficients Γ for other liquid samples. Values from literature [7–18].

3.2 Operating Frequency

3.2.1 Acoustic resonators based on the PiezoMUMPs process

Piezoelectric resonance

Before analytically obtaining the fundamental mode of the HBAR structure in Figure 3.2, it is convenient to identify the acoustic resonance corresponding to the piezoelectric film. Figure 3.4a is a 2D representation of a thin piezoelectric layer, with thickness corresponding to the manufacturing process, isolated from the other layers. Once this layer is driven by a continuous RF source, its thickness expands and contracts (mechanical strain) in the z direction. The longitudinal acoustic waves produced remain trapped in the solid domain due to the huge acoustic impedance mismatch between the AlN and the surrounding air, as represented in Figure 3.4b.

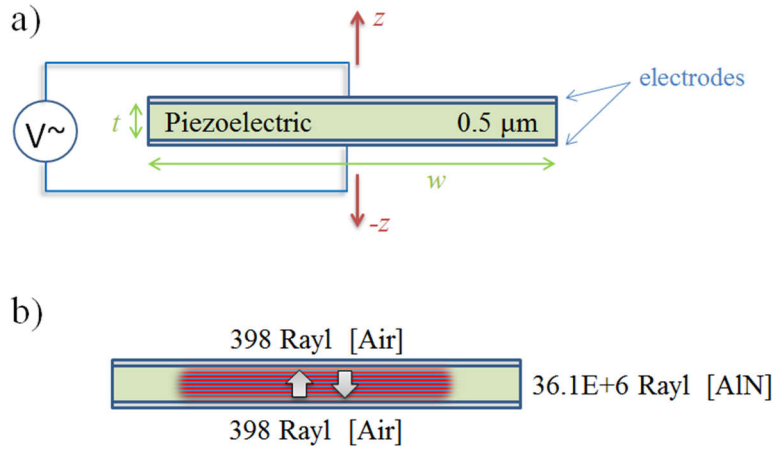


Figure 3.4: 2D representation of a thin piezoelectric layer with thickness t corresponding to the manufacturing process; isolated from the other layers. a) When this layer is coupled to a continuous RF source, its thickness expands and contracts in the z/z direction. b) The acoustic energy generated remains trapped in the solid domain due to the huge acoustic impedance mismatch between the AlN and the surrounding air

The resonating frequency of this layer operating on its thickness expansion mode is given by equation 13 of Chapter 2, using the longitudinal sound velocity indicated in Table 3.2 the fundamental mode is:

$$f_0 = \frac{10954 \text{ [m/s]}}{2 (0.5 \text{ [}\mu\text{m]})}$$

$$f_0 = 10.954 \text{ [GHz]}$$

As detailed in the previous chapter, parasitic lateral displacements could be neglected as long as their lateral dimensions (width) of this plate are much larger than its thickness, being this resonant frequency independent of the transducer width. Figure 3.5 shows analytical impedance curves corresponding to similar piezoelectric plates whose width w varies from $20 \mu\text{m}$ to $100 \mu\text{m}$, using equation 10 of Chapter 2 and considering $\epsilon_0 = 8.8542\text{E-}12 \text{ [F/m]}$ as the vacuum permittivity, $\epsilon = 9$ as the AlN dielectric constant, $c_{33}^E = 3.89\text{E+}11 \text{ [N/m}^2\text{]}$ [6], $e_{33}^S = 1.55$ as the piezoelectric coefficient $[\text{C/m}^2]$ [6] and the AlN properties in Table 3.2.

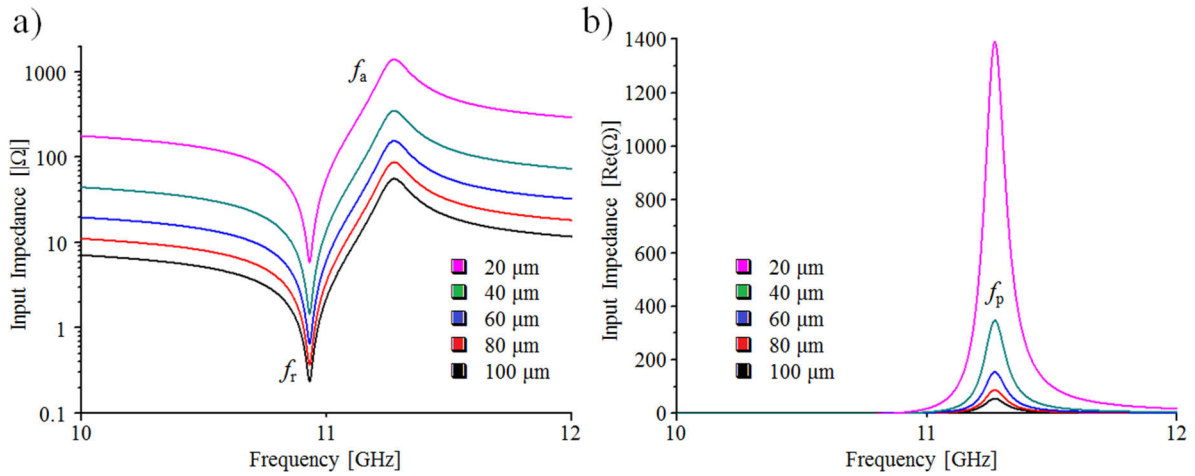


Figure 3.5: Analytical impedance curves corresponding to piezoelectric plates of same thickness ($t = 0.5 \mu\text{m}$), and different width w (from $20 \mu\text{m}$ to $100 \mu\text{m}$). The resonant frequency of devices operating on its thickness expansion mode does not depend on resonator width. a) Magnitude of the analytical input impedance. b) Real value of the analytical input impedance.

As seen in Figure 3.5a, both resonant and anti-resonant frequencies ($f_r = 10.932 \text{ GHz}$, and $f_a = 11.276 \text{ GHz}$) are independent of the transducer's width; this lateral dimension is only related with its behavior as static capacitor. Figure 3.5b shows the region where the real part of the impedance goes to a maximum (the parallel resonance [19]), at $f_p = 11.272 \text{ GHz}$.

Simple HBAR under the PiezoMUMPs manufacturing process

The PiezoMUMPs process offers a silicon substrate of thickness $t_{\text{subs}} = 10 \mu\text{m}$ to support the piezoelectric layer, creating the bimorph plate of Figure 3.6a. Once the thickness expansion mode is activated by the continuous source, the acoustic energy produced by the AlN layer leaks into the silicon substrate since both materials have acoustic impedance within the same order of magnitude (equation 1 of Chapter 2). Similar to the case of the isolated piezoelectric layer, the acoustic energy remains trapped within the solid domain because of the comparatively low acoustic impedance of the air surrounding the structure (Figure 3.6b).

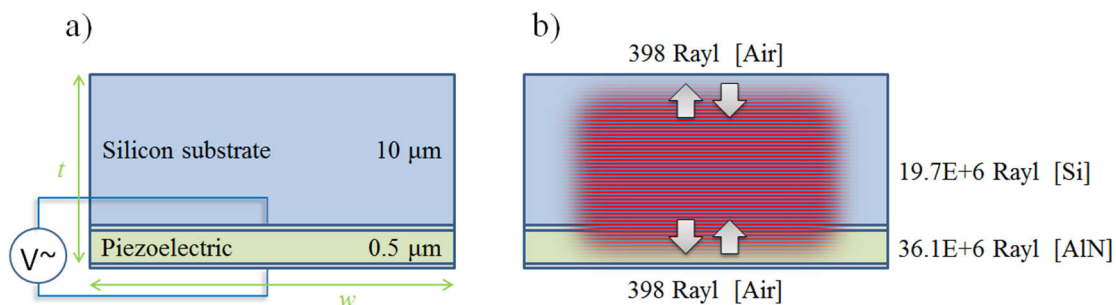


Figure 3.6: Simple HBAR composed by a thin AlN layer deposited over a silicon substrate. a) The thickness expansion mode of the AlN layer is activated by a continuous RF source. b) Strain at the piezoelectric generates acoustic energy that remains trapped into the solid structure because of the low acoustic impedance of air surrounding the device.

Since the silicon substrate is much thicker than the piezoelectric layer, the fundamental mode of the whole structure is approximated by equation 14 of Chapter 2:

$$\Delta f_0 \approx \frac{8457 \text{ [m/s]}}{2 (10.5 \text{ [\mu m]})}$$

$$\approx 402.7 \text{ [MHz]}$$

Figure 3.7 exemplifies the analytical input impedance of a structure similar to that on Figure 3.6, using equation 15 of Chapter 2 and arbitrarily considering a width $w = 100 \mu\text{m}$.

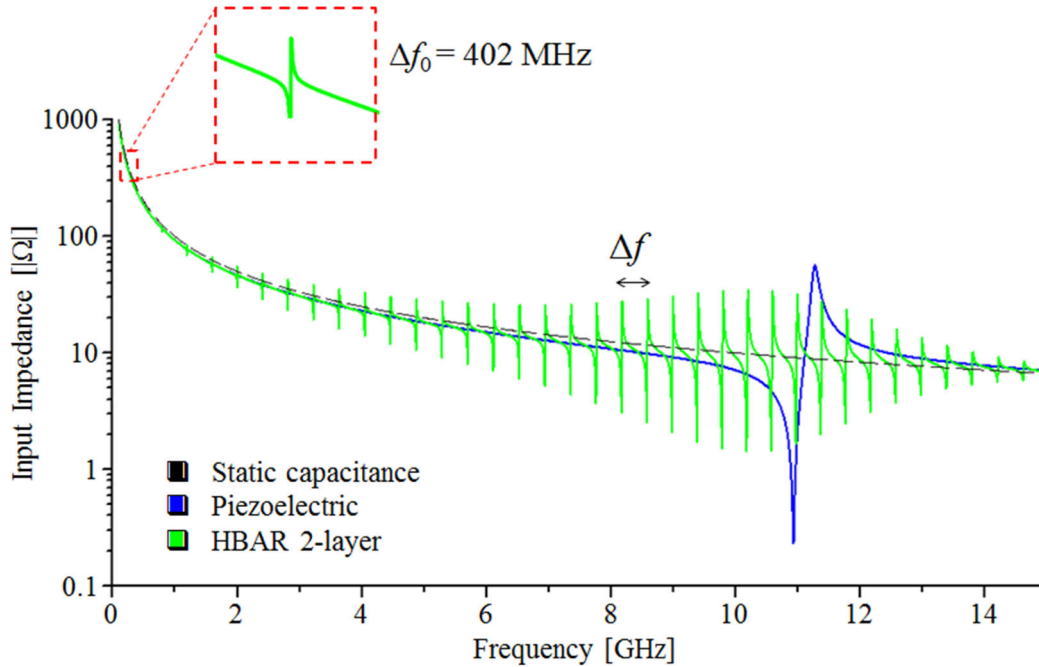


Figure 3.7: Analytical input impedance plot. The green trace show the ~ 400 MHz modes in a comb-profile for a simple bimorph HBAR ($0.5 \mu\text{m}$ of AlN + $10 \mu\text{m}$ Si) with electrodes of negligible thickness, modulated by the resonance frequency of the piezoelectric AlN film at 10.9 GHz (blue). The static capacitance curve corresponds to a squared resonator of width $w = 100 \mu\text{m}$.

Since stationary bulk waves are established between top and bottom free surfaces, all the possible harmonics of the fundamental mode of the structure can exist, therefore, the electrical response leads to a frequency comb formed by the fundamental mode of the structure and its multiple harmonics, modulated by the resonance of the piezoelectric. The fundamental mode at 402 MHz agrees with the approximation of equation 14 of Chapter 2 ($\Delta f_0 \sim 402.7 \text{ MHz}$), which is followed by its multiple harmonics separated by Δf . As expected, harmonics of this fundamental mode are much favorably excited near the resonance of the piezoelectric than anywhere else in the spectrum.

Non-negligible effect of the metallic layer

A representation of the resonating device using the actual configuration offered by PiezoMUMPs is shown in Figure 3.8a. To activate the thickness extension mode the $0.5 \mu\text{m}$ AlN film is surrounded by an Al electrode with thickness $t_{drvEl} = 1 \mu\text{m}$ and the $10 \mu\text{m}$ thick silicon substrate, whose surface is conductive and is used as electrical reference (GND electrode). In this case, the Al electrode is twice as thick as the piezoelectric and both materials have similar acoustic impedance, therefore, the mechanical energy produced by the piezoelectric is immediately transferred to this

thicker layer and then is reflected back towards the piezoelectric because of the huge acoustic impedance difference with ‘air’ in the lower boundary. In the opposite side, total reflection of the longitudinal wave is induced by the mismatch between acoustic impedances of the silicon and air, therefore, the acoustic energy remains trapped within the solid domain (Figure 3.8b).

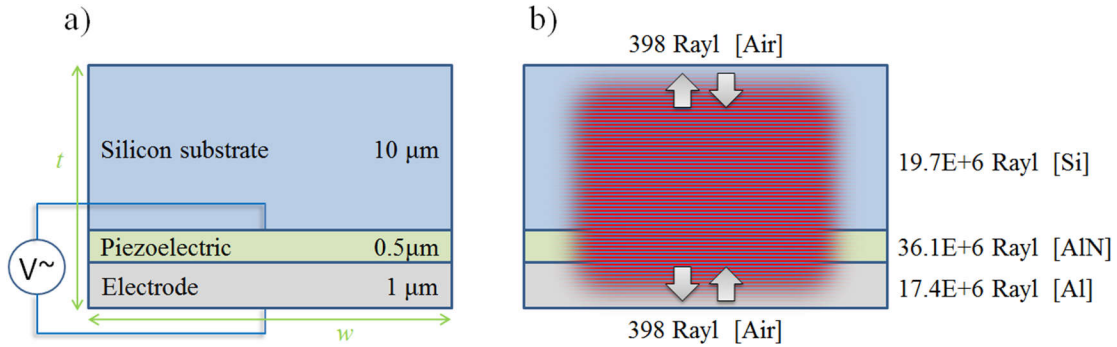


Figure 3.8: HBAR implementation in the PiezoMUMPs process. a) Layers and thicknesses constituting the device. b) Acoustic energy trapped into the solid domains because of the surrounding air.

Using equation 14 of Chapter 2, the thickness of the whole structure, and its average longitudinal sound velocity, the fundamental mode is:

$$\Delta f_0 \approx \frac{8314 \text{ [m/s]}}{2 (11.5 \text{ [}\mu\text{m]})} \approx 362 \text{ [MHz]}$$

Figure 3.9 uses equation 16 of Chapter 2 to show the effect of the non-negligible electrode.

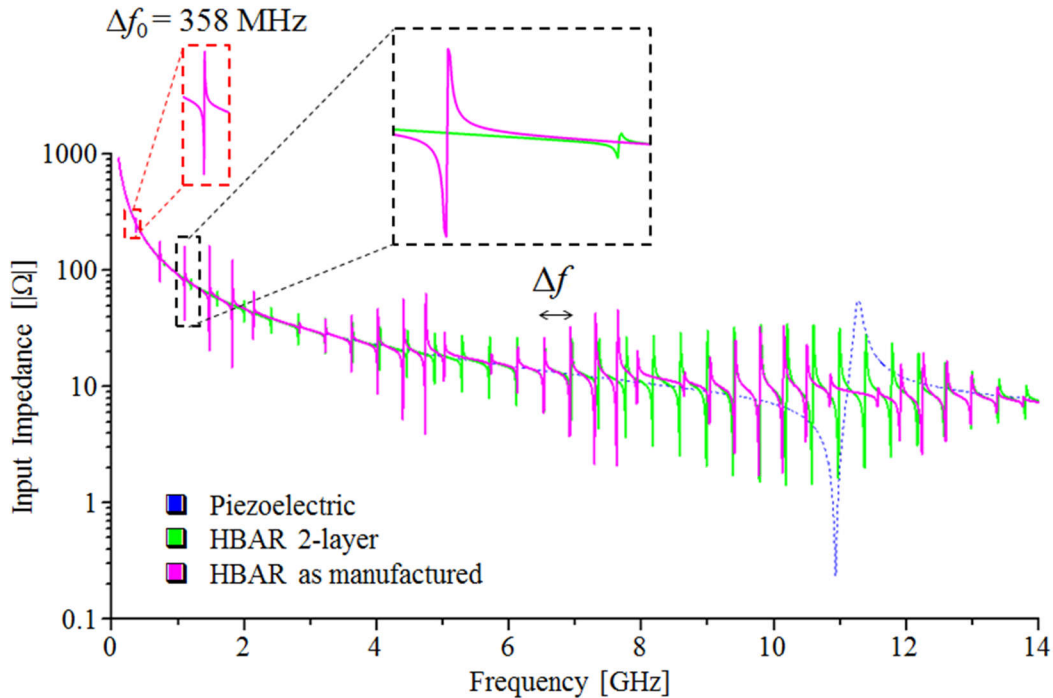


Figure 3.9: Analytical impedance plot for a device using PiezoMUMPs process (magenta). The zoomed section shows presence of higher amplitude modes (compared to the case of the bimorph HBAR, green) even at frequencies far from the piezoelectric resonance at 10.9 GHz.

The Green trace in Figure 3.9 is the magnitude of the input impedance of the simple HBAR shown in Figure 3.6; a thin piezoelectric film provided with electrodes of negligible thickness deposited on a silicon substrate. As expected for this 2-layer HBAR, the amplitude of the lower order modes is very small compared to the amplitude of the modes at frequencies close to the piezoelectric resonance f_0 . On the other hand, for the resonator with dimensions corresponding to the manufactured device (magenta trace), the acoustic energy is immediately transferred to the non-negligible Al electrode due to its similar acoustic impedance and twice the thickness of the AlN, and then is reflected back to the piezoelectric element because of the huge acoustic impedance difference with the air in the lower boundary. This causes an effect similar to increasing the thickness of the piezoelectric, as decreasing the frequency f_0 because of the extra thickness, but in this case keeping the high bandwidth and relatively low input impedance inherent of a thin piezoelectric film. Because of the effect of the extra Al thickness in the stack, modes with improved amplitude at lower frequencies were obtained, while maintaining the operative range of the device up to f_0 . The zoomed section in red shows the fundamental mode of the structure $\Delta f_0 = 358 \text{ MHz}$, agreeing well with approximation from equation 14 of Chapter 2. The zoomed section in black compares the amplitude of harmonics of both devices, showing an improvement in amplitude.

To detect the presence of liquids we can monitor decrease of amplitude or frequency shift of any of these harmonics of high amplitude; in this work the third harmonic ($\sim 1.1 \text{ GHz}$) is selected since it has adequate amplitude and its input impedance is below 100Ω , which will facilitate its integration with commercial RF circuitry

3.2.2 Pulse-echo transducers based on the PiezoMUMPs process

Although this device is designed to work in a pulse-echo scheme, that is, driven by a short train of RF pulses whose duration should be shorter than the time required to create standing waves in the structure, it is important to know the response of the structure operating as a resonator to discover frequency regions where would it be more favorable to operate (regions with greater electromechanical coupling). Figure 3.10a shows the stack of materials for the pulse-echo devices:

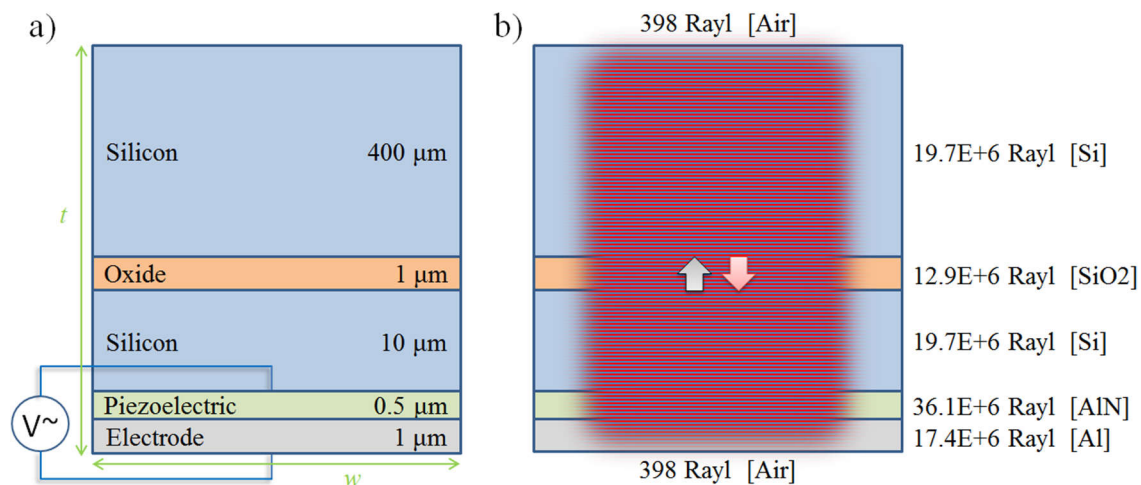


Figure 3.10: a) Stack of materials required for the pulse-echo devices. b) Representation of the acoustic pressure trapped in the solid structure when a continuous RF source activates the thickness expansion mode of the piezoelectric. Partial reflection of acoustic energy is expected by the buried oxide (red arrow).

Since the silicon substrate is much thicker than the other layers, the fundamental mode of this structure is approximated by $\Delta f_0 = v_{subs}/[2 * t_{subs}] = 10.6 \text{ MHz}$. This should lead to the dense spectrum represented in red in Figure 3.11, using equation 15 of Chapter 2 (approximation considering a simple 2-layer HBAR consisting of a $0.5 \mu\text{m}$ -thick AlN piezoelectric layer over a $400 \mu\text{m}$ -thick silicon substrate)

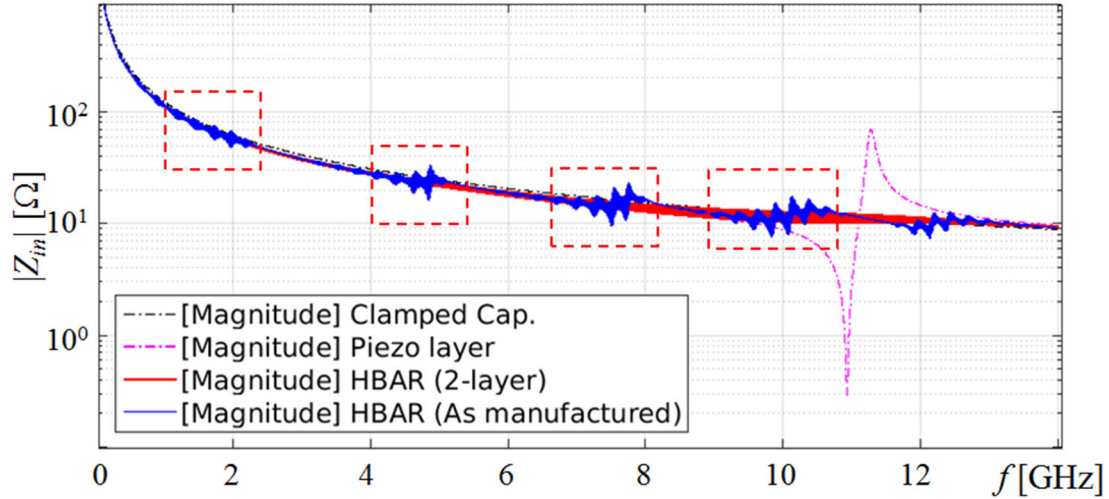


Figure 3.11: Analytical input impedance plot corresponding to the structure in Figure 3.10b (blue trace). Frequency regions confined by red squares show the effect of the thick Al electrode and the buried oxide, causing additional modulations to the characteristic frequency comb of HBAR devices.

However, for the case of the manufactured device the Al electrode is twice as thick as the piezoelectric and both materials have similar acoustic impedance. In this case, the mechanical energy produced by the piezoelectric is immediately transferred to this thicker Al electrode and then is reflected back to the piezoelectric because of the huge acoustic impedance difference with ‘air’ in the lower boundary; additionally, partial reflection of the bulk acoustic wave is produced by the buried oxide layer due to the difference in acoustic impedance respect to silicon (red arrow in Figure 3.10b). The dense blue comb in Figure 3.11 uses equation 16 of Chapter 2 to estimate the electrical input impedance (Z_{in}), including the effect of non-negligible electrodes. As seen, the extra materials and their thicknesses generate additional modulations to the input electrical impedance curve, leading to the appearance of modes of higher amplitude for certain regions of frequency such as those delimited by the red boxes.

These frequency spots with higher amplitude modes also offer a significant increase in electromechanical coupling [20], improving transduction of the pulse-echo devices and providing them with multi-frequency capability. For the sake of simplicity, this work uses the peak of transduction located $\sim 1.1 \text{ GHz}$ for the experimental part.

3.3 Microtransducer Design

The previous section showed the multi-frequency capability of both approaches: the devices operating as resonators and those operating as pulse-echo transducers. For both cases, the configuration of the layers that make up the devices favor operating frequencies from 1.1 GHz , therefore this frequency is set as the minimum operating frequency for this section.

3.3.1 Effective area (lateral dimensions) and expected Time-of-Flight for the Pulse-echo devices

Both the acoustic resonators and the pulse-echo transducers are designed to produce bulk acoustic waves within the thickness of their substrates to interact with liquid samples located over the opposite face of the wafer. In these two different approaches a single piezoelectric element is used to interact with a sample directly in front of it, then is convenient to avoid losses of acoustic energy due to diffraction in off-target zones within the substrate. Chapter 2 showed that emitters with dimensions comparable to the wavelength will produce waves that fade out in the propagation medium. If $v_{subs} = 8457 \text{ m/s}$ is the longitudinal velocity of waves in silicon and $f_{op} = 1.1 \text{ GHz}$ the lowest operating frequency, then using equation 19 of Chapter 2 the wavelength is:

$$\lambda = v_{subs}/f_{op} = 7.69 \mu\text{m}$$

The later indicates that it is not possible to use an arbitrary transducer width, such as the minimum feature size available in PiezoMUMPs to pattern Al electrodes ($3 \mu\text{m}$ [21]), since it will cause severe diffraction losses at the operating frequency of 1.1 GHz. Figure 3.12 is a 2D representation of the pulse-echo approach implemented with layers corresponding to the selected manufacturing process, where the detection surface is located $411 \mu\text{m}$ far from the AlN transducer.

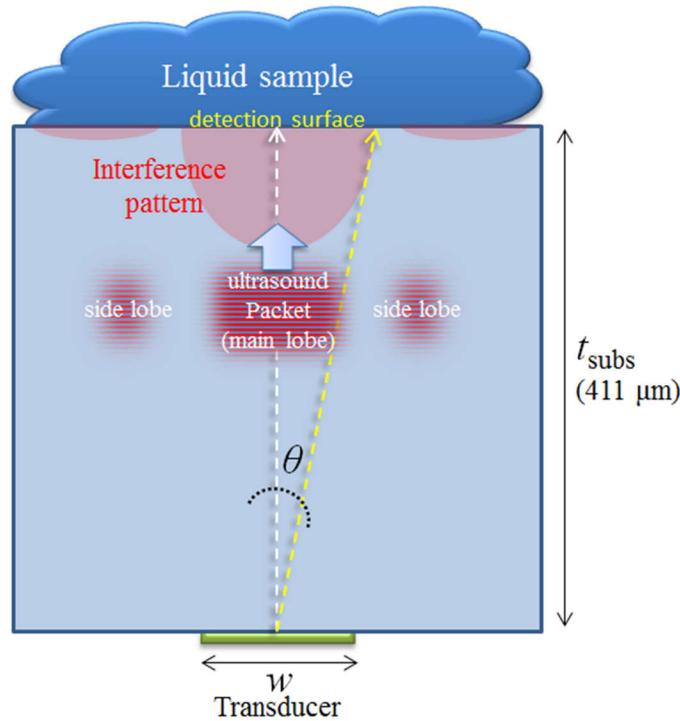


Figure 3.12: 2D representation of a sensor working under the pulse-echo scheme. The AlN transducer produces a short pulse of bulk waves traveling across the thickness of the substrate towards the sample. The angle θ indicates the position at the detection surface where the pulse interferes with itself destructively causing a diffraction minimum.

If $t_{subs} \gg w$, the approximation $\sin \theta \approx \lambda/w$ (equation 18 of Chapter 2) is useful to estimate the width of the main lobe of ultrasound interacting with the sample at the detection surface. If $f_{op} =$

1.1 GHz is set as the operating frequency, and $v_{subs} = 8457 \text{ m/s}$ is the velocity of longitudinal waves in silicon, then θ (the angle formed between the central axis of Figure 3.12 and the point in the detection interface where the minima of the main lobe will appear) only depends on the width w of the transducer.

$$\theta \approx \sin^{-1} \frac{7.688 \mu\text{m}}{w}$$

In this single-element approach the ultrasound pulse should travel across the thickness of the wafer with negligible diffraction to interact with the section of the sample that is directly in front of the transducer, i.e. the width of the main lobe at the detection surface should match with the width of the transducer. Figure 3.13 uses equation 18 of Chapter 2 to relate the width of the main lobe of ultrasound at the detection surface with the width of the piezoelectric transmitter. The case where the width of the main lobe and that of its transmitting element coincide is highlighted.

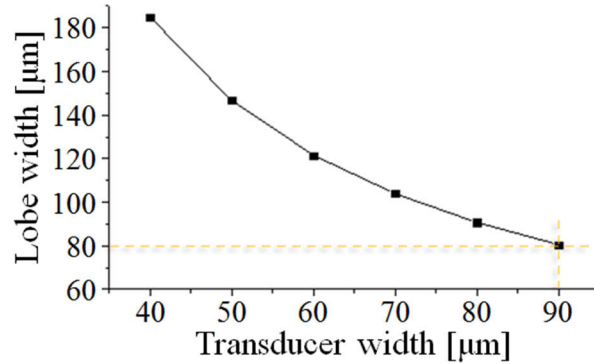


Figure 3.13: Lobe-width defined by the main-lobe pressure as a function of transducer width w . A value of w between 80 and 90 μm corresponds to the narrowest transducer that can be used avoiding diffraction considering an operating frequency $f_0 = 1.1 \text{ GHz}$.

In Figure 3.13 it is found that a value of w (width) between 80 μm and 90 μm corresponds to the narrowest transducer that can be used avoiding diffraction, considering an operating frequency $f = 1.1 \text{ GHz}$ and a detection surface 411 μm far from the transducer. Figure 3.14 show the normalized pressure distribution at the detection surface caused by transducers of different widths operating at 1.1 GHz; this 2D pressure distribution in the far field was analytically obtained from equation 21 of Chapter 2, plotting only distribution along θ .

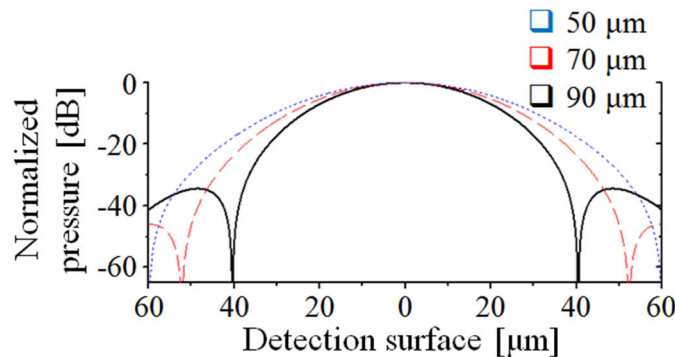


Figure 3.14: Normalized pressure showing the size of pressure lobes at the detection surface for transducers of different width. Computed at 1.1 GHz.

From equation 17 of Chapter 2, if $411 \mu\text{m}$ is the total thickness of the stack and $v_{subs} = 8457 \text{ m/s}$, the time required for pulses to reach the detection surface (where the sample is located) is $ToF = 48 \text{ ns}$ and $ToF_{x2} = 96 \text{ ns}$ for a round trip (elapsed time from pulse emission to the moment in which the reflected echo is registered again by the transducer). Figure 3.15 is a representation of the pulse-echo device as it will be implemented using the selected manufacturing process.

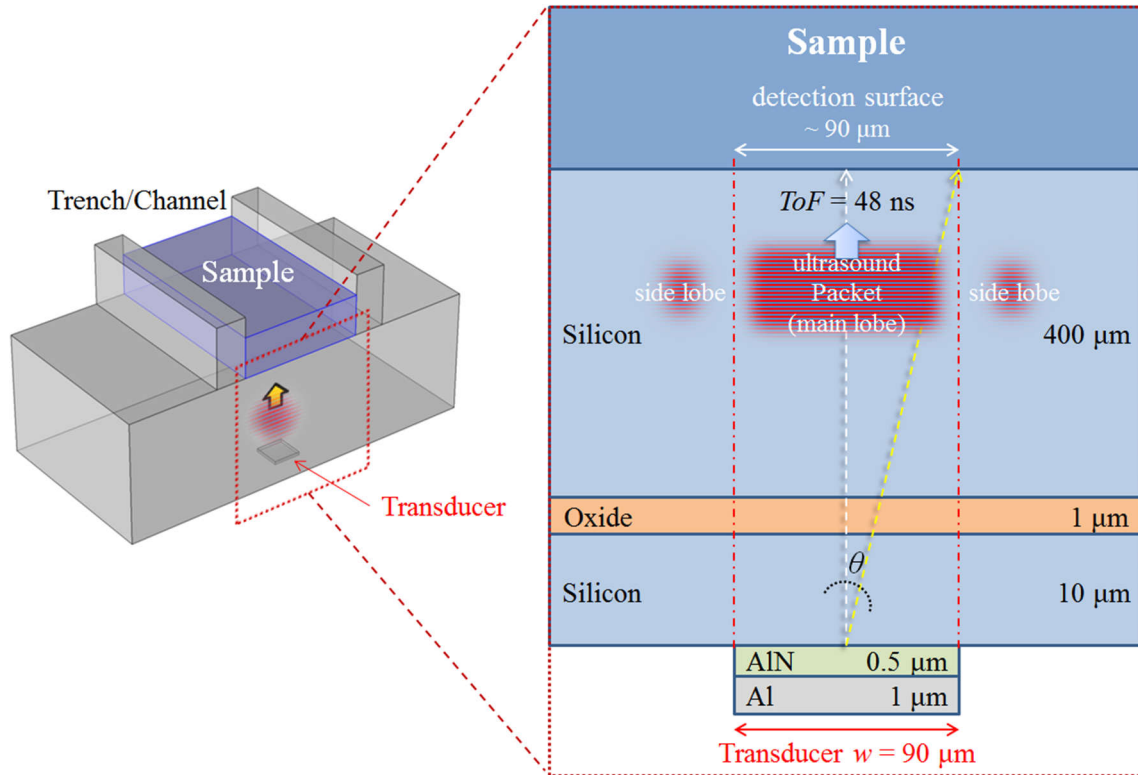


Figure 3.15: Representation of the pulse-echo device, including calculated lateral dimensions required to avoid pulse diffraction. To maximize the signal-to-noise ratio (SNR) most of the acoustic energy interacts only with the area of the detection surface that is directly in front of the transducer. The Time-of-Flight required for the pulse to reach the sample is 48 ns.

3.3.2 Effective area (lateral dimensions) of the Resonating devices

Similarly to the pulse-echo transducer, this acoustic resonator is meant to produce bulk acoustic waves within the thickness of the substrate to interact with the liquid sample located over the opposite face of the wafer. Since this approach uses a single piezoelectric element, then it is convenient to avoid losses of acoustic energy due to diffraction in off-target zones within the substrate. Figure 3.13 from the previous section showed that the minimum transducer width to avoid diffraction losses with the operating frequency $f_{op} = 1.1 \text{ GHz}$ is $w = 80 \mu\text{m}$, however in this case it is also important an input impedance close to 50-ohm to facilitate its integration with commercial RF circuitry and minimizing electrical reflections. The analytical plot in Figure 3.16 (equation 16 of Chapter 2) contains input impedance curves showing the third mode (1.1 GHz) of structures with thicknesses corresponding to Figure 3.8, but different width w , ranging from $w = 80 \mu\text{m}$ to $140 \mu\text{m}$.

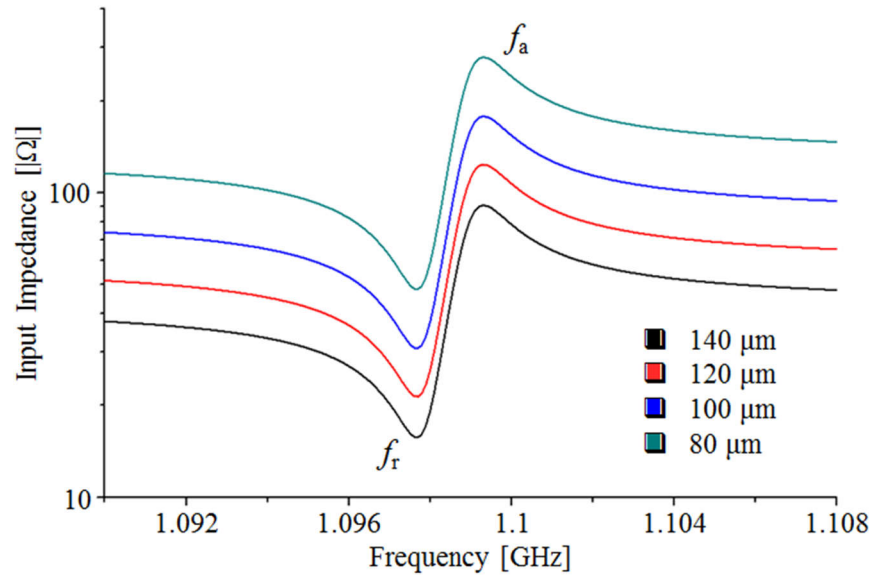


Figure 3.16: Input impedance curves showing the third mode (1.1 GHz) of structures of thicknesses corresponding to resonators implemented with the selected manufacturing process, but different width w , ranging from $w = 80 \mu\text{m}$ to $140 \mu\text{m}$. For this operating frequency the input impedance around the resonance point is 50-ohm in the case of the resonator with lateral dimension $w = 120 \mu\text{m}$, which facilitate its direct measurement using commercial equipment when performing the frequency sweep in the region of interest.

From Figure 3.16 it can be seen that the resonator with lateral dimension $w = 80 \mu\text{m}$ (green trace) has input impedance above 100-ohm out of the resonating points, which would cause electrical reflections towards the RF source when performing frequency sweep in the region of interest. On the other hand, for $w = 120 \mu\text{m}$ (red trace) the input impedance is 50-ohm, what is suitable to match the impedance of laboratory equipment. Figure 3.17 is a representation of the resonator device as it will be implemented using the selected manufacturing process.

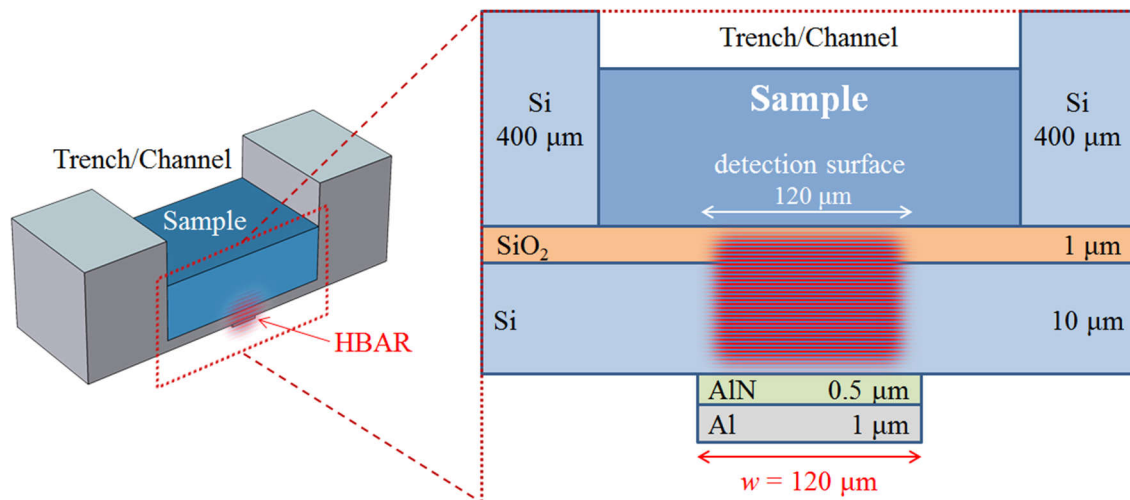


Figure 3.17: Representation of the resonating device as it will be implemented using the manufactured process. Materials and thicknesses are fixed parameters of the manufacturing process, while resonator width is selected to match the 50-ohm impedance of laboratory equipment.

The analytical plots in Figure 3.18a (blue background) were calculated using MATLAB and equation 16 of Chapter 2. These curves correspond to the third mode of the structure, for the case of 'air' at the detection surface (left) and the 'water' case (right), showing a dramatic decrease of amplitude when the channel is filled with the liquid sample. Analytical plots in Figure 3.18b (green background) correspond to the real value of the input impedance for both samples (air and water).

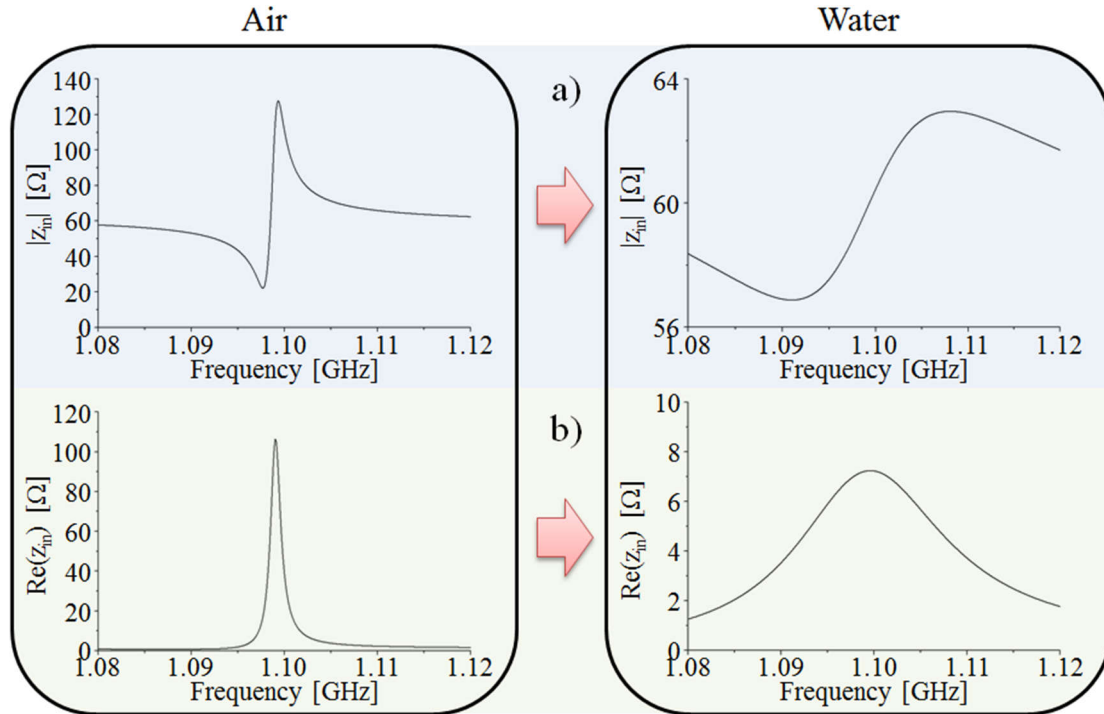


Figure 3.18: Analytical plots showing the measurement principle using the third mode of the resonating structure, obtained by equation 16 for a square resonator of width $w = 120 \mu\text{m}$ and materials and thicknesses corresponding to the selected manufacturing process. a) Comparison of the amplitude of the input impedance (magnitude) for the case of 'air' at the detection surface (left) and the 'water' case (right). b) Comparison of the amplitude of the input impedance (real value) for both materials.

3.4 Finite Element Simulations

The Finite Element Method (FEM) is a popular method to numerically solve problems governed by partial differential equations (PDE), such as structural mechanics problems, heat transfer, fluid flow, electromagnetics, etc. [22]. Once a system (or part of it) is described as “domain geometry”, this domain is discretized in much smaller sub-domains called Finite Elements. The set of these elements are called mesh, the vertex of such elements are nodes. Nodes are where the solution is computed for the different variables. Fully numerical solution of electro-acoustic equations by FEM allows abandoning many of the simplifying assumptions used in the 1D and 2D analytical models, such as the negligible lateral displacements and assumption of infinitely extending domains to avoid edge discontinuities. Also, the study of anisotropy and viscous losses of the materials can be added to FEM models.

This work uses the popular FEM solver ‘COMSOL Multiphysics’ to verify the analytical predictions described in the previous sections of this chapter, for both the resonating devices and the

pulse-echo transducers. COMSOL is a general-purpose simulation software capable of modeling any physical problem described by PDE, such as heat transfer problems, fluid motion, electromagnetism or structural mechanics, also offering integration of problems from different fields (Multiphysics capabilities) and a complete modeling workflow that includes CAD tools for 1D/2D/3D drawing the system, multiple study types (frequency domain, stationary, time domain, etc.), libraries with material properties, multiple solvers, post-processing, etc. [23].

3.4.1 FEM for Acoustic Resonators (input impedance and measuring principle)

Frequency domain analysis

For the frequency domain study a 2D model will be used in order to save computational resources. This simplification is valid since the position of the resonant frequency in the x-axis depends on the thickness of its layers and not on the transducer area (resonators in thickness expansion mode). However, to obtain correct levels of the impedance curve, the "out-of-plane thickness" and "out-of-plane extension" of the transducer must be indicated in the model. The cross section in Figure 3.19b indicates the materials and dimensions used for the FEM simulations.

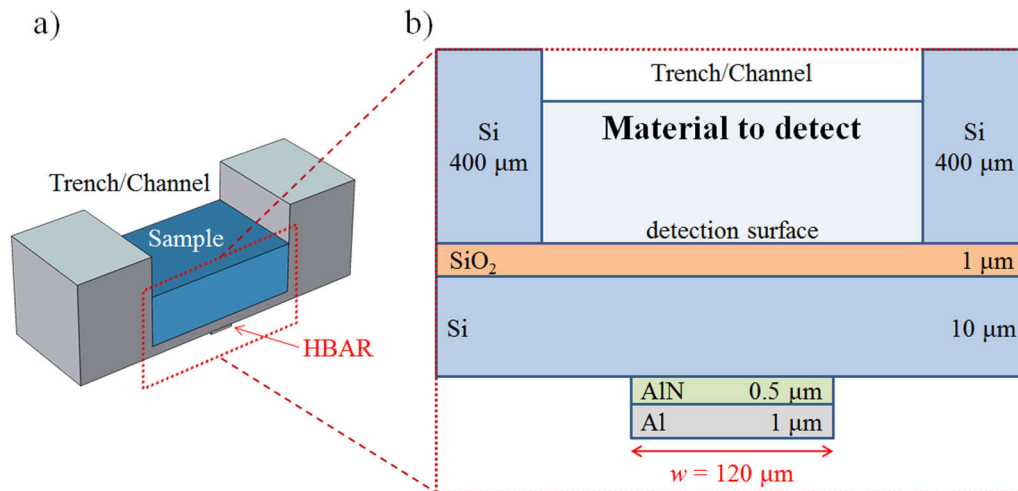


Figure 3.19: Geometry of the FEM model to simulate the acoustic resonators. a) 3D representation of the device. b) Cross section indicating materials and dimensions used in the simulations.

The Model Wizard integrated in COMSOL Multiphysics was used to build the model: In the initial step the Space Dimension is selected as "2D" and the Acoustics Module is chosen since it integrates to the model all the necessary components for interaction between both solid and fluid materials. The Acoustic Module includes an option for Acoustic-Structure Interaction called "Acoustic-Piezoelectric Interaction, Frequency Domain". The latter will include all the physics interfaces required for interaction solid-piezoelectric-fluids: Pressure Acoustic Frequency Domain (acpr), Solid Mechanics (solid), and Electrostatics (es). Also interactions between these interfaces (Multiphysics) are added to the model: Acoustic-Structure Boundary (asb1), Piezoelectric Effect (pze1). As a final step of the Model Wizard (Study Type), "Frequency Domain" has been selected.

The built-in computer-aided design (CAD) tools were used to draw the cross section in Figure 3.19b. The properties of the materials involved were included in the model by adding materials from the internal library: Al, Si and SiO₂ from the MEMS section, AlN from the piezoelectricity

section and Air from the section called "Built-in". Materials were assigned to the different domains as shown in Figure 3.20:

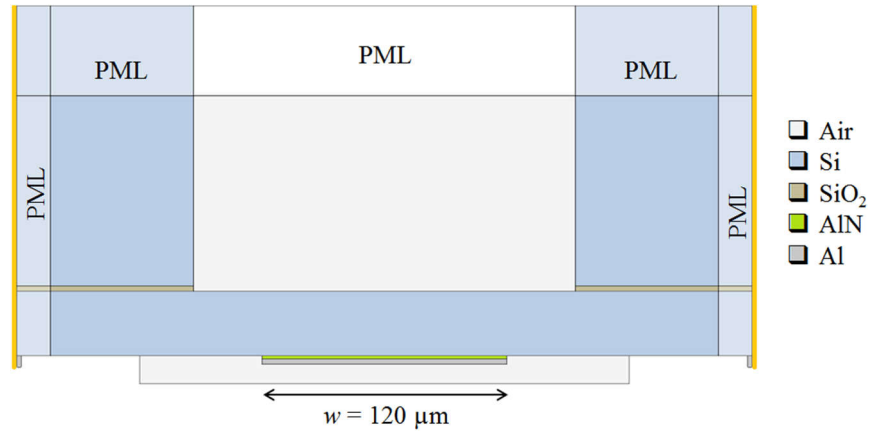


Figure 3.20: Geometry of the model as drawn using the CAD tools included in the IDE. The “view” (scale) is set to “automatic” for a better visualization of layers, therefore this picture is distorted and not to scale.

Domains surrounding the model have been defined as "Perfectly Matching Layers" (PML); this is added to acoustic models to mimic a domain that extends infinitely (avoiding wave reflections), effectively truncating the computational domain [24]. Lateral boundaries of the model (marked as orange lines) were defined as mechanically clamped.

Acoustics Module:

The Acoustic Region includes all domains corresponding to silicon, silicon oxide, and air in Figure 3.20. In this study, neither thermal conduction nor viscosity losses were considered, so the Pressure Acoustic Model is left with its default value (Linear Elastic). The Typical Wave Speed for PML is set as v_{subs} [25].

Solid Mechanics Module:

For the Solid Mechanics module, the domains corresponding to the transducer (the AlN piezoelectric and its drive Al electrode) were selected. The aluminum electrode is selected as "Linear Elastic Material", and only the AlN domain is selected as "Piezoelectric Material". "Fixed Constraint" conditions were added to mechanically clamp the lateral boundaries marked in orange (Figure 3.20).

Electrostatics Module:

For the Electrostatics Module only the material corresponding to AlN is selected. Here the Out-of-Plane Thickness parameter is set to correspond with the lateral out-of-plane dimensions of the active layer in order to obtain correct input impedance levels. The Reference Impedance parameter is set as $z_{\text{ref}} = 50 \Omega$. To excite the thickness expansion mode of the AlN layer the boundary shared by the piezoelectric domain and the 10 μm thick silicon substrate is set as "electrical reference" (Ground), while the boundary shared by the piezoelectric with the aluminum electrode is selected as "Terminal". The Terminal Type parameter is set as “Voltage”, with amplitude $V_{\text{in}} = 0.5 \text{ V}$.

Mesh:

Solutions of acoustic problems are wavelike, characterized by $\lambda = v_{subs}/f_{op}$ in space, and this wavelength has to be resolved by the mesh. To represent a wave on a discrete grid (the mesh) the mesh elements must be smaller than the wavelength in order to resolve the wave, that is, several degrees of freedom (DoFs) per wavelength are required [26]. Following the recommendations from COMSOL documentation (~ 10 DoFs per wavelength), the “automatic Free Triangular” algorithm was used to mesh the model with a maximum element size $\lambda/10$. To mesh the PML domain was used a Mapped Mesh [27] of 10 elements (layers), with thickness $\lambda/10$.

Study:

To verify the analytical prediction of Figure 3.18a (resonance when the channel is empty), the Frequency Domain Study is configured to perform a frequency sweep between 1 and 1.2 GHz to find the third mode of the structure, using a step size of 200 kHz. Figure 3.21 shows a) Description of the different domains that compose the study b) The 2D plot showing the resulting Acoustic Pressure distribution and c) The resulting magnitude of the input impedance and its real value.

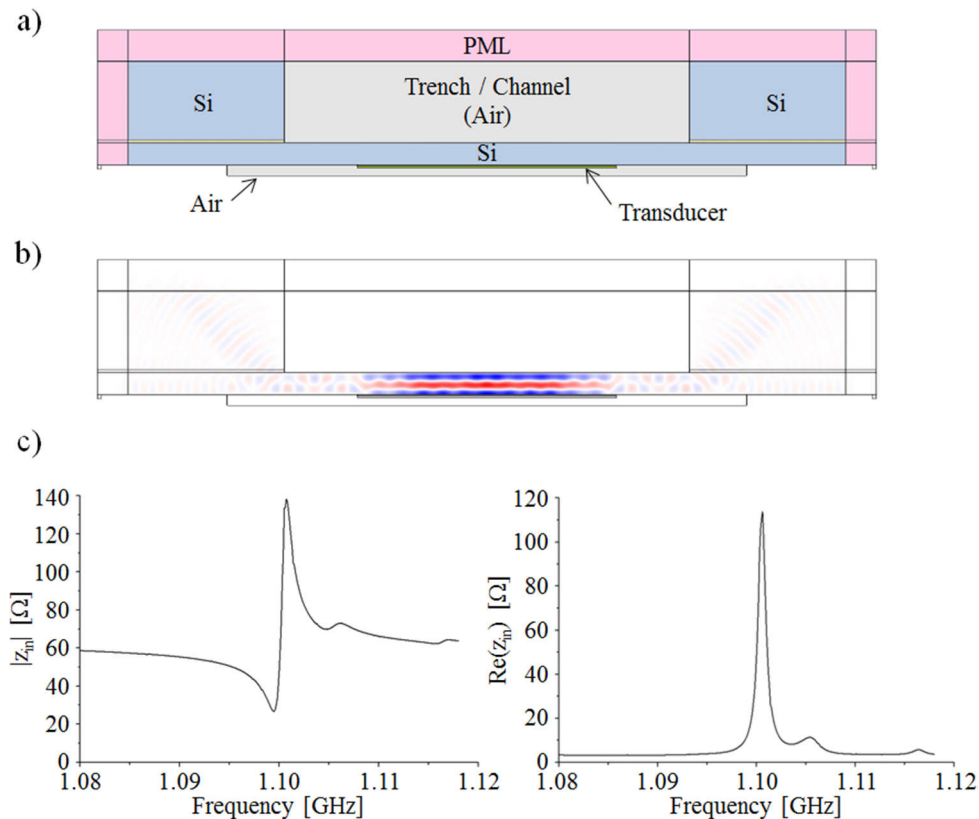


Figure 3.21: Results of the FEM simulation for the acoustic resonator. a) Domains that compose the model. b) 2D plot showing the resulting Acoustic Pressure distribution in the structure. c) Resulting input impedance (magnitude, left) and real value (right).

The Acoustic Pressure distribution plot in Figure 3.21b confirms that the energy remains confined in the solid domains of the model and is fully reflected in boundaries shared by solid domains and

those corresponding to "air". In addition to the acoustic pressure of the thickness mode, this FEM result includes some acoustic pressure escaping sideways due to the lateral spurious modes that exist in real-scaled devices [28]. This Acoustic Pressure plot also shows the effectiveness of domains defined as PML, avoiding reflection of lateral acoustic pressure and simulating a solid domain that expands infinitely. The input impedance curves in Figure 3.21c agree well with the analytical results in Figure 3.18 for the case of "air" in the detection surface, adding for the case of this FEM result small resonance peaks with slightly higher frequency than the studied thickness mode resonance; these additional peaks correspond to the spurious lateral modes.

Measuring Principle

To confirm attenuation of the resonance peak in presence of liquid, the material filling the channel in the model of Figure 3.21a has been changed to "water" and the study has been repeated. Figure 3.22b shows the resulting pressure plot and Figure 3.22c the input impedance.

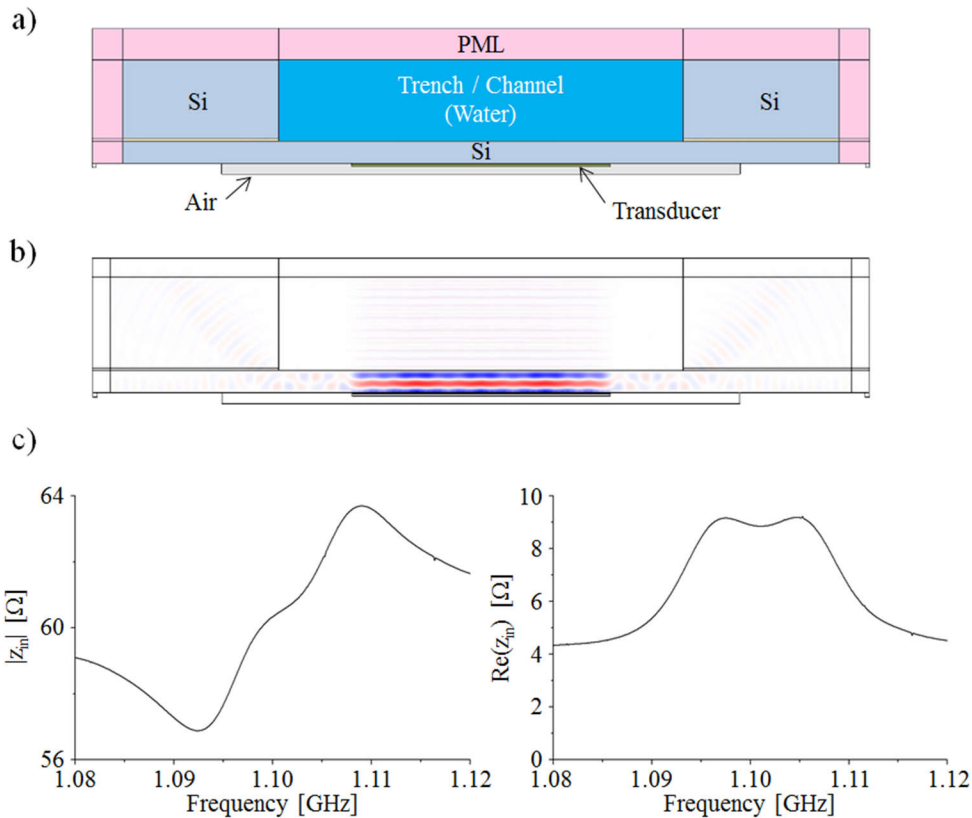


Figure 3.22: Results of the FEM simulation for the acoustic resonator when the material flooding the channel is water. a) Domains that compose the model. b) 2D plot showing the resulting Acoustic Pressure distribution in the structure. c) Resulting input impedance (magnitude, left) and real value (right).

The 2D acoustic pressure plot in Figure 3.22b confirms that when the channel is filled with water some of the acoustic pressure from the solid domain leaks into the liquid, whereas Figure 3.22c confirms attenuation of the resonance peak both in the input impedance magnitude plot (left) and in its real value plot (right). Although the sensor can very easily identify when there is liquid in the channel, the spurious lateral modes could make it difficult to classify liquids.

Figure 3.23 compares the FEM results (black) to analytical results (magenta), showing congruence between both the frequency where the third mode is located, and the amplitudes corresponding to the cases of "cleared channel" and when it is flooded by liquid.

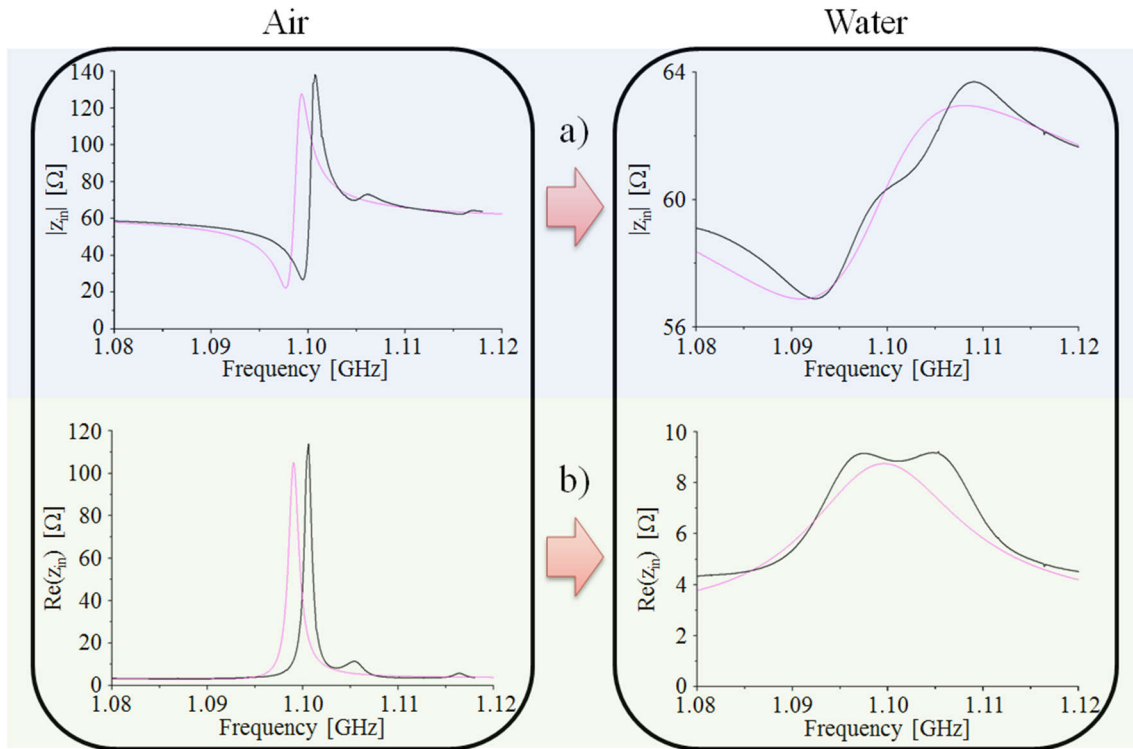


Figure 3.23: FEM results (input impedance) showing the measurement principle using the third mode of the resonating structure. a) Comparison of the amplitude of the input impedance (magnitude) for the case of 'air' at the detection surface (left) and the 'water' case (right). b) Comparison of the amplitude of the input impedance (real value) for both materials. Analytical curves (magenta) are included as reference.

3.4.2 FEM for Pulse-echo Transducers (input impedance and measuring principle)

Frequency Domain analysis

Similarly to the case of the acoustic resonators, here was used a 2D model to save computational resources. The cross section in Figure 3.24 indicates the materials and dimensions used for the model corresponding to the pulse-echo transducer.

For the Frequency Domain analysis the Acoustic Module is selected since it integrates to the model all the necessary components for interaction between both solid and fluid materials, for this is selected the option "Acoustic-Piezoelectric Interaction, Frequency Domain" which contains all the physics interfaces required for interaction solid-piezoelectric-fluids: Pressure Acoustic Frequency Domain (acpr), Solid Mechanics (solid), and Electrostatics (es). The "Study Type" for this case is "Frequency Domain".

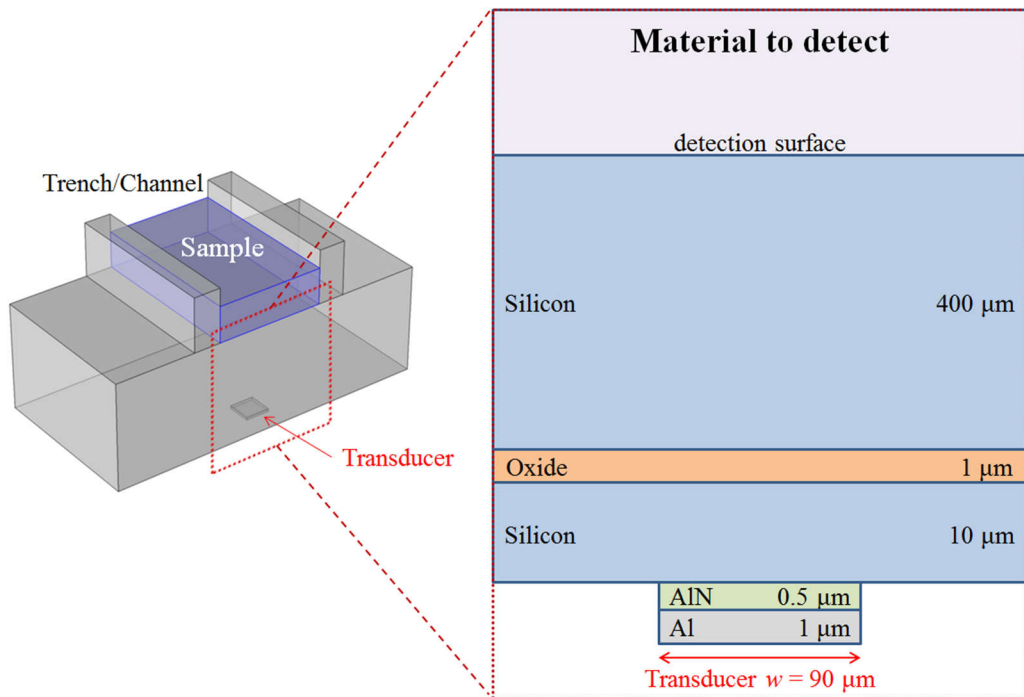


Figure 3.24: Geometry of the FEM model to simulate the pulse-echo transducer. a) 3D representation of the device. b) Cross section indicating materials and dimensions used in the simulations.

The built-in computer-aided design (CAD) tools were used to draw the cross section in Figure 3.24. The properties of the materials involved were included in the model by adding materials from the internal library: Al, Si and SiO₂ from the MEMS section, AlN from the piezoelectricity section and Air from the section called "Built-in". Materials were assigned to the different domains as shown in Figure 3.25:

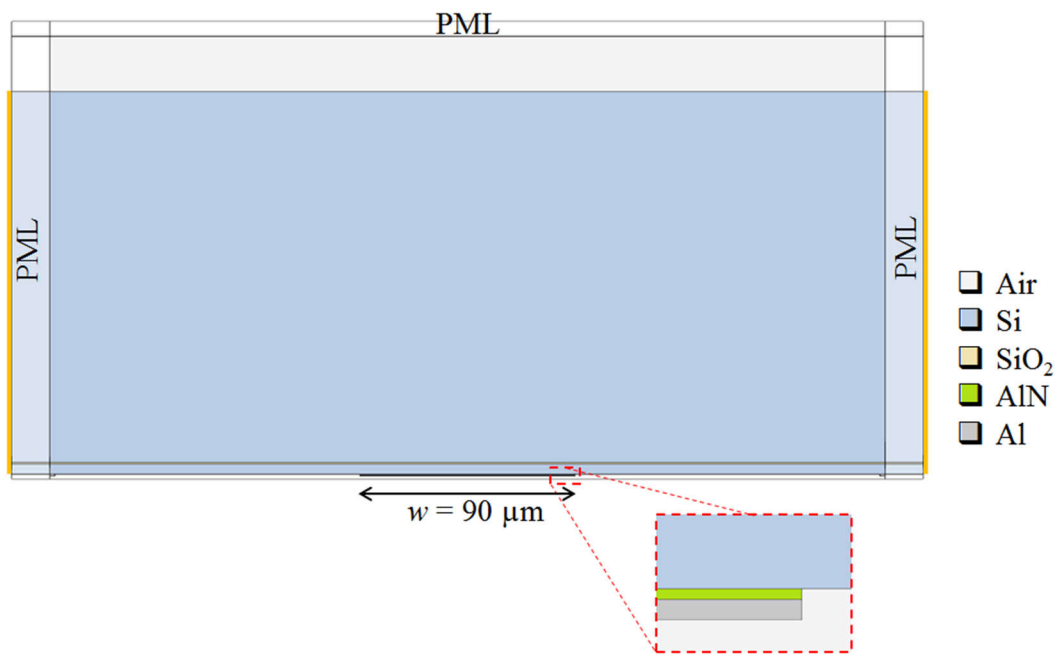


Figure 3.25: Geometry of the model for the pulse-echo transducer. The "view" option (scale) is set to "automatic" for a better visualization of layers, therefore this picture is distorted and not to scale.

Again, the solid domain is surrounded by air and therefore confinement of acoustic pressure in the silicon bulk is expected. Domains marked as PML truncate computational domain and mimic a domain that extends infinitely.

Acoustics Module:

The Acoustic Region includes all domains corresponding to silicon, silicon oxide, and air in Figure 3.25. The Pressure Acoustic Model is left with its default value (Linear Elastic) and the Typical Wave Speed for PML is set as v_{subs} [25].

Solid Mechanics Module:

For the Solid Mechanics module, the domains corresponding to the transducer (the AlN piezoelectric and its drive Al electrode) were selected. The aluminum electrode is selected as "Linear Elastic Material", and the AlN domain is selected as "Piezoelectric Material". "Fixed Constraint" conditions were added to mechanically clamp the lateral boundaries marked in orange (Figure 3.25).

Electrostatics Module:

For the Electrostatics Module only the material corresponding to AlN is selected. Here the Out-of-Plane Thickness parameter is set to correspond with the lateral out-of-plane dimensions of the active layer in order to obtain correct input impedance levels. The Reference Impedance parameter is set as $Z_{ref} = 50 \Omega$. To excite the thickness expansion mode of the AlN layer the boundary shared by the piezoelectric domain and the 10 μm -thick silicon substrate is set as "electrical reference" (Ground), while the boundary shared by the piezoelectric with the aluminum electrode is selected as "Terminal". The Terminal Type parameter is set as "Voltage", with amplitude $V_{in} = 0.5 V$.

Mesh:

The "automatic Free Triangular" algorithm has been used to mesh the model with a maximum element size $\lambda/10$. To mesh the PML domain was used a Mapped Mesh, which consists of 10 elements (layers) with thickness $\lambda/10$.

Study:

The Frequency Domain Study is configured to perform a frequency sweep between 0.8 and 2 GHz to find regions with superior electromechanical coupling in this range (as predicted by theory), using a step size of 200 kHz. Figure 3.26 shows a) The 2D plot showing the resulting Acoustic Pressure distribution and b) The resulting magnitude of the input impedance. This plot of electric impedance includes both, the case of the simple HBAR constituted by the AlN film deposited on the 400 μm -thick substrate and the case of the fabricated device, which includes multiple layers of different materials.

The electrical impedance plot in Figure 3.26b confirms that the configuration of layers and materials constituting the designed transducer cause additional modulation of the frequency comb (dark trace), respect to the case of the simple bimorph device with negligible electrodes (magenta trace). These frequency spots with higher amplitude modes also offer a significant increase in the

effective electromechanical coupling, improving transduction for the pulse-echo devices and providing them with multi-frequency capability.

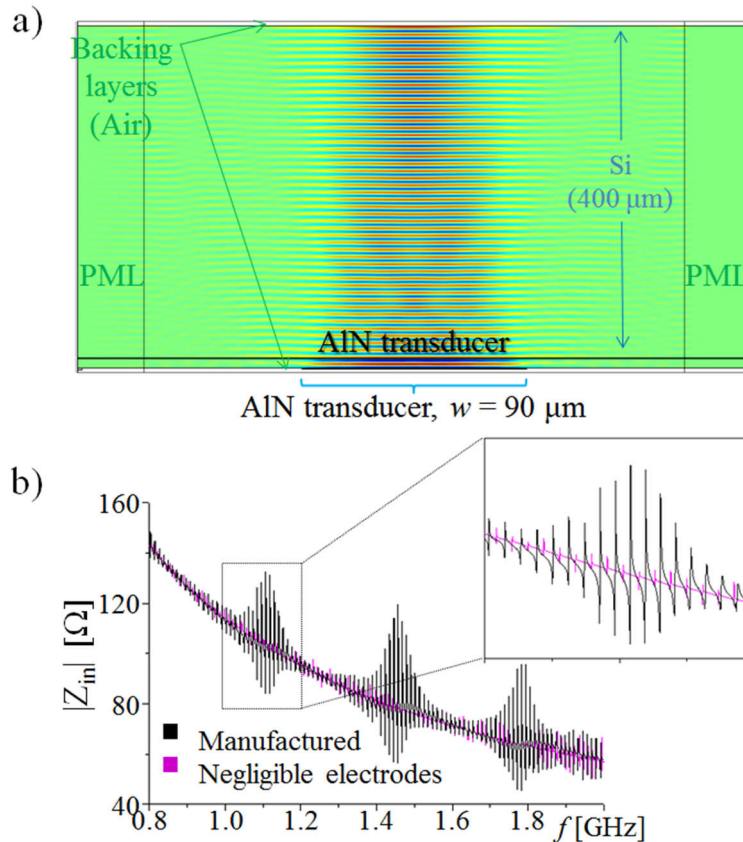


Figure 3.26: Results of the frequency-dependent FEM simulation for the pulse-echo transducer. a) 2D model illustrating the confinement of acoustic energy in the solid domain of the HBAR when the thickness extension mode of its piezoelectric layer is activated by a continuous RF source. b) Input electrical impedance plot as result of frequency domain simulations in the 0.8–2 GHz region; the configuration of layers and materials constituting the designed device cause modulation of the frequency comb.

Measuring Principle (Time-dependent simulations)

To confirm the analytical predictions regarding the measurement principle, this section details how the time-dependent FEM simulation model was prepared.

The time-dependent model was created using the Model Wizard; similarly to the resonant case this model is reduced to a 2D geometry to save computational resources. The Acoustic Module is selected since its component “Acoustic-Structure Interaction” integrates to the model all the necessary components for interaction of elastic waves in solids and pressure waves in fluids. Its “Transient” option combines the Pressure Acoustics, Transient and Piezoelectric Devices interfaces to connect the acoustic pressure variations in fluids to the structural deformation in both solids and piezoelectric solid domains. The physics interface also includes features from Electrostatics to solve for the electric field in the piezoelectric material. The Study Type is selected as “Time-Dependent”; this study is used to compute the time-varying deformation and motion of solids subject to transient loads (compute the time-varying propagation of pressure waves).

Input RF pulse:

Contrary to the previous frequency-dependent study where the pulse-echo transducer is driven by a continuous RF source, in this case it is mandatory to drive the transducer for a shorter time than that required to create stationary waves in the thickness of the whole structure, i.e. the input RF source should be active for a shorter time than the analytically predicted ToF (48 ns).

To model the input pulse the continuous Sinusoidal Function ($\sin(\omega * t)$) is added in the Global Definitions menu, where: $\omega = 2 * \pi * fop$, and $fop = 1.1 \text{ GHz}$. Then a Rectangle Function ($rect(t)$) with unitary value in the interval $0 < t < 25 \text{ ns}$ is added. Finally an Analytic Function defined as $RFin = [Vin * \sin(\omega * t) * rect(t)]$ is included, where: $Vin = 1 \text{ dBm}$. Figure 3.27 shows the input pulse, the level transition of the Rectangle Function was slightly smoothed to obtain this final appearance.

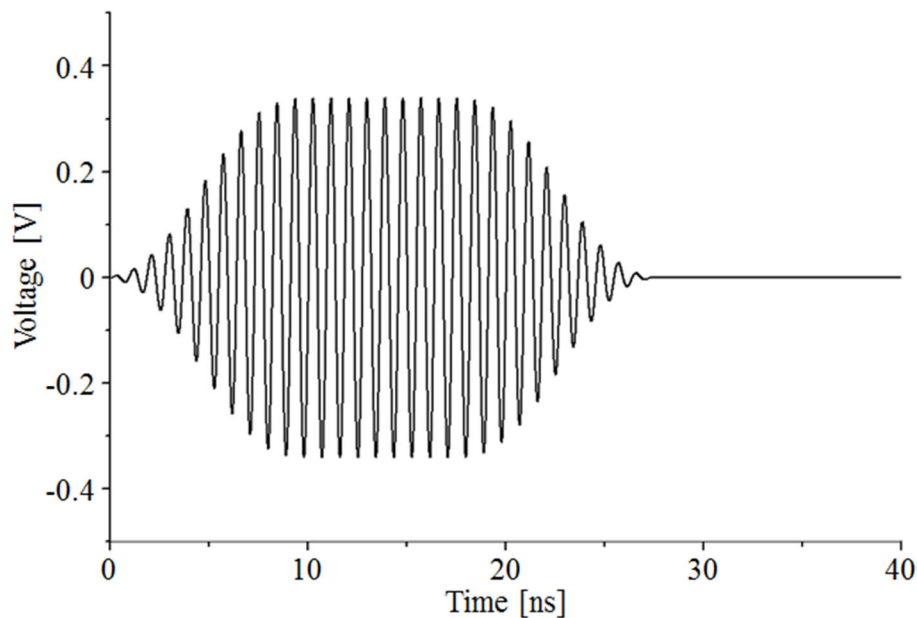


Figure 3.27: Input RF pulse to drive the pulse-echo transducer

Geometry and Materials:

The 2D Geometry used previously in Figure 3.25 has been imported for this time-dependent model. Materials were assigned to the different domains as indicated by Figure 3.25 except for the material placed on the detection surface, which is selected here as "water".

Pressure Acoustics, Transient (actd):

The Acoustic Region includes all domains corresponding to silicon, silicon oxide, and air. The Pressure Acoustic Model is left with its default value (Linear Elastic) and the Typical Wave Speed for PML is set as v_{subs} .

The lateral boundaries of Figure 3.25 (marked in orange) were defined as "Sound Soft Boundaries"; this condition causes the acoustic pressure to vanish ($p_t = 0$).

Solid Mechanics (solid):

For the Solid Mechanics module, the domains corresponding to the transducer (the AlN piezoelectric and its drive Al electrode) were selected. The aluminum electrode is selected as "Linear Elastic Material", and the AlN domain is selected as "Piezoelectric Material".

"Fixed Constraint" conditions were added to mechanically clamp the lateral boundaries (those marked in orange in Figure 3.25).

Electrostatics (es):

For the Electrostatics Module only the material corresponding to AlN is selected. Here the Out-of-Plane Thickness parameter is set to correspond with the lateral out-of-plane dimensions of the active layer in order to obtain correct input impedance levels. The Reference Impedance parameter is set as $z_{ref} = 50 \Omega$.

The boundary shared by the piezoelectric domain and the 10 μm -thick silicon substrate is defined as "electrical reference" (Ground), while the boundary shared by the piezoelectric with the aluminum electrode is selected as "Terminal". For the pulse-echo case the Terminal Type parameter is set as "Voltage", and its amplitude is set as the function $Rfin(t)$; this causes the piezoelectric to be driven by the short RF pulse of Figure 3.27.

Mesh:

The "automatic Free Triangular" algorithm has been used to mesh the model with a maximum element size $\lambda/6$ [26].

Study:

In the Study Settings the "Times" section was defined as: $0 < t < 140 \text{ ns}$. This value is larger than twice the ToF to guarantee compute of the pulse round trip.

The Time Step parameter for the Default Solver was set manually since it should resolve the wave equally well in time as the mesh does in space. The relationship between wavespeed v , maximum mesh size m_{max} and time step length Δt is given by the Courant-Friedrichs-Lewy (CFL) condition [29]:

$$\text{CFL} = \frac{v\Delta t}{m_{max}}$$

The mesh size was manually selected as: $m_{max} = \lambda/N$, with $N = 6$ to properly resolve the wavelength, and $\lambda = v_{subs}/f_{op}$. From the latter is found that the Time Step:

$$\Delta t = \frac{\text{CFL}}{Nf}$$

The CFL number should be less than 0.2, and a value of 0.1 proves to be near optimal [30].

Inverse Piezoelectric Effect:

With the Model Wizard were included all the required modules for the piezoelectric to convert the input RF pulse into acoustic pressure (direct piezoelectric effect), but the interfaces and components to convert the reflected acoustic pulse (echo) into the output electrical signal were not included in the model. For this is necessary to add a second physics interface for the electrostatics phenomena.

Electrostatics (es2):

For this interface only the material corresponding to AlN is selected, the Out-of-Plane Thickness parameter is set to correspond with the lateral out-of-plane dimensions of the active layer, and the Reference Impedance parameter is set as $z_{ref} = 50 \text{ ohm}$.

The boundary shared by the piezoelectric domain and the $10 \mu\text{m}$ -thick silicon substrate is defined as "electrical reference" (Ground), while the boundary shared by the piezoelectric with the aluminum electrode is selected as "Terminal". To convert acoustic energy into an electrical output the Terminal Type parameter is set as "Charge" with initial value $Q_0 = 0 \text{ C}$.

Piezoelectric effect (pze2):

Under the Multiphysics menu is added a second Piezoelectric Effect (pze2) interface. This is set to couple Electrostatics (es2) with the interfaces: Pressure Acoustics, Transient (actd) and Solid Mechanics (solid). Figure 3.28 show the resulting acoustic pressure in two different time slices.

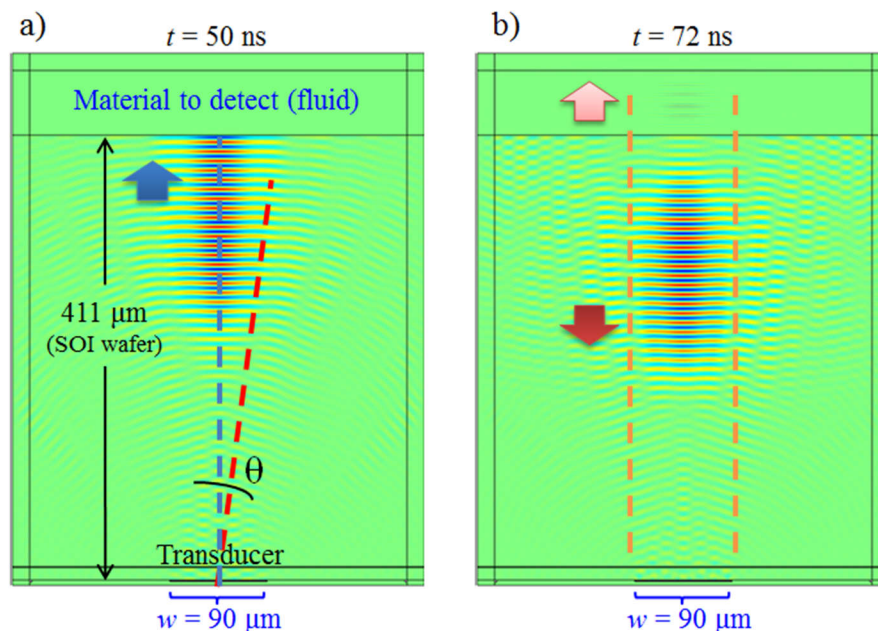


Figure 3.28: Resulting pressure acoustics plot showing time evolution of a bulk ultrasound pulse traveling across the thickness of the silicon substrate, low diffraction is observed using this $90 \mu\text{m}$ transducer working at 1.1 GHz . a) At $t = 50 \text{ ns}$ the acoustic pulse traveling with direction indicated by the blue arrow has already reached the detection surface. b) At $t = 72 \text{ ns}$ part of the acoustic energy has been transferred to the liquid media and it continues its flight in the direction indicated by the pink arrow, meanwhile, the complementary portion of the emitted acoustic energy was reflected back towards the emitter (red arrow).

In Figure 3.28 it is shown that the width of the main lobe is similar to the width of the transducer (delimited by the dashed lines in orange), confirming low diffraction of the pulse for the selected operating frequency. Figure 3.29a is the output voltage from $t = 0$ to $t = 140$ ns, registered when the channel is empty (air in the detection surface). This confirms the Time-of-Flight as $ToF \approx 49$ ns (or 98 ns for a round trip, i.e. once the acoustic echo is received by the transducer). Figure 3.29b shows the envelope (Hilbert transform) of received echoes for different materials placed on the detection surface.

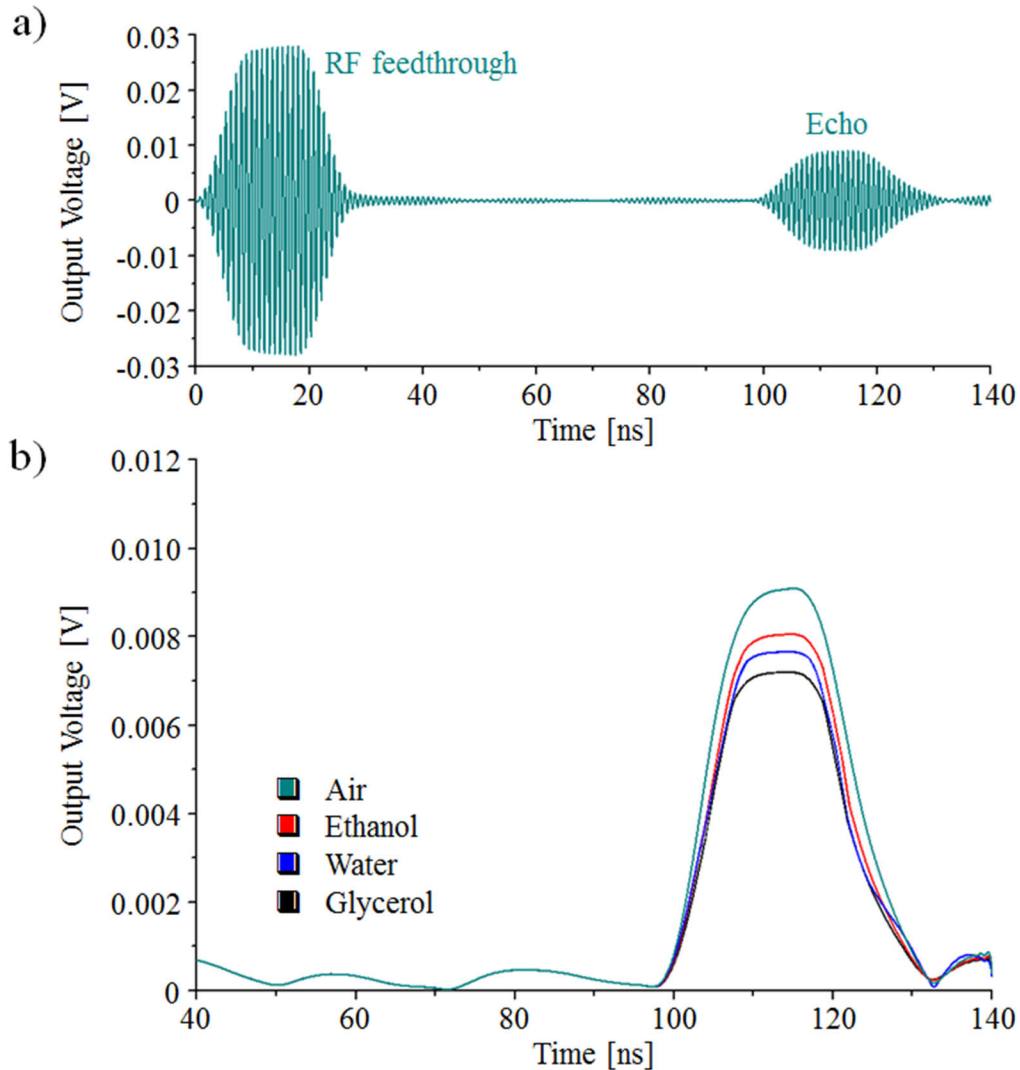


Figure 3.29: Resulting output voltage produced for the inverse piezoelectric effect (FEM simulations). a) Output voltage from $t = 0$ to $t = 140$ ns registered when the channel is empty (air in the detection surface), this confirms the analytical prediction $ToF \approx 48$ ns. b) Envelope (Hilbert transform) of received echoes for different materials placed on the detection surface.

Each reflection coefficient in Figure 3.30 is obtained from the V_{liq}/V_{ref} relation, where V_{ref} is the voltage generated by received echoes when the detection surface is clear ('air' causes total reflection of the acoustic pulse and therefore a reference value), whereas V_{liq} is voltage generated in the case of channel filled by each sample (where voltage level will depend on the amount of acoustic energy absorbed by each liquid).

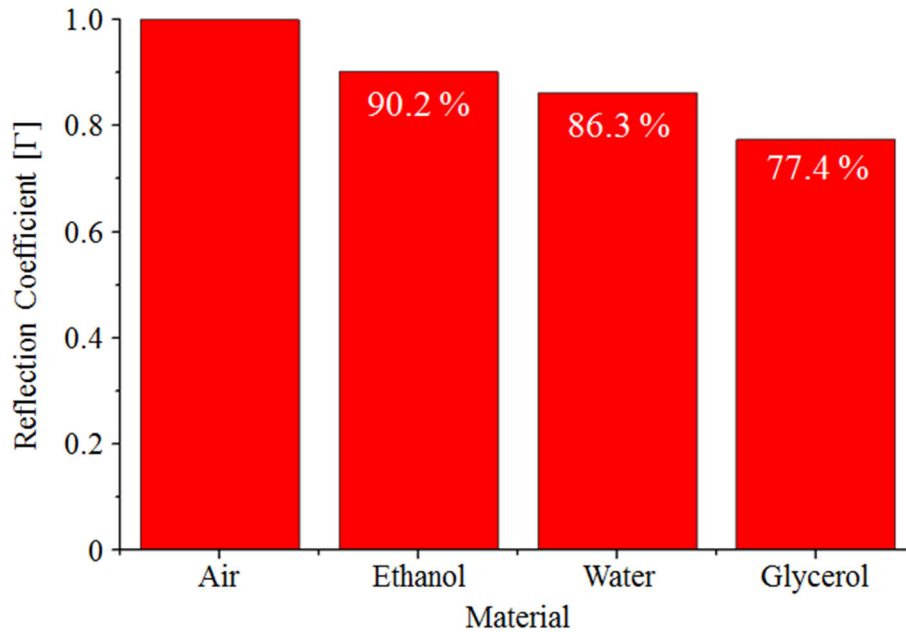


Figure 3.30: Reflection coefficient Γ of several liquid samples when the measure of ‘air’ is taken as the reference value. Values correspond to the peak value of envelopes in Figure 3.29 (FEM simulations).

Note that the reflection coefficient value for each sample in Figure 3.30 agrees well with analytical predictions of Table 3.3. The latter confirms the measuring principle of the pulse-echo transducer.

3.5 Fabrication

PiezoMUMPs is a commercial multi-user process by MEMSCAP, designed for general purpose micromachining of piezoelectric MEMS in a Silicon-on-Insulator framework [31]. This is a simple 5-mask level patterning and etching process which provides a 0.5 μm layer of AlN for the creation of devices such as energy harvesters, sensors, ultrasonic transducers, microphones, and actuators [32–36]. Figure 3.31 shows layers and materials available in the PiezoMUMPs process.

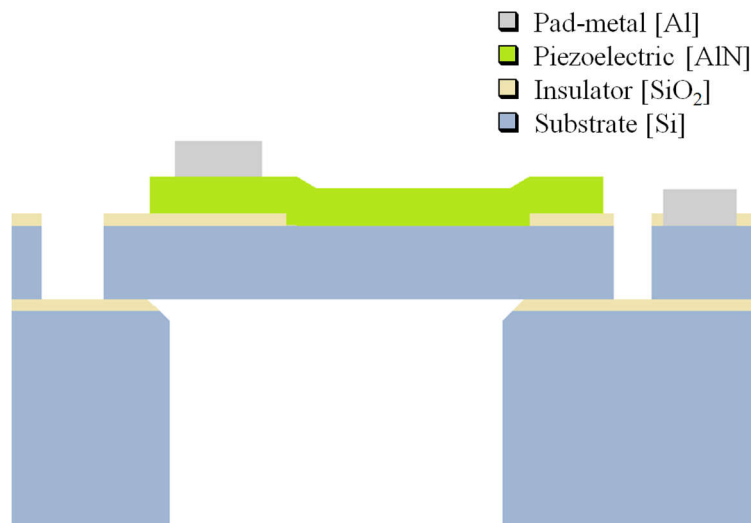


Figure 3.31: Cross sectional representation showing the available layers of the PiezoMUMPs process (not to scale)

3.5.1 Process overview

This process starts with a double-side polished SOI wafer of diameter equal to 150 mm. One face of the wafer is doped by depositing phosphosilicate glass (PSG), which is annealed and then removed leaving a conductive surface that can be used for electrical routing. Over the conductive silicon surface is a 2000 Å thermal oxide layer to isolate selected areas on the surface, this layer is defined by the first lithography mask called PADOXIDE. In this step the wafer is coated with positive photoresist, so that areas of resist exposed to light will become soluble to the developer and the oxide below will be removed via wet etching. Next, the piezoelectric film (AlN) is deposited by reactive sputtering. To sculpt this 0.5 μm layer the wafer is covered with positive photoresist and the pattern is transferred exposing with light through the mask defined by the layer PZFILM; then the piezoelectric material is wet-etched. The second deposited layer is a metal stack of 20 nm of chrome and 1 μm of aluminum; this upper metal layer is patterned by using negative photoresist and a liftoff process (opaque areas in the PADMETAL mask will represent metal pads and routes preserved after lithography).

The superficially doped silicon substrate is then lithographically sculpted using positive photoresist and the mask called SOI. The insulating SiO₂ layer is etched by RIE, whereas DRIE is used to etch the silicon layer until reaching the buried SiO₂ of the SOI wafer. As a last step, a front side protection material is applied to the the patterned silicon layer and the wafers are flipped upside down to allow patterning of both the 400 μm holding substrate and the buried oxide. This last step is defined by the layer TRENCH and allows the creation of cavities (or the mechanical release of structures) at the opposite face of the wafer. Table 3.4 presents a summary of the layer names, their associated masks, their purpose, and their minimum feature size.

Material	Mask name / GDS number	Purpose	Type of photoresist	Process	Min. feature [μm]
Insulating oxide	PADOXIDE 10	Electrical isolation of the piezoelectric and/or the metal layers from the conductive silicon	Positive	Grown of thermal oxide	5
Piezoelectric (AlN)	PZFILM 20	Provide the piezoelectric material	Positive	Deposition by sputtering	10
Pad metal (Cr + Al)	PADMETAL 30	Provide metal for pads and electrical interconnects	Negative	Deposition and definition by liftoff	3
Structural silicon	SOI 40	Define structures in the doped silicon layer	Positive	Etching by RIE + DRIE	2
Buried oxide (SiO ₂)	TRENCH 50	Creation of cavities or releasing of structures	Positive	Etching DRIE + RIE	200
Substrate (Si <100>)					

Table 3.4: Layer names, masks involved and their purpose.

PiezoMUMPs provides an additional level called SOIHOLE (GDS: 41) in order to provide a simpler way to create holes in the layer "SOI". In this way, the digitized area in 40 represent "material to keep", whereas areas defined by 41 (holes in layer 40) represent "material to be removed". The process flow for the construction of both the resonant device and the pulse-eco transducer is described below.

3.5.2 Process flow for Acoustic Resonators

Figure 3.32 shows the implementation of the acoustic resonator, using the PiezoMUMPs process. Masks for these designs were drawn by Eyglis Ledesma to be used as piezoelectric flexural membranes, however, in this work they are used as solid resonators.

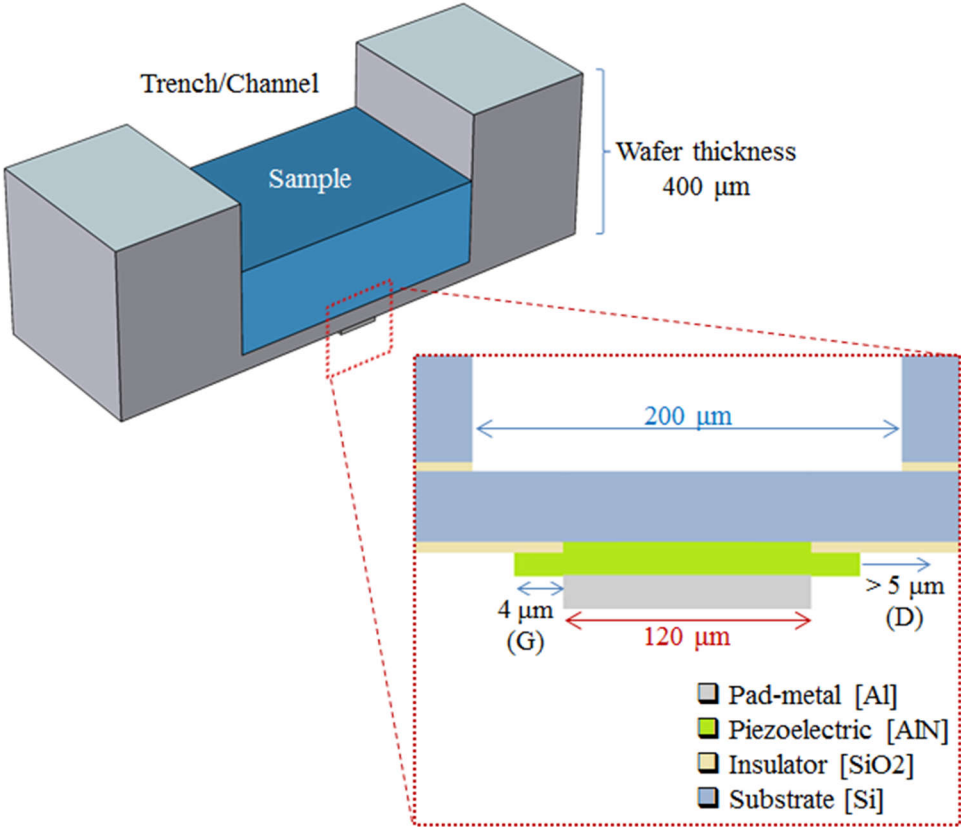


Figure 3.32: Cross sectional representation of the implementation of the acoustic resonator using the PiezoMUMPs technology (square shaped, side = 120 micrometers).

In Figure 3.32 some rules were considered in order to prevent short circuits due to misalignment of layers: On the one hand the insulating layer was extended for more than 5 micrometers beyond other materials to avoid contact with the conductive silicon (design rule "D") while the piezoelectric layer was defined in such way to enclose the metal electrode with at least 4 micrometers of clearance (rule "G"). Design rules and recommendations were consulted in the Design Handbook of this technology [37].

Definition of the PADOXIDE level

The piezoelectric material should be sandwiched between electrodes to activate its thickness extensional mode, therefore, the first step is to pattern the 200 nm thermally grown oxide to uncover

the electrically conductive silicon beneath (which will be used as GND electrode). Figure 3.33 shows the lithography process using the PADOXIDE mask.

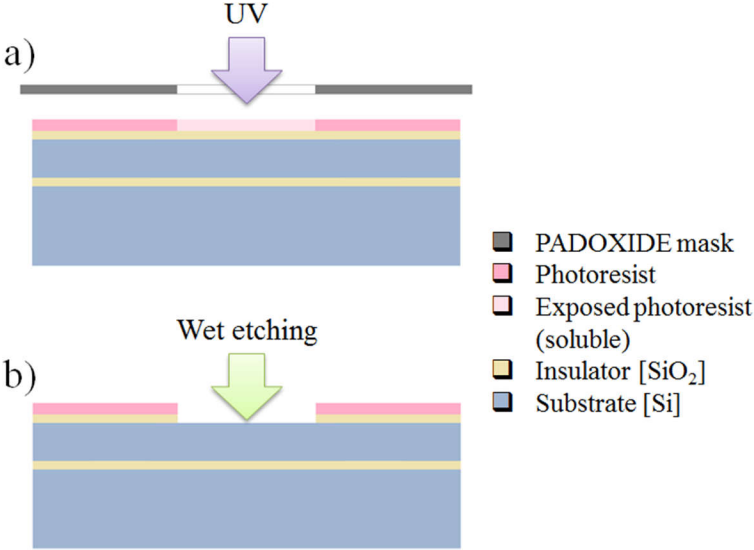


Figure 3.33: Cross section showing lithography of the PADOXIDE layer. a) The mask allows UV exposure of a squared area of side 120 μm to make soluble the photoresist. b) The soluble protector is removed with the developer allowing selective etching of the oxide.

To mold the 20 nm layer of thermal oxide with the PADOXIDE layer the wafer is covered with positive photoresist. In Figure 3.33a the mask allows UV exposure of a squared area of side 120 μm to make soluble the photoresist, whereas in Figure 3.33b the soluble protector is removed with the developer allowing selective etching of the oxide. Figure 3.34 is the layout of the PADOXIDE mask; opaque areas (blue) represent sections where the insulating oxide will be preserved, in this case, oxide regions intended to isolate the Drive electrode and vias from the conductive substrate.

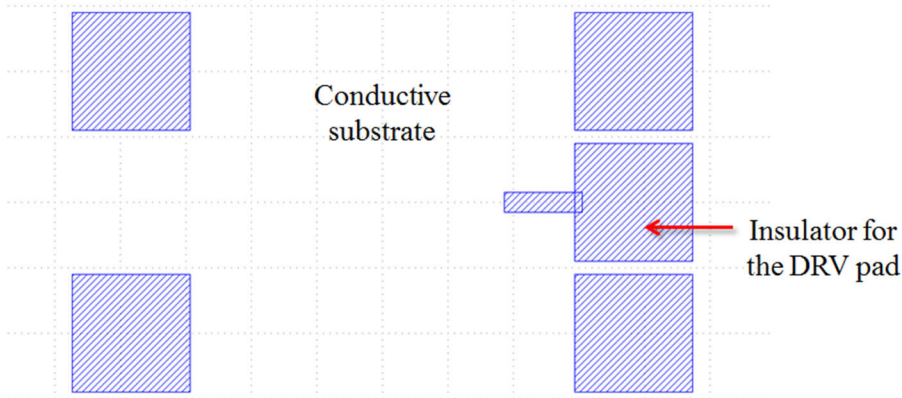


Figure 3.34: Layout of the PADOXIDE mask to pattern the insulator for the DRV pad. Additional insulating pads are intended to land GSG probes to perform measurements of scattering parameters.

Definition of the PZFILM level

The process continues with physical deposition of the piezoelectric layer (500 nm of AlN) and subsequent application of positive photoresist. Figure 3.35 shows the lithography process using the PZFILM mask.

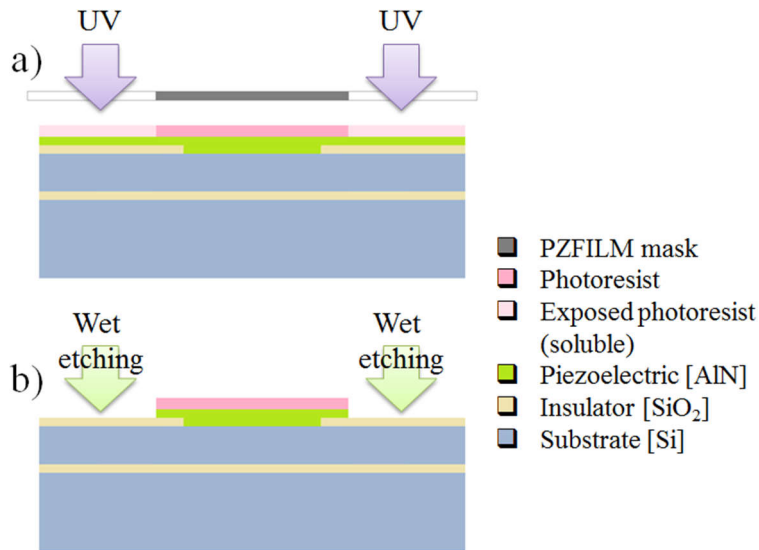


Figure 3.35: Cross section showing lithography of the PZFILM layer. a) The opaque section of the PZFILM mask blocks UV in the AlN transducer area, while exposed areas of the coating become soluble. b) Once the soluble protector is removed, wet etching is performed on the piezoelectric material to mold the transducer.

The mask is used to cover photoresist where the AlN layer will be defined, leaving uncovered areas of the protector exposed to UV (Figure 3.35a). The soluble protector is removed with developer allowing selective removal of piezoelectric material (Figure 3.35b). Figure 3.36 shows the layout of the PZFILM layer superimposed to the previous mask; the green square represents the area where the piezoelectric material will be preserved (the AlN transducer directly deposited over the conductive substrate).

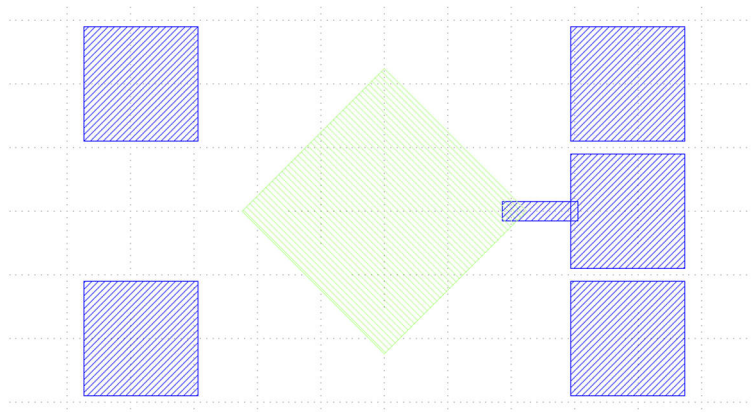


Figure 3.36: Layout of the PZFILM mask (green) superimposed to the PADOXIDE mask (blue).

Definition of the PADMETAL level

This device is provided with electrodes, pads and vias by defining the PADMETAL layer. Figure 3.37 shows the liftoff process for the metal layer.

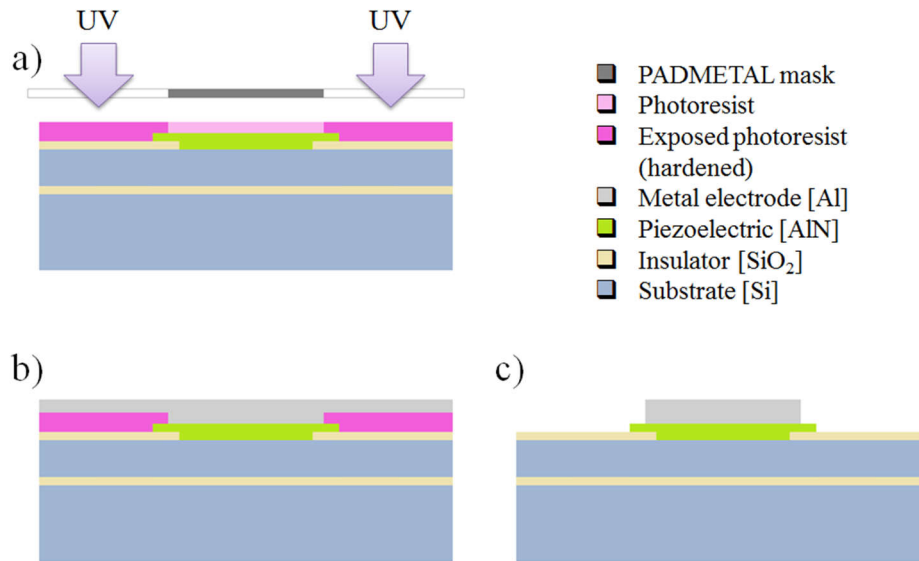


Figure 3.37: Cross section showing lithography of the PADMETAL layer. a) Exposed areas of the negative photoresist are hardened, which allows them to be used as sacrificial material. b) The unexposed section of the protective coating is developed, allowing the deposition of the metal electrode directly onto the piezoelectric material and the sacrificial material. Sacrificial material is dissolved, leaving metal only on the transducer.

Clear areas of the PADMETAL mask allow exposure of sections of the negative photoresist which will be used as a sacrificial material (Figure 3.37a). After developing of the protective film, a metal stack (20 nm of chrome and 1000 nm of aluminum) is deposited over the pattern (Figure 3.37b). As shown in Figure 3.37c, dissolution of the sacrificial layer also removes the metal layer except where it is in direct contact with the piezoelectric layer. Figure 3.38 is the layout of the PADMETAL mask (dark green) superimposed to previous masks; drawn areas represent regions where metal will be preserved (electrodes and characters).

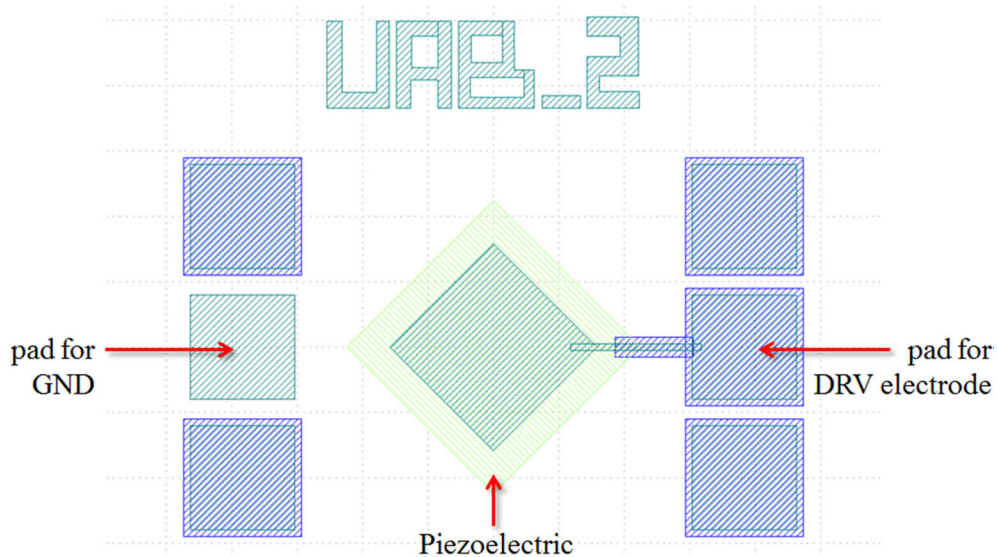


Figure 3.38: Layout of the PADMETAL mask (dark green) superimposed to the previous masks to pattern pads, electrodes and vias.

Definition of the SOIHOLE level

Since the silicon surface on the front side is electrically conductive, a trench in this surface should be created to electrically isolate each design. Figure 3.39 shows creation of this trench by using the SOIHOLE layer to define the SOI mask. Clear areas of the SOI mask allow exposure of sections of the photoresist (Figure 3.39a). The photoresist in exposed areas is removed and the oxide layer is etched by a RIE process (Figure 3.39b). Deep Reactive Ion Etching (DRIE) is then used to etch the doped silicon substrate, isolating electrically each design in the wafer.

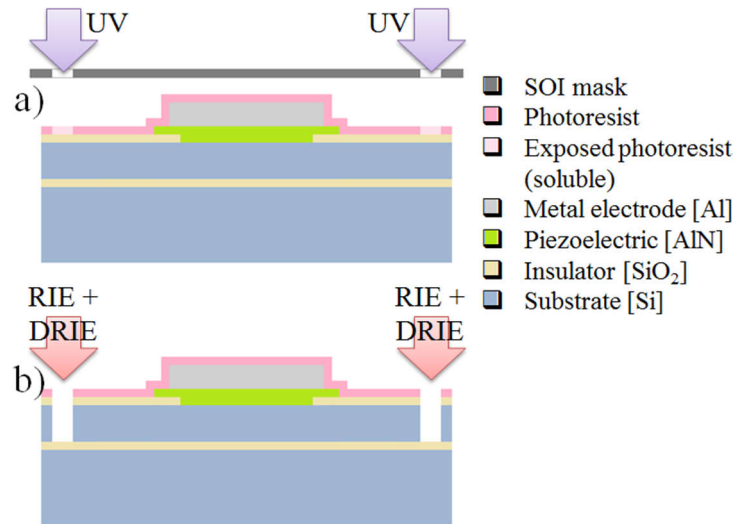


Figure 3.39: Cross section showing lithography of the SOI layer. a) The SOI mask allows UV exposure of regions where doped silicon will be removed. b) Conductive substrate from exposed areas is removed, isolating the design electrically from the rest of the wafer.

Figure 3.40 is the layout of the SOI & SOIHOLE masks superimposed to the previous masks; The whole cell is covered by the SOI mask in order to define areas to preserve, while the darker outline indicates the section to be etched to the buried oxide in the SOI wafer to isolate this cell from the rest of the design (as seen in Figure 3.39b)

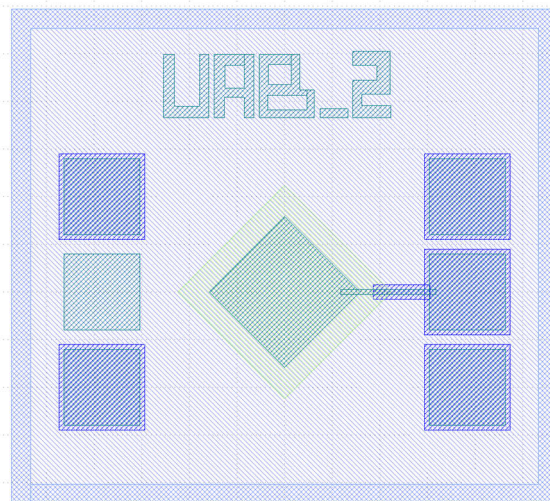


Figure 3.40: Layout of the SOI mask superimposed to the previous masks.

Substrate patterning (TRENCH mask)

To create the microchannel, a front side material (polyimide) is applied to the patterned face of the wafer to “hold” the wafer together during the subsequent trench etching, and then the wafer is flipped upside down (Figure 3.41a). The bare silicon substrate is coated with photoresist and it is patterned using the TRENCH mask. The front side protection material is then removed, leaving the structure in Figure 3.41b.

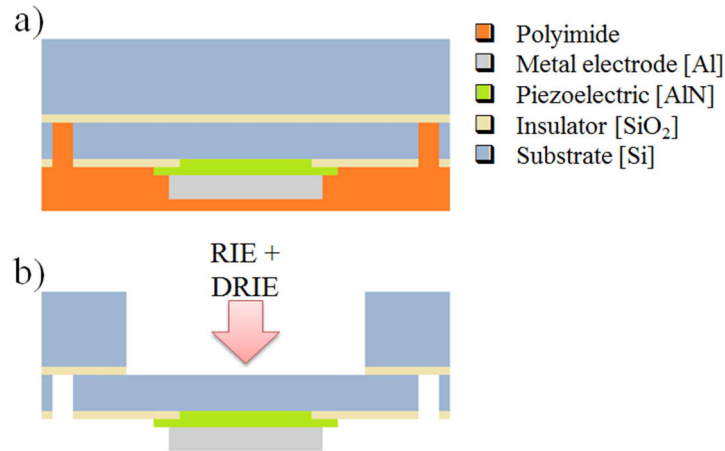


Figure 3.41: Cross section showing lithography of the TRENCH layer, to create the microchannel. a) The patterned face of the wafer is protected with polyimide and the wafer is flipped upside down. b) The bare face of the wafer is lithographically patterned using the TRENCH mask, creating the microchannel.

Figure 3.42 shows the layout of the TRENCH mask superimposed to the previous masks; this red square at the center indicates the area of the opposite face of the wafer to be etched to the buried oxide to create the trench in Figure 3.41b.

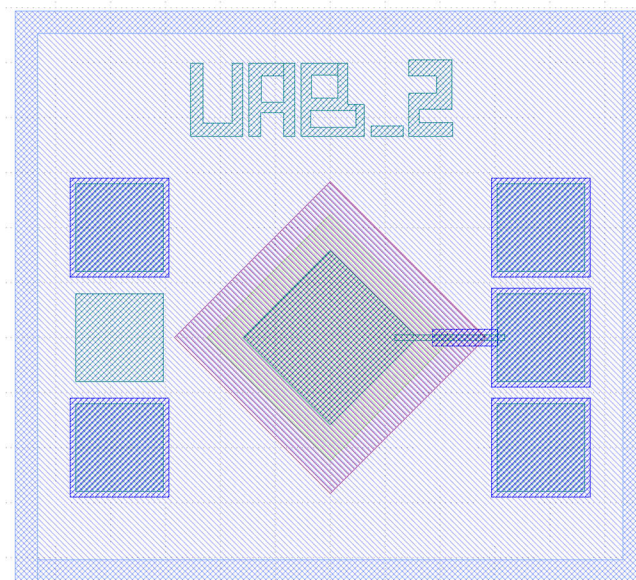


Figure 3.42: Layout of the TRENCH mask (red) superimposed to the previous masks, this template defines the area of the opposite face of the wafer to be etched (to create the microchannel/trench)

3.5.3 Process flow for the Pulse-Echo Transducer

Figure 3.43 shows the implementation of the pulse-echo transducer, using the PiezoMUMPs process.

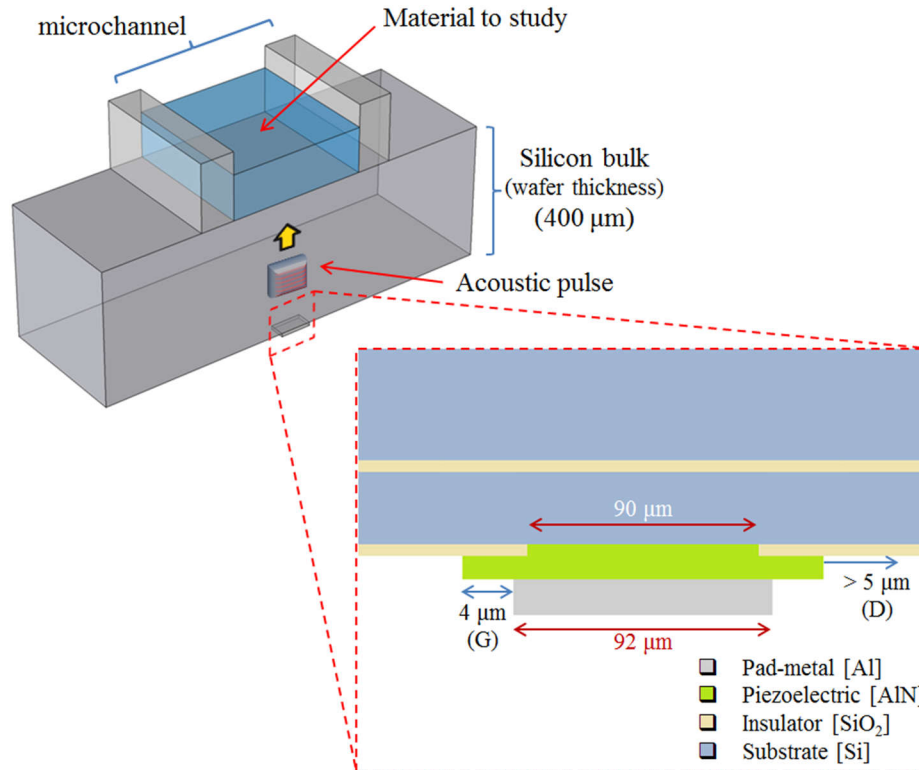


Figure 3.43: Cross sectional representation of the implementation of the pulse-echo transducer using the PiezoMUMPs technology (square shaped, side = 90 μm).

Since the same 5-layer process is being used as for resonators, the design flow is mostly similar: Definition of the Ground electrode with the PADOXIDE mask (Figure 3.44a), AlN deposition and patterning of the transducer with the PZFILM mask (Figure 3.44b), deposition of the Drive electrode and patterning with the PADMETAL mask (Figure 3.44c) and isolation of the design from the rest of the wafer by means of the SOIHOLE mask (Figure 3.44d).

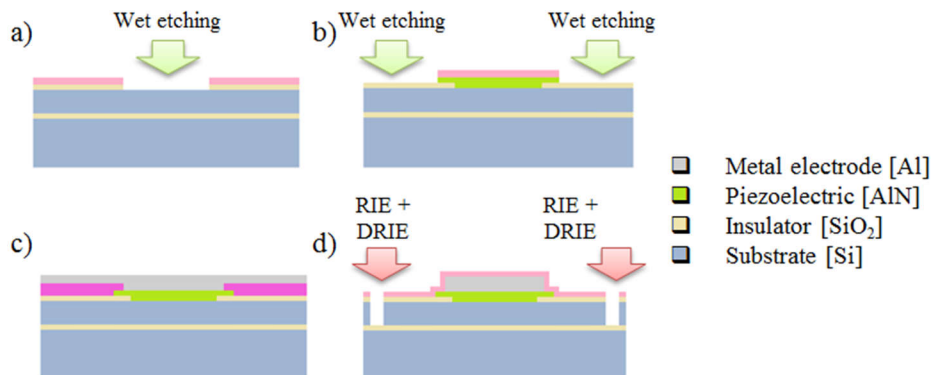


Figure 3.44: Design flow for the pulse-echo transducers: a) Patterning of the insulating layer b) Definition of the piezoelectric transducer c) Adding metal electrodes & vias d) Cell isolation.

Figure 3.45 is the layout of the PADOXIDE mask, showing the template for creating a linear array of three AlN transducers and their respective reference electrodes. Most of the area remains opaque (blue) in order to preserve the insulating oxide. Cleared areas marked as T_1 - T_2 - T_3 will allow depositing AlN directly on the conductive silicon and thus be connected to the reference electrodes (which will be created later by adding metal over the areas marked as G_1 - G_2 - G_3).

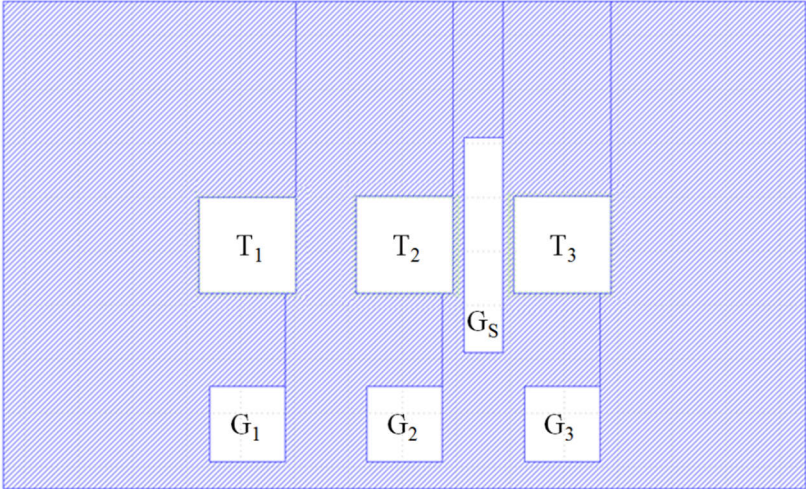


Figure 3.45: Layout of the PADOXIDE mask.

Arrays of transducers have been created in most cells to study the collaborative behavior of simultaneous transmitters focusing acoustic energy in a specific point of the detection surface to improve both sensitivity and spatial resolution, however, this thesis focuses in the case of a single central transducer (T2) used both to transmit the pulse and to receive it. The area marked as G_s is meant to be covered by metal and will be connected to GND to compare electromagnetic coupling between the T_1 - T_2 pair with respect to the T_2 - T_3 pair (this study is not covered in this thesis either). Figure 3.46 shows the layout of the PZFILM mask (green) superimposed to the PADOXIDE mask; this lithographic template is meant to pattern three piezoelectric transducers deposited on the exposed conductive substrate.

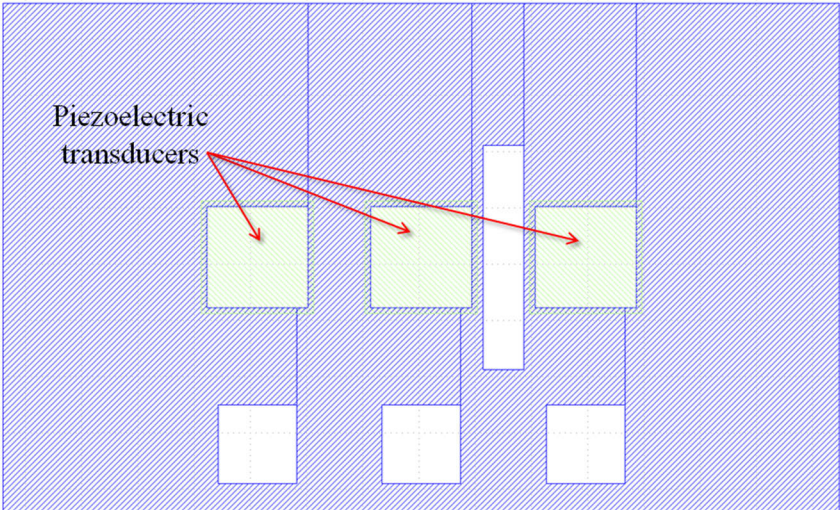


Figure 3.46: PZFILM mask (green) superimposed to PADOXIDE mask (blue).

Figure 3.47 shows the PADMETAL mask superimposed to previous masks; this level is meant for creation of metal electrodes and vias. As shown, the GND pad rests in direct contact over the conductive silicon substrate while the DRV pad lies on the insulator layer to prevent short circuit.

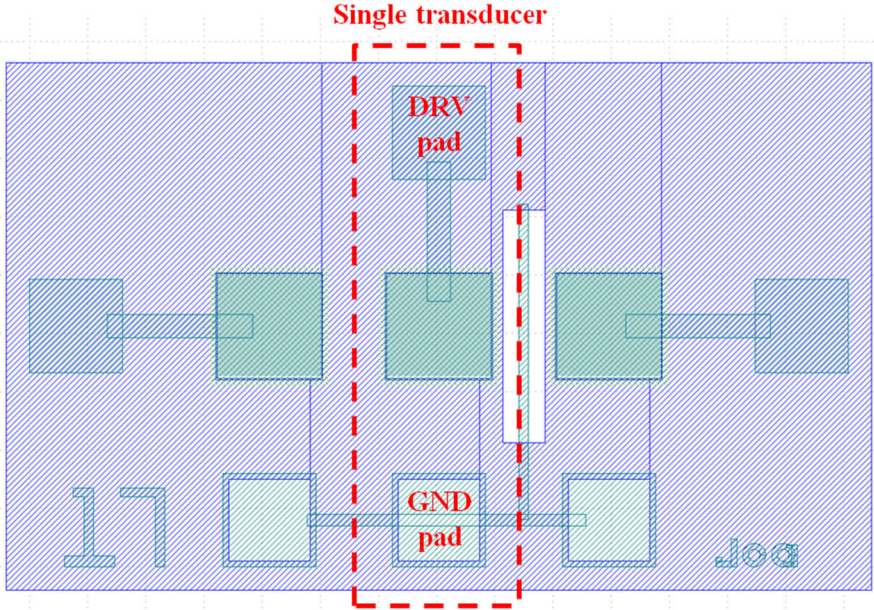


Figure 3.47: Layout of the PADMETAL mask (dark green) superimposed to the previous masks.

Figure 3.48 shows the SOI and SOIHOLE masks superimposed to the previous masks; these masks are intended to electrically isolate the cell from other designs.

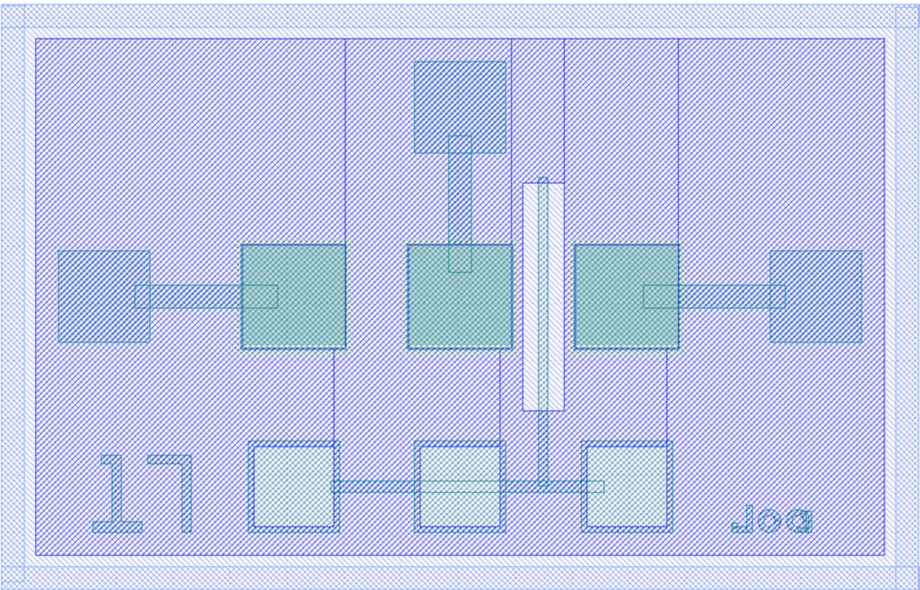


Figure 3.48: Layout for the SOI mask superimposed to previous masks.

Contrary to resonators, this process skips the TRENCH mask in order to preserve the 400-micron-thick substrate that will serve as a means of propagation for the acoustic pulses. Figure 3.49 is a cross-sectional representation of a pulse-echo device obtained by following the later steps.

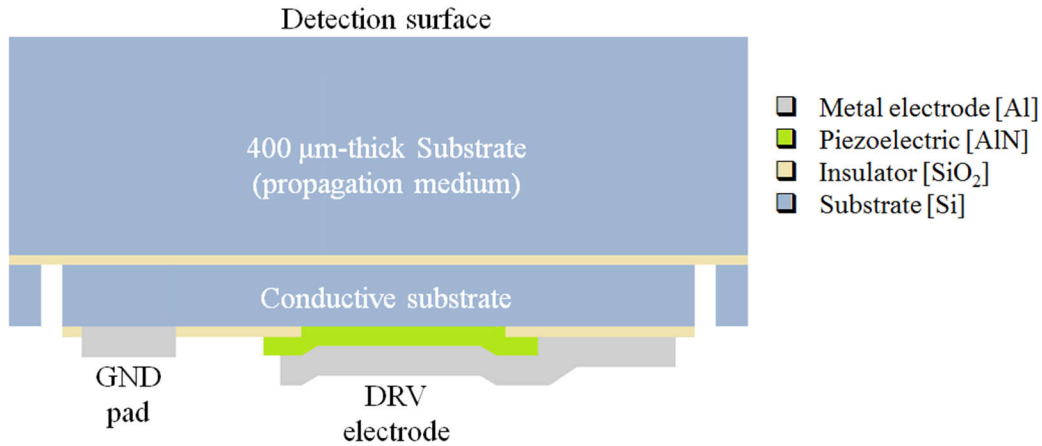


Figure 3.49: Cross-sectional representation of a pulse-echo transducer obtained with the design flow described in this section (not to scale)

Figure 3.50 is the whole 8 mm-side layout, containing both resonators (blue) and pulse-echo transducers (red) of different sizes, and arrays of these devices. Designs in the blue part of the layout have been drawn by Eyglis Ledesma to create piezoelectric flexural membranes, however, in this work they are used as solid resonators.

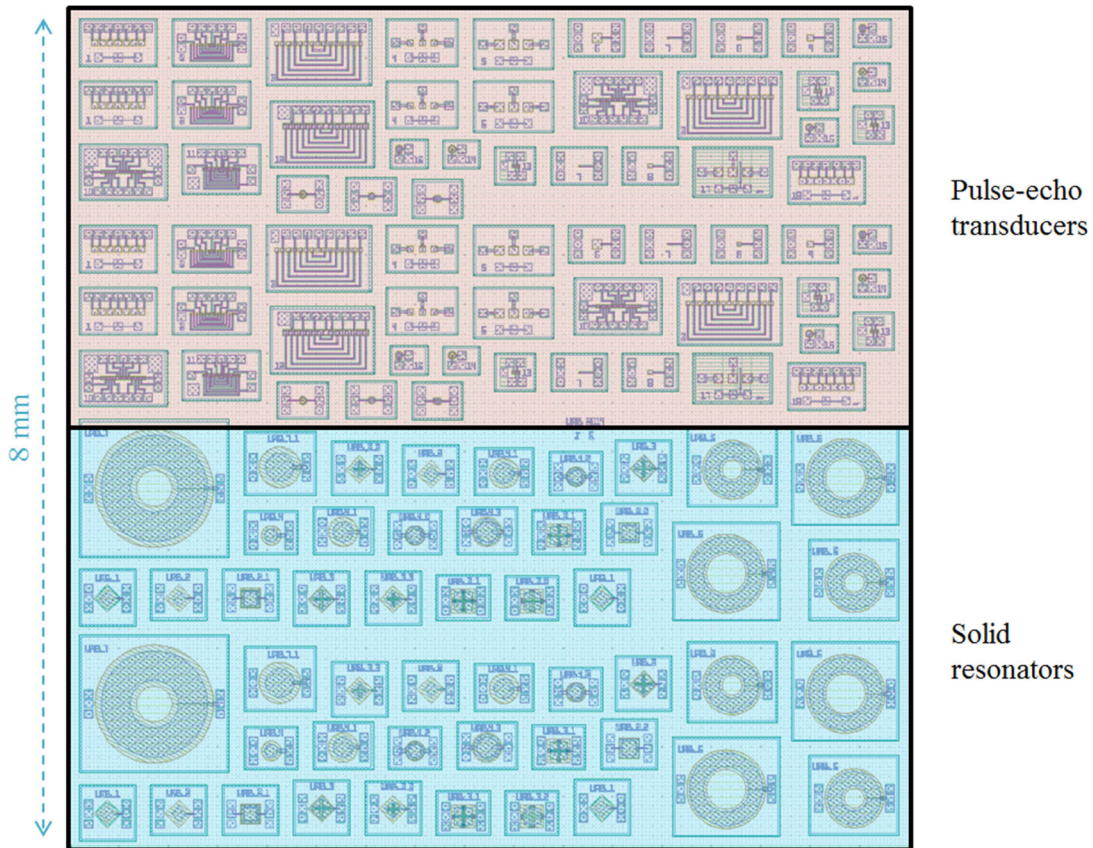


Figure 3.50: Layout to fabricate the 8 mm-side die, containing multiple cells. Designs in the blue part of the layout have been drawn by Eyglis Ledesma to create piezoelectric flexural membranes, however, in this work they are used as solid resonators.

References

- [1] Y.Q. Fu, J.K. Luo, N.T. Nguyen, A.J. Walton, A.J. Flewitt, X.T. Zu, Y. Li, G. McHale, A. Matthews, E. Iborra, H. Du, W.I. Milne, Advances in piezoelectric thin films for acoustic biosensors, acoustofluidics and lab-on-chip applications, *Progress in Materials Science*, vol. 89, pp. 31 – 91, 2017, <https://doi.org/10.1016/j.pmatsci.2017.04.006>
- [2] A. Mujahid, A. Afzal, and Franz L. Dickert, An Overview of High Frequency Acoustic Sensors—QCMs, SAWs and FBARs—Chemical and Biochemical Applications, *Sensors*, vol. 19, 2019, <https://doi.org/10.3390/s19204395>
- [3] Wei Pang, Hongyuan Zhao, Eun Sok Kim, Hao Zhang, Hongyu Yu, and Xiaotang Hu, Piezoelectric microelectromechanical resonant sensors for chemical and biological detection, *Lab on a Chip*, vol. 12 (1), pp. 29 – 44, 2012, <https://doi.org/10.1039/c1lc20492k>
- [4] Ioana Voiculescu and Anis Nurashikin Nordin, Acoustic wave based MEMS devices for biosensing applications, *Biosensors and Bioelectronics*, vol. 33, pp. 1 – 9, 2012, <https://doi.org/10.1016/j.bios.2011.12.041>
- [5] Y.Q. Fu, J.K. Luo, X.Y. Du, A.J. Flewitt, Y. Li, G.H. Markx, A.J. Walton, and W.I. Milne, Recent developments on ZnO films for acoustic wave based bio-sensing and microfluidic applications: a review, *Sensors and Actuators B: Chemical*, vol. 143, pp. 606 – 619, 2010, <https://doi.org/10.1016/j.snb.2009.10.010>
- [6] COMSOL Multiphysics (version 5.3a; COMSOL Inc: 2017)
- [7] J. Kestin, J.H. Whitelaw, The viscosity of dry and humid air, *International Journal of Heat and Mass Transfer*, vol. 7 , pp. 1245 – 1255, 1964, [https://doi.org/10.1016/0017-9310\(64\)90066-3](https://doi.org/10.1016/0017-9310(64)90066-3)
- [8] Owen Cramer, The variation of the specific heat ratio and the speed of sound in air with temperature, pressure, humidity, and CO₂ concentration, *The Journal of the Acoustical Society of America*, vol. 93, pp. 2510 – 2516, 1993, <https://doi.org/10.1121/1.405827>
- [9] Khasanshin, T.S., Aleksandrov, A.A., Thermodynamic properties of ethanol at atmospheric pressure, *Journal of Engineering Physics*, vol. 47, pp. 1046 – 1052, 1984, <https://doi.org/10.1007/BF00873717>
- [10] J Tong, M J W Povey, X Zou, B Ward and C P Oates, Speed of sound and density of ethanol-water mixture across the temperature range 10 to 50 degrees Celsius, *Journal of Physics: Conference Series*, vol. 279, 2011, <https://doi.org/10.1088/1742-6596/279/1/012023>
- [11] Khattab, I.S., Bandarkar, F., Fakhree, M.A.A. et al. Density, viscosity, and surface tension of water+ethanol mixtures from 293 to 323 K. *Korean Journal of Chemical Engineering*, vol. 29, pp. 812 – 817, 2012, <https://doi.org/10.1007/s11814-011-0239-6>
- [12] 3M Fluorinert Electronic Liquid FC-70, https://www.3m.com/3M/en_US/p/d/b40045189/, 2021, (accessed 2 July 2021)

- [13] L. M. Krutyanskiy, F. Zoueshtiagh, P. Pernod, P. Shirkovskiy & A. P. Brysev, Separation of two fractions of immiscible liquids by ultrasound in microgravity. *Physics of Wave Phenomena*, vol. 25, pp. 151 – 155, 2017, <https://doi.org/10.3103/S1541308X17020133>
- [14] J B Patterson and E C Morris, Measurement of Absolute Water Density, 1 °C to 40 °C, *Metrologia*, vol. 31, pp. 277, 1994, <https://doi.org/10.1088/0026-1394/31/4/001>
- [15] Nykolai Bilaniuk and George S. K. Wong, Speed of sound in pure water as a function of temperature, *The Journal of the Acoustical Society of America*, vol. 93, 1609 – 1612, 1993, <https://doi.org/10.1121/1.406819>
- [16] Joseph Kestin, Mordechai Sokolov, and William A. Wakeham , Viscosity of liquid water in the range –8 °C to 150 °C, *Journal of Physical and Chemical Reference Data*, vol. 7, pp. 941 – 948, 1978, <https://doi.org/10.1063/1.555581>
- [17] Nian-Sheng Cheng, Formula for the Viscosity of a Glycerol–Water Mixture, *Industrial & Engineering Chemistry Research*, vol. 47, pp. 3285 – 3288, 2008, <https://doi.org/10.1021/ie071349z>
- [18] Ana P.V. Egas, Nieves M.C. Talavera-Prieto, Abel G.M. Ferreira, Jaime B. Santos, Mário J. Santos, Zaida L. Almeida, Isabel M.A. Fonseca, Speed of sound and derived thermodynamic properties of glycerol, *The Journal of Chemical Thermodynamics*, vol. 156, 2021, <https://doi.org/10.1016/j.jct.2020.106367>
- [19] IEEE Standard on Piezoelectricity, ANSI/IEEE Std 176-1987, 1988, <https://doi:10.1109/IEEESTD.1988.79638>
- [20] J. Yanez, A. Uranga and N. Barniol, Multi-frequency thin film HBAR microsensor for acoustic impedance sensing over the GHz range, 21st International Conference on Solid-state sensors, Actuators and Microsystems (Transducers), pp. 1347 – 1350, 2021, <https://doi.org/10.1109/Transducers50396.2021.9495750>
- [21] PiezoMUMPs Design Handbook, http://www.memscapinc.com/_data/assets/pdf_file/0020/5915/PiezoMUMPs.DR.1.3a.pdf, 2012, (accessed May 26, 2022)
- [22] O. C. Zienkiewicz, R. L. Taylor, and J. Z. Zhu, *The Finite Element Method: Its Basis and Fundamentals* (Seventh Edition), Butterworth-Heinmann, 2013
- [23] COMSOL Multiphysics - Simulation Software, <https://www.comsol.com/comsol-multiphysics>, 2022, (accessed May 26, 2022)
- [24] Perfectly Matched Layers (PMLs), https://doc.comsol.com/5.5/doc/com.comsol.help.aco/aco Ug_pressure.05.106.html, 2021, (accessed May 26, 2022)
- [25] Acoustic-Structure Interaction with a Perfectly Matched Layer (PML), https://www.comsol.com/model/download/1000971/acoustic_structure_PML_60.pdf, 2012, (accessed May 26, 2022)

- [26] Meshing (Resolving the Waves), using Lagrange and Serendipity elements & meshing the perfectly matched layer (PML), https://doc.comsol.com/5.5/doc/com.comsol.help.aco/aco Ug_pressure.05.101.html, 2021, (accessed May 26, 2022)
- [27] Setup and meshing of Infinite Elements, Perfectly Matched Layers and Absorbing Layers, <https://www.comsol.com/support/knowledgebase/1272>, 2022, (accessed May 26, 2022)
- [28] Nian Li, Bin Wang, and Zhenghua Qian, Suppression of Spurious Lateral Modes and Undesired Coupling Modes in Frame-Like FBARs by 2-D Theory, IEEE Transactions on Ultrasonics, Ferroelectrics, and Frequency Control, vol. 67 (1), pp. 180 – 190, 2020, <https://doi.org/10.1109/TUFFC.2019.2942343>
- [29] Time Steepling in Transient Models, https://doc.comsol.com/5.5/doc/com.comsol.help.aco/aco Ug_pressure.05.103.html, 2021, (accessed May 26, 2022)
- [30] Resolving time-dependent waves, <https://www.comsol.com/support/knowledgebase/1118>, 2022, (accessed May 26, 2022)
- [31] MEMSCAP program: <http://www.memscap.com/products/mumps/piezomumps>, 2022, (accessed May 26, 2022)
- [32] Biswal, P., Kar, S.K. & Mukherjee, B. Design and Optimization of High-Performance through-hole Based MEMS Energy Harvester Using PiezoMUMPs. Journal of Electronic Materials, vol. 50, pp. 375 – 388, 2021, <https://doi.org/10.1007/s11664-020-08528-6>
- [33] S. Hashwan, M. Khir, Y. Al-Douri, A. Ahmed, A. Algamili, S. Alabsi, and M. Junaid, Analytical Modeling of AIN-Based Film Bulk Acoustic Wave Resonator for Hydrogen sulfide Gas detection Based on PiezoMUMPs, Journal of Physics: Conference Series, vol. 1962, 2021, <https://doi.org/10.1088/1742-6596/1962/1/012003>
- [34] J. A. Balasingam, S. Swaminathan, and A. Emadi, A Low-Frequency Piezoelectric Micromachined Ultrasonic Transducer Based on Multi-User MEMS Process with Enhanced Output Pressure, 2020 IEEE International Ultrasonics Symposium (IUS), pp. 1 – 4, 2020, <https://doi.org/10.1109/IUS46767.2020.9251361>
- [35] A. Rahaman, A. Ishfaque and B. Kim, Effect of Torsional Beam Length on Acoustic Functionalities of Bio-Inspired Piezoelectric MEMS Directional Microphone, IEEE Sensors Journal, vol. 19 (15) , pp. 6046 – 6055, 2019, <https://doi.org/10.1109/JSEN.2019.2909501>
- [36] M. Ruppert, S. Moore, M. Zawierta, A. Fleming, G. Putrino, and Y. Yong, Multimodal atomic force microscopy with optimized higher eigenmode sensitivity using on-chip piezoelectric actuation and sensing, Nanotechnology, vol. 30, 2019, <https://doi.org/10.1088/1361-6528/aae40b>
- [37] Design Rules PiezoMUMPs: <http://www.memscap.com/products/mumps/piezomumps>, 2022, (accessed May 26, 2022)

Characterization & Experimental Setup

Figure 4.1a is an optical image of a manufactured die at MEMSCAP. As a first step, an optical inspection (microscope) was carried out to identify possible short circuits caused by incorrect alignment of the stacked materials over the conductive silicon substrate.

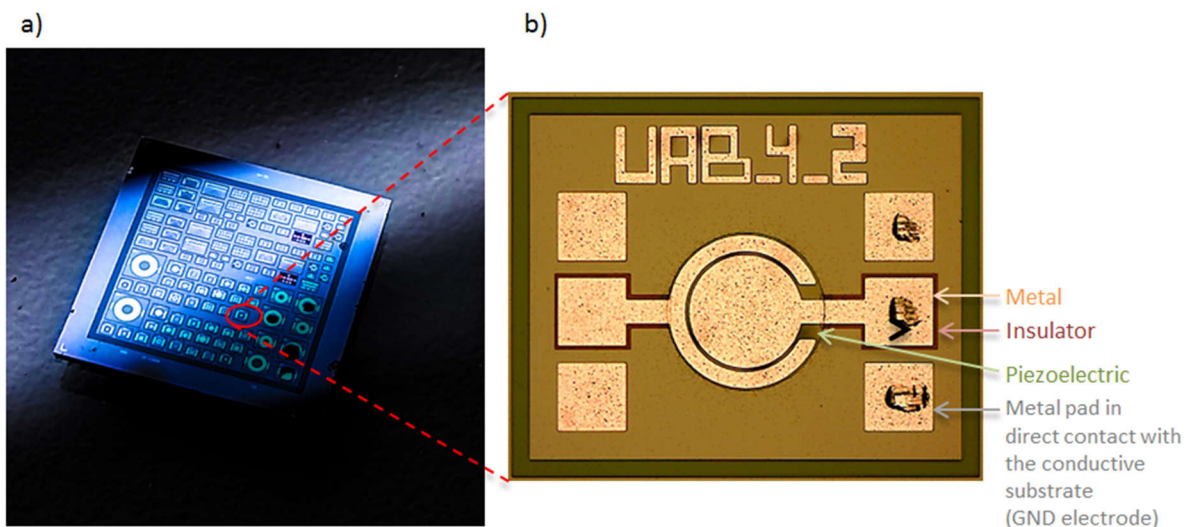


Figure 4.1: a) Optical image of a manufactured die containing multiple cells of different designs. b) Optical image of a single cell containing a device meant to work as resonator; this device consists of a central Tx element surrounded by a Rx element (Only the central resonator is used for the purposes of this thesis).

Figure 4.1b is an optical image of one of the manufactured devices. The circular metal element in the center is the DRV electrode of the resonator, whose pad (on the right) lies over an insulating layer that prevents contact with the conductive substrate. Below the circular DRV electrode is the upper face of the piezoelectric element, while the opposite face of the piezoelectric is in contact with the conductive substrate (acting as the GND electrode). Pads in direct contact with the conductive substrate allow connection to ground reference.

4.1 Electrical Characterization for Acoustic Resonators

4.1.1 Measurement of scattering parameters

Thin film acoustic resonators are typically characterized with a vector network analyzer (VNA), obtaining measurement of their scattering parameters (S_{ij}) [1]. S-parameters are complex numbers, having real and imaginary parts or magnitude and phase parts, they provide a relationship between the incident wave and the reflected and transmitted waves at each port of a network over a range of frequencies. In contrast to the impedance, admittance, and hybrid parameters, the scattering parameters do not require short-circuiting neither open circuiting input and output ports; instead, these ports are terminated in fixed and known characteristic impedances used as reference.

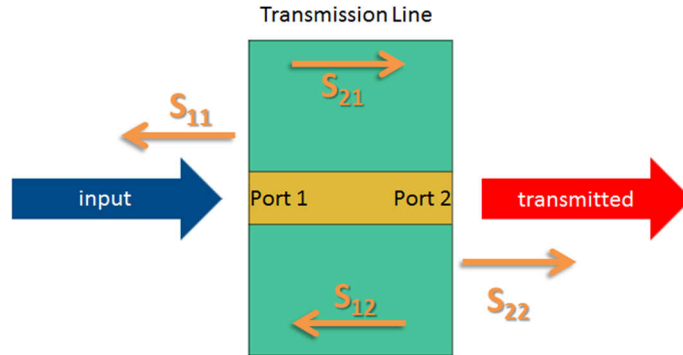


Figure 4.2: Example of a 2-port network. Analysis of S-parameters provides a relationship between the incident wave and the reflected and transmitted waves at each port over a range of frequencies.

S-parameters are usually displayed in a matrix format, with the number of rows and columns equal to the number of ports. For the S-parameter S_{ij} the j subscript stands for the port that is excited (the input port), and the i subscript is for the output port (Figure 4.2). Since a "1-port" measurement represents the ratio of the reflected wave to the incident wave, the value of S_{11} provides a direct measure of the port matching condition, that is, $S_{11} = 0$ (no reflection) represents perfectly matching between the device and the reference. As the static impedance of the acoustic resonator designed in Chapter 3 was intended to be close to 50-ohm @ 1.1 GHz, an S_{11} sweep around 1.1 GHz should remain close to 0 dB except for the resonance point, where the impedance value abruptly moves away from the reference value, allowing characterization of the resonant frequency of the device under test (DUT). Figure 4.3 is a schematic describing connections for measurements in resonators.

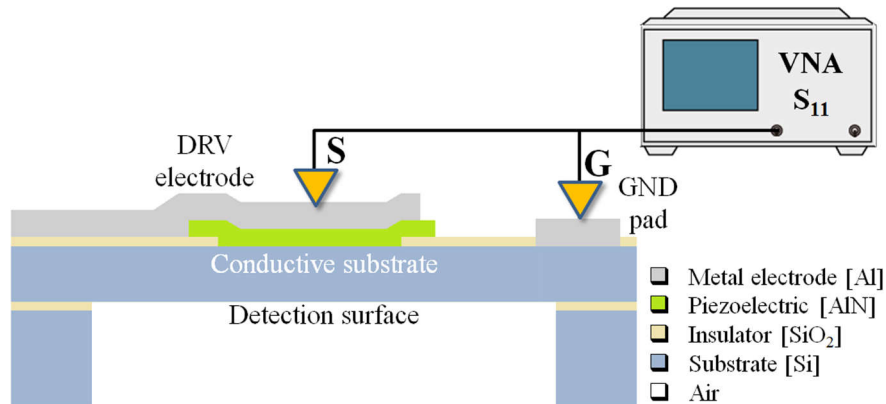


Figure 4.3: Schematic describing connections for S_{11} measurements in resonators; the signal terminal S is connected to the DRV electrode whereas the G terminal is connected to the GND pad.

One of the manufactured dies, such as the one shown in Figure 4.1a, has been laid over the Süss MicroTec PM8 probe station and the selected DUT was connected to the Agilent E5071B Network Analyzer through one of the GSG probes shown in Figure 4.4a. The probe used is a $|Z|$ -Probe Z040-K3N-GSG-100, with a pitch of 100 μm .

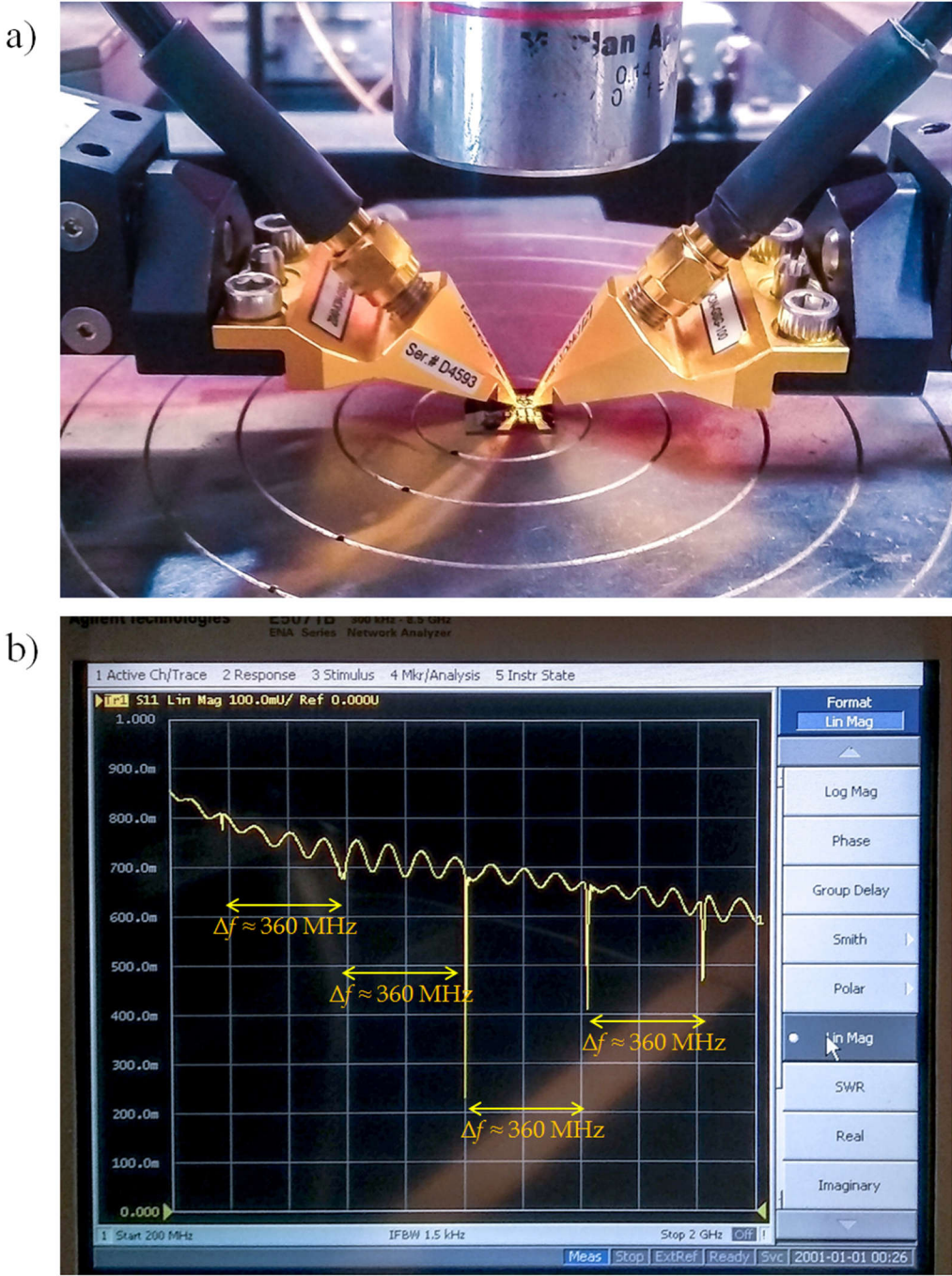


Figure 4.4: a) One of the dies rests on the Probe Station to extract the S_{11} measurement of the resonating device, using the GSG probe at the left. b) Screenshot of the Network Analyzer during a measurement of the resonator's Linear Magnitude of S_{11} , from 200 MHz to 2 GHz (uncalibrated).

Figure 4.4b is a screenshot of the VNA throughout a measurement of the Linear Magnitude of S_{11} . This frequency sweep from 0.2 to 2 GHz validates the analytical prediction in Figure 3.9, where resonances should appear roughly every 360 MHz due to materials and thicknesses used to construct these devices. In addition to the expected resonance peaks, the S_{11} trace in Figure 4.4b shows an oscillatory parasitic behavior due to the contribution of the cables and connectors used. Procedure for measurement calibration (to remove parasitic contributions from cables and connectors) and the conversion from S_{11} to Input Impedance Z_{in} are performed in the section 4.2, once the die is wire bonded to the carrier waveguide.

4.1.2 Measurement of electromechanical coupling k_{eff}^2

The S_{11} measurement in Figure 4.4 verifies another unique feature of the manufactured devices; the presence of modes with high amplitude at frequencies far from the piezoelectric resonance (10.9 GHz), such as the case of the resonance seen at 1.1 GHz. Equation 22 has been used to quantize the electromechanical coupling of each harmonic [2]:

$$k_{eff}^2(m) = \frac{f_p^2(m) - f_s^2(m)}{f_p^2} \quad (22)$$

With $f_p(m)$ and $f_s(m)$ as the m -order parallel and series resonant frequencies. Based on the IEEE Standard the parallel resonance frequencies f_p are calculated when the real part of the impedance goes to a maximum and the series resonance frequencies f_s are calculated when the real part of the admittance goes to a maximum. The complex impedance of the resonator is calculated with [3]:

$$Z_{in} = Z_0 \frac{1 + S_{11}}{1 - S_{11}} \quad (23)$$

The analytical plot in Figure 4.5 presents the expected behavior of k_{eff}^2 for both the case of an HBAR consisting of a 0.5 μm -thick AlN layer over a 10 micron silicon substrate and electrodes of negligible thickness and the case of the manufactured device (1 μm -thick Al electrode), up to 14 GHz.

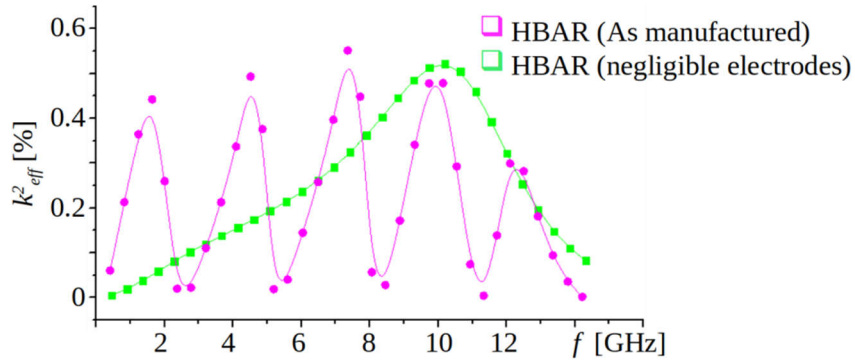


Figure 4.5: Analytical comparison of effective coupling of an ideal HBAR with electrodes of negligible thickness (green) and an HBAR with dimensions corresponding to the manufactured device (magenta) [4].

The case of negligible electrodes (green) exhibits small values of k_{eff}^2 for low frequency modes and a maximum value in modes close to the piezoelectric resonance f_0 . Contrary, a different distribution of the magnitude of k_{eff}^2 is identified for the modes in the resonator with dimensions similar to the manufactured device (magenta), spotting oscillation between maximum and minimum values of electromechanical coupling throughout the operative range. To verify analytical predictions, S-parameter measurement of each of the first 20 modes (0 to 7 GHz) was performed individually, then, S-parameter to impedance conversion was performed using equation 23 to obtain the series and parallel resonant frequencies of each mode, and equation 22 was used to obtain Figure 4.6.

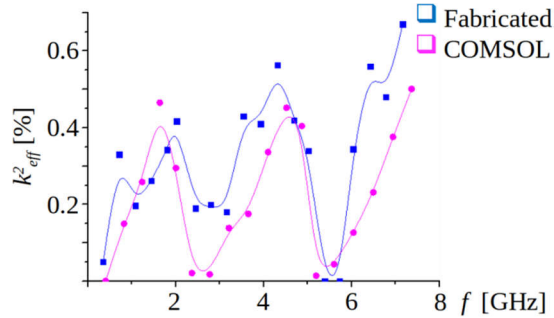


Figure 4.6: Comparing magnitude of k_{eff}^2 between FEM simulations (magenta) and experimental (blue) [4].

Figure 4.6 shows the magnitude of k_{eff}^2 (blue trace) calculated from measurement data for each mode, using equation 22. Results agree with analytical predictions in Figure 4.5. Figure 4.6 is also complemented with results from FEM simulations using COMSOL Multiphysics (magenta). Experimental results in Figure 4.6 verify capability of multi-frequency operation while maintaining reasonable electromechanical transduction [4].

4.2 Carrier waveguide, S_{11} measurement calibration, and S_{11} to Z conversion

4.2.1 Design of the carrier PCB (Grounded Coplanar Waveguide)

For liquid sample detection tasks, the die must be placed upside down since the resonant device and its corresponding detection surface are on opposite faces of the wafer, this makes it impossible to carry out measurements with the probe station as shown in Figure 4.7a, where the probes are placed directly on the resonator pads and the detection surface faces downwards. Figure 4.7b shows the proper orientation of the die to take measurements of liquid samples.

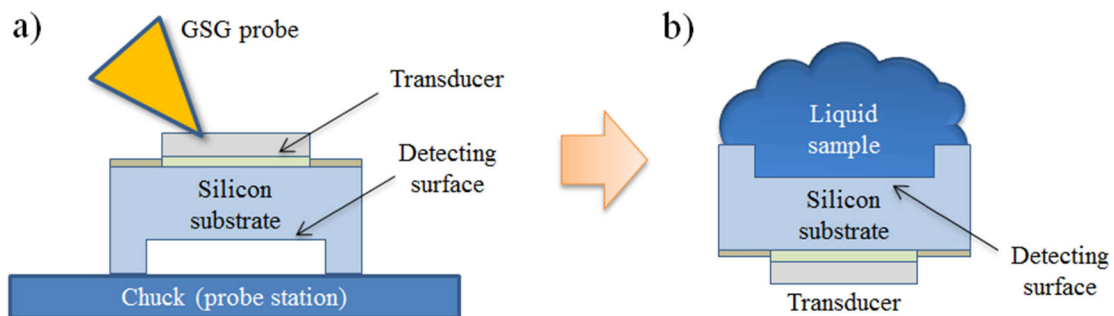


Figure 4.7: a) Transducers, vias and pads face upwards for characterization with S_{11} measurements. b) The manufactured die must be flipped upside down to carry out interaction with liquid samples, this makes impossible direct measurements using the probe station and GSG probes.

Figure 4.8a shows the concept of the carrier waveguide to connect resonators directly to the Network Analyzer. It consists of a Grounded Coplanar Waveguide (GCPW) with an SMA connector; the hole at the center allows interaction between liquid samples and the detecting surface of the silicon die as indicated in the 2D sagittal view of Figure 4.8b:

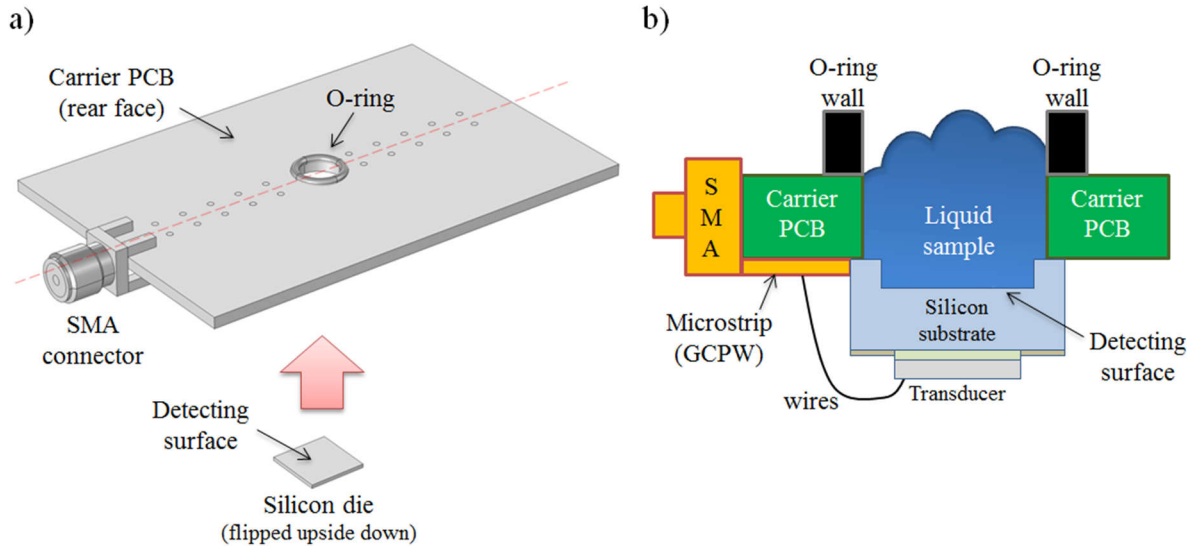


Figure 4.8: a) The squared silicon die of side equals to 8 mm is glued to the front face of the carrier PCB and wire bonded to a grounded coplanar waveguide. A hole in the rear face (enclosed by an o-ring with diameter equal to 6 mm) allows containment of liquid samples and interaction with the detecting surface of the chip. b) 2D sagittal representation of the concept: the silicon die remains glued to the front face of the carrier PCB and it is wire bonded to the waveguide which leads to the SMA connector. The opposite face of the PCB has an o-ring to contain liquid samples that are in direct contact with the detection surface.

The GCPW is a type of electrical planar transmission line which consists of a single conducting track (Signal) printed onto a dielectric substrate, together with a pair of return conductors (Ground), one to either side of the track. All three conductors are on the same side of the substrate while the opposite face of the PCB is completely covered by a reference ground plane (Figure 4.9).

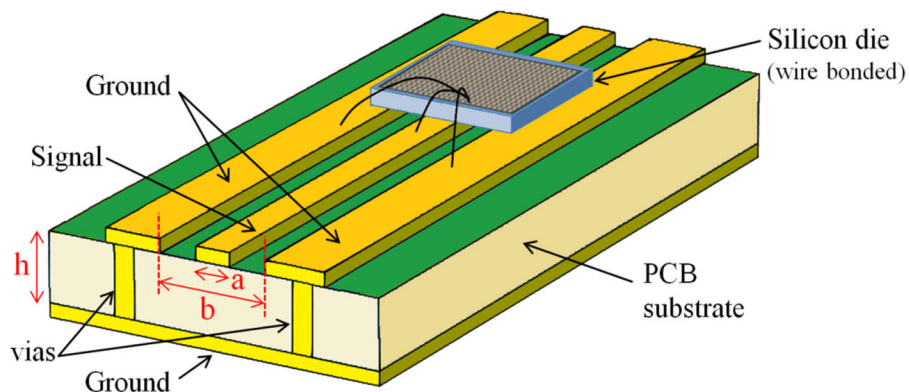


Figure 4.9: 3D representation of the Grounded Coplanar Waveguide carrying the silicon die (wire bonded). This representation is flipped upside up (respect to Figure 4.8) to improve visualization of the waveguide.

Where 'a' is the width of the Signal conductor, 'b' is separation between the coplanar Ground planes and 'h' is the thickness of the substrate. To prevent it from acting as a microstrip, it is

recommended that $h > b$, and $b < \lambda/2$ to avoid propagation of higher modes [5]. Assuming that a quasi-static TEM mode propagates in this structure, the effective dielectric constant ϵ_{eff} and the characteristic impedance of the waveguide Z_0 are approximated with [6].

$$Z_0 = \frac{60\pi}{\sqrt{\epsilon_{eff}}} \frac{1}{\frac{K(k)}{K(k')} + \frac{K(k_3)}{K(k'_3)}} \quad (24)$$

With $k = a/b$; $k_3 = \tanh(\pi a/4h) / \tanh(\pi b/4h)$; $k' = \sqrt{1.0 - k^2}$; $k'_3 = \sqrt{1.0 - k_3^2}$; and:

$$\epsilon_{eff} = \frac{1 + \epsilon_r \frac{K(k') K(k_3)}{K(k) K(k'_3)}}{1 + \frac{K(k') K(k_3)}{K(k) K(k'_3)}}$$

Where $K(k)$ is the complete elliptic integral of the first kind. Although there are plenty of combinations of 'a', 'b' and 'h' leading to a 50-ohm characteristic impedance; $h = 1.6$ mm was used since it is the standard substrate width offered by the local PCB manufacturer 2CISA [7], while $a = 1.6$ mm was selected for its convenience when soldering the SMA connector. Selecting $b = 0.3$ mm results in $Z_0 = 52 \Omega$. In Figure 4.10a one of the resonators is wire bonded to the coplanar waveguide; it shows a silicon die attached to the manufactured waveguide. In Figure 4.10b the carrier PCB is connected directly to the Network Analyzer to perform S_{11} measurements; a frequency sweep from 200 MHz to 2 GHz reveals the expected resonance peaks every 360 MHz.

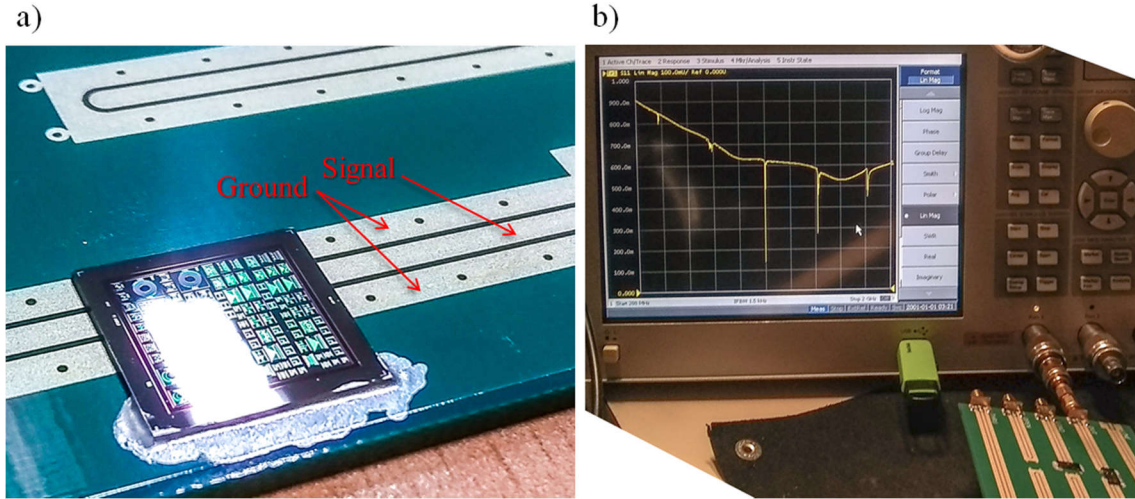


Figure 4.10: a) One of the resonators is wire bonded to the coplanar waveguide manufactured at 2CISA. b) This carrier PCB is connected directly to the Network Analyzer to perform S_{11} measurements; a linear frequency sweep from 200 MHz to 2 GHz reveals the expected resonance peaks every 360 MHz.

4.2.2 S_{11} measurement calibration (de-embedding)

De-embedding is a procedure that consists of modeling contributions of all the elements present between the VNA and the DUT (cables, connectors, waveguides, etc.) and then mathematically remove those contributions in order to isolate the DUT response [8]. Among the different de-

embedding procedures, the Open-Short de-embedding methodology has been selected because it is simpler, widely used in the industry for semiconductor characterization and it offers sufficient accuracy for frequencies below to 30 GHz [9]. In this approach it is assumed that all parallel parasitic components are located in the Signal pads (conductances) and all the series parasitic are located in the interconnect lines (inductances), as indicated in Figure 4.11:

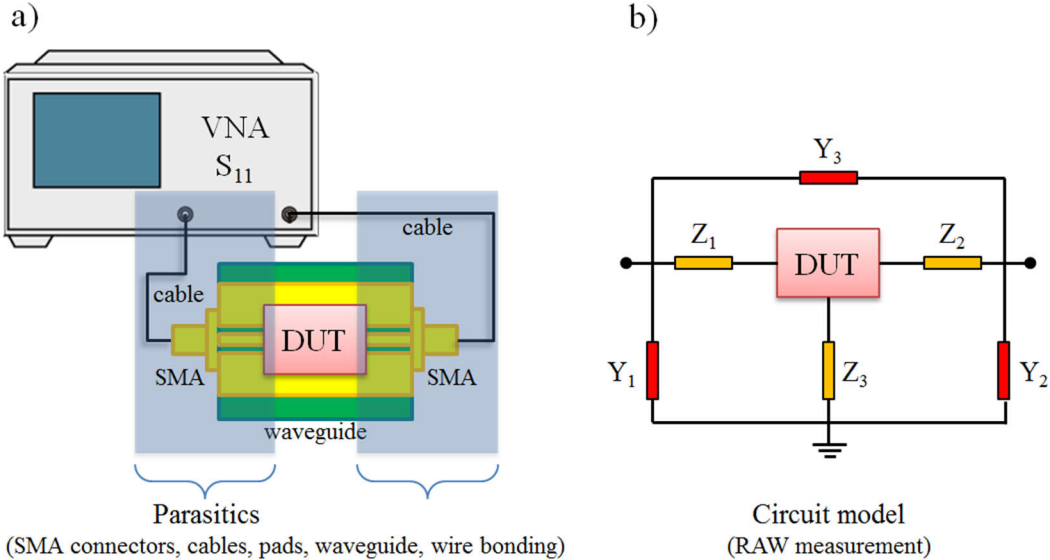


Figure 4.11: a) Schematic of the measurement system; cables, connectors, pads and the waveguide itself add parasitic contributions to the measurement. b) Circuit model for the measurement setup, modeling parallel parasitic components as "conductances" and series parasitics as "inductances".

To move the reference plane of the measurements to the DUT (de-embedding procedure), it is necessary to add two dummy structures to the carrier PCB:

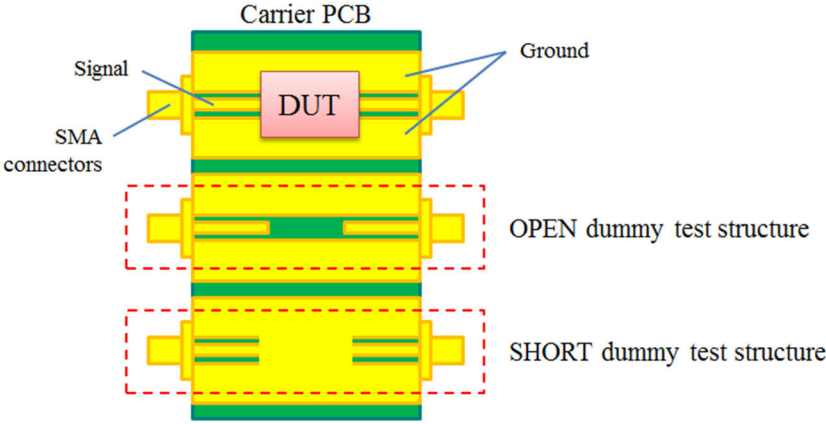


Figure 4.12: Schematic of the carrier PCB; a couple of dummy structures are added to carry out the de-embedding procedure. The OPEN structure simply removes the DUT from the waveguide, while in the SHORT structure all the terminals are short-circuited.

To implement the OPEN dummy, an identical waveguide to the one carrying the DUT is created; this transmission line is kept open (without any DUT installed). On the other hand, to create the SHORT dummy all the terminals of a similar waveguide (Ground-Signal-Ground) are shorted together. Figure 4.13 offers a graphic description of the Open-Short de-embedding procedure: As a

first step, measurements of the system described in Figure 4.11a are obtained, that is, a “raw” measurement including parasitic contributions from cables, connectors and the waveguide.

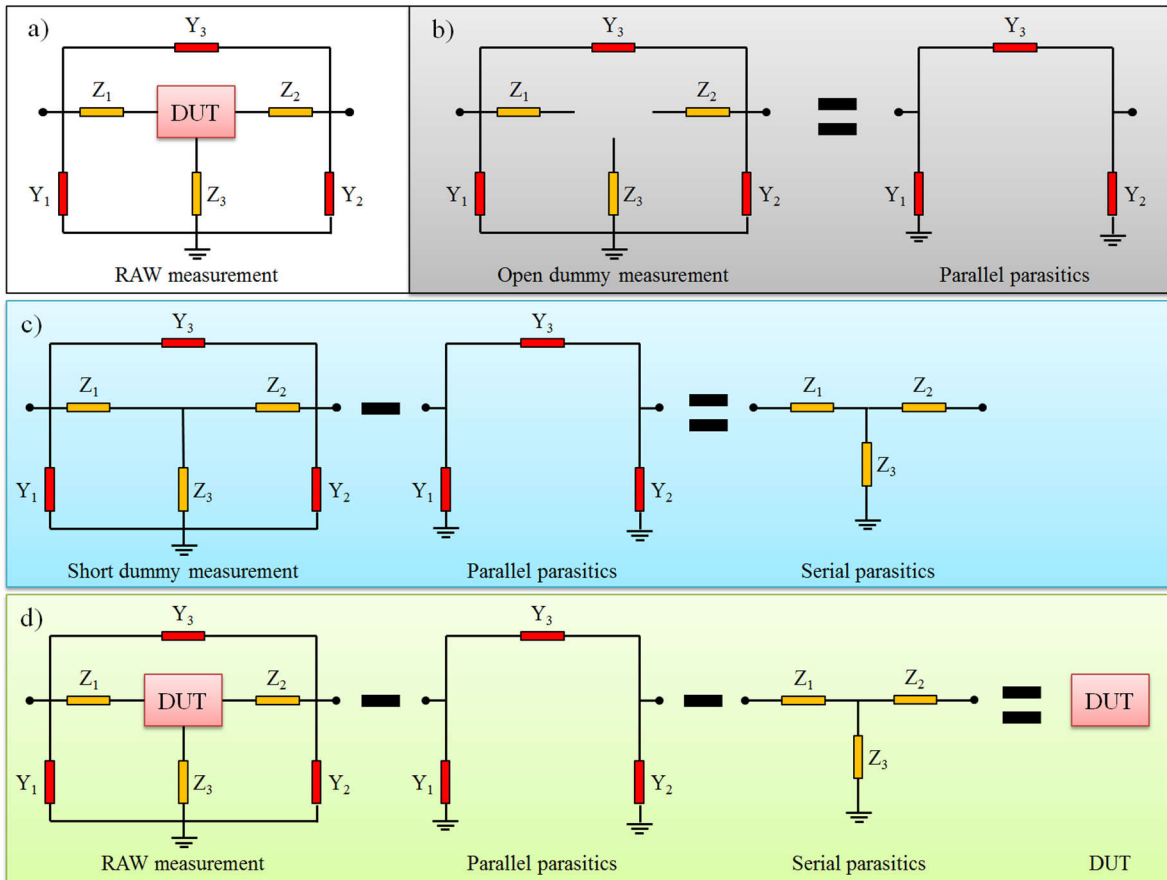


Figure 4.13: Equivalent circuit models for Open-Short de-embedding. a) Circuit model for a “raw” measurement; it includes the Device Under Test (DUT), and parasitic contributions from connectors, pads, waveguide, etc. b) Circuit model for OPEN dummy test structure; it helps to reveal parallel parasitics. c) Circuit model for SHORT dummy test structure; serial parasitics are obtained subtracting the parallel parasitics from the SHORT measurement. d) Both the parallel parasitics and the serial parasitics are mathematically subtracted from the RAW measurement (Figure 4.13d), moving the reference plane from the VNA ports to the DUT plane.

Figure 4.13b indicates how parallel parasitics are obtained by measuring the OPEN dummy test structure. As a third step the serial parasitics are obtained by measuring the SHORT dummy test structure and with their mathematical subtraction against the previously obtained parallel parasitics (Figure 4.13c). Then both the parallel parasitics and the serial parasitics are mathematically subtracted from the RAW measurement (Figure 4.13d), moving the reference plane from the VNA ports to the DUT plane.

To perform de-embedding in the resonant mode close to 1.1 GHz, the waveguide carrying the DUT has been connected directly to the Network Analyzer (as shown in Figure 4.10b) and the S_{11} measurement has been obtained from 1.064 to 1.104 GHz, with a 25 kHz step. These readings (real and imaginary) were labeled as "RAW measurement", since they include measurement of the DUT, cables, pads and waveguide. Subsequently, the same procedure was carried out for the OPEN and

SHORT dummy test structures of the carrier PCB to obtain "OPEN measurement" and "SHORT measurement", respectively. The reflection factor Γ_{RAW} for the waveguide combined with the DUT is [10]:

$$\Gamma_{RAW} = S_{11} + \frac{S_{12}S_{21}\Gamma_{DUT}}{1 - S_{22}\Gamma_{DUT}}$$

Where Γ_{DUT} is the isolated reflection coefficient of the DUT. Assuming the symmetry condition $S_{11} = S_{22}$ for a 1-port DUT, the reflection coefficient Γ_{DUT} is [11]:

$$\Gamma_{DUT} = \frac{A - \Gamma_{RAW}}{A^2 - A\Gamma_{RAW} - B} \quad (25)$$

Where:

$$A = \frac{\Gamma_{OPEN} + \Gamma_{SHORT}}{2 + \Gamma_{OPEN} - \Gamma_{SHORT}}$$

$$B = (\Gamma_{OPEN} - A)(1 - A)$$

Figure 4.14 compares the magnitude of the "RAW measurement" against the magnitude of the reflection coefficient Γ_{DUT} obtained in MATLAB from equation 25 and the RAW, OPEN and SHORT measurements (*.csv files).

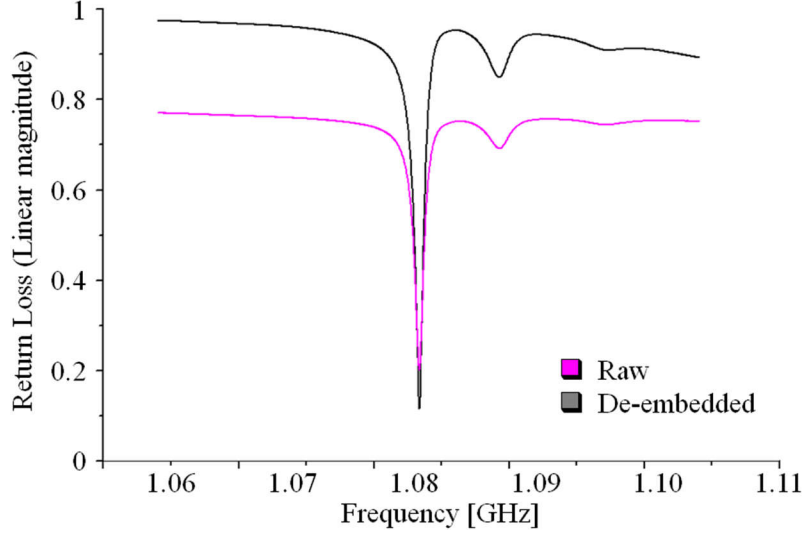


Figure 4.14: Magnitude of S_{11} measurements obtained from 1.064 to 1.104 GHz (25 kHz step) to reveal the third mode of the resonating device shown in Figure 4.3 (side = 120 μm); the trace corresponding to the de-embedded measurement (black) is closer to reference as expected.

4.2.3 Conversion from S_{11} to Z_{in}

Once parasitic contributions from cables, connectors, waveguide, etc. have been removed, a MATLAB script uses equation 23 to obtain the input impedance Z_{in} from the files containing the S_{11} measurement of the DUT:

$$Z_{in} = Z_0 \frac{1 + S_{11}}{1 - S_{11}}$$

Where S_{11} is the S_{11} measurement after the de-embedding process and $Z_0 = 50 \Omega$ is the reference impedance. Figure 4.15 shows the magnitude of Z_{in} for the third mode of the designed squared resonator of side equal to $120 \mu\text{m}$.

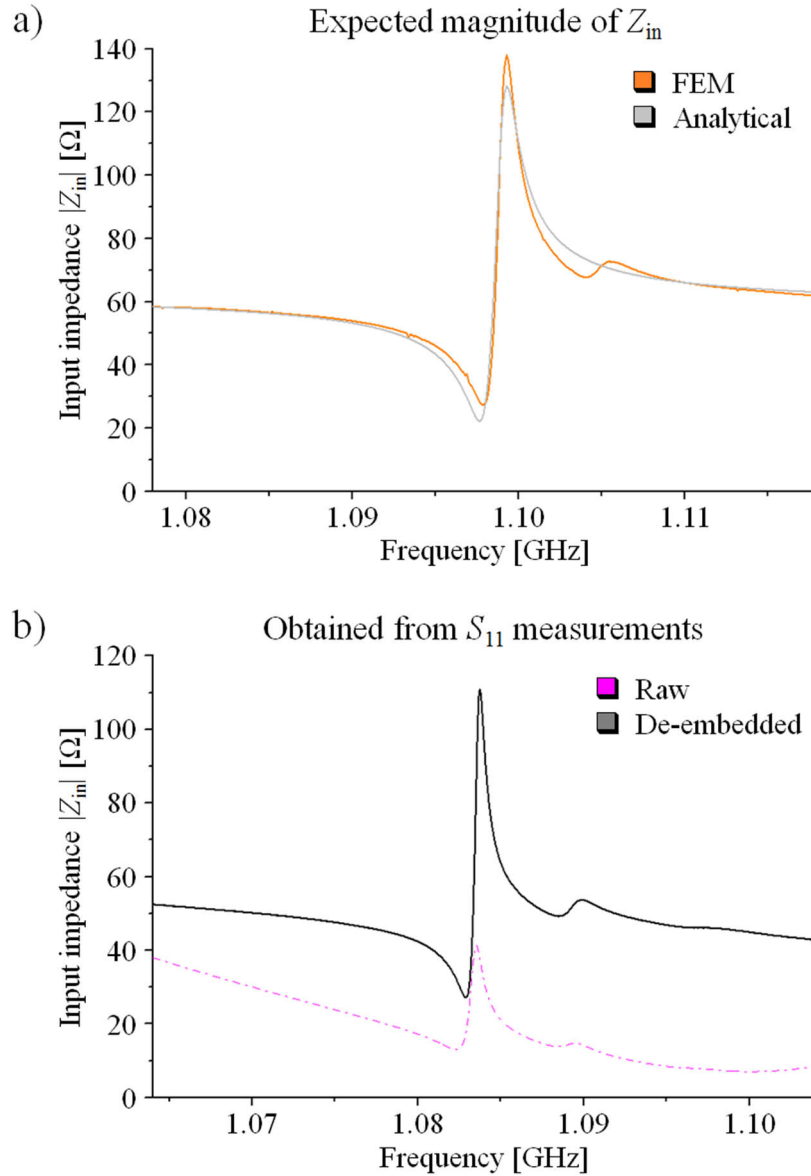


Figure 4.15: Input impedance Z_{in} for the third mode of the designed squared resonator of side = $120 \mu\text{m}$.
a) Expected magnitude of Z_{in} (analytical & FEM). b) Magnitude obtained from S_{11} measurements.

The dashed magenta trace in Figure 4.15b corresponds to the combination of equation 23 and the "RAW" S_{11} measurement, while the black trace was obtained from the combination of equation 23 and the "de-embedded" measurement. When comparing to the expected curves in Figure 4.15a, the black trace boasts a significant improvement over its magenta counterpart. The latter confirms that resonating devices work as expected; the input impedance of the manufactured devices presents

resonant modes separated by ~ 360 MHz, and the selection of materials and thicknesses allow the existence of high resonance peaks from 1 GHz ($Z_{in} \approx 50 \Omega$). Measurements show agreement with both analytical predictions and Finite Element simulations. Figure 4.16 presents the real part of the third mode of the resonator.

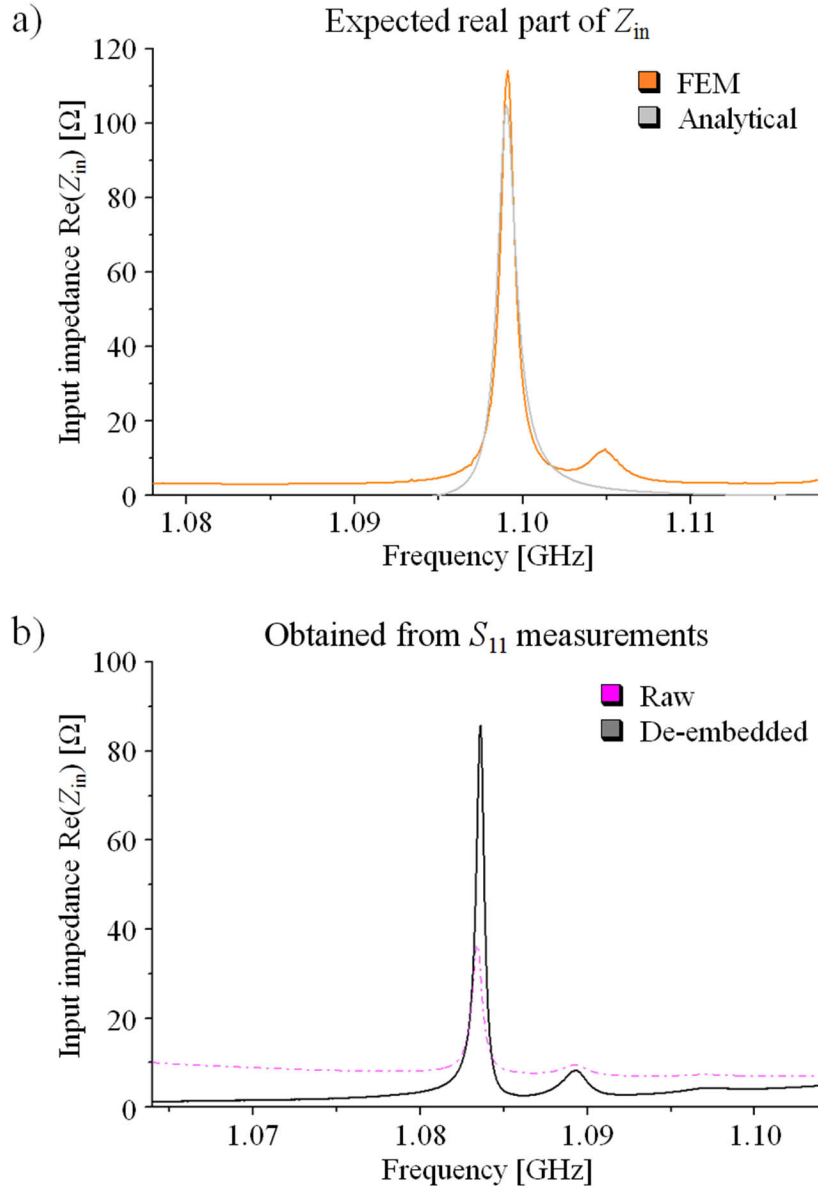


Figure 4.16: Real part of the Input impedance Z_{in} for the third mode of the designed squared resonator of side = $120 \mu\text{m}$. a) Expected real part of Z_{in} (analytical & FEM). b) Obtained from S_{11} measurements.

4.3 Electrical Characterization for the Pulse-echo Transducers

Although this device is designed to work in a pulse-echo scheme, that is, driven by a short train of RF pulses whose duration should be shorter than the time required to create standing waves in the structure, it is important to know the response of the structure operating as a resonator to discover frequency regions where would it be more favorable to operate (regions with greater electromechanical coupling). As seen in section 3.2.2 of Chapter 3, for the case of pulse-echo

transducers the silicon substrate is much thicker than the other layers ($t_{\text{subs}} = 400 \mu\text{m}$), and consequently the fundamental mode of this structure is approximated by:

$$\Delta f_0 = v_{\text{subs}} / [2 * t_{\text{subs}}] = 10.6 \text{ MHz}$$

With v_{subs} as the speed of sound in silicon equal to 8457 m/s. This should lead to the analytical dense spectrum presented in Figure 3.11 of Chapter 3, where small resonance peaks are expected to appear every 10.6 MHz. To verify this analytical prediction the squared transducer with side = 92 μm designed for the pulse-echo operation is wire bonded to the carrier waveguide and connected directly to the Network Analyzer to to perform S_{11} measurements:

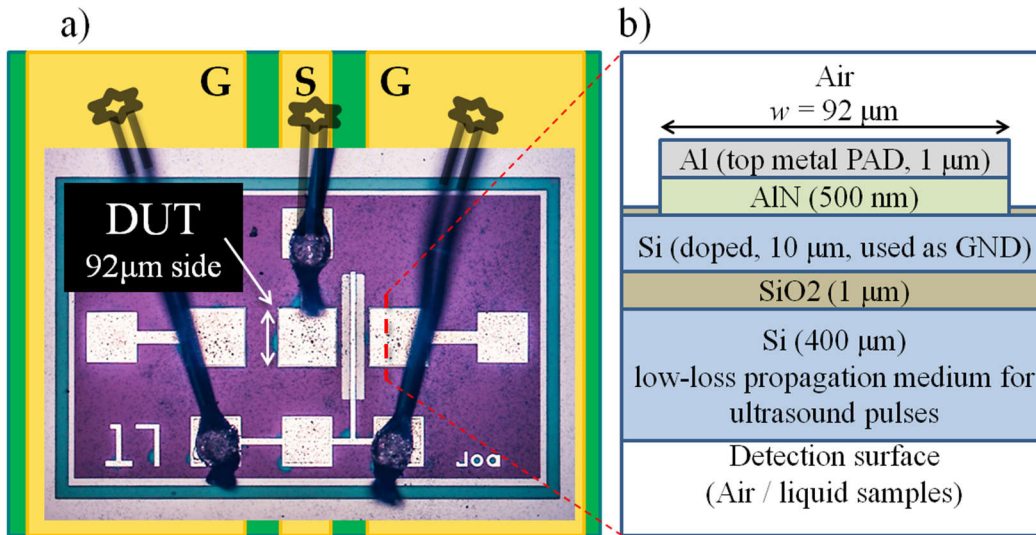


Figure 4.17: Representation of the DUT connected to the carrier waveguide to perform S_{11} measurements.

- a) Optical image of a manufactured 1-D linear array consisting of three HBAR structures; each square transducer is 92 μm wide and only the central element is connected to the waveguide representation. b) Cross section profile of the stack of materials used to fabricate each HBAR structure (this representation is not to scale and it is flipped upside up, showing the Al electrode first and sensing surface all the way down).

Figure 4.18 is a screenshot of the VNA throughout a measurement of the Linear Magnitude of S_{11} . This frequency sweep from 0.2 to 2 GHz validates the analytical prediction in Figure 3.11 of Chapter 3, where the electrical response for the pulse-echo transducers is a dense spectrum of resonances. The zoomed section enclosed in the red square present two consecutive resonances at 1.4029820 GHz and 1.4133133 GHz, separated by $\Delta f = 10.33 \text{ MHz}$, ratifying analytical predictions. Similar to resonant devices, the S_{11} measurement in Figure 4.18 reveals the presence of frequency regions where resonant modes show higher amplitude. This effect, predicted by equation 16 of Chapter 2 in Figure 3.11 and the FEM simulations in Figure 3.26 (Chapter 3), is caused due to ultrasound reflection in the internal layers of the device; as seen in Figure 4.17b, the Al electrode is twice as thick as the piezoelectric, therefore the mechanical energy produced by the active layer is immediately transferred to it and then reflected back to the piezoelectric because of the huge acoustic impedance difference with 'air' in the upper boundary. Additional partial reflection of the bulk acoustic wave is produced by the buried oxide layer due to the difference in acoustic impedance respect to silicon. In the next section is verified that these frequency spots with higher

amplitude modes also offer a significant increase in the effective electromechanical coupling k_{eff}^2 , improving transduction and providing the pulse-echo transducers with multi-frequency capability.

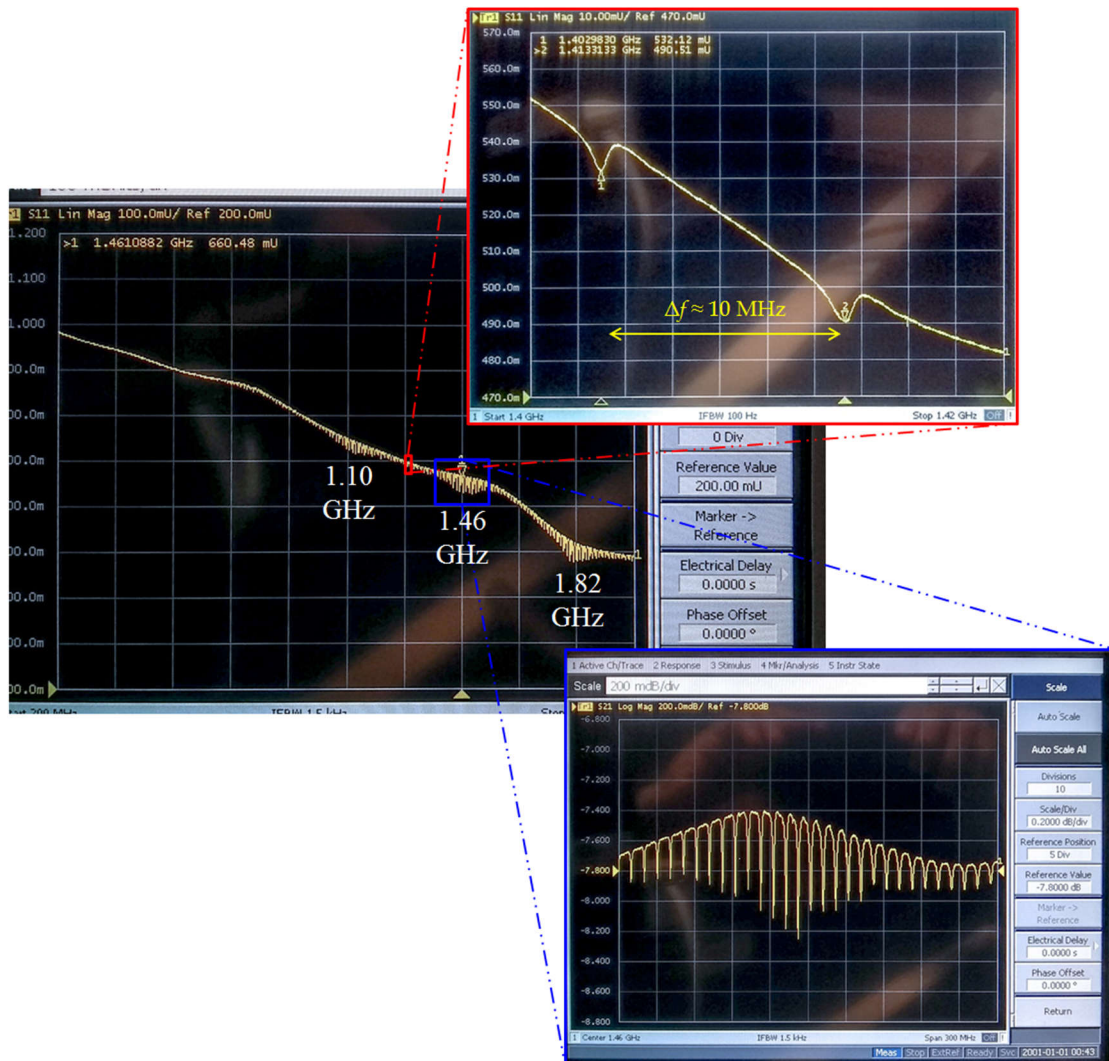


Figure 4.18: Screenshot of the Network Analyzer during a S_{11} measurement of the pulse-echo transducer (Linear Magnitude), from 200 MHz to 2 GHz (uncalibrated). The zoomed section enclosed in the red square present two consecutive resonances at 1.40298 GHz and 1.41331 GHz, separated by $\Delta f=10.33$ MHz, whereas the section enclosed in the blue square reveals frequency regions with higher amplitude modes.

4.4 Test Setup for pulse-echo transducers, Frequency & Time response, and Digital Filtering (post-processing)

4.4.1 Test setup for pulse-echo transducers

Prior to looking for frequencies where it is more favorable to operate the pulse-echo device, it is necessary to build a test setup that allows the transducer to send short ultrasound pulses through its silicon substrate and read the reflected echoes. Figure 4.19 offers a 2D representation of the detection mechanism of the pulse-echo transducer over the time.

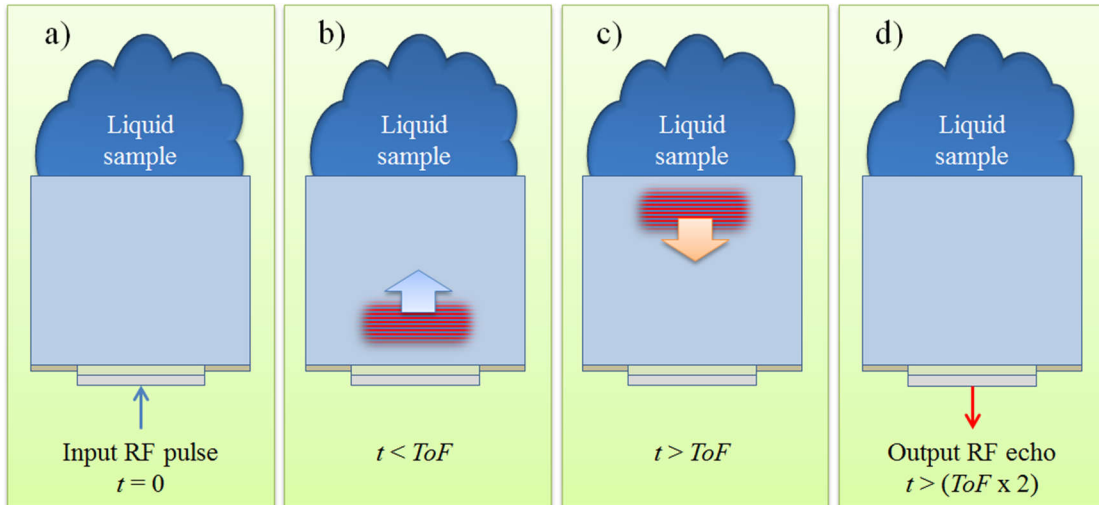


Figure 4.19: 2D representation of the detection mechanism for the pulse-echo transducer over the time. a) At $t = 0$ an input RF pulse is applied to the DRV electrode. b) The piezoelectric layer, operating in its thickness extension mode, produces a short pulse of longitudinal acoustic waves in the silicon bulk in response to the input RF pulse. c) At $t > ToF$ the acoustic pulse has already interacted with the liquid sample in the detection surface and has been reflected back towards the transducer. d) At $t > (2 * ToF)$ the acoustic pulse has completed a round trip through the wafer thickness and the piezoelectric produces an RF output signal in response to the received acoustic echo.

Since the Time-of-Flight (ToF) of longitudinal acoustic waves traveling across the thickness of the 400- μm silicon substrate is 48 ns, the purpose of the circuit is: a) To drive the AlN transducer with an RF pulse whose duration should be lower than 48 ns to avoid creating standing waves in the silicon thickness, and b) Routing the resulting RF echo to the measurement device 96 ns after the emission of the excitation pulse. Figure 4.20 shows the schematic of the test setup meant to drive transducers in the pulse-echo scheme.

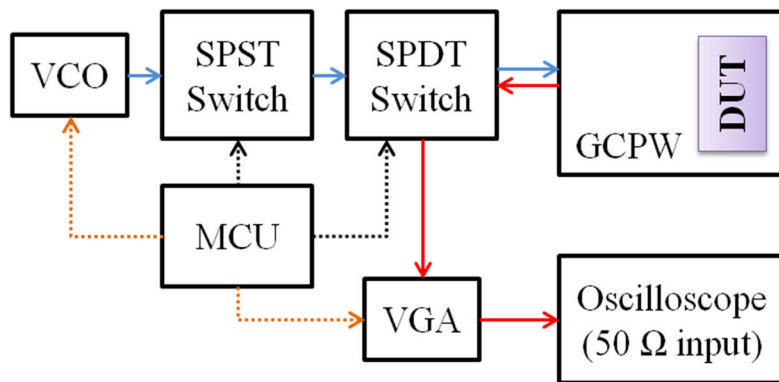


Figure 4.20: Schematic of the test setup meant to drive transducers in the pulse-echo scheme.

The circuit in Figure 4.20 starts with the Voltage Controlled Oscillator (VCO) ZX95-1750 W-S+ generating a continuous 6 dBm RF signal (indicated as the blue arrow coming out of the VCO block). The VCO frequency is manipulated by an analog signal (dashed orange line) coming from the MCU block (a microcontroller based on the ARM Cortex-M7 CPU). Then two of the "High-Resolution Timer" (HRTim) modules included in the MCU are used as the digital signals (dashed

black lines) activating both the single-pole single-throw (SPST) RF switch ADG901 and the single-pole double-throw (SPDT) RF switch ADG918 as detailed in Figure 4.21.

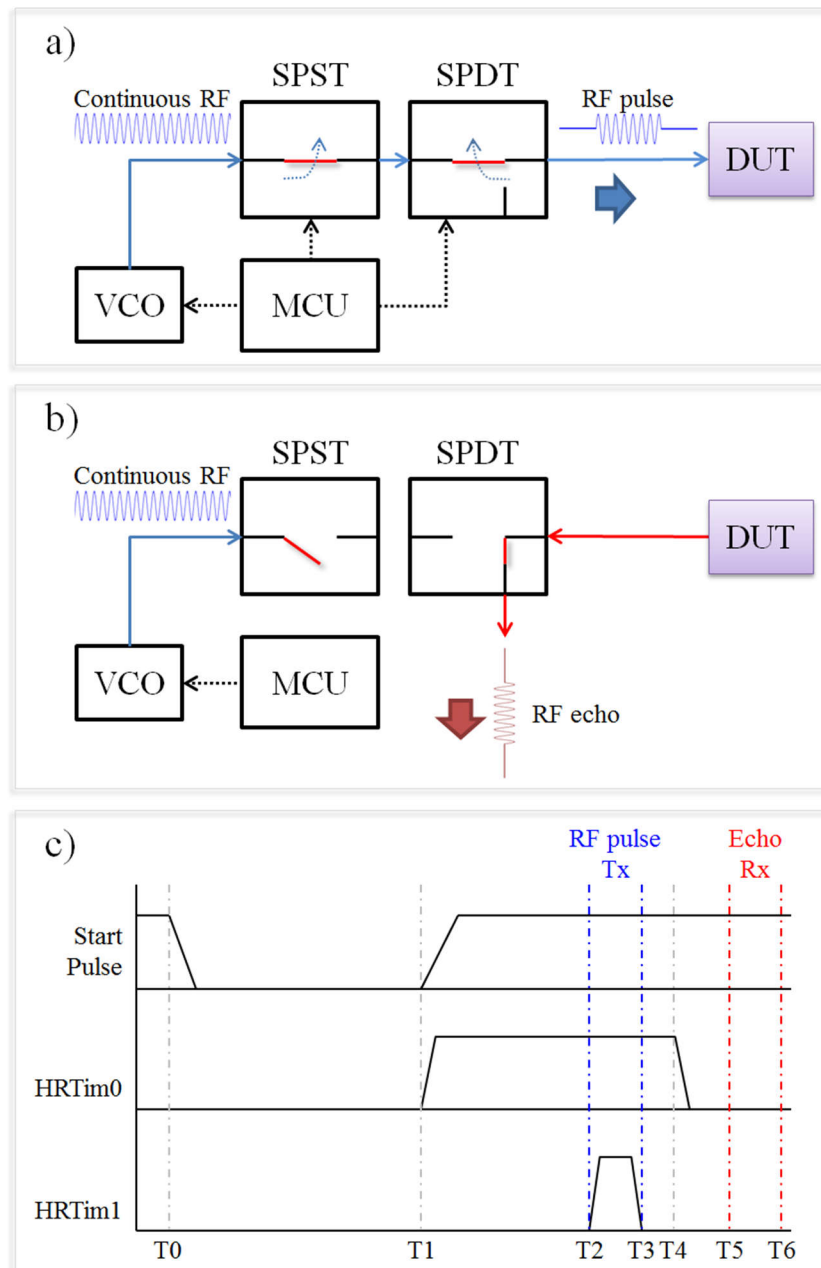


Figure 4.21: Schematics for RF switch states. a) RF pulse emission. b) RF echo reception. c) Timing diagram. T0: Fall of the StartPulse signal starts the sequence with a 1 μ s delay. T1: The SPST switch is activated by the HRTim0 signal, then a 50 ns delay starts. T2: The HRTim1 signal changes the position of the SPDT switch, allowing the DUT to be driven by the excitation signal. T3: The fall of the HRTim1 signal (25 ns later) truncates the length of the excitation pulse to 25 ns, then the SPDT switch is restored to its original position (connecting the DUT with the VGA). T4: Ten nanoseconds later the SPST switch is disabled, improving attenuation of the continuous RF input coming from the VCO. T5: The DUT response (echo) is expected to arrive at T2 + 98 ns. T6: Echo reception ends 25 ns later.

Both switches remain active for 25 ns, allowing the DUT to be driven during such period as represented in Figure 4.21a. Once both switches are disabled (Figure 4.21b), the VCO signal is attenuated up to 40 dB by the SPST switch [12], and the SPDT will route the resulting RF echo to amplification and measurement. Specific timing details are described in Figure 4.21c. Once the ToF has been achieved, the output echo is amplified 25.8 dB by the Variable Gain Amplifier (VGA) ZFL-1200 G+, and then captured at the 50 Ω input port of the Rohde&Schwarz RTO2064 scope.

Figure 4.22 shows the appearance of an excitation pulse, captured by the oscilloscope. Figure 4.23 presents an optical image of the excitation/read setup for the pulse-echo transducers

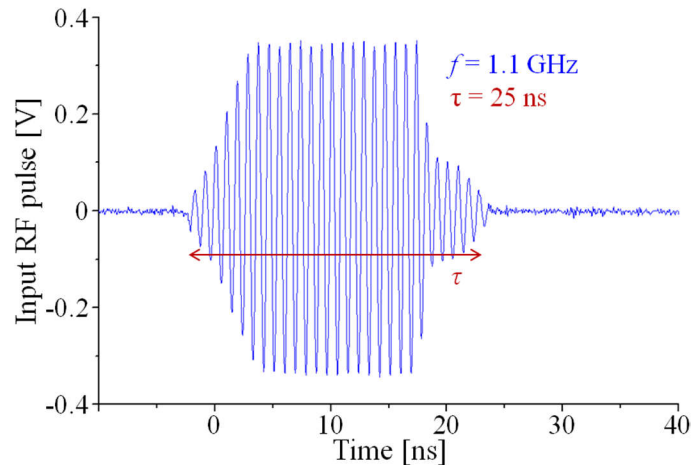


Figure 4.22: Scope measurement showing characteristics of the excitation RF pulse.

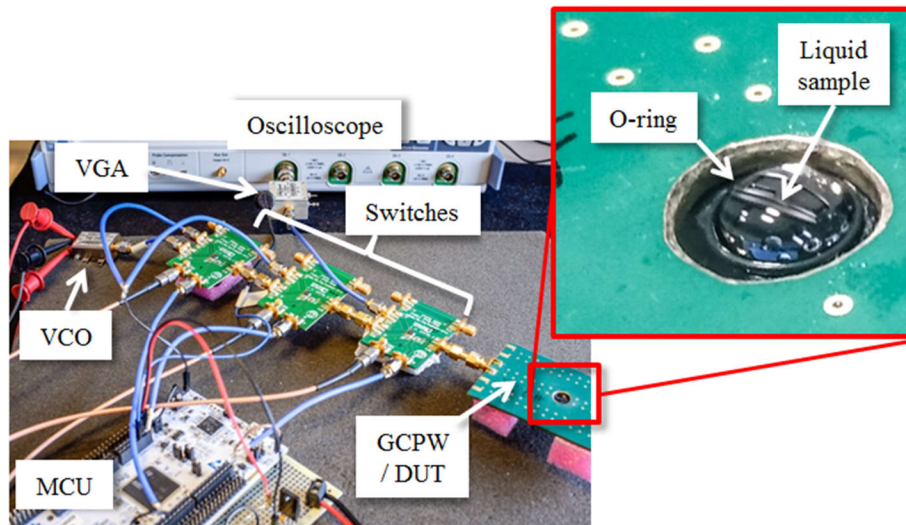


Figure 4.23: Optical image of the excitation/read setup for the pulse-echo transducers. An additional SPST switch is cascaded to improve attenuation of the VCO signal, increasing the signal to noise ratio.

4.4.2 Frequency and Time responses for the pulse-echo system

To find the analytically predicted transduction peaks, the range between 0.8 – 2.2 GHz was explored by sending pulses and receiving its corresponding echoes with a step size of 10 MHz (Figure 4.24); the detection surface of the 92 μm transducer has been cleaned of liquids and it is only in contact with air. Furthermore, since insertion loss in the RF switches is not constant in

frequency, the voltage amplitude of the input excitation RF pulse was also recorded every 20 MHz to verify that its slight variation in amplitude is not related to the expected transduction peaks.

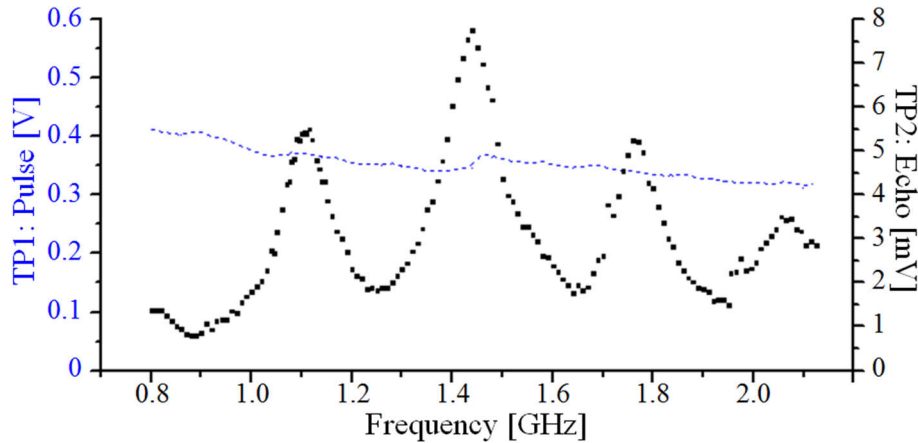


Figure 4.24: Measured voltage level (VRMS) of input RF pulses applied to the DUT in the 0.8 – 2.2 GHz range (blue dots) and voltage level for corresponding RF echoes (black marks) [13].

As seen in Figure 4.24, amplitude of the input pulses applied to the transducer varies smoothly in the 0.8 – 2.2 GHz range (blue dots), whereas amplitude of output voltage (received echoes) is notably improved for the expected frequencies (black marks). Frequency regions of Figure 4.24 with significant improvement in electromechanical coupling match with regions of the S_{11} curve in Figure 4.18 where resonant modes showed higher amplitude, and consequently with analytical predictions and FEM simulations in Chapter 3 (Figures 3.11 and 3.26, respectively). The latter demonstrates multi-frequency operation capabilities of the sensor and suggests frequency spots where operation of the device is more favorable [13]. Figure 4.25 presents oscilloscope captures of received echoes, showing differences between operation at 1.1 GHz and operation at 1.27 GHz.

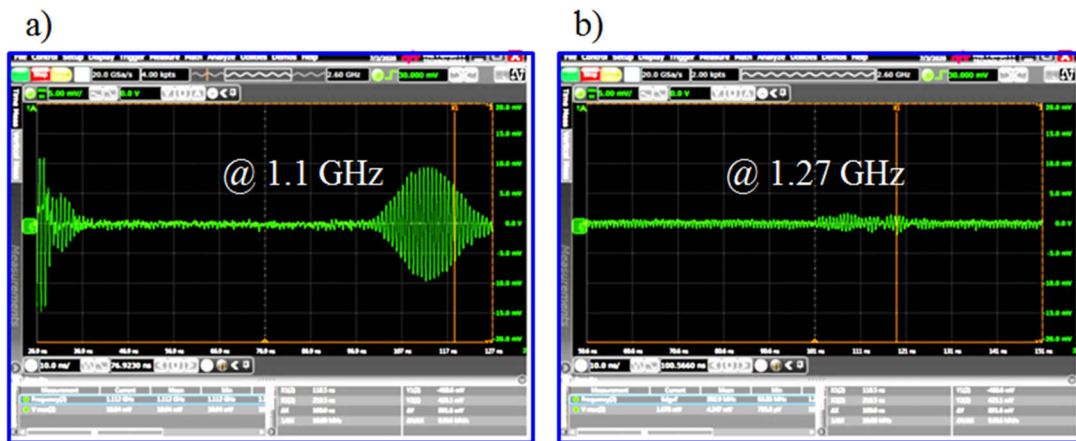


Figure 4.25: Screenshots of received echoes with no amplification (VGA removed). a) Transducer operating at 1.1 GHz. b) Transducer operating at 1.27 GHz.

4.4.3 Digital filtering & post-processing for received echoes

Figure 4.26 shows a 500 ns recording of the output signal coming from the VGA, when a 30 ns pulse ($f_{op} = 1.1$ GHz, 3 dBm) passes through the RF switches and feeds the central transducer of Figure 4.17a, wire bonded to the carrier waveguide (there is only “air” in the detection surface).

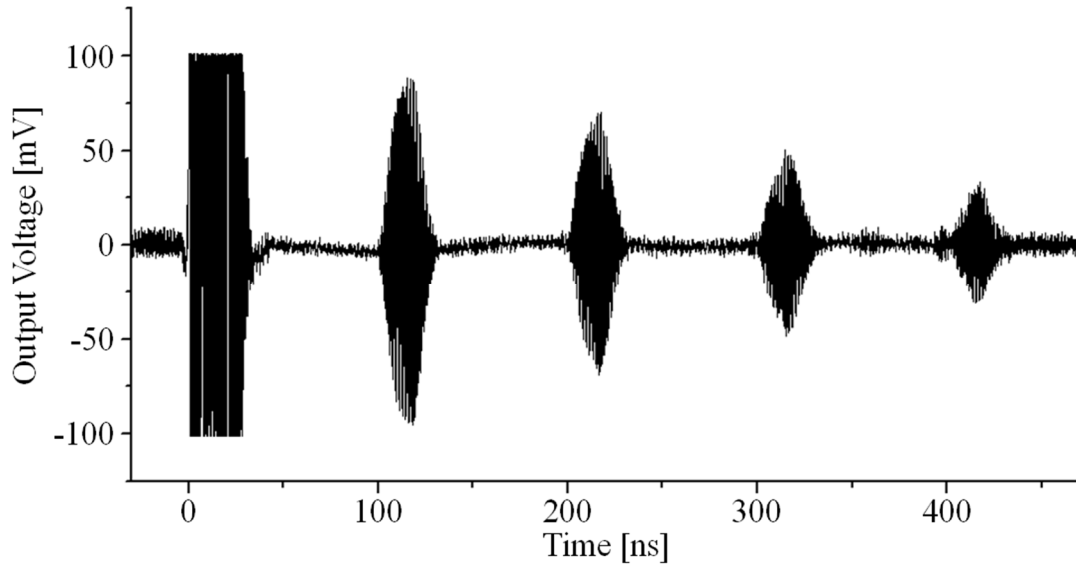


Figure 4.26: A 500 ns recording of the output signal coming from the VGA.

Measurement in Figure 4.26 matches with the FEM simulation plot in Figure 3.29a of Chapter 3, where RF feedthrough is expected at $t = 0$ and the first echo appears at $t = 98$ ns; which is the analytically projected value for a round trip through the silicon thickness ($ToF \times 2$). In this 500 ns recording it is also possible to distinguish a second, third and fourth echoes, caused by further reflections, separated by around 98 ns. The spectrum of the output signal shown in Figure 4.26 reveals frequency components surrounding the frequency of interest (1.1 GHz).

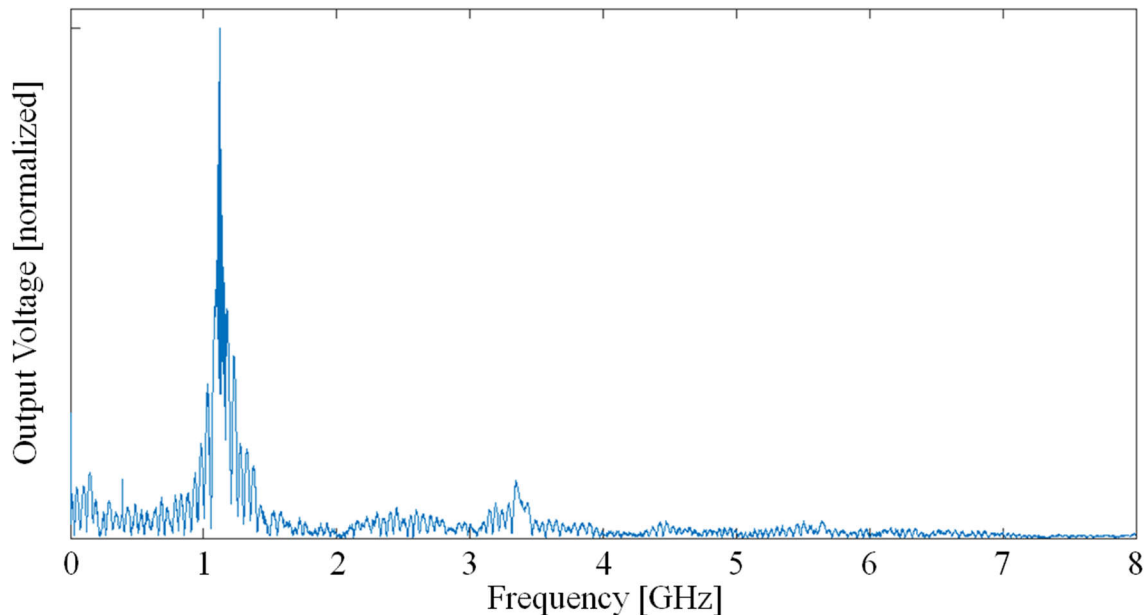


Figure 4.27: Normalized spectrum of the output signal in Figure 4.26.

In order to reduce the uncertainty caused by random noise, a MATLAB script takes the output signal in Figure 4.26 and applies to it a Chebyshev filter with order $n = 4$. Figure 4.28 shows the magnitude of the frequency response for the filter, Figure 4.29 presents the output signal after filtering, and Figure 4.30 shows the envelope of the filtered signal (Hilbert Transform).

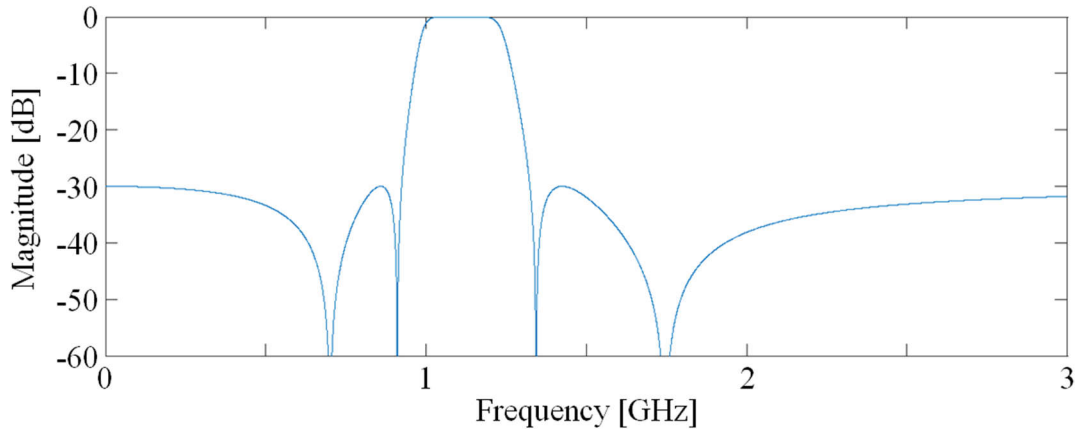


Figure 4.28: Type 2 Chebyshev filter, order $n = 4$. The passband has a 100 MHz span around the center frequency (1.1 GHz) and maximum attenuation of 1 dB, whereas the stopband is located 200 MHz on either side of the center frequency, with 30 dB attenuation.

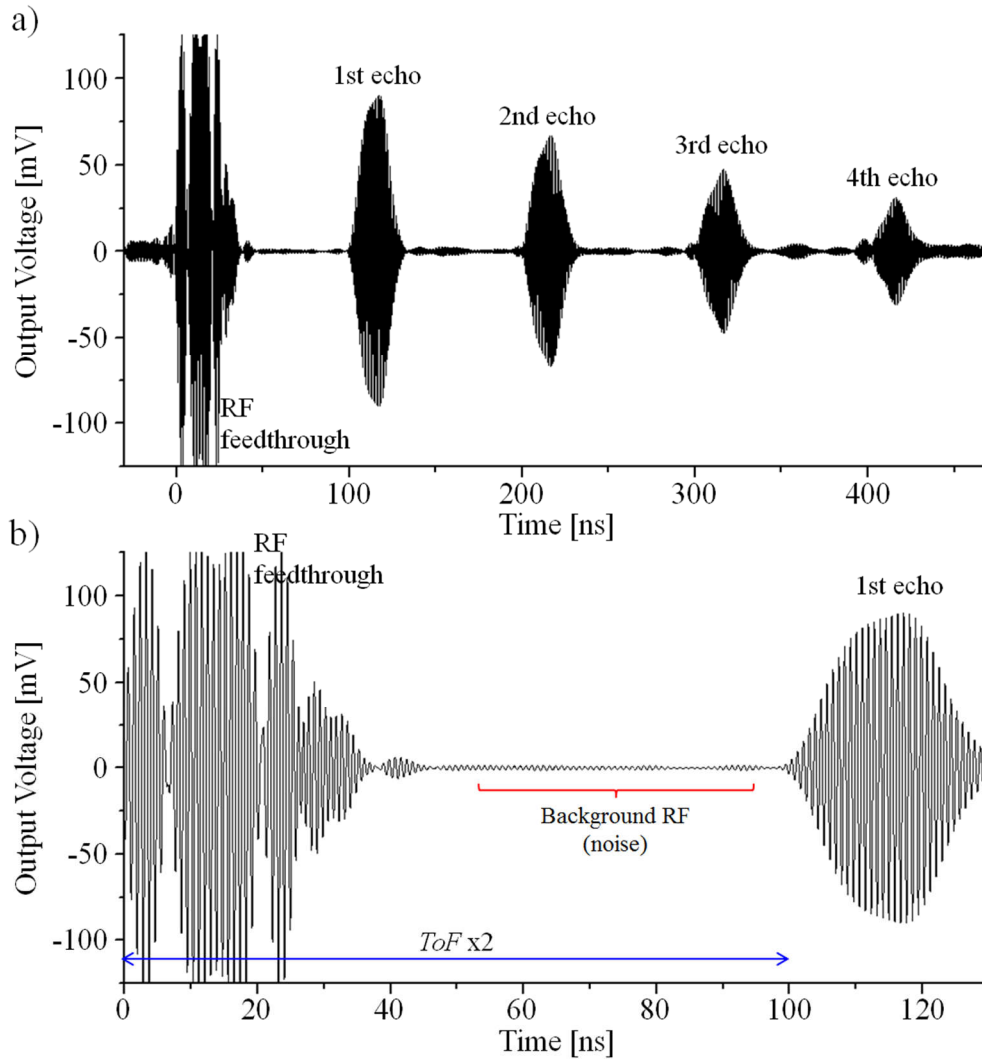


Figure 4.29: Output signal after filtering. a) Output signal in Figure 4.26 after filtering. b) Record of the first echo in detail.

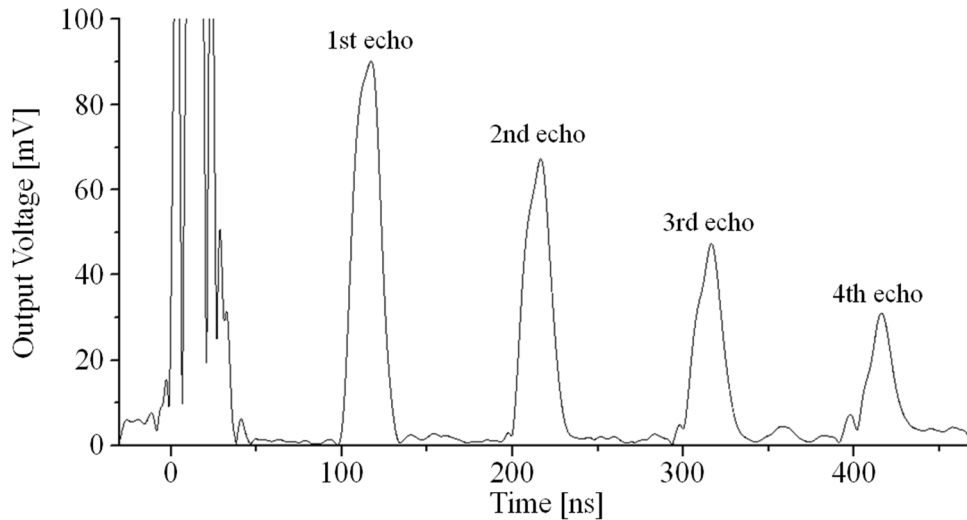


Figure 4.30: Envelope of the filtered output signal.

Figure 4.29 has presented the output signal after filtering (Chebyshev, $n = 4$), whereas Figure 4.30 has presented the envelope of such signal, obtained by the Hilbert Transform in MATLAB. As a result, the first echo rises up to 38 dB above the background RF signal, currently consisting solely of the continuous 1.1 GHz signal that leaks through the switches.

In this Chapter it has been shown that both systems (pulse-echo transducers and acoustic resonators) fulfill the electrical and mechanical characteristics predicted by the theory and FEM simulations. The operation of its detection principle has been shown for both cases and the test setup has been designed. The next Chapter shows applications for both systems.

References

- [1] Emmanuel Defay, Integration of Ferroelectric and Piezoelectric Thin Films: Concepts and Applications for Microsystems, Wiley, 2013, <https://doi.org/10.1002/9781118616635>
- [2] Harmeet Bhugra, Gianluca Piazza, Piezoelectric MEMS Resonators, Springer, 2017, <https://doi.org/10.1007/978-3-319-28688-4>
- [3] Ken-Ya Hashimoto, RF Bulk Acoustic Wave Filters for Communications, Artech House, 2009, ISBN 13: 9781596933217
- [4] J. Yanez, E. Ledesma, A. Uranga and N. Barniol, Improved Electromechanical Transduction for PiezoMUMPS HBAR Impedance Sensors, 2020 Joint Conference of the IEEE International Frequency Control Symposium and International Symposium on Applications of Ferroelectrics (IFCS-ISAF), 2020, 1–5. <https://doi.org/10.1109/IFCS-ISAF41089.2020.9234913>
- [5] Brian C Wadell, Transmission Line Design Handbook, Artech House, 1991, ISBN: 9780890064368
- [6] Rainee N. Simons, Coplanar Waveguide Circuits, Components, and Systems, Wiley, 2001, <https://doi.org/10.1002/0471224758>
- [7] Circuitos Impresos 2CI, S.L. (<https://www.2cisa.com/es/>), 2022, (accessed 2 December 2022)

- [8] G. Crupi, D. Schreurs, Microwave De-Embedding: From Theory to Applications, Elsevier, 2013, ISBN: 9780124017009
- [9] S. K. Goudos, Microwave Systems and Applications, IntechOpen, 2017 <https://doi.org/10.5772/62931>
- [10] Guillermo Gonzalez, Microwave Transistor Amplifiers: Analysis and Design, Prentice Hall, 1996, ISBN 0-13-254335-4
- [11] H. Xu and E. Kasper, A de-embedding procedure for one-port active mm-wave devices, 2010 Topical Meeting on Silicon Monolithic Integrated Circuits in RF Systems (SiRF), 2010, 37–40, <https://doi.org/10.1109/SMIC.2010.5422795>
- [12] ADG901 Overview, (<https://www.analog.com/en/products/adg901.html#product-overview>), 2022, (accessed 2 December 2022)
- [13] J. Yanez, A. Uranga and N. Barniol, Multi-frequency thin film HBAR microsensor for acoustic impedance sensing over the GHz range, 21st International Conference on Solid-state sensors, Actuators and Microsystems (Transducers), 2021, 1347–1350, <https://doi.org/10.1109/Transducers50396.2021.9495750>

Results and Conclusions

5.1 HBAR device operating under a pulse-echo regime

Figure 5.1a presents the optical image of the DUT connected to the excitation/read setup; the zoomed section shows the orifice that allows placing samples on the detecting surface of the chip. Figure 5.1b is a 2D representation of the operation principle; the piezoelectric transducer emits an ultrasound pulse that travels within the silicon bulk to interact with the liquid sample and it is reflected back towards the transducer to be measured. This process is completed in $ToF \approx 98$ ns.

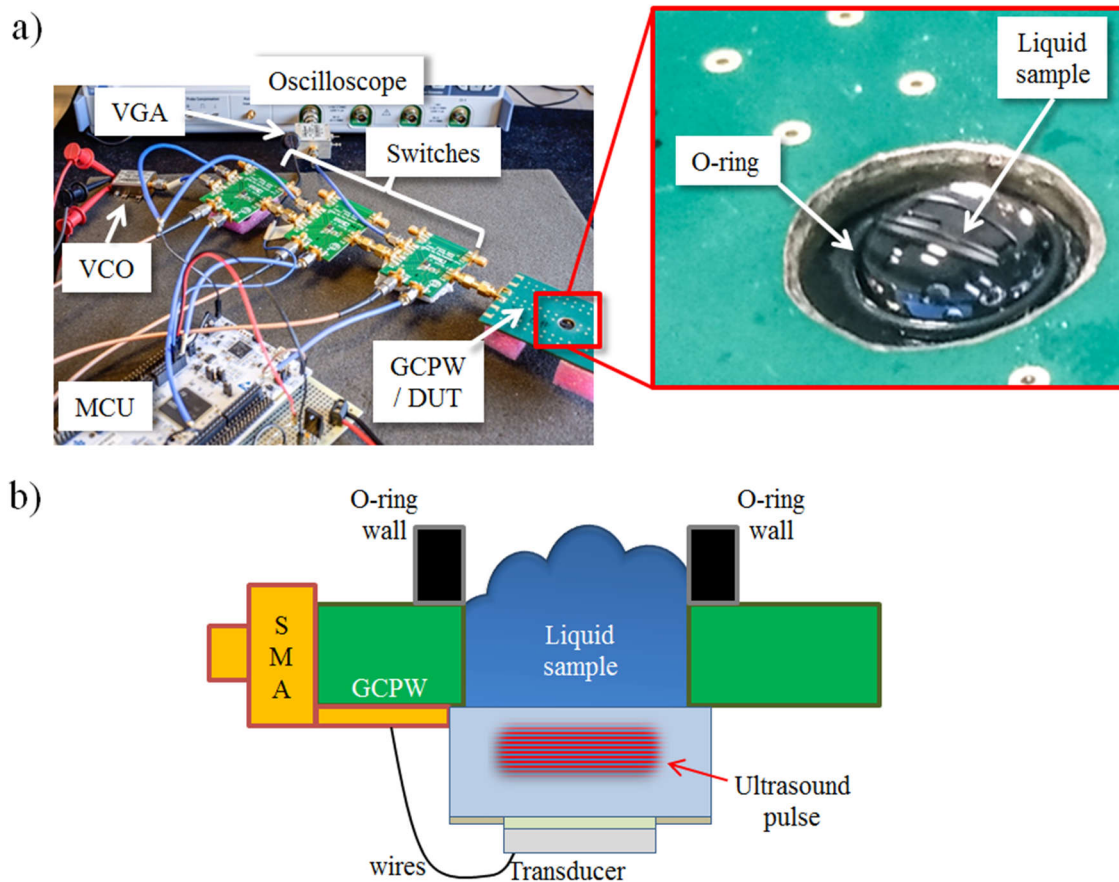


Figure 5.1: Pulse-echo sensor. a) Optical image of the setup. b) 2D representation of the operating principle.

As result, the reflected acoustic pulse is converted into the measurable electrical signal of Figure 5.2. The amplitude of the recorded echo will depend on the specific acoustic properties of each sample, allowing the identification and classification of liquids or detecting changes in temperature and concentration of mixtures. The following sections show some of the possible applications for these sensors.

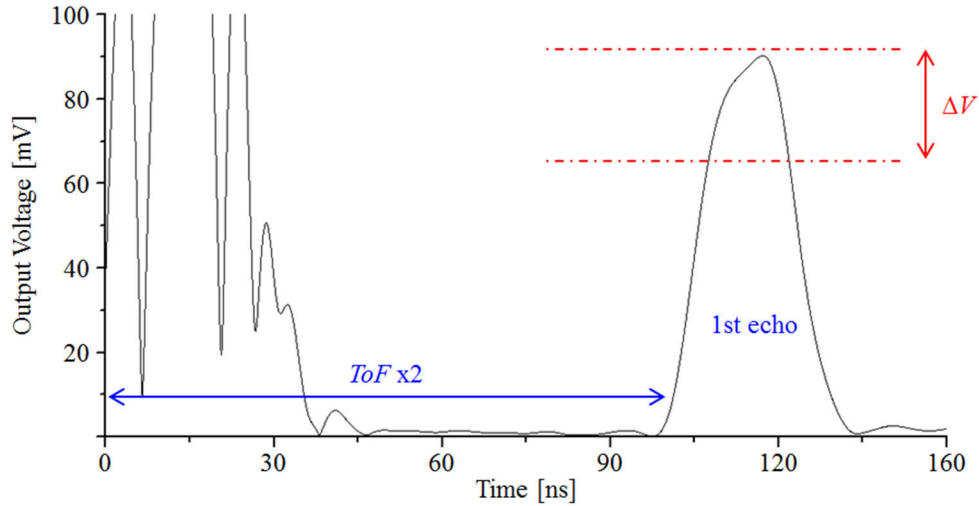


Figure 5.2: Output signal of the 92 μm wide transducer operating at 1.1 GHz, under the pulse-echo scheme. The amplitude of the recorded echo (ΔV) will depend on the specific acoustic properties of each sample.

5.2 Applications of pulse-echo transducers

Figure 5.3a is the block diagram of the setup presented in Figure 5.1; the solid blue arrows represent RF inputs whereas the solid red lines describe the path of the RF output (echo). Dotted orange lines are analog control signals, and dotted black lines are digital control signals. This circuit drives the DUT with 30 ns RF pulses at $f_{\text{op}} = 1.1$ GHz (3 dBm). Figure 5.3b is an optical image of the manufactured 1D array consisting of three independent HBAR structures; the sensor (DUT) is the central element of the array, which is connected to the waveguide (GCPW). The output voltage signals (echo) were registered by the 50 Ω input of the oscilloscope (Rohde&Schwarz RTO2064) and post-processed with MATLAB (Chebyshev band-pass filter and Hilbert Transform).

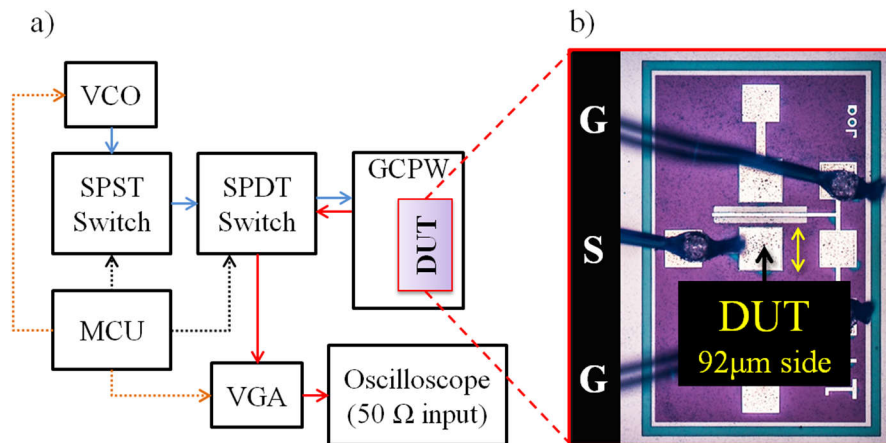


Figure 5.3: Pulse-echo sensor. a) Schematic of the excitation/read setup. b) Optical image of the sensor.

As speed of sound of both solids and liquids change with temperature and hence their acoustic impedance, all the measurements were performed at the same room temperature (31 °C). Most of the following results for the pulse-echo transducers correspond to a Journal publication [1].

5.2.1 Identification and classification of liquids by their specific acoustic impedance

Since different substances have dissimilar densities and longitudinal sound velocities, it is possible classification by measuring the degree of acoustic impedance mismatch between the silicon body of the sensor and each fluid, i.e., depending on the physical properties of each sample, a different amount of acoustic energy will be reflected back towards the transducer and therefore an specific voltage level will be recorded for each sample. Figure 5.4 offers an example; it compares the output signal when distilled water is present at the detection surface to the output signal of a cleared surface (air).

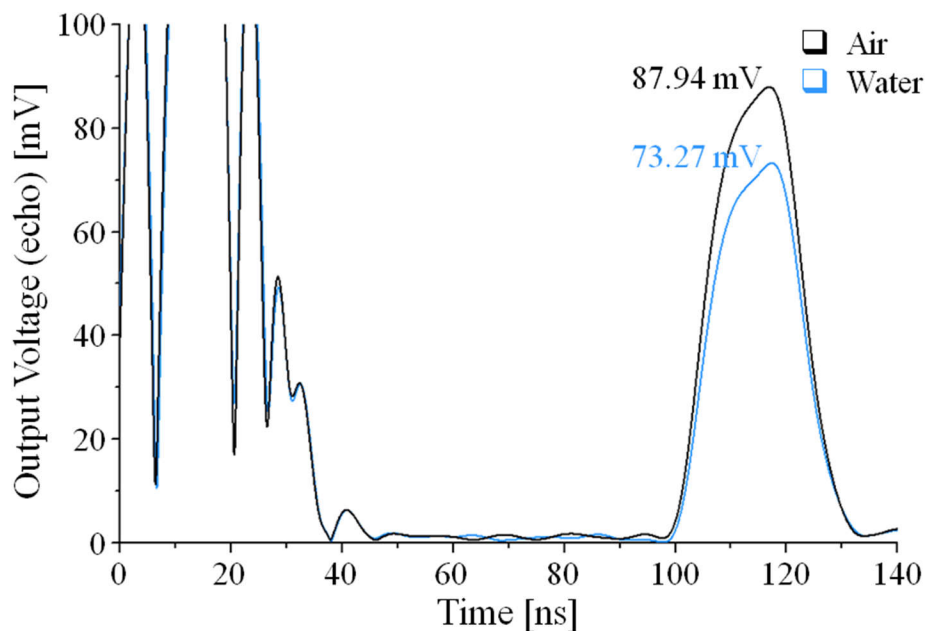


Figure 5.4: Comparison of the output voltages for both the case of “air” at the detection surface (black) and the case of “distilled water” (blue).

Measurement results in Figure 5.4 agree with theoretical predictions of Table 3.3 in Chapter 3, since the amplitude of the envelope corresponding to the case of distilled water (blue trace) drops close to 16% respect to the maximum amplitude obtained when the detection surface is cleared (black trace). Additionally, the ToF for a round-trip corresponds with the expected time (~ 98 ns). To demonstrate classification capability, measurements have been made to air, ethanol, Fluorinert FC-70, deionized water, and glycerol on the detection surface; the volume of each sample confined by the o-ring is approximately 0.1 mL. Table 5.1 collects the values: density ρ , acoustic velocity v , and viscosity μ , of each liquid (from Table 3.3 of Chapter 3), as well as their acoustic impedance ($Z \approx \rho v$) and the expected value of their reflection coefficient Γ at the silicon-liquid interface. The experimental values for reflection coefficient Γ_m are the mean value obtained from five measurements of each liquid, using the relation: V_{liq}/V_{ref} , where V_{ref} is the voltage generated by a

received echo when the detection surface is clear ('air' causes total reflection of acoustic pulses and therefore a reference value), whereas V_{liq} is the voltage generated in the case of each liquid.

Material	Density 31 °C ρ [kg/m ³]	Acoustic velocity v [m/s]	Viscosity μ [cP]	Acoustic impedance $Z \approx \rho v$ [Rayl]	Γ (Eq. 1)	Γ_m (V_{liq} / V_{ref})
Air	1.14	349.1	0.018	398	0.9999	1
Ethanol	780.1	1105.7	1.06	0.8625E+06	0.9161	0.9047
FC-70	1924	680	3.36	1.3083E+06	0.8754	0.8611
DI Water	995.6	1511.4	0.79	1.5047E+06	0.8580	0.8423
Glycerol	1254	1902	552.1	2.3851E+06	0.7839	0.7379

Table 5.1: Experimental values of reflection coefficient Γ_m , compared to literature values from Table 3.3 of Chapter 3.

Figure 5.5 relates values of reflection coefficient in Table 5.1 with their respective acoustic impedance value. Values obtained from Finite Element simulations are also included.

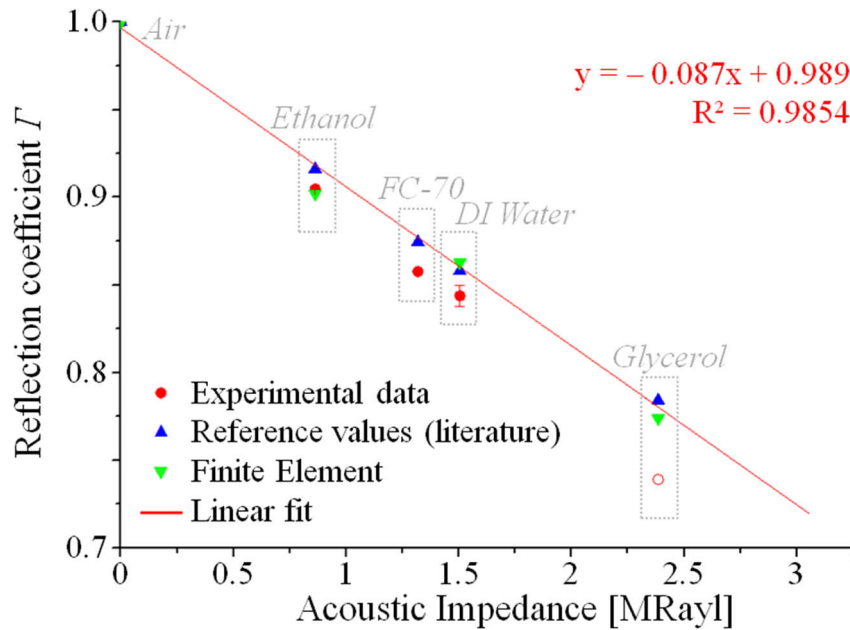


Figure 5.5: Reflection coefficient obtained from measurements and related to the specific acoustic impedance of each substance.

The reflection coefficient obtained from the measured output voltage of each liquid shows a linear relationship with the reference values for acoustic impedance, except for the case "glycerol", where it is appreciated major dispersion. This inconsistency is due to both the relative high viscosity of glycerol and the frequency of operation in the GHz range, that were not considered either in the analytic approximation $Z \approx \rho v$, nor in the Finite Element Model, which was constructed using a simply linear elastic fluid model in COMSOL. To obtain a realistic analytical value of acoustic impedance for glycerol and its respective reflection coefficient value it is necessary to consider the complex term in equation 4 from Chapter 2:

$$Z_{liquid} = Z_{real} \sqrt{\left[1 + i \frac{\omega}{\rho v^2} \left(\mu_B + \frac{4}{3} \mu\right)\right]}$$

Where μ is the shear viscosity (also known simply as “viscosity”), and μ_B is the bulk viscosity. By using $\mu = 552$ [cP] (Table 5.1) and $\mu_B = 2\mu/3$ [2, 3], it is found for glycerol:

$$Z = 3.22 \text{ MRayl}$$

$$\Gamma = 0.7186$$

Figure 5.6 includes the adjusted value of the reflection coefficient for glycerol (marked with a black square). The reflection coefficient value obtained by measurements is now related with the corrected value of acoustic impedance.

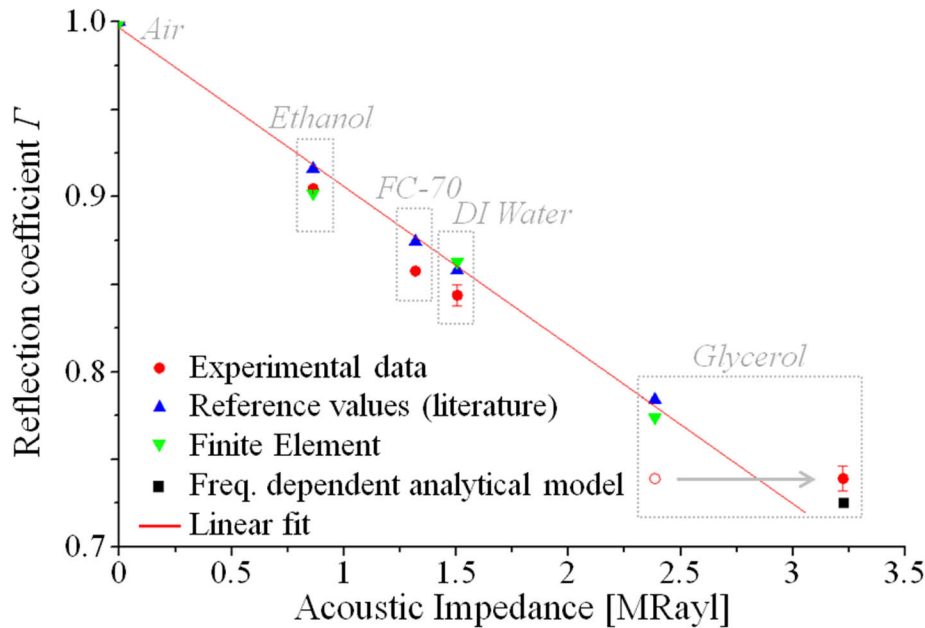


Figure 5.6: Reflection coefficient obtained from measurements and related to the specific acoustic impedance of each substance [1]. Due to the relatively high viscosity of glycerol (>500 cP), a frequency-dependent acoustic impedance value has also been included.

Experimental results in Figure 5.5 demonstrate the ability of the pulse-echo sensor to identify and classify different liquids placed on its sensing surface, as long as their viscosity does not exceed a few tens of cP. For higher viscosity values further adjustments are required, as shown in Figure 5.6 for the case of glycerol.

5.2.2 Detection of concentration changes in solutions

Figure 5.7 compares the output signal of measurements performed to water on the detection surface, up to 350 ns, and measurements performed when glycerol is present on the detection surface.

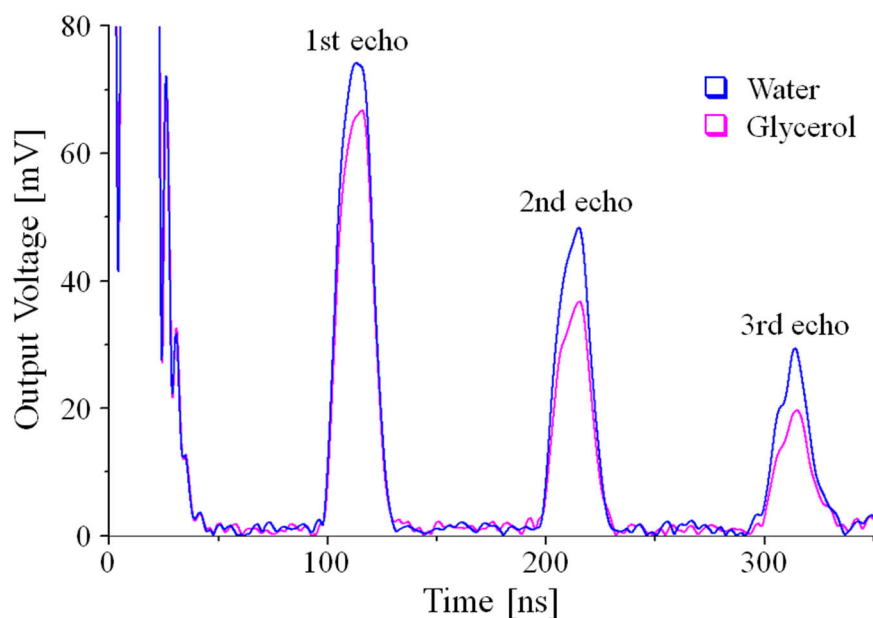


Figure 5.7: Output voltage, up to 350 ns, of measurements performed to water flooding the detection surface and measurements to glycerol. For both fluids, a first echo arrives at the expected ToF (~ 98 ns), and it is followed by multiple reflections of the same single emitted pulse. There is an increased difference in amplitude in the second echo compared to the case of the first echo since the acoustic pulse experience two times reflection and consequently the amplitude will be reduced two times the reflection coefficient.

As expected, the echo arrives at the ToF (~ 98 ns) for both the case of water in the detection surface and for the case of glycerol. This first echo is followed by other remaining echoes of lower amplitude caused by multiple reflections of the same emitted pulse traveling across the low-loss acoustic medium, i.e., a single emitted pulse interacts more than once with each sample until it faded in time; these remaining echoes are separated by the ToF, since they travel the same distance. There is an increased difference in amplitudes in the second echo compared to the case of the first echo since acoustic pulses experience two times reflection and consequently their amplitude was reduced by the reflection coefficient value on each interaction with the sample. To demonstrate the sensor's ability to distinguish voltage levels between the peak value obtained for water and the peak value obtained for glycerol, that is, to detect concentration changes, glycerol/water mixtures ranging from 10% to 90% (percentage by weight) have been prepared. Each of the experimental points in Figure 5.8 represents the average value of five measurements performed at each concentration value, normalized to 'water' (0% glycerol). The analytical value of viscosity at 31 °C (blue curve) has been included as a reference [4].

Experimental values in Figure 5.8 demonstrate that the level of acoustic energy absorbed by the liquid sample increases linearly ($R^2 > 0.97$) as the concentration of glycerol in the mixture increases up to 80% (viscosity = 32.7 cP). From that point, experimental data show slight sensitivity to abrupt changes in viscosity, where its value increases rapidly up to 550 cP. This confirms both the correlation between the output voltage and changes in compressional properties of liquids, and also the lack of sensitivity to viscosity, as long as its value does not exceed a few tens of cP.

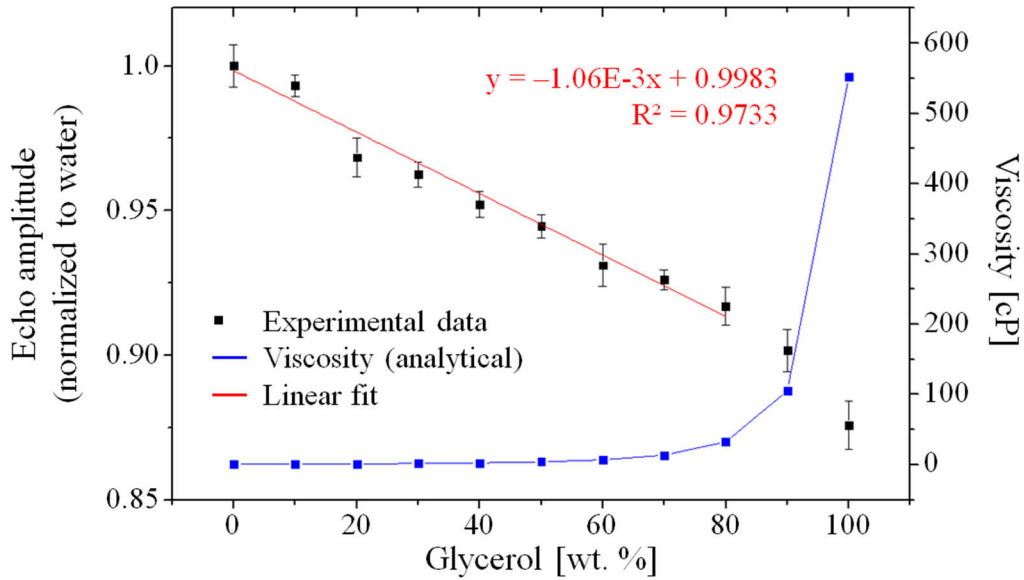


Figure 5.8: Measured reflection coefficient as a function of glycerol content in glycerol/water mixtures [1]. Samples range from 0% glycerol (pure water) to pure glycerol and each step represents a 10% increment of glycerol content (percentage by weight).

Despite of the satisfactory results achieved in Figure 5.8 using information from the first echo, both linearity and resolution can be improved by using information from the second echo. As seen in Figure 5.7, there is a greater difference between the peak voltage of both the water and glycerol measurements in the second echo, and therefore it would lead to calibration curve with a steeper slope than that shown in Figure 5.8. Each of the experimental points in Figure 5.9 represents the average value of five measurements performed at each concentration value (second echo), normalized to ‘water’.

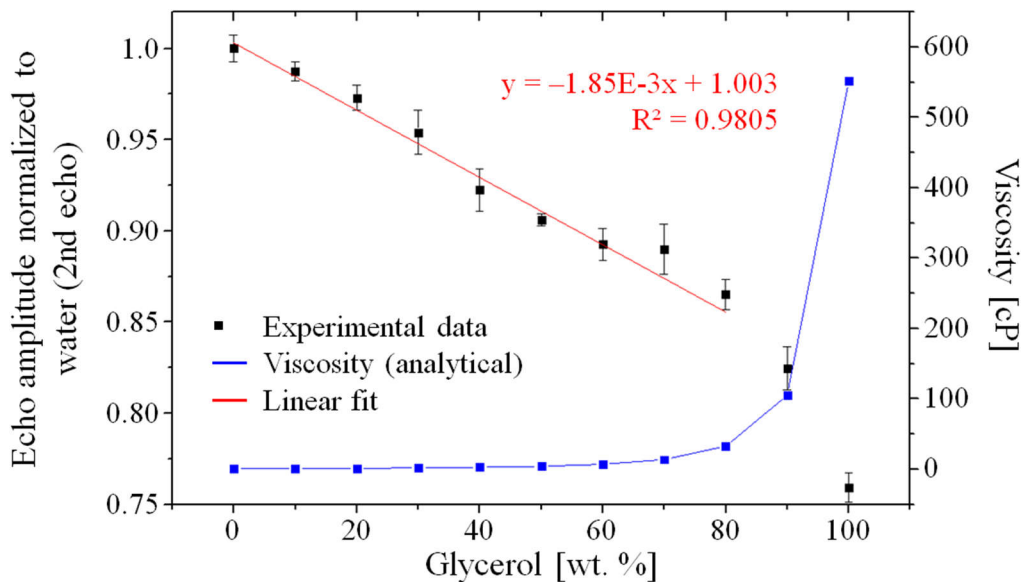


Figure 5.9: Measured reflection coefficient (second echo) as a function of glycerol content [1].

The latter demonstrates that this sensor provides an alternative for noninvasive study of biological fluids at microscale, where viscosity rarely exceeds 10 cP [5].

5.2.3 Sensing of compressional properties of liquids (Acoustic impedance and Bulk modulus)

Figure 5.10 relates experimental results from Figure 5.9 with their respective acoustic impedance value ($Z \approx \rho v$) obtained from literature [3], whereas Figure 5.11 relates experimental values with their correspondent bulk modulus value ($K' \approx \rho v^2$).

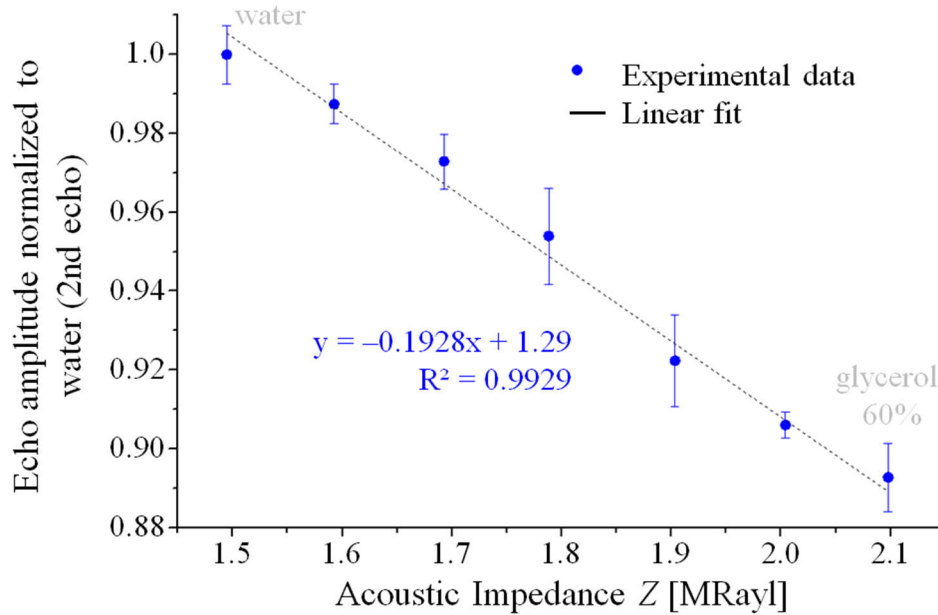


Figure 5.10: Measured reflection coefficient of each glycerol concentration (0 – 60%) [1], as a function of reported Acoustic impedance.

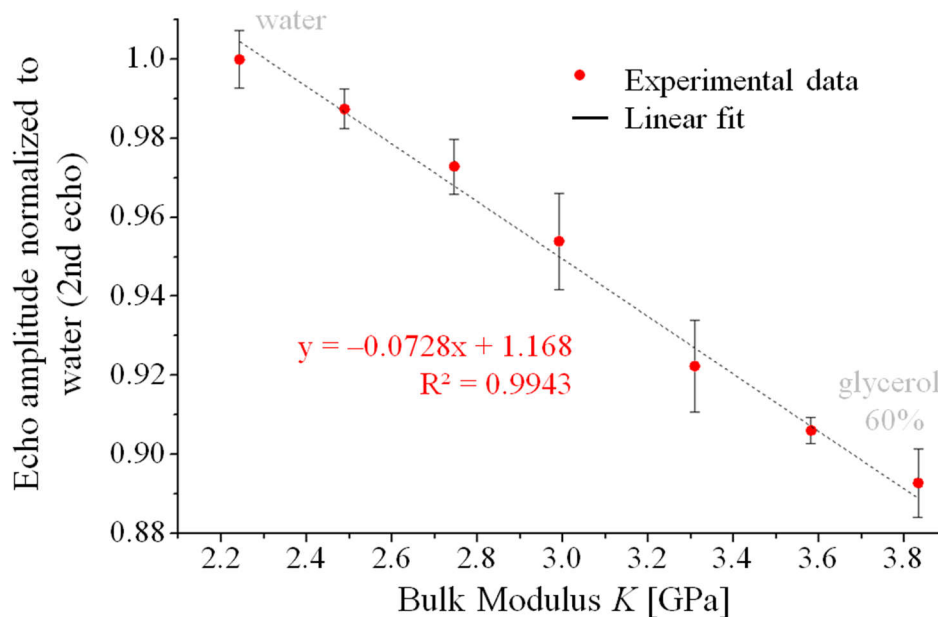


Figure 5.11: Measured reflection coefficient of each glycerol concentration (0 – 60%) [1], as a function of Bulk modulus.

In Figure 5.10 the output voltage decreases 1.8% for each 100 kRayl increment in the acoustic impedance Z , whereas in Figure 5.11 it decreases 6.9% per GPa in the case of changes in Bulk

modulus K , showing in both cases high linearity ($R^2 > 0.99$). Studies on compressional properties of liquids are mainly carried out by large-scale systems making it difficult to find direct competitors to compare; Table 5.2 compares this pulse-echo microsensor to a recently reported acoustic resonator based on SMR technology.

	[6] 2019	This transducer
Acoustic device type	SMR (FBAR)	HBAR
Mode of operation	Resonating	Pulse-echo
Sensitive area	0.01 mm ²	0.008 mm ²
Drive voltage	10 dBm (continuous)	4 dBm (25 ns pulse)
Frequency of operation	2.5 GHz	1 – 10 GHz range
Liquid operation	Yes (by passivation layer)	Yes (native)
Parameter to detect	Change of resonant frequency	Voltage amplitude
Bulk modulus sensitivity	5.83 MHz / GPa	6.89% / GPa

Table 5.2: Comparing the manufactured pulse-echo device to a reported resonant sensor of liquid bulk-modulus at microscale.

Despite sharing some characteristics such as similar dimensions of the active area or wavelength, this pulse-echo HBAR-based microsensor offers lower drive voltage, simpler manufacture and increased reliability respect to FBAR/SMR devices. Additionally, its multi-frequency capabilities allow controlling penetration in liquids to avoid unwanted reflections in narrow channels or due to low sample volumes. Moreover, the pulse-echo mode of operation offers a much simpler drive/lecture method, where only output voltage amplitude should be recorded.

5.3 Application of the alternative readout method (resonator)

Figure 5.12 is a 2D representation of the assembly containing the sensor; a silicon die containing acoustic devices is glued to the carrier waveguide (GCPW) and the selected resonator is wire bonded to its GSG lanes. Since the detecting surface of the resonator is at the opposite side of the chip, the waveguide has a trench to place and remove liquid samples. When a continuous low-power RF signal drives the piezoelectric device, its thickness extensional mode is activated producing longitudinal pressure waves in the silicon cavity. This acoustic energy remains trapped within the substrate thickness if air is present in both the upper and in the lower side of the stack, i.e. when the microchannel is empty, because of the high degree of acoustic impedance mismatch between solid materials and gas, causing the appearance of multiple well-defined resonance peaks corresponding to the fundamental mode of the structure and its harmonics. Contrarily, acoustic leaks appear once the channel is filled with a liquid sample due to decrease in acoustic impedance mismatch (some of the energy leaks into the liquid domain) causing both a decrease in amplitude of the resonance peaks and a detectable change of resonant frequency [6].

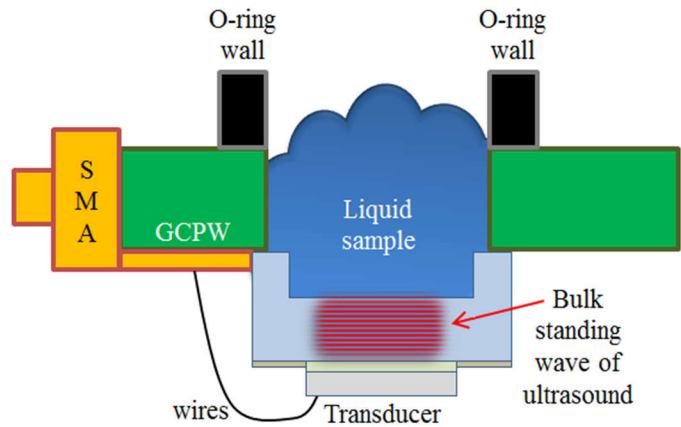


Figure 5.12: 2D representation of the assembly containing the HBAR device operating as an acoustic resonator.

Figure 5.13a offers an optical image of the carrier waveguide and its trench whereas Figure 5.13b presents the whole assembly that includes the silicon die wire bonded to the waveguide. The DUT is the inner circular resonator of diameter $d = 133 \mu\text{m}$ shown in Figure 4.1b of Chapter 4. To experimentally demonstrate the principle of operation and its applicability to detection of samples in microchannels or as a multiphase flow sensor, the assembly was connected to a network analyzer via its SMA connector, and S_{11} measurements around the third mode of the resonator were performed (Figure 5.13c).

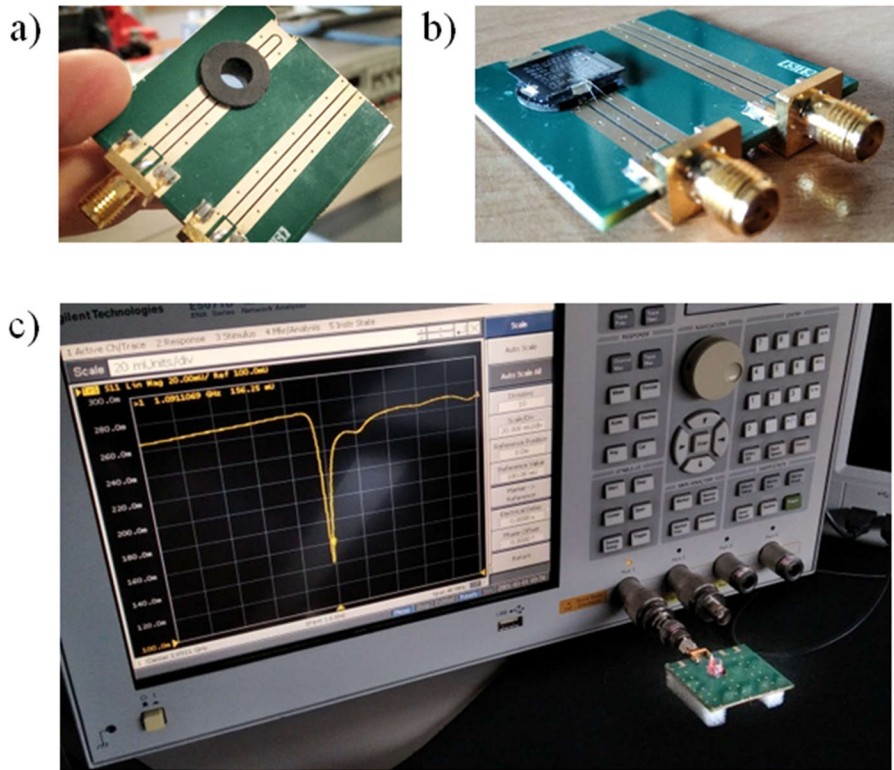


Figure 5.13: Experimental setup for the HBAR device operating as an acoustic resonator. a) Optical image of the carrier waveguide and its trench to place liquid samples. b) Optical image of the assembly consisting of a silicon die wire bonded to the waveguide. c) Assembly connected to the network analyzer to perform S_{11} measurements.

The input impedance curves in Figure 5.14a correspond to results presented in an international conference [7], and were obtained from experimental S_{11} measurements. They compare the response of the resonator when the detection surface is clean (empty channel, black curve) against to its response when the channel is filled with liquid (red curve). Input impedance curves of Figure 5.14b correspond to results from Finite Element simulations and were included as comparison.

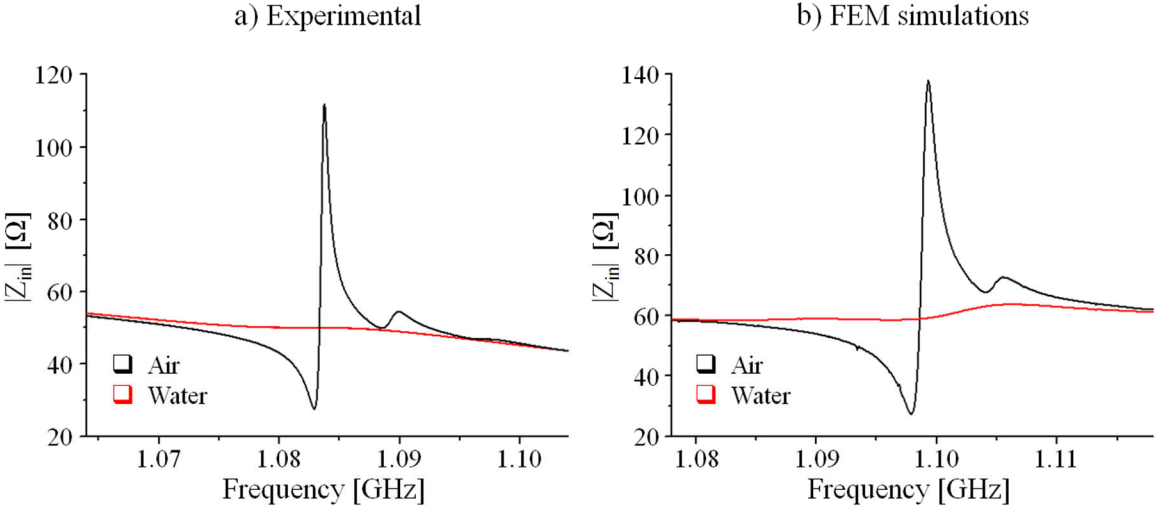


Figure 5.14: Comparison of sensor response when the detecting surface is clean (black) versus when it is flooded with a liquid sample (red) [7]. a) Curves obtained from S_{11} measurements. b) Curves obtained from Finite Element simulations (COMSOL Multiphysics 5.3).

As seen in Figure 5.14, exists a remarkable difference in amplitude of the magnitude of input impedance between both cases (air or water on the detection surface), demonstrating the sensor ability to identify presence of liquids in microchannels. This behavior is also present if the electrical resistance is measured; experimental results in Figure 5.15a compare the real part of the input impedance for both cases. Results in Figure 5.15b correspond to Finite Element simulations.

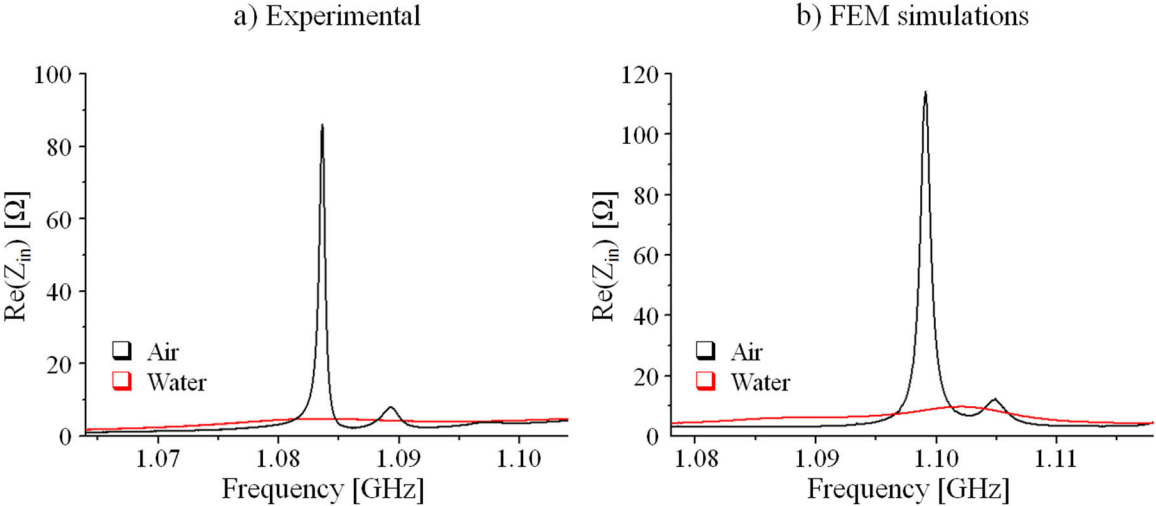


Figure 5.15: Comparison of sensor response (electrical resistance) when the detecting surface is clean (black) versus when it is flooded with a liquid sample (red) [7]. a) Curves obtained from S_{11} measurements. b) Curves obtained from Finite Element simulations (COMSOL Multiphysics 5.3).

5.4 Conclusion and Outlook

The pulse-echo transducer presented in this work has proven to be a valid alternative for noninvasive study of liquid samples at the microscale; applications such as identification and classification of liquids, detection of concentration changes in solutions, and sensing of compressional properties of liquids have been presented, showing repeatability and linearity in measurements.

Rather than the classic frequency shift detection approach to monitor changes in the material of study, this transducer interrogates the samples with short ultrasound pulses at GHz, obtaining an output voltage level according to the characteristics of each studied material. Characteristics and main features of the device can be summarized in the following points:

- **Multi-frequency operation:** The configuration of materials and thicknesses that make up the transducer allow the operation of the device at multiple points throughout the operating range (1 - 10 GHz), maintaining similar level of electromechanical transduction and controlling penetration depth of ultrasound in the sample as well as the heat transferred.
- **Reduced footprint:** In this approach, transducers are located on the underside of the wafer and therefore they do not require an area for their implementation in microfluidic systems. The presented transducer, located at the lower face of the wafer, has lateral dimensions equal to 90 μm , demonstrating negligible diffraction of acoustic pulses when operating at 1.1 GHz. The operating frequency range would allow the use of transducers with lateral dimension of 25 μm , operating at 10 GHz, without significant diffraction of emitted acoustic pulses [1].
- **Low power consumption and high SNR:** In this work the 90 μm transducer has been driven by an input RF source of 4 dBm (~ 0.5 V), achieving a Signal-to-Noise Ratio up to 38 dB for the reference measurement (detection surface cleared).
- **Sensitive area (resolution):** Due to its low diffraction at 1.1 GHz, the presented 90 μm transducer is capable of scan 0.008 mm^2 of the detection surface if a single transducer is used for both transmission and reception of the pulse.
- **Sensitivity and linearity:** Concentration change in solutions showed increment of 6.89% in the output voltage level per GPa in the case of Bulk modulus measurements and a change of 1.8% per 100 kRayl for the case of Acoustic Impedance. Calibration curves boast linearity $R^2 > 0.99$ as long as the viscosity of solutions does not exceed 10 cP.
- **Acquisition time:** It corresponds with twice the Time-of-Flight (~ 98 ns).

Moreover, the manufactured device stands out from classic FBAR approaches because of its ease of manufacture; providing superior mechanical robustness and a sensing surface free of electronics where microchannels can be constructed carrying even conductive liquids. This work is envisioned for real-time applications where low-power consumption, easy readout method and size matters; this pulse-echo transducer simply requires measurement of peak voltage.

The following section presents other feasible applications for the pulse-echo transducers.

5.4.1 Other feasible applications: Multiphase flow sensor for real-time detection of slug velocity in microchannels and impedance imaging (fingerprint sensor)

Multiphase flow sensor

Two-phase flow microfluidics involving gas–liquid and liquid–liquid flows has received considerable interest since it overcomes challenges of conventional single-phase microfluidics, such as dispersion, which interferes with the control of mixing time [8]; rapid mixing of miscible liquids can be accomplished efficiently by introducing gas phase bubbles, whereas liquid–liquid systems are of interest for food processing, drug delivery, and material synthesis [9]. Moreover, microscale gas–liquid flow occurs in micro heat exchangers and in microreactors, where the multiphase flow has been shown to significantly increase mass transfer compared to single-phase liquid flow of the same carrying fluid [10].

Introducing gas bubbles or liquid droplets of an immiscible liquid can lead to various flow patterns depending on channel diameter, liquid properties, or liquid and gas volumetric flux; however, in capillaries with diameter of 2 millimeters or less the “slug flow” regime is normally the dominant flow regime [10]. Slug flow is referred in the literature with various other terms including Taylor flow, segmented flow, plug flow, bubble train flow, and intermittent flow. In this condition, alternating segments (bubbles) of immiscible fluids occupy most of the cross section of the microchannel [11]. The scheme in Figure 5.16 is a 2D representation (sagittal view) of a possible system for detecting the size and speed of slugs in immiscible fluids (multiphase flow).

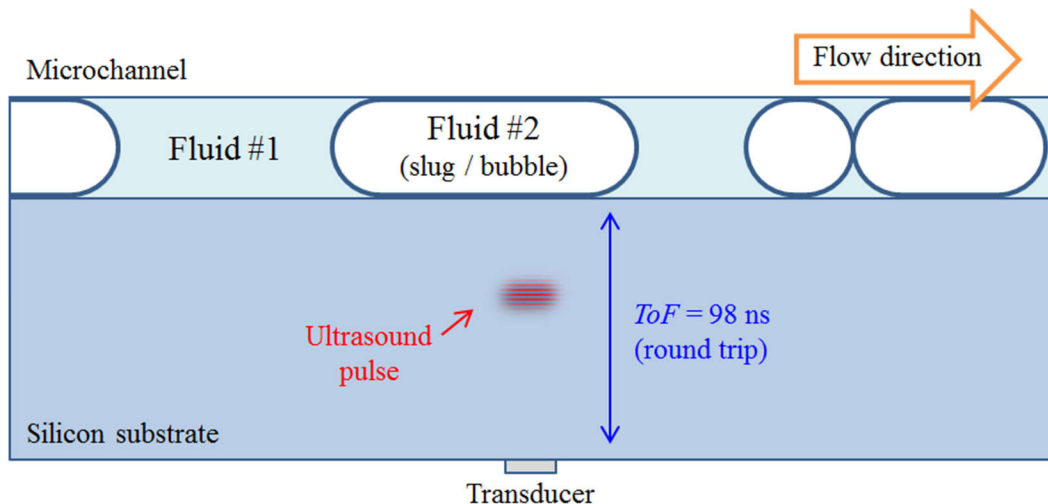


Figure 5.16: 2D representation (sagittal view) of a possible system for detecting the size and velocity of slugs in immiscible fluids (multiphase flow); the system would consist of a microchannel fabricated directly on the detection surface of the pulse-echo sensor, while bulk ultrasound pulses travel inside the thickness of silicon to interact with the fluids ($ToF = 98$ ns). According to theoretical predictions, an air bubble occupying the entire cross section of the channel should reflect more than 99% of the energy emitted by the transducer whereas if water slugs are flowing in front of the transducer more than 14% of the acoustic energy of the pulse enters the liquid medium, thus providing contrast between measurements.

The system in Figure 5.16 consist of a microchannel fabricated directly on the detection surface of the fabricated pulse-echo sensor, while bulk ultrasound pulses travel inside the thickness of silicon

to interact with the fluids in the microchannel and they return to the emitter transducer within a total $ToF \approx 98$ ns. According to the theoretical predictions of Table 3.3 in Chapter 3, an air bubble occupying the entire cross section of the channel should reflect more than 99% of the energy emitted by the transducer whereas if water slugs are flowing in front of the transducer more than 14% of the acoustic energy of the pulse enters the liquid medium and the remainder is reflected back to the transducer, thus providing contrast between measurements depending on the fluid that is in front of the transducer at any given time. To emulate such system, measurements were performed using the setup shown in Figure 5.1, comparing the condition "distilled water on the detection surface" against the condition "air" (detection surface cleared). Figure 5.17 presents the output signal, up to 550 ns, of measurements performed of both conditions.

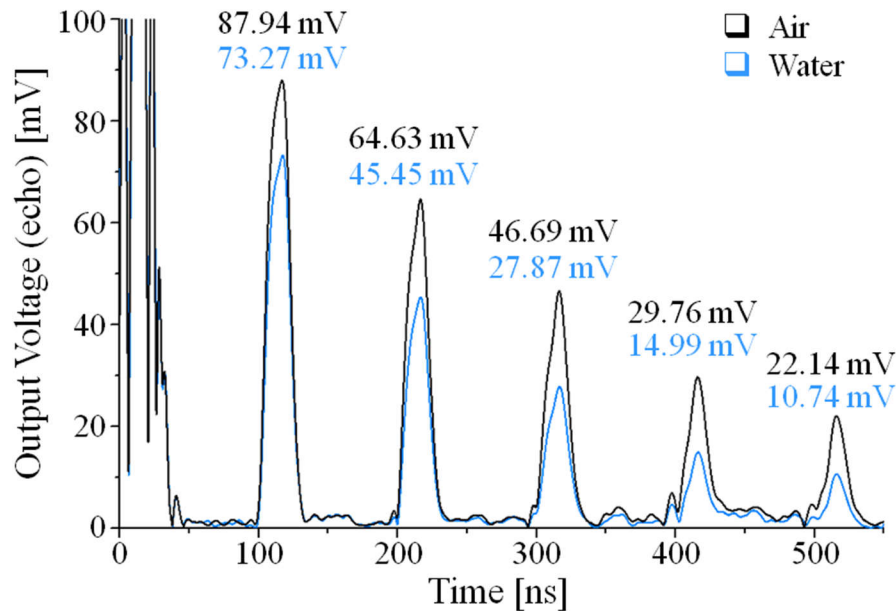


Figure 5.17: Output voltage showing up to five consecutive echoes for both the case of "air" at the detection surface (black) and the case of "water" (blue).

Results correspond with theoretical predictions, since the amplitude of the envelope corresponding to the case of distilled water (blue trace) drops close to 16% respect to the maximum amplitude obtained when the detection surface is cleared (black trace). Current optical methods for continuous fluid monitoring offer detailed and precise flow information, but with the drawback of costly and bulky equipment such as CCD cameras or Particle Image Velocimetry (PIV) [12], therefore, this pulse-echo sensor could be a low-cost alternative of low power requirement and high integration capabilities.

Fingerprint sensor

Since acoustic impedance of skin is close to that of water, an array of these transducers could be used for imaging purposes, i.e., as an ultrasonic fingerprint sensor. Figure 5.18a offers a 3D representation of such a system consisting of a linear array of pulse-echo transducers that emit ultrasound pulses through the silicon mass to interrogate materials on their sensing surface. These AlN transducers should interact individually with different microscopic sections of the fingerprint, thus offering contrast in output voltage between transducers interacting with air on their sensing

surface (fingerprint valleys) and transducers interacting with skin (fingerprint ridges) [13]. This is shown in the 2D representation of Figure 5.18b.

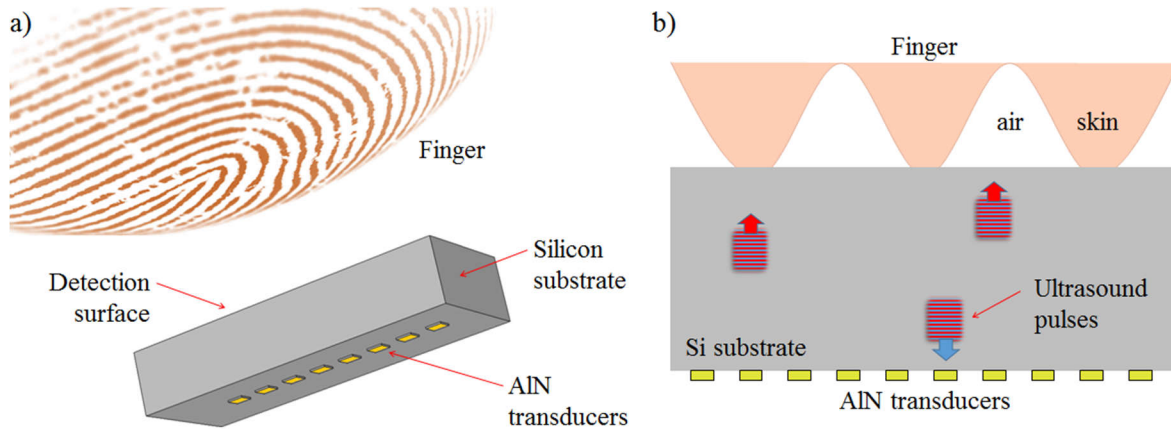


Figure 5.18: Pulse-echo transducers as fingerprint sensor. a) 3D representation. b) 2D cross section.

Table 5.3 offers a comparison to a similar transducer in literature, implemented as an imaging element. In the case of our sensor, the fourth echo has been used to enhance contrast between air and water measurements, at a cost of longer acquisition time (Figure 5.17).

	[14] 2019	This transducer
Technology	AlN MEMS + 0.18 μm CMOS (monolithic)	AlN MEMS + Off the shelf electronics
Mode of operation	Pulse-echo	Pulse-echo
Number of transducers	2 (Transmitter + Receiver)	1 (Same element for Tx & Rx)
Drive voltage	> 1 V	< 0.4 V
Frequency of operation	1.69 GHz	1 – 10 GHz range
Contrast	2.3 : 1	2 : 1
Acquisition time	344 ns (Second echo)	400 ns (Fourth echo)

Table 5.3: Comparison to a similar transducer implemented as a fingerprint sensor [1].

Our pulse-echo transducer consist of only one single element for both Tx and Rx, reducing significantly the footprint in the wafer and it requires half of the drive voltage to obtain similar contrast. Moreover, according with the diffraction condition $w \sin \theta = \lambda$, our approach with multi-frequency capability up to 10 GHz would allow single transducers of width $w = 25 \mu\text{m}$ sending low diffraction pulses of ultrasound to scan the detection surface with a lateral resolution of $30 \mu\text{m}$, improving current ultrasonic sensors while offering a low input impedance of 150Ω .

Future work in this regard should include the study of collaborative behavior of arrays of this pulse-echo transducers either to improve SNR (focusing) or to perform a 2D sweep of the detecting surface (steering), i.e., by using phased arrays. The latter is not a trivial endeavor, since coupling of higher input impedance transducers and issues regarding to electrical/mechanical coupling should be solved.

References

- [1] Jesus Yanez, Arantxa Uranga, Nuria Barniol, Fluid compressional properties sensing at microscale using a longitudinal bulk acoustic wave transducer operated in a pulse-echo scheme, *Sensors and Actuators A: Physical*, vol. 334, 2022, <https://doi.org/10.1016/j.sna.2021.113334>
- [2] F. Jaeger, O. Matar, and E. Müller, Bulk viscosity of molecular fluids, *Journal of Chemical Physics*, vol. 148, 2018, <https://doi.org/10.1063/1.5022752>
- [3] H. Antlinger, S. Clara, R. Beigelbeck, S. Cerimovic, F. Keplinger, and B. Jakoby, Sensing the characteristic acoustic impedance of a fluid utilizing acoustic pressure waves, *Sensors and Actuators A: Physical*, vol. 186, pp. 94–99, 2012, <https://doi.org/10.1016/j.sna.2012.02.050>
- [4] Cheng Nian-Sheng, Formula for the viscosity of a glycerol–water mixture, *Industrial & Engineering Chemistry Research*, vol. 47 (9), pp. 3285–3288, 2008, <https://doi.org/10.1021/ie071349z>
- [5] Cédric Ayela and Liviu Nicu, Micromachined piezoelectric membranes with high nominal quality factors in newtonian liquid media: a Lamb’s model validation at the microscale, *Sensors and Actuators B: Chemical*, vol. 123, pp. 860–868, 2007, <https://doi.org/10.1016/j.snb.2006.10.048>
- [6] Yao Lu, Menglun Zhang, Hongxiang Zhang, Yuan Jiang, Hao Zhang, Wei Pang, Microfluidic bulk-modulus measurement by a nanowavelength longitudinal-acoustic-wave microsensor in the nonreflective regime, *Physical Review Applied*, vol. 11, 2019, <https://doi.org/10.1103/PhysRevApplied.11.044091>
- [7] J. Yanez, E. Ledesma, A. Uranga and N. Barniol, AlN-based HBAR ultrasonic resonator for fluid detection in microchannels with multi-frequency operation capability over the GHz range, *IEEE International Ultrasonics Symposium (IUS)*, pp. 1–4, 2021, <https://doi.org/10.1109/IUS52206.2021.9593369>
- [8] A. Bordbar, A. Taassob, A. Zarnaghsh, and R. Kamali, Slug flow in microchannels: Numerical simulation and applications, *Journal of Industrial and Engineering Chemistry*, vol. 62, pp. 26–39, 2018, <https://doi.org/10.1016/j.jiec.2018.01.021>
- [9] T. Kraus, A. Günther, N. de Mas, M. Schmidt, and K. Jensen, An integrated multiphase flow sensor for microchannels, *Experiments in Fluids*, vol. 36, 819–832, 2004, <https://doi.org/10.1007/s00348-003-0764-0>
- [10] T. Bandara, N. Nguyen, and G. Rosengarten, Slug flow heat transfer without phase change in microchannels: A review, *Chemical Engineering Science*, vol. 126, pp. 283–295, 2015, <https://doi.org/10.1016/j.ces.2014.12.007>
- [11] V. Hessel, A. Renken, J. Schouten, and J. Yoshida, *Micro Process Engineering: A Comprehensive Handbook*, Wiley-VCH First Ed., 2009
- [12] S. Gagliano, G. Stella, and M. Bucolo, Real-Time Detection of Slug Velocity in Microchannels, *Micromachines*, vol. 11 (3), 2020, <https://doi.org/10.3390/mi11030241>

- [13] J. Kuo, J. Hoople, M. Abdelmejeed, M. Abdel-moneum and A. Lal, 64-Pixel solid state CMOS compatible ultrasonic fingerprint reader, 2017 IEEE 30th International Conference on Micro Electro Mechanical Systems (MEMS), pp. 9–12, 2017, <https://doi.org/10.1109/MEMSYS.2017.7863326>
- [14] M. Abdelmejeed, J. Kuo, A. Ravi and A. Lal, CMOS Controlled GHz Ultrasonic Impedance Imager, 20th International Conference on Solid-State Sensors, Actuators and Microsystems & Eurosensors XXXIII (TRANSDUCERS & EUROSENSORS XXXIII), pp. 57–60, 2019, <https://doi.org/10.1109/TRANSDUCERS.2019.8808493>

APPENDIX A

Code

Appendix A contains relevant code (some functions) of the tools that were created for the design of the devices, as well as those that were used for post-processing of *.CSV files (measurements or FEM results). MCU configuration is also included.

A.1 Pulse-echo post-processing

Figure A.1 shows the Graphical User Interface (GUI) of the tool used for post-processing of echo measurements (*.CSV files coming from the scope). This tool loads to memory the file content and displays it on the first plot (electrical signal in blue color relating voltage amplitude (volts) and time (seconds)).

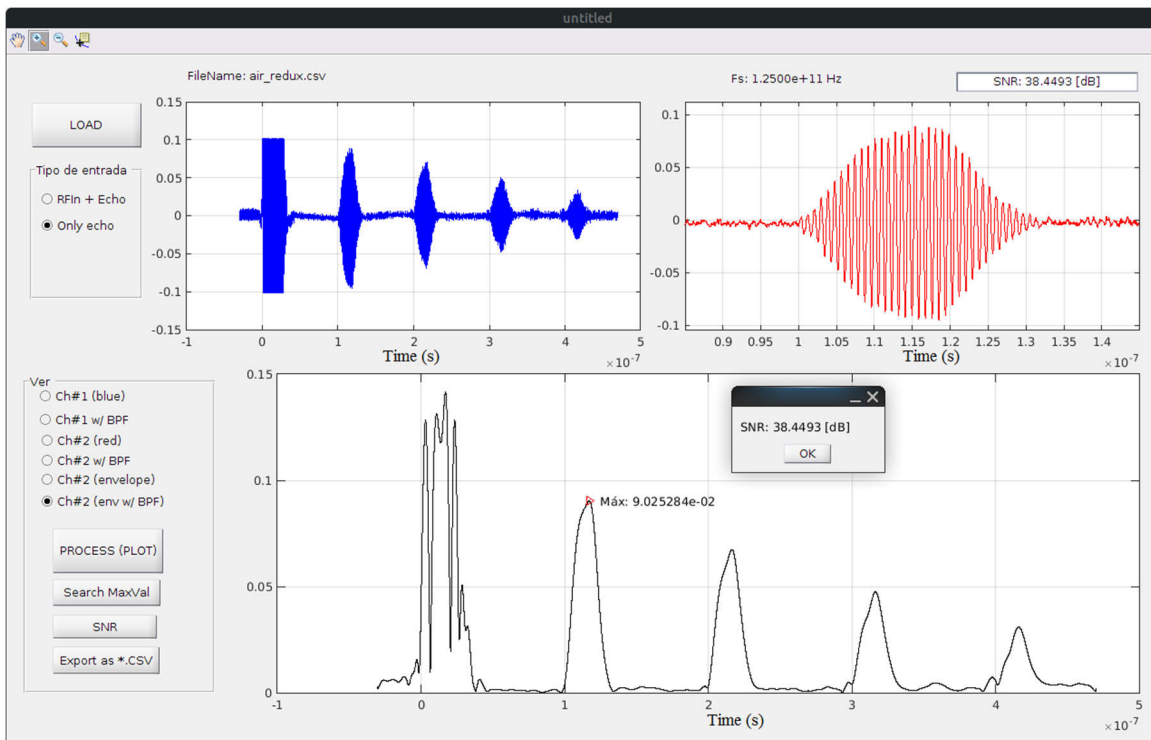


Figure A.1: Graphical User Interface of the tool created for post-processing of echo measurements.

The largest plot in Figure A.1 (electrical signal in black color) presents the result of the post-processing, which depends on the current state of the radial buttons; the "BPF" option applies a band-pass filter to the input signal, the "envelope" option obtains the Hilbert transform, and "env w/ BPF" does both.

Additionally, the "Search MaxVal" button allows selection of regions where a maximum value of amplitude will be searched and the "SNR" button obtains the Signal to Noise Ratio. The "Export" button creates a *.CSV from the curve in the results plot and optionally downsampling can be performed to reduce the number of points

Function to apply a band-pass filter:

```

1. function [signal, filtro] = filtroBP(tiempo, y, Fs, handles)
2. tSamples = length(tiempo);
3. Y = fft(y);
4. P2 = abs(Y / tSamples);
5. P1 = P2(1 : tSamples/2 + 1);
6. P1(2 : end-1) = 2 * P1(2 : end-1);
7. f = Fs * (0 : (tSamples / 2)) / tSamples;
8. plot(handles.axes3, f, P1);
9. grid(handles.axes3, 'on');
10. grid minor;
11. xlim([0 8e9]);
12. info = msgbox('Selecciona dónde se buscará el pico de frecuencia (banda de paso)');
13. waitfor(info);
14. [freq , ~] = ginput(2);
15. [~, iInf] = min(abs(f - freq(1)));
16. [~, iSup] = min(abs(f - freq(2)));
17. freqP = f(iInf : iSup);
18. specP = P1(iInf : iSup);
19. [maxY, ifrP] = max(specP);
20. frP = freqP(ifrP);
21. hold(handles.axes3, 'on');
22. plot(handles.axes3, frP, maxY, 'r>');
23. hold(handles.axes3, 'off');
24. text(frP, maxY, sprintf(' frP: %.6e [Hz]', frP));
25. info = msgbox(sprintf('Se encontró máximo en: %.4e', frP));
26. waitfor(info);
27. Fn = Fs/2;
28. passFreqSpan = 100e6;
29. stopFreq = 200e6;
30. Wp = [(frP - passFreqSpan), (frP + passFreqSpan)] / Fn;
31. Ws = [(frP - stopFreq), (frP + stopFreq)] / Fn;
32. Rp = 1;
33. Rs = 30;
34. [n, Ws] = cheb2ord(Wp, Ws, Rp, Rs);
35. [z, p, k] = cheby2(n, Rs, Ws);
36. sosbp = zp2sos(z, p, k);
37. signal = filtfilt(sosbp, 1, y);
38. freqMedia = meanfreq(signal, Fs);
39. set(handles.editAux, 'String', sprintf('Freq Media: %.6e', freqMedia));
40. filtro = sosbp;

```

Function to obtain the Hilbert Transform (envelope of the signal):

1. function [env] = envelope(signal)
2. complex = hilbert(signal);
3. env = abs(complex);

Function to obtain the maximum amplitude:

1. function btnMax_Callback(~, ~, handles)
2. ejeX = handles.ejeX;
3. ejeY = handles.outputSgnl;
4. info = msgbox('Selecciona dónde se buscará el pico');
5. waitfor(info);
6. [x, ~] = ginput(2);
7. [~, iInf] = min(abs(ejeX - x(1)));
8. [~, iSup] = min(abs(ejeX - x(2)));
9. subX = ejeX(iInf : iSup);
10. subY = ejeY(iInf : iSup);
11. [maxY, indx] = max(subY);
12. maxX = subX(indx);
13. hold(handles.axes3, 'on');
14. plot(handles.axes3, maxX, maxY, 'r>');
15. hold(handles.axes3, 'off');
16. text(maxX, maxY, sprintf(' Máx: %.6e', maxY));
17. set(handles.editAux, 'String', sprintf('MaxVal: %.6e', maxY));
18. info = msgbox(sprintf('Se encontró máximo en: t = %.4e', maxX));
19. waitfor(info);

Function to obtain the Signal-to-Noise Ratio:

1. function btnSNR_Callback(~, ~, handles)
2. tiempo = handles.ejeX;
3. amplitud = handles.outputSgnl;
4. info = msgbox('Selecciona un segmento con RUIDO');
5. waitfor(info);
6. [t, ~] = ginput(2);
7. [~, iInf] = min(abs(tiempo - t(1)));
8. [~, iSup] = min(abs(tiempo - t(2)));
9. noise = amplitud(iInf : iSup);
10. rmsNoise = rms(noise);
11. info = msgbox('Selecciona un segmento con Señal');
12. waitfor(info);
13. [t, ~] = ginput(2);
14. [~, iInf] = min(abs(tiempo - t(1)));
15. [~, iSup] = min(abs(tiempo - t(2)));
16. signal = amplitud(iInf : iSup);
17. rmsSignal = rms(signal);
18. snRatio = snr(rmsSignal, rmsNoise);
19. set(handles.editAux, 'String', sprintf('SNR: %.4f [dB]', snRatio));
20. info = msgbox(sprintf('SNR:'));
21. waitfor(info);

A.2 HBAR calculation tool (up to four layers)

This tool has been used to predict the electrical response (frequency) of both pulse-echo transducers and resonators; it is basically the implementation of equations 10, 15 and 16 from Chapter 2. Figure A.2 shows the response of a device corresponding to materials and dimensions shown in Figure 3.8 of Chapter 3, using material properties from Table 3.2 (Chapter 3) and the COMSOL Multiphysics materials library.

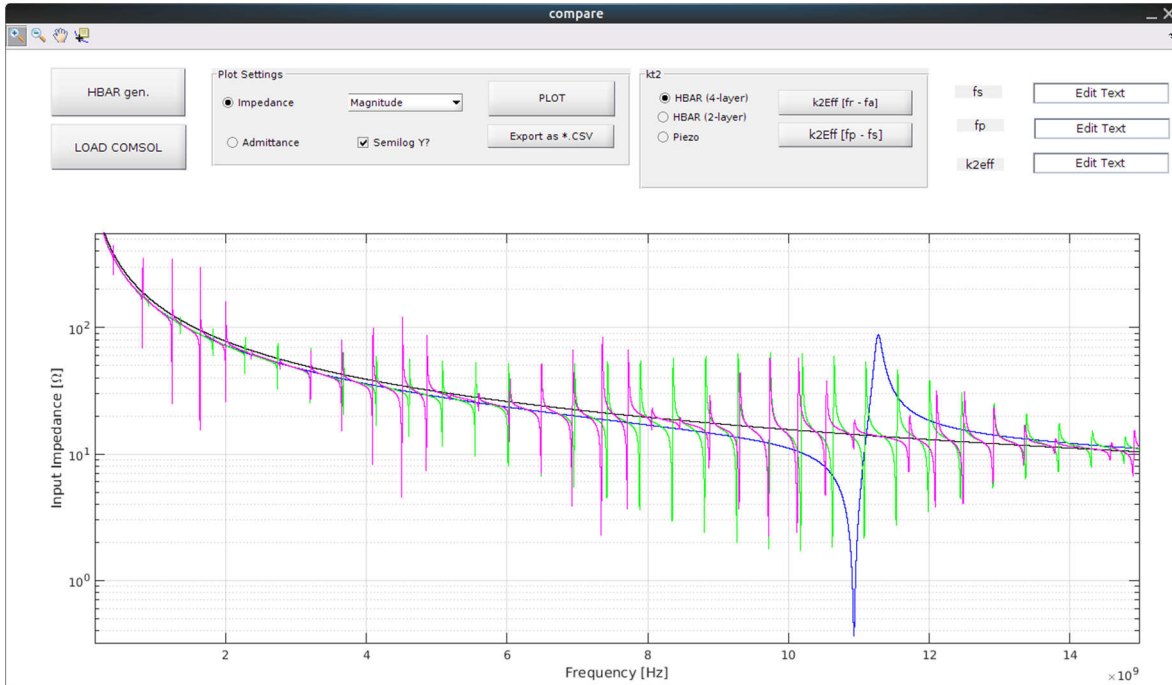


Figure A.2: Graphical User Interface of the tool created to predict electrical response (frequency) of HBARs.

Curves in the plot area correspond to static capacitance (black trace), isolated response of the piezoelectric layer (blue), simple HBAR (green), and HBAR including the effect of electrodes (magenta). The plot allows visualization as Impedance, Admittance and their magnitude value, real or imaginary, as well as zoom in and obtain amplitude and frequency value at a selected point. The tool allows importing *.CSV files (measurements or FEM results) to calculate k_{eff}^2 and exports the plot content as *.CSV. The most relevant function is the one that implements equations 10, 15 and 16 from Chapter 2:

Function: generateHBAR()

1. function [freqHbar, zHbar, zCap, zPiezo, zHbarE] = generateHbar()
2. *% INPUT DATA*
3. prompt = {'Init. Freq. [Hz]', 'Final Freq. [Hz]', 'Freq. Step [Hz]', ...
4. 'Vac. Permittivity [F/m]', 'PIEZO: Diel. constant', 'PIEZO: Area [m^2]', ...
5. 'PIEZO: Thickness [m]', 'PIEZO: Density [Kg/m3]', 'PIEZO: Sound vel. [m/s]', ...
6. 'SUBS: Density [Kg/m3]', 'SUBS: Sound vel. [m/s]', 'SUBS: Thickness [m]', ...
7. 'cE_{33} [N/m^2]', 'eS_{33} [C/m^2]', 'TopElec. Thickness [m]', ...
8. 'TopElec Densty [Kg/m3]', 'TopElec Snd vel. [m/s]', 'BottomElec. Thick [m]', ...
9. 'BottomElec. Density [Kg/m3]', 'BottomElec. Sound vel. [m/s]};
10. dlgtitle = 'Settings';

```

11. dims = [0.8 35];
12. definput = {'100e6', '15e9', '0.1e6', '8.8542e-12', '9', '6.4e-9', '0.5e-6', ...
13.   '3300', '10954 + 5i', '2329', '9660 + 5i', '10e-6', '3.89e11 + 0.1i', '1.55 + 0.1i', ...
14.   '1e-6', '2700', '6450 + 5i', '0.0001e-6', '2700', '6450 + 5i'};
15. opts.Interpreter = 'tex';
16. inputS = inputdlg(prompt, dlgtitle, dims, definput, opts);
17. fi = str2double(inputS(1));
18. ff = str2double(inputS(2));
19. fstp = str2double(inputS(3));
20. e0 = str2double(inputS(4));
21. er = str2double(inputS(5));
22. m2 = str2double(inputS(6));
23. l = str2double(inputS(7));
24. p = str2double(inputS(8));
25. V = str2double(inputS(9));
26. pb = str2double(inputS(10));
27. Vb = str2double(inputS(11));
28. b = str2double(inputS(12));
29. cE33 = str2double(inputS(13));
30. eS33 = str2double(inputS(14));
31. d1 = str2double(inputS(15));
32. pE1 = str2double(inputS(16));
33. VE1 = str2double(inputS(17));
34. d2 = str2double(inputS(18));
35. pE2 = str2double(inputS(19));
36. VE2 = str2double(inputS(20));
37. % OPERATIONS
38. freqHbar = fi : fstp : ff;
39. zCap = zeros(size(freqHbar));
40. zHbar = zeros(size(freqHbar));
41. epsS33 = e0 * er;
42. cCap = (epsS33 * m2) / l;
43. h33 = eS33/epsS33;
44. cD33 = cE33 + (eS33 * h33);
45. k2t = (h33^2 * epsS33)/cD33;
46. fp = sqrt(cD33/(4 * p * l^2));
47. % Clamped capacitance
48. for m = 1 : length(freqHbar)
49.   zCap(m) = -1i / (2 * pi * freqHbar(m) * cCap);
50. end
51. Zbs = pb * Vb;
52. Z = p * V;
53. zb = Zbs / Z;
54. % Hbar (1999 - Wang)
55. for k = 1 : length(freqHbar)
56.   gb = 2 * pi * freqHbar(k) * (b / Vb);
57.   g = 2 * pi * freqHbar(k) * (l / V);
58.   num = (2 * tan(g/2)) + (zb * tan(gb));
59.   den = (1 + (zb * (tan(gb) / tan(g))));
60.   A = 1/(1i * 2 * pi * freqHbar(k) * cCap);
61.   B = k2t / g;
62.   C = num / den;
63.   zHbar(k) = A * (1 - (B * C));

```

```

64. end
65. % Piezo Only (IEEE std, thickness mode), pp59
66. zPiezo = zeros(size(freqHbar));
67. for m = 1 : length(freqHbar)
68.     alph = (2 * pi * freqHbar(m))/(4 * fp);
69.     fact2 = 1 - (k2t * (tan(alph)/alph));
70.     fact1 = 1/(1i * m2 * 2 * pi * freqHbar(m) * epsS33);
71.     zPiezo(m) = fact1 * fact2;
72. end
73. % Hbar with electrodes (Zhang 2000/2003)
74. Ze1 = pE1 * VE1;
75. Ze2 = pE2 * VE2;
76. zHbarE = zeros(size(freqHbar));
77. for k = 1 : length(freqHbar)
78.     gE1 = 2 * pi * freqHbar(k) * (d1 / VE1);
79.     gE2 = 2 * pi * freqHbar(k) * (d2 / VE2);
80.     gb = 2 * pi * freqHbar(k) * (b / Vb);
81.     g = 2 * pi * freqHbar(k) * (l / V);
82.     Zb = 1i * Ze1 * tan(gE1);
83.     num = (Zbs * cos(gE2) * sin(gb)) + (Ze2 * sin(gE2) * cos(gb));
84.     den = (cos(gE2) * cos(gb)) - ((Zbs / Ze2) * sin(gE2) * sin(gb));
85.     ZLo = 1i * (num/den);
86.     zb = Zb / Z;
87.     z2 = ZLo / Z;
88.     num = ((zb + z2) * sin(g)) + (1i * 2 * (1 - cos(g)));
89.     den = ((zb + z2) * cos(g)) + (1i * (1 + (zb * z2)) * sin(g));
90.     A = 1 / (1i * 2 * pi * freqHbar(k) * cCap);
91.     B = k2t / g;
92.     C = num / den;
93.     zHbarE(k) = A * (1 - (B * C));
94. end

```

A.3 De-embedding and S11-to-Zin tool.

This tool performs the measurement calibration (de-embedding) procedure described in section 4.2.2 from Chapter 4, and the conversion from S_{11} to Z_{in} described in section 4.2.3 (Chapter 4). It requires as input *.CSV files containing both real and imaginary values of the "raw" measurement, as well as measurements to the "open" and "short" dummy structures described in Chapter 4, i.e., six measurements as shown in Figure A.3.







Name	Size	Type	Date Modified
 air_opn_s11_Im.csv	100.8 kB	CSV document	sáb 10 dic 2022 20:06:12
 air_opn_s11_Re.csv	100.8 kB	CSV document	sáb 10 dic 2022 20:06:19
 air_raw_s11_Im.csv	100.8 kB	CSV document	sáb 10 dic 2022 20:06:27
 air_raw_s11_Re.csv	100.8 kB	CSV document	sáb 10 dic 2022 20:06:34
 air_sht_s11_Im.csv	100.8 kB	CSV document	sáb 10 dic 2022 20:06:41
 air_sht_s11_Re.csv	100.8 kB	CSV document	sáb 10 dic 2022 20:06:47

Figure A.3: Measurements required for measurement calibration.

Figure A.4 shows the graphical interface of this tool, once all the required files have been loaded using the "Load files <S11>" button and the reference impedance has been selected, the plot at the top will show the information from the input files, as well as the de-embedded measurement (the black curve).

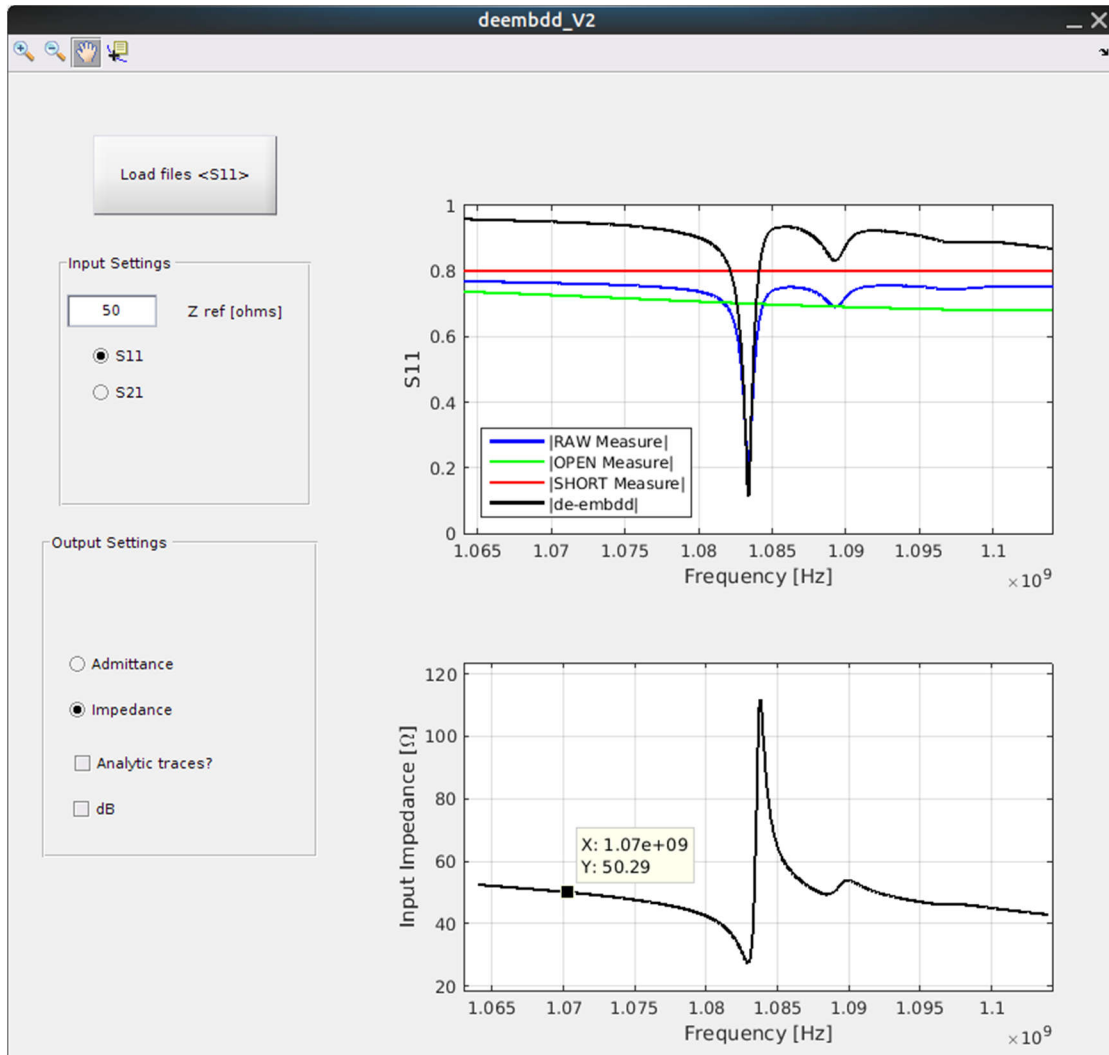


Figure A.4: Graphical interface of the tool created for measure calibration and S11-to-Zin conversion.

The plot at the bottom shows the conversion of the S_{11} measurement (de-embedded) to input impedance Z_{in} . The de-embedded measurement and the input impedance curve are exported as *.CSV files in the same folder where the input measurements are located. Relevant functions are:

Function: loadS11()

It loads the files and creates the complex vectors "raw_cmplx", "opn_cmplx", and "sht_cmplx", containing the information of the raw measurement and that for the "open" and "short" structures, respectively.

```

1. function [freq, raw_cmplx, opn_cmplx, sht_cmplx, outFileNames] = loadS11()
2. freq = 1;
3. rawS11Re = 1;
4. rawS11Im = 0;
5. opnS11Re = 1;
6. opnS11Im = 0;
7. shtS11Re = 1;
8. shtS11Im = 0;
9. outFileNames = 'error.csv';
10. strng = strcat('Debes contar con archivos:', ...
11. ' <filename>_raw_s11_Re.csv', ...
12. ' <filename>_raw_s11_Im.csv', ...
13. ' <filename>_opn_s11_Re.csv', ...
14. ' <filename>_opn_s11_Im.csv', ...
15. ' <filename>_sht_s11_Re.csv', ...
16. ' <filename>_sht_s11_Im.csv', ...
17. 'Selecciona el archivo "<filename>_raw_s11_Re.csv"', ...
18. '* Deben contener un renglon de "cabecera" y columnas con datos', ...
19. ' freq val', ...
20. ' 000 231', ...
21. ' ... ...');
22. info = msgbox(strng);
23. waitfor(info);
24. [fileRawRe, path] = uigetfile('*.csv', 'S11 (Real)');
25. fileRawRe = fullfile(path, fileRawRe);
26. k = strfind(fileRawRe, 'raw_s11_Re.csv');
27. if(k ~= 0) % El archivo contiene 'raw_s11_Re.csv'
28. fileRawIm = strrep(fileRawRe, 'raw_s11_Re', 'raw_s11_Im');
29. fileOpnRe = strrep(fileRawRe, 'raw_s11_Re', 'opn_s11_Re');
30. fileOpnIm = strrep(fileRawRe, 'raw_s11_Re', 'opn_s11_Im');
31. fileShtRe = strrep(fileRawRe, 'raw_s11_Re', 'sht_s11_Re');
32. fileShtIm = strrep(fileRawRe, 'raw_s11_Re', 'sht_s11_Im');
33. fRe_id = fopen(fileRawRe, 'r');
34. fIm_id = fopen(fileRawIm, 'r');
35. if(fRe_id > 0 && fIm_id > 0)
36. fgetl(fRe_id);
37. fgetl(fIm_id);
38. csvData = textscan(fRe_id, '%f %f %f', 'Delimiter', ',', 'MultipleDelimsAsOne', 1);
39. freq = csvData{1};
40. rawS11Re = csvData{2};
41. csvData = textscan(fIm_id, '%f %f %f', 'Delimiter', ',', 'MultipleDelimsAsOne', 1);
42. rawS11Im = csvData{2};
43. else
44. msgbox('Error abriendo archivos "raw_s11_xx.csv"');
45. end
46. fRe_id = fopen(fileOpnRe, 'r');
47. fIm_id = fopen(fileOpnIm, 'r');
48. if(fRe_id > 0 && fIm_id > 0)
49. fgetl(fRe_id);
50. fgetl(fIm_id);
51. csvData = textscan(fRe_id, '%f %f %f', 'Delimiter', ',', 'MultipleDelimsAsOne', 1);
52. opnS11Re = csvData{2};
53. csvData = textscan(fIm_id, '%f %f %f', 'Delimiter', ',', 'MultipleDelimsAsOne', 1);

```

```

54.     opnS11Im = csvData{2};
55. else
56.     msgbox('Error abriendo archivos "opn_s11_xx.csv");
57. end
58. fRe_id = fopen(fileShtRe, 'r');
59. fIm_id = fopen(fileShtIm, 'r');
60. if(fRe_id > 0 && fIm_id > 0)
61.     fgetl(fRe_id);
62.     fgetl(fIm_id);
63.     csvData = textscan(fRe_id, '%f %f %f', 'Delimiter', ',', 'MultipleDelimsAsOne', 1);
64.     shtS11Re = csvData{2};
65.     csvData = textscan(fIm_id, '%f %f %f', 'Delimiter', ',', 'MultipleDelimsAsOne', 1);
66.     shtS11Im = csvData{2};
67. else
68.     msgbox('Error abriendo archivos "sht_s11_xx.csv");
69. end
70. fclose('all');
71. msgbox('Archivos cargados, clic en "Plot" para continuar');
72. outFileFileName = fileRawRe;
73. else
74.     msgbox('El archivo seleccionado no contiene "raw_s11_Re.csv");
75. end
76. raw_cmplx = rawS11Re + (1i * rawS11Im);
77. opn_cmplx = opnS11Re + (1i * opnS11Im);
78. sht_cmplx = shtS11Re + (1i * shtS11Im);

```

Function: deemb(raw_cmplx, opn_cmplx, sht_cmplx)

It uses the complex vectors “raw_cmplx”, “opn_cmplx”, and “sht_cmplx” to obtain the de-embedded vector (complex), using equation 25 of Chapter 4.

1. function [demb_cmplx] = deemb(raw_cmplx, opn_cmplx, sht_cmplx)
2. A = (opn_cmplx + sht_cmplx) ./ (2 + opn_cmplx - sht_cmplx);
3. B = (opn_cmplx - A) .* (1 - A);
4. demb_cmplx = (A - raw_cmplx) ./ (A.^2 - (A .* raw_cmplx) - B);

Function: convStoZ(handles, freq, zRef, sRe, sIm)

It uses the reference impedance value and the de-embedded vector to obtain the input impedance (magnitude), using equation 23 in Chapter 4.

1. function [zRe, zIm] = convStoZ(handles, freq, zRef, sRe, sIm)
2. zRe = zeros(size(freq));
3. zIm = zeros(size(freq));
4. if get(handles.radS11, 'value') == 1
5. for m = 1 : length(freq)
6. num = 1 - sRe(m)^2 - sIm(m)^2;
7. den = (1 - sRe(m))^2 + sIm(m)^2;
8. zRe(m) = zRef * (num/den);
9. end
10. for m = 1 : length(freq)
11. num = 2 * sIm(m);
12. den = (1 - sRe(m))^2 + sIm(m)^2;

13. $zIm(m) = zRef * (num/den);$
14. end
15. end

A.4 Acoustic pulse distribution, diffracting arrays, & Phased arrays for steering and focusing

This tool is a compilation of several methods to obtain the pressure distribution of an acoustic pulse at the detection surface. It includes implementation of equations for a "single element" radiating acoustic energy and also arrays of elements interfering with each other. Models predicting the behavior of phased arrays are also included; the required phase shift or time delay is calculated for either steering of the beam or focusing.

Figure A.5 shows the GUI of the program, the "Cargar Datos" button allows entering input data and the "Panel" section contains the implemented methods. Pressing the "PLOT" button prints the pressure distribution in the plot area and the required phase shift will appear in case of phased arrays.

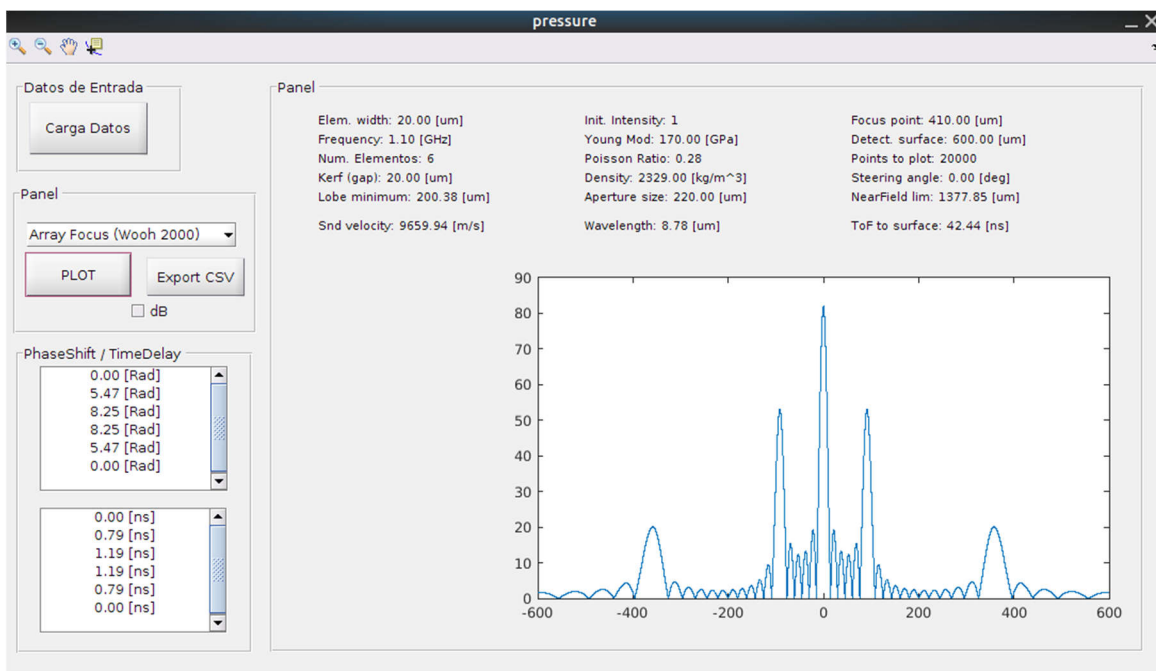


Figure A.5: Graphical interface of the tool created to predict pressure distribution of the acoustic pulse at the detection surface.

For the case of arrays it is required that the user of the program understand the theory behind the equations, since some methods print incorrect results when inadequate input data is provided, for example, trying to focus in the far field.

Function to obtain input data and basic operations:

1. function btnLoad_Callback(hObject, eventdata, handles)
2. cla(handles.axes1,'reset');
3. handles.panelPhase.Visible = 'off';
4. *% input data*
5. prompt = {'Element width [m]', 'Frequency [Hz]', '# of elements', ...

```

6. 'Kerf width (Gap) [m]', 'Initial intensity', '(Medium) Young Modulus [Pa]', ...
7. '(Medium) Poisson Ratio', '(Medium) Density [kg/m^3]', ...
8. 'Distance to Detection (Focus point) [m]', 'Detection Surface size [m]', ...
9. 'Graph Points', 'Steering angle [deg]';
10. dlgtitle = 'Settings';
11. dims = [0.8 30];
12. definput = {'50e-6', '1.1e9', '1', '20e-6', '1', '170e9', '0.28', ...
13. '2329', '410e-6', '600e-6', '20000', '0'};
14. opts.Interpreter = 'tex';
15. inputS = inputdlg(prompt, dlgtitle, dims, definput, opts);
16. w = str2double(inputS(1));
17. f = str2double(inputS(2));
18. N = str2double(inputS(3));
19. krf = str2double(inputS(4));
20. p0 = str2double(inputS(5));
21. E_Si = str2double(inputS(6));
22. v_Si = str2double(inputS(7));
23. p_Si = str2double(inputS(8));
24. D = str2double(inputS(9));
25. rng = str2double(inputS(10));
26. qlty = str2double(inputS(11));
27. Sa = str2double(inputS(12));
28. % operaciones y reserva de memoria para vectores
29. num = E_Si * (1 - v_Si);
30. den = p_Si * (1 + v_Si) * (1 - (2 * v_Si));
31. c_Si = sqrt(num/den);
32. G_Si = E_Si / (2 * (1 + v_Si));
33. c_Si_s = sqrt(G_Si / p_Si);
34. lamb = c_Si / f;
35. vf_Si = lamb * f;
36. ToF = D / c_Si;
37. omeg = 2 * pi * f;
38. k = (2 * pi) / lamb;
39. y = -rng : rng / qlty : rng;
40. x = D;
41. A = zeros(1, length(y));
42. r = zeros(1, length(y));
43. t = zeros(1, length(y));
44. for i = 1 : length(y)
45.     A(i) = atan(y(i)/x);
46. end
47. x2 = x^2;
48. for i = 1 : length(y)
49.     y2 = y(i)^2;
50.     r(i) = sqrt(x2 + y2);
51. end
52. for i = 1 : length(y)
53.     t(i) = r(i) / c_Si;
54. end
55. eMin = D * tan(asin(lamb/w));
56. Ap = ((krf + w) * (N - 1)) + w;
57. nF = (Ap^2) / (4 * lamb);
58. guidata(hObject, handles);

```


Function for single element (Reference 23, Chapter 2):

```
1. function pressure = single_resnick(handles)
2. p0 = handles.p0;
3. w = handles.w;
4. lamb = handles.lamb;
5. A = handles.A;
6. pressure = zeros(1, length(A));
7. for i = 1 : length(A)
8.     alpha = ((pi * w)/lamb) * sin(A(i));
9.     pressure(i) = p0 * (sin(alpha)/alpha)^2;
10. end
```

Function for single element (Equation 21, Chapter 2):

```
1. function pressure = single_fan(handles)
2. A = handles.A;
3. k = handles.k;
4. r = handles.r;
5. w = handles.w;
6. c_Si = handles.c_Si;
7. c_Si_s = handles.c_Si_s;
8. omeg = handles.omeg;
9. t = handles.t;
10. y = handles.y;
11. x = handles.D;
12. p_Si = handles.p;
13. A2 = zeros(1, length(y));
14. for i = 1 : length(y)
15.     A2(i) = atan(y(i)/x);
16. end
17. pressure = zeros(1, length(handles.A));
18. for i = 1 : length(A)
19.     alpha = (k * w * sin(A(i)) * sin(A2(i)))/2;
20.     beta = (k * w * sin(A(i)) * cos(A2(i)))/2;
21.     p1 = (1i * k * c_Si * c_Si_s * p_Si * w * w) / (2 * r(i) * pi);
22.     s1 = sin(alpha) / alpha;
23.     s2 = sin(beta) / beta;
24.     ex = exp(1i * (omeg * t(i)) - (k * r(i)));
25.     pressure(i) = p1 * s1 * s2 * ex;
26. end
```

Function for an array of elements (steering capabilities):

```
1. function pressure = array_wooh1998(handles)
2. A = handles.A;
3. k = handles.k;
4. r = handles.r;
5. w = handles.w;
6. c_Si = handles.c_Si;
7. omeg = handles.omeg;
8. t = handles.t;
9. N = handles.N;
```

```

10. d = w + handles.krf;
11. Sa = handles.Sa;
12. Sr = (pi / 180) * Sa;
13. At = (d * sin(Sr)) / c_Si;
14. pressure = zeros(1, length(A));
15. for i = 1 : length(A)
16.     alpha = (k * w * sin(A(i))) / 2;
17.     beta = ((omeg * At) - (k * d * sin(A(i)))) / 2;
18.     p0 = r(i) * ((2 * k * r(i)) / pi) * exp(1i * (pi/2));
19.     pIn = p0 / r(i);
20.     s1 = sin(alpha) / alpha;
21.     s2 = sin(beta * N) / sin(beta);
22.     ex1 = exp(-1i * alpha);
23.     ex2 = exp(-1i * beta * (N - 1));
24.     ex3 = exp(1i * ((omeg * t(i)) - (k * r(i))));
25.     pressure(i) = pIn * s1 * s2 * ex1 * ex2 * ex3;
26. end
27. handles.panelPhase.Visible = 'on';
28. phRad = 2 * pi * handles.f * At;
29. strPh = sprintf('Ph. Shift: %.2f [Rad]', phRad);
30. strDl = sprintf('T. Delay: %.2f [ns]', At * 1e9);
31. set(handles.editPhase, 'String', strPh);
32. set(handles.editDelay, 'String', strDl);

```

Function for an array of elements (focusing capabilities):

```

1. function pressure = array_wooh2000(handles)
2. A = handles.A;
3. k = handles.k;
4. r = handles.r;
5. w = handles.w;
6. c_Si = handles.c_Si;
7. omeg = handles.omeg;
8. t = handles.t;
9. N = handles.N;
10. f = handles.f;
11. D = handles.D;
12. Sa = handles.Sa;
13. d = w + handles.krf;
14. if Sa == 0
15.     Sa = 0.0000001;
16. end
17. Sr = (pi / 180) * Sa;
18. N2 = (N - 1)/2;
19. At = zeros(1, N);
20. phRad = zeros(1, N);
21. for n = 1 : N
22.     a = 1 + (((N2 * d)/D)^2) + (((2 * N2 * d)/D) * sin(Sr));
23.     b = 1 + (((n - 1) - N2) * d)/D)^2) - ((2 * d * ((n - 1) - N2) * sin(Sr))/D);
24.     At(n) = (D / c_Si) * (sqrt(a) - sqrt(b));
25.     phRad(n) = 2 * pi * f * At(n);
26. end
27. handles.panelPhase.Visible = 'on';

```

```

28. if N > 1
29.   numDelays = length(phRad);
30.   set(handles.editPhase, 'Max', numDelays);
31.   set(handles.editDelay, 'Max', numDelays);
32.   strPh = sprintf("%.2f [Rad]\n", phRad);
33.   strDl = sprintf("%.2f [ns]\n", At * 1e9);
34.   set(handles.editPhase, 'String', strPh);
35.   set(handles.editDelay, 'String', strDl);
36. end
37. dt = (d * sin(Sr)) / c_Si;
38. pressure = zeros(1, length(A));
39. for m = 1 : length(A)
40.   p0 = r(m) * ((2 * k * r(m)) / pi) * exp(1i * (pi/2));
41.   c1 = sqrt(p0 / r(m));
42.   alpha = (k * w * sin(A(m))) / 2;
43.   s1 = sin(alpha) / alpha;
44.   ex1 = exp(-1i * alpha);
45.   suma = 0;
46.   for n = 0 : N-1
47.     Al = (((c_Si * (N - 1)) / (2 * D * tan(Sr)^2)) * dt^2) - (omeg * dt) + (k * d * sin(A(m)));
48.     Be = (c_Si * dt^2) / (2 * D * tan(Sr)^2);
49.     temp = exp(1i * ((Al * n) + (Be * n^2)));
50.     suma = suma + temp;
51.   end
52.   ex2 = exp(1i * ((omeg * t(m)) - (k * r(m))));
53.   pressure(m) = c1 * s1 * ex1 * suma * ex2;
54. end

```

A.5 MCUs High-Resolution Timer setup

To achieve the rise and fall time requirements to obtain the RF excitation pulse shown in Figure 4.22 of Chapter 4 it is necessary proper configuration of the clocks. Clocks and high-resolution timers have been prepared using the initialization code generator STM32CubeMX, included in the STM32Cube IDE. Figure A.6 shows clock configuration for Core and high-resolution timers.

Activation of HR Timers:

The STM32CubeMX initialization tool generates the code necessary for correct configuration of the MCU, therefore, the user simply has to add their routine within a "while()" control structure. The following code is the implementation of the timing diagram shown in Figure 4.21c from Chapter 4.

```

1. HAL_HRTIM_SimplePWMStart(&hhrtim, HRTIM_TIMERINDEX_TIMER_A, HRTIM_OUTPUT_TA1);
2. HAL_HRTIM_SimplePWMStart(&hhrtim, HRTIM_TIMERINDEX_TIMER_B, HRTIM_OUTPUT_TB1);
3. while (1)
4. {
5.   if(HAL_GPIO_ReadPin(GPIOC, GPIO_PIN_13)==GPIO_PIN_SET)
6.   {
7.     HAL_GPIO_WritePin(GPIOE, GPIO_PIN_1, GPIO_PIN_SET);
8.     HAL_Delay(2000);
9.     HAL_GPIO_WritePin(GPIOE, GPIO_PIN_1, GPIO_PIN_RESET);
10.    for (int a1=1; a1<2; a1++)
11.    {
12.      HRTIM1_COMMON->CR2 = 0x400;
13.      HRTIM1_COMMON->CR2 = 0x200;

```

```

14.     HAL_Delay(10);
15.     }
16. }
17. }

```

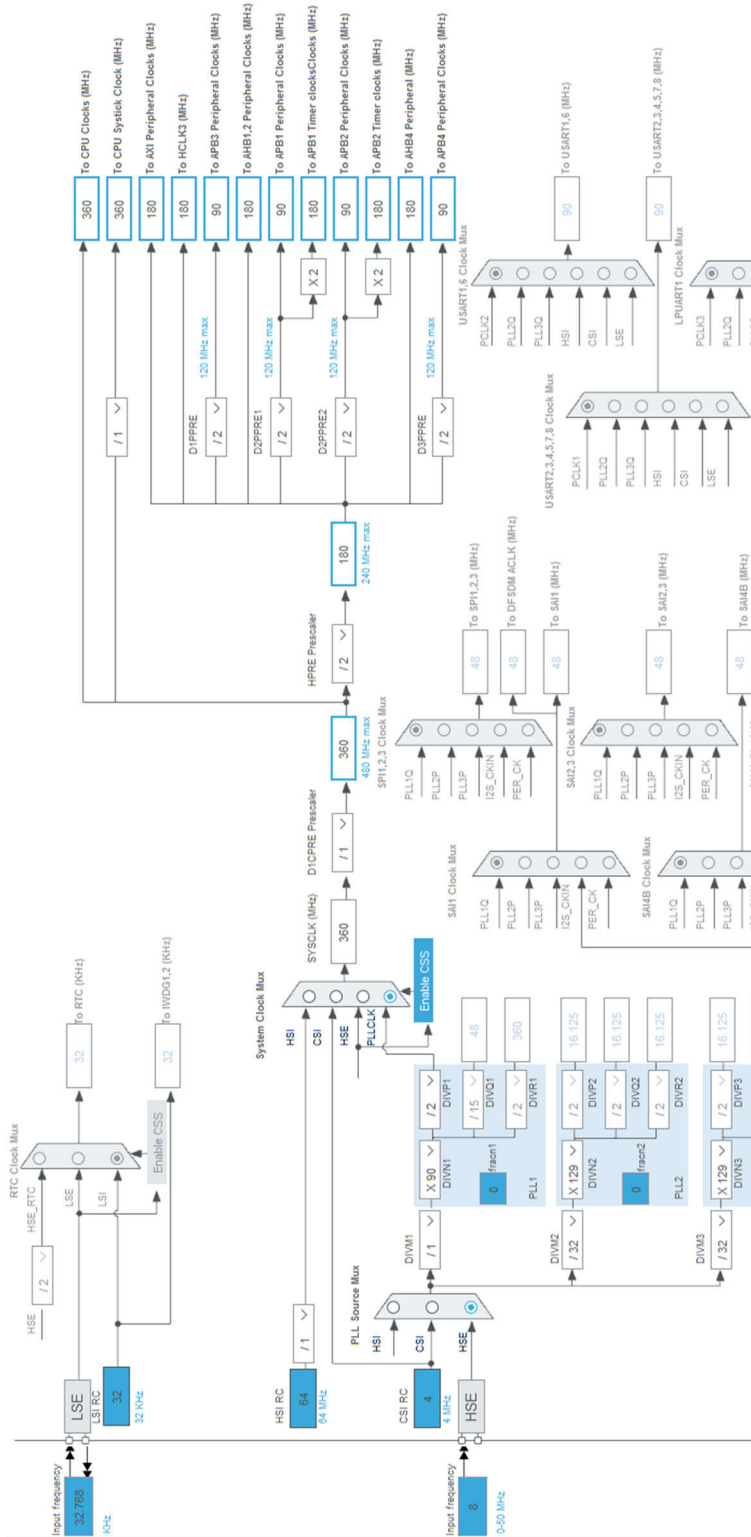


Figure A.6: Clock configuration for Core and high-resolution timers with the STM32CubeMX tool.

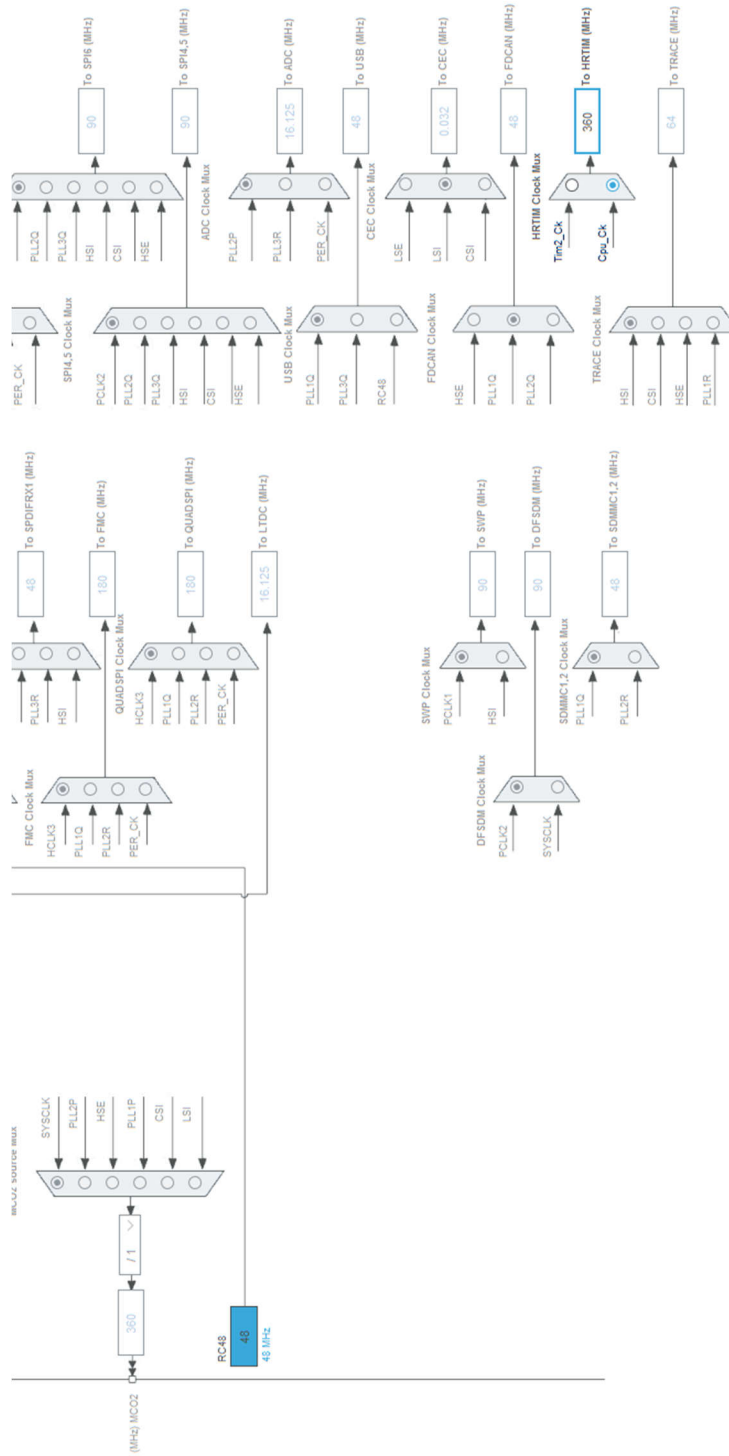


Figure A.6: (Continued).

Figure A.7 shows the Timer configuration to generate a Single pulse.

HRTIM Mode and Configuration

Mode

Master Timer Enable

Timer A TA1 output active v

Configuration

Reset Configuration

✔ User Constants	✔ NVIC Settings	✔ DMA Settings	✔ GPIO Settings
✔ Fault Lines Configuration	✔ ADC Triggers Configuration	✔ Burst Mode Configuration	✔ Timer A
✔ HRTIM Interrupt Configuration	✔ Synchro Configuration	✔ External Event Configuration	

Configure the below parameters :

i

- Timer Idx Timer A
 - Basic/Advanced Configuration Basic (using HAL_Simple methods)
- Prescaler Ratio HRTIM Clock (HRTIM Clock is set in Clock Configuration T...
 - fHRCK Equivalent Frequency 3.6E8 Hz
 - Period 0x0003
 - Resulting PWM Frequency 1.2E8 Hz
 - Repetition Counter 0x00
 - Mode The timer operates in continuous (free-running) mode
- Channel Configuration Disable
- Channel Configuration Disable
- Channel Configuration Enable
 - Polarity Output is active HIGH
 - Idle Level Output at inactive level when in IDLE state
 - Compare Value 0xFFFFD
- Channel Configuration Disable
- Capture Channel Configuration Disable
- Capture Channel Configuration Disable
- Channel Configuration Disable
- Channel Configuration Disable

Figure A.7: Timer configuration to generate a Single pulse.